STUDIES ON COMPOSITES OF GRAPHENE AND TRANSITION METAL COMPOUNDS FOR ELECTROCATALYTIC REACTIONS

Thesis submitted in partial fulfillment

for the award of the degree of

Doctor of Philosophy

by

PRERNA TRIPATHI

Department of Sciences & Humanities

Rajiv Gandhi Institute of Petroleum Technology

JAIS, Amethi, India – 229304

21BS0005 **2025**

CERTIFICATE

It is certified that the work contained in the thesis titled "**Studies on Composites of Graphene and Transition Metal Compounds for Electrocatalytic Reactions**" by "**Prerna Tripathi**" has been carried out under my supervision and this work has not been submitted elsewhere for a degree.

It is further certified that the student has fulfilled all the requirements of Comprehensive, Candidacy, and SOTA.

(Supervisor)

Dr. Shikha Singh

(Co-Supervisor)

Prof. A.S.K. Sinha

DECLARATION BY THE CANDIDATE

I, "**Prerna Tripathi**", certify that the work embodied in this thesis is my own bonafide work and carried out by me under the supervision of "**Dr. Shikha Singh**" and co-supervision of "**Prof. A.S.K. Sinha**" from "AUGUST 2021" to "May 2025", at Rajiv Gandhi Institute of Petroleum Technology, Jais, India.

The matter embodied in this thesis has not been submitted for the award of any other degree. I declare that I have faithfully acknowledged and given credits to the research workers wherever their works have been cited in my work in this thesis. I further declare that I have not willfully copied any other's work, paragraphs, text, data, results, etc., reported in journals, books, magazines, reports dissertations, theses, etc., or available at websites and have not included them in this thesis and have not cited as my own work.

Date:

Place: **RGIPT**

Prerna Tripathi

Roll No.: **21BS0005**

CERTIFICATE BY THE SUPERVISOR(S)

It is certified that the above statement made by the student is correct to the best of my knowledge.

Dr. Shikha Singh		**Prof. A.S.K. Sinha**
(Supervisor)	**Prof. Atul Sharma**	(Co-Supervisor)
	Signature & Seal of Head of Department	

CERTIFICATE

Certified that the work contained in the thesis titled "**Studies on Composites of Graphene and Transition Metal Compounds for Electrocatalytic Reactions**" by Mrs. Prerna Tripathi" has been carried out under my supervision. It is also certified that she fulfilled the mandatory requirement of TWO quality publications arose out of her thesis work.

It is further certified that the three publications (copies enclosed) of the aforesaid Mrs. Prerna Tripathi have been published in the Journals indexed by –

(a) SCI
(b) SCI Extended
(c) SCOPUS
d) *Non-indexed Journals-(only in special cases)(*Please enclose DPGC resolution in this regard)

Dr. Shikha Singh	**Prof. A.S.K. Sinha**	**Dr. Praveen Kumar Srivastava**
(Supervisor)	(Co-Supervisor)	(Convener, DPGC)

N.B.: Please strike out the category (a, b, c, d) that is not applicable

COPYRIGHT TRANSFER CERTIFICATE

Title of the thesis: "Studies on Composites of Graphene and Transition Metal Compounds for Electrocatalytic Reactions"

Name of the student: PRERNA TRIPATHI

Copyright Transfer

The undersigned hereby assigns to the Rajiv Gandhi Institute of Petroleum Technology, Jais all rights under copyright that may exist in and for the above thesis submitted for the award of the" DOCTOR OF PHILOSOPHY".

Date:

Place: **RGIPT**

Prerna Tripathi

Roll No.: **21BS0005**

Note: However, the author may reproduce or authorize others to reproduce material extracted verbatim from the thesis or derivative of the thesis for author's personal use provided that the source and the Institute's copyright notice are indicated.

In loving memory of my grandmother,
'श्रीमती सावित्री देवी'

a guiding light whose love and strength continue to inspire me.....

Dedicated to Papa, Mummy, Didi, Bhai and my Husband....

for their love, support and encouragement....

Acknowledgement

कर्म प्रधानं कर्तव्यम्, ईश्वरः सर्वशक्तिमान्। एतत् केवलं मनुष्यानाम् ज्ञातव्यम्।

"Work is our foremost duty, and God is the supreme power - The ultimate truth mankind must embrace"

First and foremost, I offer my deepest gratitude to the **Almighty**, whose infinite grace and wisdom have brought me to the completion of this Ph.D. journey. It is through His divine will that I have found the strength and clarity to pursue higher knowledge. I thank God not only for opening the doors of academic pursuit but for making me capable of walking through them. With folded hands and a grateful heart, I dedicate the beginning of this journey to Him, the unseen force behind every step, every thought, and every possibility.

I sincerely thank **Rajiv Gandhi Institute of Petroleum Technology (RGIPT)** and the **Department of Sciences and Humanities** for providing me with the opportunity to pursue their Doctoral Program. This milestone would not have been possible without the institute's unconditional support, rich academic environment, and advanced research facilities. I further extend my gratitude to the **National Thermal Power Corporation - National Energy Technology Research Alliance** (**NTPC-NETRA**), for providing me with a fellowship through the project grant (NTPC NETRA − 9100000216-151-1001) on the topic entitled "Development of electrodes and design of a prototype for the Hard/Sea water electrolysis" during the early days of my PhD. I acknowledge the Department of Sciences and Humanities, Rajiv Gandhi Institute of Petroleum Technology, Jais for the Institute Assistantship award during the later part of my Ph.D. program.

I would like to express my profound gratitude to my thesis supervisor, **Dr. Shikha Singh**, for her guidance, patience, and unwavering support throughout my Ph.D. journey, offering me numerous opportunities to explore new ideas, the freedom to conduct independent research, and the space to express myself openly. Dr. Singh has not only been a supervisor but also a mentor, guardian, and a well-wisher. While the student-supervisor relationship can sometimes be complex, I have always found in her a source of constant support and reassurance. Despite the challenges of balancing personal and professional life, particularly after marriage, her silent support gave me the strength to manage both aspects with grace. During times of doubt, her unwavering confidence in my abilities uplifted my spirits. I will forever cherish her strong mentorship and the lesson that the student-guide relationship is not just about research, but about trust, respect, and compassion.

I would like to express my deepest gratitude to my thesis co-supervisor as well as former Director of this institute, **Prof. A. S. K. Sinha**, for his visionary leadership, continuous support, and commitment to fostering an enriching academic environment. I also extend my heartfelt gratitude to the members of my Research Progress Evaluation Committee (RPEC), **Prof. Umaprasana Ojha, Dr. Milan Kumar,** and **Dr. Arshad Aijaz**, for their thorough evaluations and invaluable suggestions, which significantly contributed to the quality and direction of my research.

I would also like to extend my profound gratitude to **Prof. A. K. Choubey**, former **Head of the Department** (Sciences & Humanities), for fostering a welcoming, disciplined, and student-friendly environment within the department. His humility and sincerity leave a lasting impression, making students feel seen, heard, and valued. It is this blend of wisdom and warmth that makes Prof. Choubey a truly respected and cherished figure among

students. I feel privileged to have had his unconditional support and presence during my academic journey.

I would like to sincerely thank our current **Head of the Department, Prof. Atul Sharma** (Sciences & Humanities) for providing advance research facilities and a supportive academic environment that greatly contributed to the successful completion of my work. I am especially grateful to him for regularly checking in on the well-being and needs of students in their lab, an act that reflects not only professional commitment but also deep personal kindness.

Further, I would like to express my sincere gratitude to **Dr. Deepak Dwivedi** (Department of Chemical Engineering), who has been a constant source of support since the beginning of my coursework. His exceptional teaching style rooted in simplifying complex concepts from the basics greatly enhanced my understanding in the subject. Beyond academics, Dr. Dwivedi's kindness, empathy, and unwavering support have been invaluable throughout my PhD journey. Also, my experimental research would not have been possible without the invaluable assistance of **Dr. Deepak Dwivedi** and **Dr. Milan Kumar** (Department of Chemical Engineering) in providing Autolab instrument facility of their respective labs for performing several electrochemical and corrosion studies.

I would like to express my deepest gratitude to **J. Karthikeyan Sir** (Assistant Professor, NIT Durgapur) for understanding my perspectives and working accordingly on it to provide me with the desired theoretical DFT results that helped me in my research.

I would Further like to thank all the teachers especially **Dr. Debashish Panda** (for all the positive criticism and his invaluable guidance during my presentations)**, Dr. Vipin Amoli**

(for his supporting nature and addressing our lab-related concerns with attentiveness and care), **Dr. Malaya Kumar Sahoo**, **Dr. Omveer Singh**, **Dr. Tathamay Basu**, **Dr. V. S. Sistla**, **Dr. Karan Malik**, **Dr. Praveen Srivastava and Dr. Shivanjali Sharma** who have helped me in some way or the other during my PhD journey.

The support of technical and office staff is equally vital for the smooth progression of a long academic journey. I extend my heartfelt gratitude to the office staff **Mahesh Ji**, **Adig Bhaiya**, **Karan Bhaiya** and **Aniruddh Ji** whose constant assistance and goodwill have made my experience smoother and more fulfilling.

The **Central Instrumentation Facilities (CIF)** at Rajiv Gandhi Institute of Petroleum Technology (RGIPT) have been an essential pillar in my research, providing access to state-of-the-art characterization tools. Further, I would like to sincerely acknowledge **Prof. Biswajit Ray Sir** from the **Chemistry Department** of **BHU** for providing insightful discussions and technical support in material characterization and CIF of BHU, Varanasi for helping in TEM characterization, which played a crucial role in my analysis. I further thank **Indian Institute of Science, Bangalore** (**IISC**) for providing me with SEM and TEM facilities that helped me in my research.

A PhD tests not only academic skill but also resilience and emotional strength and having a friend to share both the highs and lows with has truly been a blessing. I'm deeply grateful to my lab mate, **Amit Kumar Verma**, for the countless moments that made this journey easier and more fulfilling, whether it was discussing experiments, solving lab issues late at night, or celebrating small wins like a paper acceptance. Being two different individuals, we've certainly had our share of disagreements and fights, but what made our bond stronger

was our willingness to rise above those differences, choosing unity and mutual respect because that's what true lab mates do! I'll always cherish our shared memories of having lunches filled with laughter, milestone celebrations, chai breaks, and the quiet support during stressful pre-submission days.

As I move forward, I carry with me not just the academic knowledge I've gained, but also the meaningful human connections that have shaped my journey. I sincerely thank my batchmate, **Akash Dubey**, for his friendship, valuable suggestions, and ever-helpful nature. His warm and welcoming personality, paired with a rare blend of wit and wisdom, has made a lasting impression on me and added immense joy to this journey.

I would like to thank my juniors, **Devendra** and **Akansha**, for always being there whenever I needed help. Their cheerful presence brought joy to the lab, and their constant willingness to support us is something I truly appreciate. A special mention goes to Akansha for her aesthetic and artistic talents, which added color and creativity to all our lab celebrations. I would also like to thank the B. Tech project students, **Raju** and **Anurag**, for the wonderful time they've given us and for creating amazing memories together and the summer interns, **Himanshi**, **Nishi**, and **Yuvraj**, for their hard work and dedication in the lab. I would further like to extend my heartfelt thanks to our neighboring lab partners **Shubham, Hemant and Dilip ji** for maintaining a positive atmosphere that made working in proximity a truly enriching experience. Their contributions, both academically and personally, have been invaluable in making the lab environment more dynamic and enjoyable. I feel incredibly fortunate to have had the guidance and support of some amazing seniors throughout my journey. A heartfelt thank you to **Vinamra Bhushan Sharma**, **Yogendra Mishra**, **Gargi Dey**, **Shadab Saifi**, and **Yogendra Yadawa** for always being there when I needed help.

For a woman aspiring to pursue a PhD, having a strong support system at home isn't just helpful, it's essential. I have been supremely fortunate to have the unwavering support of my parents, **Mr. Vinod Kumar Tripathi** and **Mrs. Pratima Tripathi**, throughout my academic journey. Their immense faith in my potential has been a constant source of strength. My father's unconditional love and unwavering belief in me have profoundly shaped who I am today. He has always encouraged me to dream freely and pursue my goals wholeheartedly. I take great pride in carrying forward the values he instilled in me which are honesty, hard work, and kindness. I am deeply thankful to my beloved grandparents **Mr. Gorakhnath Tripathi** and Late **Mrs. Savitri Devi** for their blessings and heartfelt prayers which have kept me safe to this day and paved the way towards a better future.

A huge shout-out to my siblings, **Pragati Tripathi** and **Vishesh Tripathi**, for being the true heroes of my PhD saga. They kept me sane, provided a never-ending stream of unsolicited advice, and pretended to understand the scientific mumbo-jumbo I babbled on about (while secretly Googling half of it). I honestly wouldn’t have made it through without their constant moral support, and their uncanny ability to never ask the dreaded question, “When is this PhD actually going to end?”. I am, indeed, a proud and grateful daughter of a truly progressive family.

This acknowledgment section concludes with a special mention of my husband, **Dr. Upendra Kumar Shukla,** who has been my unwavering pillar of strength. Although he joined me in my PhD journey much later, the emotional support he provided was exactly what I needed. From staying awake with me during late nights in the lab to becoming my punching bag when I needed to vent, to playing the role of a dietician at times by guiding on health, and even acting as my unpaid therapist, my husband has embraced countless

roles that made my otherwise mundane PhD life a vibrant and colorful one. He stood by me through the toughest days, witnessed my vulnerabilities, and helped me rise above all the challenges in pursuit of my goals. Through him, I gained not only a life partner but a wonderful companion to walk this path with.

I would also like to thank my loving father-in-law, **Mr. Prabhakar Shukla**, and my kind-hearted mother-in-law, **Mrs. Renu Shukla**, whose immense affection and unwavering support gave me the desired strength to complete my degree. Each time I returned to campus from home, they sent me off with a smile and warmth that stayed with me. I feel fortunate to be part of such a supportive family, and I'm especially grateful to all my amazing brothers-in-laws, who never failed to make me laugh and lift my spirits along the way.

Thank you to everyone for being such an important part of this journey and making it lighter, warmer, and unforgettable!

- Prerna Tripathi

Table of Contents

List of Tables

List of Figures

List of Abbreviation

HER	Hydrogen Evolution Reaction
OER	Oxygen Evolution Reaction
ORR	Oxygen Reduction Reaction
CER	Chlorine Evolution Reaction
COR	Chlorine Oxidation Reaction
OWS	Overall Water Splitting
CV	Cyclic Voltammetry
LSV	Linear Sweep Voltammetry
CA	Chronoamperometry
OCP	Open-Circuit Potential
RRDE	Rotating Ring Disc Electrode
ECSA	Electrochemical Surface Area
RHE	Reversible Hydrogen Electrode
XPS	X-Ray Photoelectron Spectroscopy
XRD	X-Ray Diffraction
FESEM	Field Emission Scanning Electron Microscopy
HRTEM	High-Resolution Transmission Electron Microscopy
UV-vis	Ultraviolet-Visible
BET	Brunauer-Emmett Teller
BJH	Barrett-Joyner-Halenda
EIS	Electrochemical Impedance Spectroscopy
SAED	Selected Area Electron Diffraction
EDX	Energy Dispersive X-ray
GO	Graphene Oxide
rGO	Reduced Graphene Oxide
NF	Ni foam
Pt	Platinum
K	Kelvin
μ	Micro
m	Milli
λ	Lambda (Wavelength)
Ω	Ohm
°C	Degree Celsius
V	Volt
eV	Electron Volt
e^-	electron

Preface

A wide range of electrochemical technologies, particularly in the fields of energy conversion, storage, and sensors, rely heavily on fundamental reactions like the oxygen evolution reaction (OER), the hydrogen evolution reaction (HER), the oxygen reduction reaction (ORR), Sulfion oxidation reaction (SOR) and the hydrogen peroxide reduction reaction (H_2O_2RR). These days, transition metal compounds (TMCs), such as transition metal oxides, phosphides, sulphides, nitrides, carbides, and selenides, are thought to be promising materials for electrocatalytic reactions because of their remarkable catalytic capabilities and plentiful reserves. Nevertheless, despite TMC's outstanding performance, catalysts based on precious noble metals are still proven to be more effective. To enhance TMC's electrocalytic performance, hybrids with graphene-based materials, TMC phase and structural alteration, and heteroatom-based chemical doping have all been studied. Graphene-TMC hybrids, materials made by fusing graphene with transition metal compounds, hold enormous potential for addressing the challenges TMC presents. Combined graphene helps with H^+ adsorption, increases electrochemical conductivity, decreases charge-transfer resistance at the catalyst/electrolyte contact, and shields the catalyst from poisoning.

Chapter 1: In this chapter, we give a brief introduction of Transition metal compounds (TMCs) and TMCs-graphene derived electrocatalysts. An overview of the fundamental principles as well as the parameters used to assess the performance of electrocatalytic reactions have been discussed. Finally, the report summarises the most recent developments in the development of transition metals-

graphene compounds, as well as the activity and efficacy data of electrocatalytic reactions for practical applications.

Chapter 2: Hydrogen production *via* acidic water splitting is of great importance in electrolyzer industries. In this chapter, synthesis of self-assembled, freestanding, three-dimensional (3D) graphene- non-noble tungsten oxide (SA-GWO) electrode with remarkable electrocatalytic activity in acidic media has been summarized. Bi-functional (HER and OER) acidic H_2O electro-splitting has been attainable by SA-GWO electrodes at full potential of ~1.90 V, 10 mA cm^{-2}. Remarkably, it exhibited oxygen evolution (OER) activity in the acidic medium, which is so far very limited. Most importantly, the WO_3 polymorph, typically responsible for the distinct mechanism of HER and OER action in 1M H_2SO_4, has been identified and proven. Graphene served as a stable foundation for creating independent 3D SA-GWO electrodes through a straightforward self-assembly method, eliminating the need for extra binders. This approach reduced expenses and ensured the electrocatalyst's durability and mechanical robustness, enabling it to withstand the corrosive conditions without degradation.

Chapter 3: This chapter reports the development of a double-layer anode that is composed of a molybdenum sulphide electrocatalyst layer that is uniformly deposited over a Sulfonated Graphene-Ni foam electrode (G-Ni-MoOS) using a straightforward one-step hydrothermal method. The in situ-generated polyatomic sulfate ions imbibed over the graphene sheets having repellant properties towards chlorine along with contribution from GO towards conserving the mechanical integrity during OER, were responsible for activity, durability, and superior corrosion resistance of the seawater-splitting anode. The successful in-situ functionalization of sulphonic moieties onto the graphene oxide skeleton of the

GNiMoOS electrode has been confirmed by XPS, RAMAN, SEM, TEM, and IR techniques. The density of states (DOS) and DFT calculations clearly validated the preference of sulphonic moieties towards OH^- compared to Cl^- ions. Outstanding and stable OER and HER activity in harsh sea has been observed at a very low overpotential of 180 and 165 mV, respectively, to reach current densities of 100 mA cm^{-2} at 27ºC.

Chapter 4: This chapter describes the synthesis of three-dimensional (3D), self-assembled and freestanding graphene-based sulphide (MoOS-G), selenide (MoOSe-G), and oxide (MoO-G) electrodes for the application of HER under H_2SO_4, KOH, and H_2S medium. Among them, MoOS-G showed the best bifunctional electrocatalytic performance for overall water splitting in acidic media, requiring only 280 mV to reach 10 mA cm^{-2}, outperforming MoO-G (390 mV) and MoOSe-G (540 mV). MoOS-G also exhibited excellent H_2S splitting activity in simulated seawater, achieving 35 mA cm^{-2} at 350 mV, and superior stability over MoOSe-G and graphite electrodes. Structural analyses confirmed that the enhanced performance stems from efficient charge transport and Mo-S/graphene synergy. Additionally, MoOS-G catalyzed the four-electron ORR with an onset potential of 0.97 V in alkaline media, making it a versatile, durable, and low-energy catalyst for green energy applications.

Chapter 5: In this chapter, Palladium incorporated Nitrogen doped Graphene oxide nanospheres (Pd-N-GO) nanocomposite as a bifunctional catalyst for the oxygen reduction reaction (ORR) and non-enzymatic H_2O_2 detection has been put forward. Synthesized via a simple, surfactant-free reduction of $PdCl_2$, Pd-NGO features uniformly dispersed Pd nanoparticles (3-8 nm) on the NGO matrix. Control experiments with Ru-NGO confirmed that ORR activity is primarily due to Pd. Pd-NGO follows a four-electron reduction of

oxygen to water whereas, the bare N-GONs reduces oxygen *via* a two-electron pathway in alkaline medium. ORR pathway. Furthermore, a screen-printed electrochemical sensor (Pd-N-GO/SPE) was fabricated via the drop-casting of Pd-N-GO over SPE for the sensitive electrochemical detection of H_2O_2 *via* H_2O_2 RR, it exhibited an excellent detection limit (LOD) of 260 μM with a decent sensitivity of 0.055 $\mu A \mu M^{-1} cm^{-2}$. In addition, Pd-N-GO/SPE also showed excellent selectivity, repeatability, and stability for detecting H_2O_2. These results highlight Pd-NGO as a scalable, efficient catalyst for both fuel cell and sensing applications.

Chapter 6: In this chapter, based on the current studies we have drawn the conclusion. Future directions of the work and key recommendations are also discussed.

***

Chapter 1: Introduction and Literature Survey

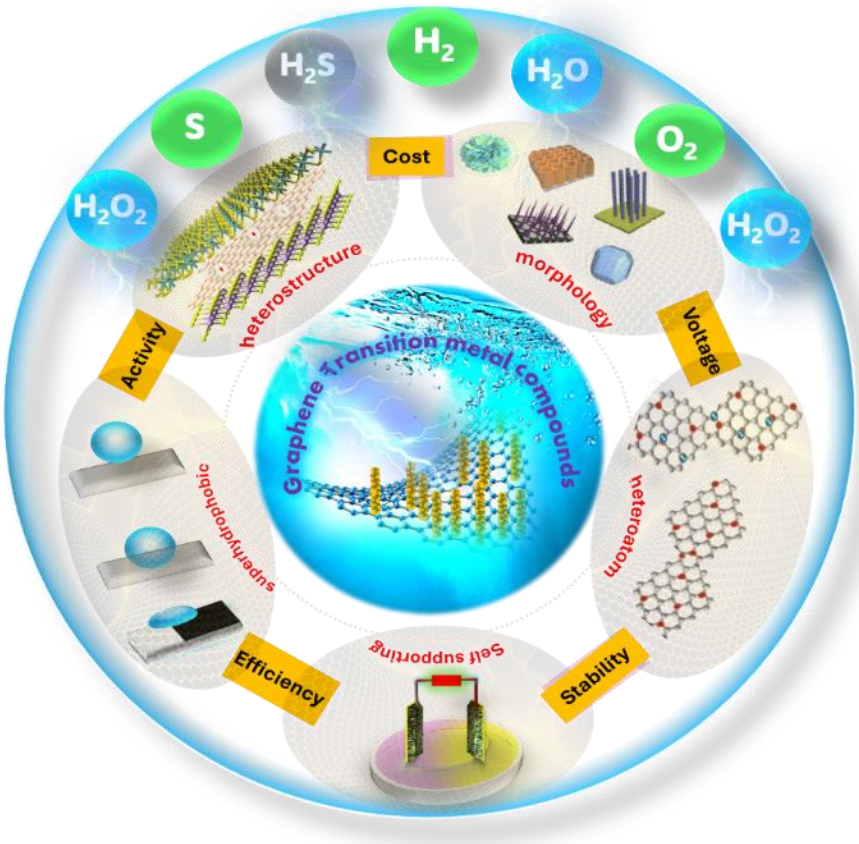

Transition metal compounds (TMCs) are promising noble-metal alternatives for water splitting due to their abundance, tunable electronic structures, and catalytic activity. Incorporating graphene enhances their dispersion, conductivity, stability, and electronic properties through synergistic interactions. This chapter outlines the recent advances in the design and development of graphene-TMC hybrid electrocatalysts, with a particular focus on their potential across a range of electrochemical applications.

1.1 Background

The ongoing era of industrial and technological advancement has triggered a substantial increase in global energy demand. According to the Union of Concerned Scientists (UCS), energy usage has steadily risen over the past several decades [1]. Recent surveys indicate that global energy utilization has nearly doubled in recent years [2,3]. For instance, global primary energy consumption reached approximately 146,000 terawatt-hours (TWh) in 2015, nearly 25 times greater than the levels recorded in 1800 [4,5]. Furthermore, global power consumption rose from about 136,129 TWh in 2008 to 161,250 TWh in 2018, marking a 2.9% increase over the decade. Another report recorded primary energy consumption at 149,634 TWh in 2015, increasing to 157,064 TWh in 2018 before experiencing a 4% decline to 150,781 TWh in 2020 primarily due to global transportation restrictions and industrial shutdowns caused by the COVID-19 pandemic [4,6]. Despite this temporary dip, projections suggest that global energy demand will grow by 41% by 2040. **Figure 1.1** illustrates the projected regional trends in global energy consumption [8].

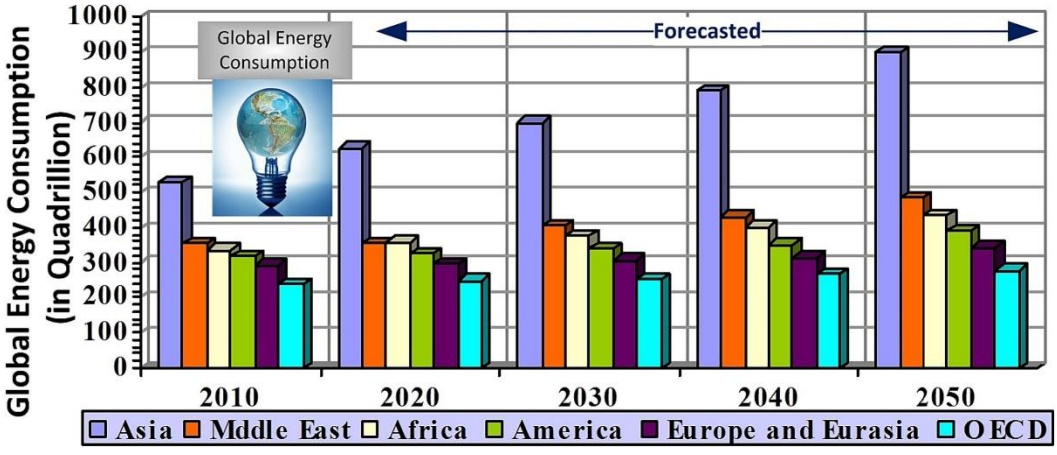

Figure 1.1 Global energy consumption by region till 2050. [Reprinted with permission from ref. 8, Copyright 2023 Elsevier]

Regionally, Asia and the Americas are the leading energy consumers, while African nations report the lowest energy usage [7]. As global energy demand continues to rise, addressing these inequalities will be crucial for fostering sustainable development and economic growth across all regions [9]. It has been reported that over 80% of the global energy supply is derived from fossil fuels, including coal and oil, which are major contributors to environmental pollution [10]. However, fossil fuel reserves are both finite and non-renewable, posing significant long-term sustainability concerns [11]. Consequently, the development of clean, renewable energy sources and the optimization of the global energy structure are considered essential strategies to reduce dependence on fossil fuels. In this context, electrocatalytic technologies have emerged as pivotal enablers of key energy conversion, storage, and chemical synthesis processes, facilitating a transition toward more sustainable energy systems. Among various renewable sources, solar and wind energy are particularly attractive due to their abundance and accessibility; however, their utilization is often hindered by geographic and temporal variability [12]. To address these limitations, advanced electrochemical energy conversion and storage technologies have been proposed to compensate for the intermittent nature of renewable energy sources and to enhance overall system reliability [13]. By efficiently integrating energy conversion and storage systems, several practical and portable energy devices have been developed, including water electrolyzers, fuel cells, solar cells, and rechargeable batteries, among others [14]. Batteries and fuel cells play a pivotal role in energy storage, particularly in applications such as electric vehicles and renewable energy systems. Simultaneously, electrolyzers enable the production of green hydrogen via water splitting, offering not only a clean fuel alternative but also an effective means of storing surplus renewable electricity.

Collectively, batteries, electrolyzers, and fuel cells represent fundamental components of the evolving energy landscape. Each contributes uniquely to the global transition toward cleaner and more sustainable energy systems by reducing reliance on fossil fuels, enhancing energy conversion and storage efficiency, and supporting the integration of intermittent renewable energy sources. The significance and functions of these energy conversion and storage technologies are summarized in **Table 1.1.**

Table 1.1 Importance of few energy conversion and storage systems.

Technology	Function	Key Benefits	Important Reactions	Electrocatalysts Role	Applications
Batteries (ORR-based)	**Energy Storage**	-High energy density - Lightweight - Longer range for EVs - Low-cost, eco-friendly materials	Oxygen Reduction Reaction (ORR)	Enhance ORR efficiency and reduce energy barriers	- EVs - Grid-scale energy storage - Portable electronics - Renewable energy integration
Electrolyzers (Green H_2)	**Green Hydrogen Production**	- Decarbonizes hard-to-abate sectors (e.g., steel, chemicals) - Flexible energy storage - Renewable energy integration	Hydrogen Evolution Reaction (HER) Oxygen Evolution Reaction (OER)	Speed up hydrogen production by optimizing HER and OER	- Industrial decarbonization - Renewable energy storage - Power generation
Fuel Cells	**Clean Energy Conversion**	-Zero-emission power - Fast refuelling and long range for hydrogen vehicles - High efficiency	Oxygen Reduction Reaction (ORR)	Accelerate ORR to enhance power generation efficiency	- Hydrogen-powered vehicles - Backup power systems - Microgrids - Integration with renewables
Hybrid Systems (Batteries + Fuel Cells)	**Combination of Energy Storage and Conversion**	- High power and high efficiency -Optimal for renewable energy integration	Both ORR and HER	Improve energy conversion and storage by integrating battery and fuel cell technologies	- Renewable energy systems - Electric vehicles - Heavy-duty transport

Significant progress has been achieved in enhancing the efficiency, durability, and scalability of these technologies, driven by advances in materials science and a deeper understanding of the underlying electrochemical processes. Central to these developments

are green electrochemical reactions such as Hydrogen Evolution Reaction (HER), Oxygen Evolution Reaction (OER), Oxygen Reduction Reaction (ORR), Sulfur Oxidation Reaction (SOR), Hydrogen Peroxide Reduction Reactions (H_2O_2 RR) etc., which form the core of these modern energy conversion and storage systems.

1.2 Electrochemical Reactions and their significance

Electrode reactions are critically important today because they lie at the heart of many technologies that address the world's urgent need for clean energy, environmental sustainability, and resource efficiency. They also play a key role in making industrial processes greener by reducing energy consumption and chemical waste. Thus, advancing electrode reactions is essential for building a low-carbon, circular, and climate-resilient future. HER and OER are vital for water-splitting technologies used in green hydrogen production, a key pillar of the emerging hydrogen economy. ORR is central to the operation of fuel cells and metal-air batteries, which are critical for decarbonizing the transportation and power sectors. Meanwhile, SOR provides an environmentally beneficial route to valorize industrial waste gases like hydrogen sulfide (H_2S), converting them into valuable products such as hydrogen, while mitigating pollution. Additionally, the H_2O_2 RR is gaining attention for enabling on-site, clean, and selective generation of hydrogen peroxide, which has important applications in wastewater treatment, industrial oxidation processes, and medical disinfection, offering a safer and more sustainable alternative to centralized chemical production. Thus, these electrochemical reactions such as HER, OER, ORR, H_2O_2 RR and SOR etc. are essential for advancing clean energy technologies because they often operate with minimal environmental impact. They rely on abundant, non-toxic materials and are typically performed under mild, ambient conditions, reducing the carbon

footprint compared to traditional energy technologies. Green reactions help in integrating intermittent renewable energy sources (like wind and solar) into the grid by providing efficient energy storage and conversion mechanisms. This allows for energy to be stored during periods of high production and used when demand is high, or production is low. These reactions are integral to a wide range of energy conversion and storage technologies, including fuel cells, electrolyzers, and metal-air batteries, as they directly impact the efficiency, sustainability, and performance of these systems [15-19] (**Figure 1.2**).

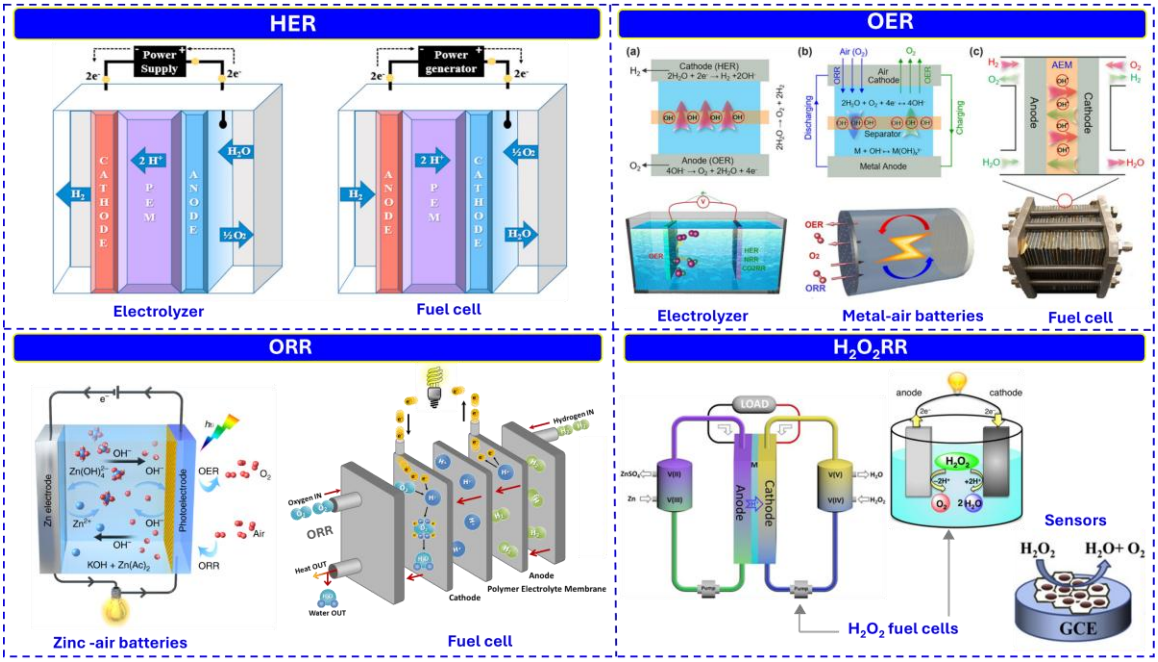

Figure 1.2 Schematic illustrations of key electrochemical reactions and their applications. [Reprinted and reproduced with permission from ref. 15, Copyright 2021 Cell Press; ref. 16, Copyright 2022 Springer Nature; ref. 17, Copyright 2019 Nature Portfolio; ref. 18, Copyright 2019 Springer Nature; ref. 19, Copyright 2015 Elsevier]

These catalytic reactions stand as indispensable pillars for achieving enhanced efficiency and sustainability on a global scale. They enable the integration of these processes into contemporary energy landscape, from storage to delivery, ultimately facilitating a more

sustainable and efficient world. In short, green electrode reactions matter today because they are at the intersection of chemistry, energy, and sustainability. They provide not just a cleaner way to perform electrochemical transformations, but a vital tool in building a resilient, low-carbon future.

1.3 Need for Advanced Electrocatalysts

Innovations in materials science, system integration, and manufacturing techniques have led to more cost-effective and high-performing conversion and storage devices. Central to these advancements are electrocatalysts, which accelerate the chemical reactions in energy conversion and storage processes. The development of efficient catalysts for these reactions (such as advanced electrocatalysts for HER, OER, ORR, and SOR) is crucial to reducing energy losses and improving the performance of energy devices. The design of catalysts that lower activation energy and improve reaction rates is at the core of advancing sustainable energy technologies. They enable the production of green hydrogen, facilitate efficient energy conversion in fuel cells, provide scalable energy storage solutions, and support the decarbonization of various sectors. By improving these reactions and the catalysts that drive them, we can accelerate the transition to a sustainable, low-carbon energy future. The design of novel electrocatalysts requires careful consideration of several criteria, including high catalytic activity, long-term stability, low cost, and abundant availability. Additionally, electrocatalysts should exhibit strong selectivity, appropriate electronic structure, high surface area, and robust resistance to corrosion or poisoning under operating conditions. The ongoing research into new materials ranging from transition metal compounds to nanostructured carbons and single-atom catalysts is driving the development of next-generation energy systems that are both efficient and sustainable.

Advanced electrocatalysts reduce energy barriers, improve reaction kinetics, and enhance overall system efficiency. Their importance cannot be overstated, as they directly impact the viability and scalability of clean energy technologies. As a result, there is a growing research focus on designing novel, cost-effective, stable, and high-performance electrocatalysts often based on abundant transition metals, doped carbon materials, or nanostructures. Before delving into the design of efficient electrocatalysts, it is crucial to first understand the underlying mechanisms associated with each of the various electrode reactions, such as the **ORR, HER,** and others.

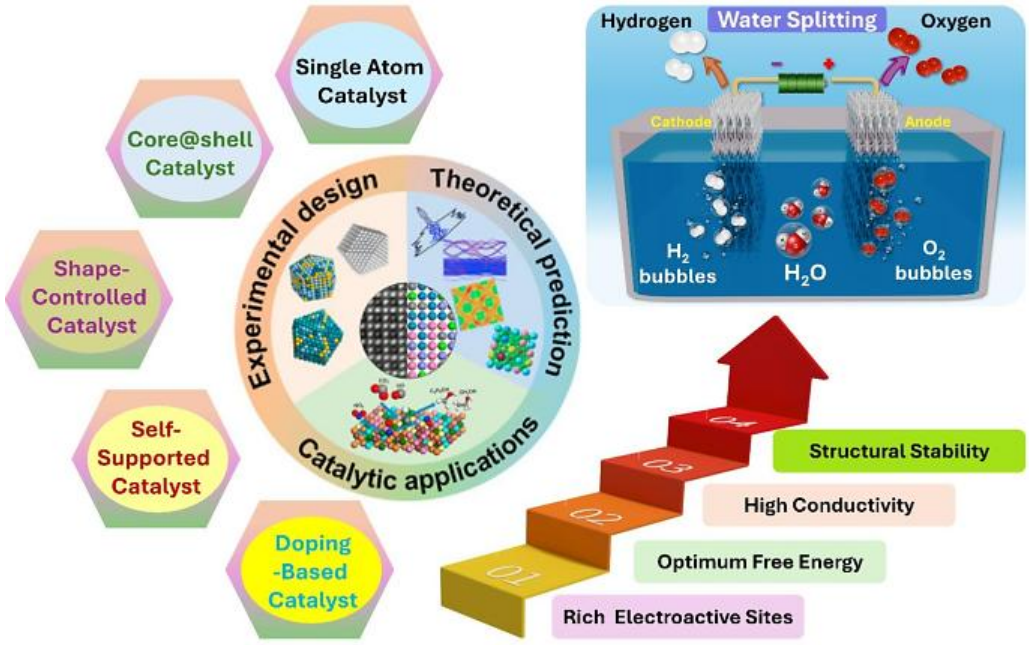

Figure 1.3 Different catalyst engineering approaches for electrocatalyst development. [Reprinted with permission from ref. 20, Copyright 2025 Springer Open]

Each of these reactions involves complex electrochemical processes that determine the overall performance of energy conversion and storage devices like batteries, electrolyzers, and fuel cells. For example, in the ORR**,** the process of oxygen molecules being reduced at

the cathode surface involves multiple electron and proton transfers, which can be hindered by high energy barriers. Similarly, the HER involves the generation of hydrogen gas from water, which also requires overcoming significant activation energies. These electrochemical reactions are highly dependent on the electronic structure, surface area, and stability of the catalyst materials, all of which directly impact their efficiency. To optimize electrocatalysts, it is essential to evaluate several parameters such as catalytic activity**,** overpotentials**,** long-term stability**,** conductivity, and resistance to corrosion or poisoning under operating conditions. Additionally, factors like selectivity and the mechanism of charge transfer at the catalyst surface are critical in determining how efficiently a catalyst can facilitate the desired reaction. Understanding these mechanisms and evaluating the performance of catalysts based on these parameters are key steps in developing catalysts that can enhance the efficiency, durability, and scalability of energy systems, enabling their integration into real-world applications (**Figure 1.3**) [20]**.**

1.4 Understanding the Mechanisms of Green Electrode Reactions: Key to Optimizing Electrocatalysts for Efficient Energy Conversion and Storage

1.4.1 Fundamentals of water splitting

Although hydrogen is the most abundant element on Earth, it does not naturally exist in its elemental form. Instead, it must be produced from various hydrogen-containing compounds such as water, hydrogen sulfide, biomass, fossil fuels, or ammonia, typically with the aid of an external energy source such as heat or electricity. Among the available methods, water electrolysis stands out as a practical and environmentally friendly approach for producing hydrogen without carbon dioxide emissions, particularly when powered by

nuclear or renewable energy sources. Electrolysis involves the application of an electric current to split water molecules into hydrogen and oxygen gases. Hydrogen is widely regarded as a key enabler in restructuring the global energy system and achieving carbon neutrality by 2050, owing to its versatility, clean combustion, and potential for integration across various sectors of society (**Figure 1.4**).

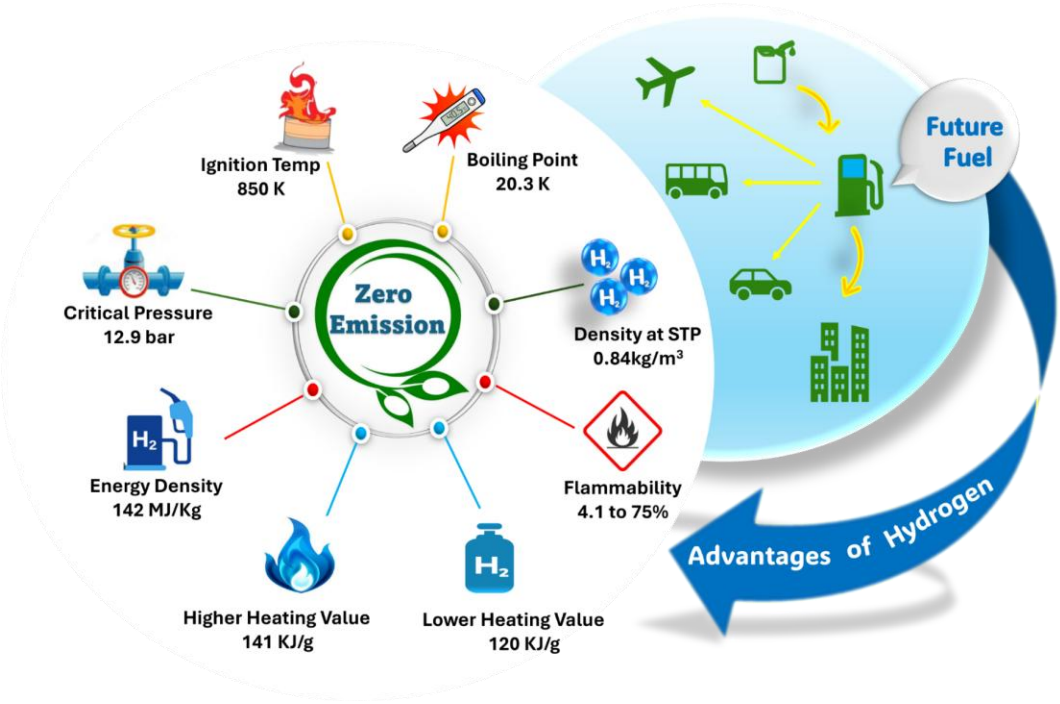

Figure 1.4 Advantages of Hydrogen as a fuel.

The central device in this process is the electrolyzer, which facilitates the water-splitting reaction. A typical water electrolyzer consists of three primary components: an anode, a cathode, and an electrolyte. The water-splitting process involves two half-reactions which are oxygen evolution reaction (OER) at the anode and hydrogen evolution reaction (HER) at the cathode given in **eq 1.1 to 1.5** (**Figure 1.5**). During electrolysis, oxygen gas is generated at the surface of the anode, while hydrogen gas is evolved at the cathode.

Importantly, the nature of the half-reactions depends on the electrochemical environment, particularly the pH of the electrolyte. When the electrolyte is acidic,

$$HER:\ 4H^+ + 4e^- = 2H_2 \qquad E° = 0\ \text{V vs SHE} \quad (1.1)$$

$$OER:\ O_2 + 4H^+ + 4e^- = 2H_2O \qquad E° = 1.23\ \text{V vs SHE} \quad (1.2)$$

When the electrolyte is basic,

$$4H_2O + 4e^- = 2H_2 + 4OH^- \qquad E° = -0.83\ \text{V vs SHE} \quad (1.3)$$

$$2H_2O + O_2 + 4e^- = 4OH^- \qquad E° = 0.40\ \text{V vs SHE} \quad (1.4)$$

Here, SHE stands for Standard Hydrogen Electrode.

Overall,

$$2H_2O = 2H_2 + O_2 \quad (1.5)$$

Regardless of the reaction medium, the theoretical (thermodynamic) potential required for overall water splitting at standard conditions of 25 °C and 1 atm is 1.23 V [11]. However, in practical applications, a higher potential is always required to drive the reaction effectively. This excess voltage is referred to as the overpotential (E_{op}), which represents the additional energy needed to overcome various kinetic and resistive barriers. Specifically, the overpotential accounts for the activation energy associated with the HER at the cathode (E_c) and the OER at the anode (E_a), as well as other contributing losses such as interfacial contact resistance and electrolyte solution resistance (E_{other}). Thus, the total operational potential E_{op} required for effective water splitting can be expressed as:

$$E_{OP} = 1.23 + E_a + E_c + E_{other}$$

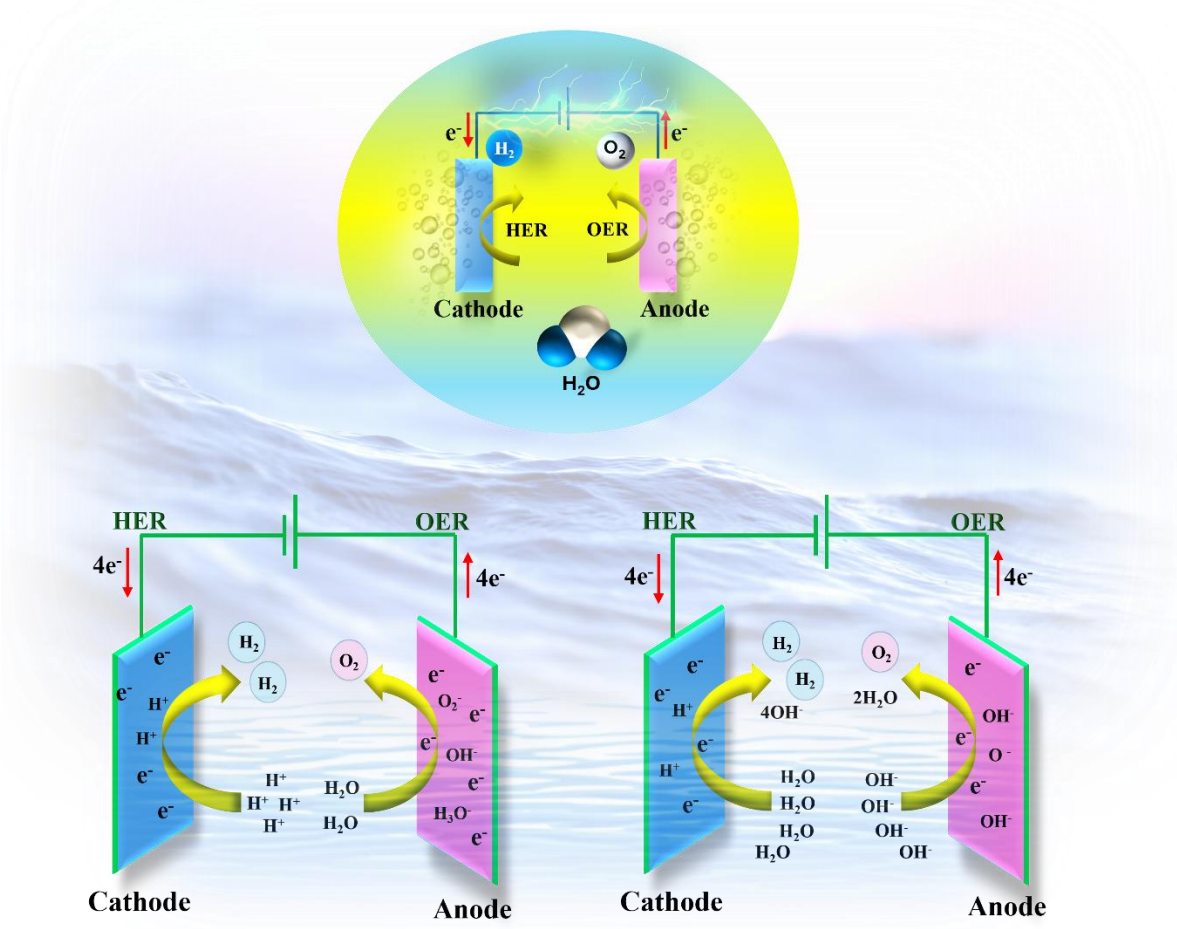

Figure 1.5 Schematic setup for water electrolysis reaction (top) in acidic (left) and alkaline (right) media.

According to the above equation, minimizing the overpotential is a critical factor in achieving an energy-efficient water splitting process. Highly active electrocatalysts can significantly reduce the activation overpotentials associated with the hydrogen evolution reaction (E_c) and the oxygen evolution reaction (E_a), while thoughtful electrolyzer design and engineering can mitigate additional losses represented by E_{other}. Despite these advancements, the primary challenge remains the development of sustainable, earth-abundant, and cost-effective electrocatalyst materials. These materials are essential for

making large-scale water splitting economically viable and for facilitating the widespread adoption of green hydrogen as a clean energy vector.

1.4.1.1 Hydrogen evolution reaction (HER)

The hydrogen evolution reaction (HER) occurs at the cathode surface and proceeds via a two-electron transfer process, typically involving two sequential steps. These steps follow well-established mechanistic pathways, namely the Volmer-Tafel and Volmer-Heyrovsky mechanisms, which are operative in both acidic and alkaline electrolytes during electrochemical hydrogen production [21] (**Figure 1.6**).

(a)Volmer mechanism

$$H^+ + M + e^- = M - H^* \qquad \text{(acidic solution)}$$

$$H_2O + M + e^- = M - H^* + OH^- \qquad \text{(alkaline solution)}$$

The Volmer reaction represents the initial electrochemical step in the HER, involving the adsorption of hydrogen onto the catalyst surface. In acidic media, a proton (H^+), and in alkaline media, a water molecule (H_2O), reacts with an electron at the catalyst surface (denoted as M) to form an adsorbed hydrogen intermediate (H*), which serves as the active species for subsequent reaction steps.

(b)Heyrovsky mechanism

$$M - H^* + H^+ + e^- = M + H_2 \qquad \text{(acidic solution)}$$

$$M - H^* + H_2O + e^- = M + OH^- + H_2 \qquad \text{(alkaline solution)}$$

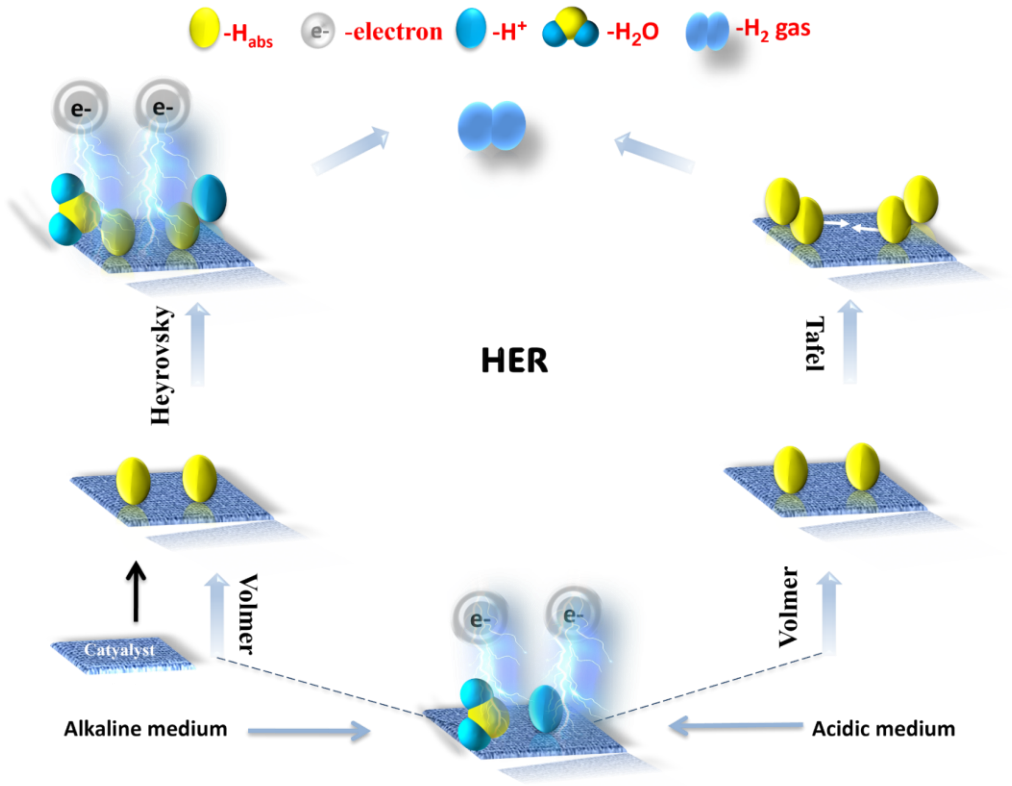

Figure 1.6 HER mechanism in acidic and alkaline medium.

The Heyrovsky reaction is a type of electrolytic desorption. Here, H_2 molecules are produced by H* and H^+ association in an acidic electrolyte or H* and H_2O association in an alkaline electrolyte.

(a) Tafel mechanism

$$2M - H^* = 2M + H_2 \qquad \text{(acidic or alkaline solution)}$$

The Tafel reaction, a chemical desorption process, involves the combination of two adsorbed hydrogen intermediates (H*) on the catalyst surface to form molecular hydrogen. Following the initial Volmer step, H_2 can subsequently be generated through either the Heyrovsky or Tafel mechanism. In all HER pathways, the adsorbed hydrogen intermediate

(H*) is central to the reaction mechanism. The free energy of hydrogen adsorption (ΔG_{H^*}) is a key indicator of catalytic activity. An ideal HER catalyst, such as platinum, has a ΔG_{H^*} near zero. Weak adsorption limits proton interaction, while strong adsorption hinders H_2 release, reducing overall efficiency [22].

1.4.1.2 Oxygen evolution reaction (OER)

The oxygen evolution reaction (OER), a four-electron transfer process occurring at the anode, is kinetically more complex than the HER due to its multiple intermediates and sluggish reaction steps. In acidic media, water is oxidized to generate oxygen and protons, whereas in alkaline media, hydroxide ions are oxidized to form water and oxygen. The commonly involved adsorbed intermediates in OER pathways include OH*, O*, and OOH* [23]. In alkaline conditions, the reaction typically begins with OH^- adsorption to form OH*, which then converts to O*. Subsequently, O* reacts with another H_2O to form OOH*, which leads to O_2 evolution. The efficiency of OER is largely governed by the catalyst's ability to adsorb and convert these intermediates particularly OOH*, a property influenced by the catalyst's electronic structure. The step with the highest energy barrier is generally rate-limiting. The widely accepted OER pathways under acidic and alkaline conditions on metal surfaces are represented below [21] (**Figure 1.7**).

In an acidic medium,

$$H_2O + M = M{-}^{*}OH + H^+ + e^-$$

$$M{-}^{*}OH = M - O^* + H^+ + e^-$$

$$M - O^* + H_2O = M{-}^{*}OOH + H^+ + e^-$$

$$M{-}^{*}OOH = M + O_2 + H^+ + e^-$$

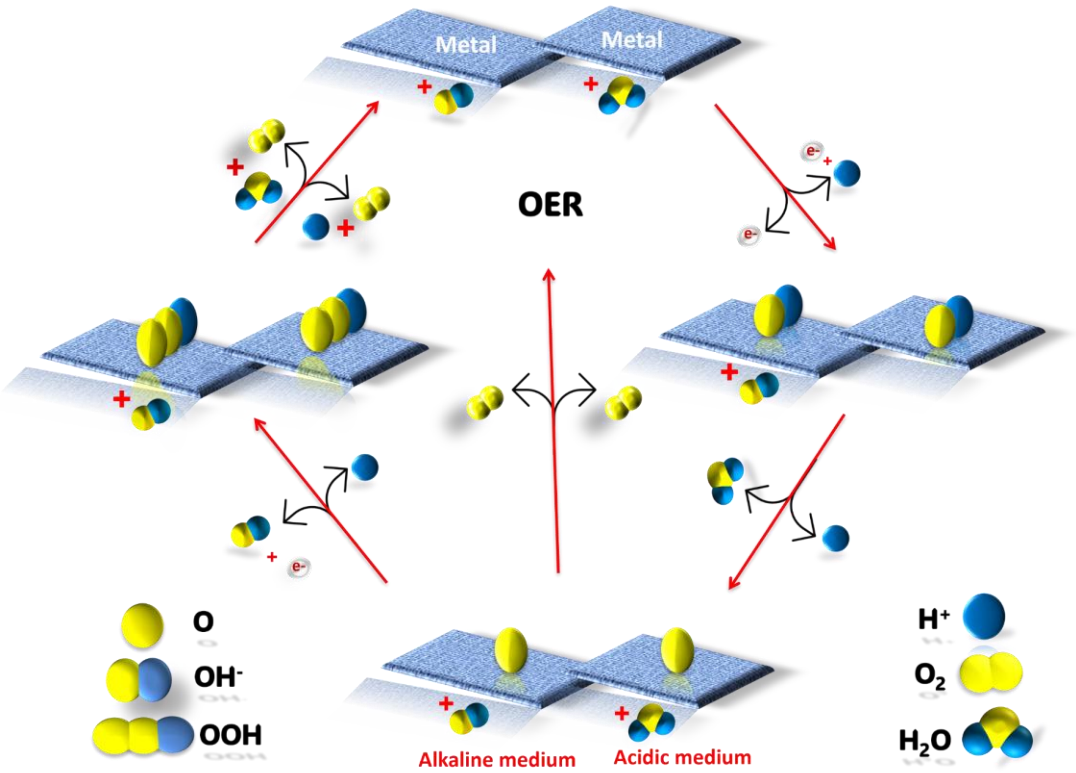

Figure 1.7 OER mechanism in acidic and alkaline medium.

In an alkaline medium,

$$M + OH^- = M{-}^*OH + e^-$$

$$M{-}^*OH + OH^- = M - O^* + H_2O + e^-$$

$$M - O^* + OH^- = M{-}^*OOH + e^-$$

$$M{-}^*OOH + OH^- = M + O_2 + H_2O + e^-$$

Recently, density functional theory (DFT) has been widely used to study the thermodynamics of each step in the OER process. It has revealed that overly strong or weak oxygen binding can hinder reaction rates by affecting intermediate stability [24]. The Tafel slope, closely related to overpotential, provides kinetic insights and has been extensively

used to probe the OER mechanism [25,26]. While ΔG_{OER} offers thermodynamic information on reaction intermediates and catalyst interactions, the Tafel slope reflects kinetic performance. Among various proposed pathways, the adsorbate evolution mechanism (AEM) is the most widely accepted (**Figure 1.8a**) [27]. In this mechanism, the catalyst surface structure remains largely unchanged during OER, apart from valence changes at the active metal sites.

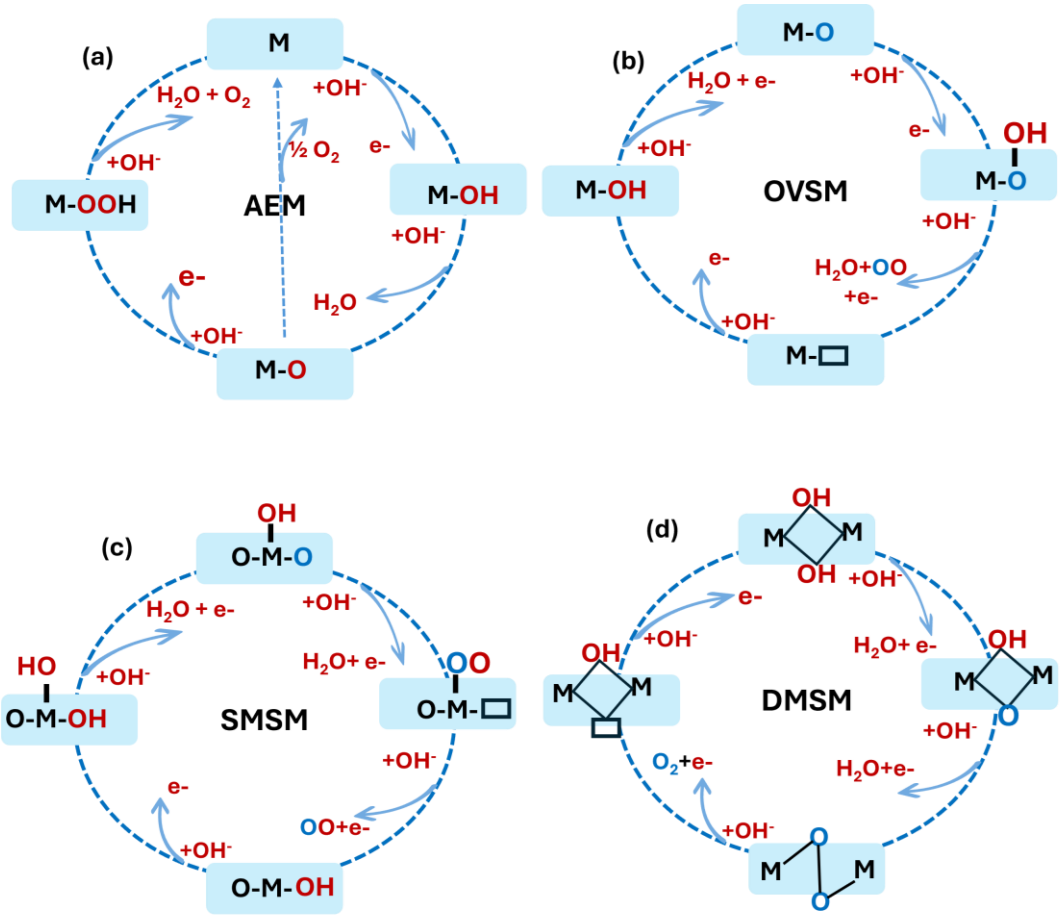

Figure 1.8 (a) Schematic of the AEM pathway in alkaline media (b-d) Schematics of three alternative routes of LOM in alkaline media with different catalytic centers, the chemically active lattice oxygen involving OER and oxygen from the electrolyte are marked in blue and red colors, respectively, and □ represents lattice O vacancy {(b)Oxygen-vacancy-site mechanism (OVSM) (c) single-metal-site mechanism (SMSM) and (d) dual-metal-site mechanism (DMSM)}.

As illustrated in Figure 1.8a, the adsorbate evolution mechanism (AEM) for OER begins with the formation of M-OH and M-O species, followed by oxygen evolution via two main pathways: (a) *O reacts with OH^- to form *OOH, which undergoes proton-coupled electron transfer to release O_2; (b) two *O species couple to form O_2. The binding energies of key intermediates (M-OH, M-O, and M-OOH) are critical in determining electrocatalytic performance. Among the two, the **M → M–OH → M–O → M–OOH** pathway is widely regarded as dominant. The step with the highest energy barrier, or rate-determining step (RDS), largely controls catalytic efficiency. Ideally, each step should proceed with a free energy change of 1.23 eV for zero overpotential. However, DFT studies show that the binding energies of *OH, *O, and *OOH are linearly related, and for many catalysts, $\Delta G_{*OOH} - \Delta G_{*OH} \approx 3.2$ eV, imposing a theoretical overpotential limit of ~0.3 V in the AEM pathway [28].

With the advancement of efficient OER catalysts particularly, metal oxides and hydroxides with strong metal-oxygen bonds such as perovskites, it has been discovered that lattice oxygen atoms can actively participate in the OER process through the lattice oxygen-mediated mechanism (LOM) [29]. This mechanism involves the electrochemical activation and release of oxygen ligands from the catalyst lattice. Based on different catalytic sites, three main LOM pathways have been proposed (**Figure 1.8b–d**) [30]. In the oxygen-vacancy site mechanism (OVSM), surface lattice oxygen is oxidized by a hole, followed by a water molecule attack that adds an OH group, eventually leading to O_2 release and restoration of the surface. The single-metal-site mechanism (SMSM) involves hole-induced O_2 release, leaving an oxygen vacancy that is later refilled by OH^-. In contrast, the dual-metal-site mechanism (DMSM), commonly seen in metal (oxy)hydroxides, resembles

the AEM but includes direct coupling between lattice oxygen and adsorbed intermediates. Unlike AEM, LOM pathways are strongly influenced by factors such as elemental composition, crystallinity, structural defects, and oxygen vacancies. These structural attributes play a crucial role in defining OER performance, underscoring the complexity of the reaction mechanism and the need for detailed mechanistic analysis.

1.4.2 Fundamentals of Seawater Electrolysis

Traditionally, freshwater electrolysis has been the standard due to its relative simplicity and purity. However, with increasing pressure on global freshwater resources and the expanding demand for hydrogen, there is a significant shift toward utilizing seawater which is an abundant and underexploited resource for hydrogen production. Seawater, comprising over 97% of Earth's water, offers a virtually limitless alternative, especially for coastal regions and island nations. Moreover, coupling seawater electrolysis with offshore renewable energy sources (like wind and solar farms) presents a highly integrated and decentralized green energy solution, reducing transmission losses and infrastructure demands. Despite these advantages, seawater electrolysis presents several formidable challenges which are mentioned below:

1.4.2.1 Effects of Intricate Cation Components

Seawater possesses high ionic conductivity due to its 3.5 wt.% salt content, with over 99% comprising Na^+, K^+, Ca^{2+}, Mg^{2+}, Cl^-, and SO_4^{2-} ions [31,32]. While these ions enhance conductivity, they also introduce significant challenges during electrolysis, as illustrated in **Figure 1.9(a–c)**. The presence of various dissolved ions, microbes, and particulates leads to unwanted side reactions and electrode degradation. High electrolysis currents can elevate local pH at the cathode, causing precipitation of $Ca(OH)_2$ and $Mg(OH)_2$, which

block active sites and hinder hydrogen evolution (**Figure 1.9b**) [33]. Additionally, microbial activity can form insoluble deposits on catalyst surfaces, further impairing HER efficiency [34].

1.4.2.2 Competition between OER and CER/COR

The main challenge for OER at the anode during seawater electrolysis is the interference from chloride ions (Cl^-), which trigger competing side reactions such as the chlorine evolution reaction (CER) and chlorine oxidation reaction (COR) (given in **eq 1.6 and 1.7**) [35]. These processes generate chlorine gas or hypochlorites, reducing OER efficiency. Although the OER has a lower thermodynamic potential (1.23 V) than CER (1.36 V), its four-electron pathway is kinetically slower than the two-electron CER, making the latter more favorable at high current densities. Additionally, catalysts that promote water oxidation often also catalyze chloride oxidation, further complicating selective OER.

In an acidic solution,

$$2Cl^- = Cl_2 + 2e^- \qquad E° = 1.36\ V \text{ vs SHE} \quad (1.6)$$

In an alkaline solution,

$$Cl^-(aq) + 2OH^-(aq) = ClO^-(aq) + 2e^- \qquad E° = 0.89\ V \text{ vs SHE} \quad (1.7)$$

Since the overpotential of CER is pH-independent, increasing the electrolyte pH can effectively suppress it. At higher pH, the formation of hypochlorous acid or hypochlorite becomes more favorable than CER, and the equilibrium potential of CER shifts higher relative to OER. This widens the potential gap (ΔE), reaching up to 480 mV at pH >7.5, creating a larger thermodynamic window for selective OER. Under such conditions, well-designed electrocatalysts can drive efficient OER while minimizing CER and hypochlorite formation.

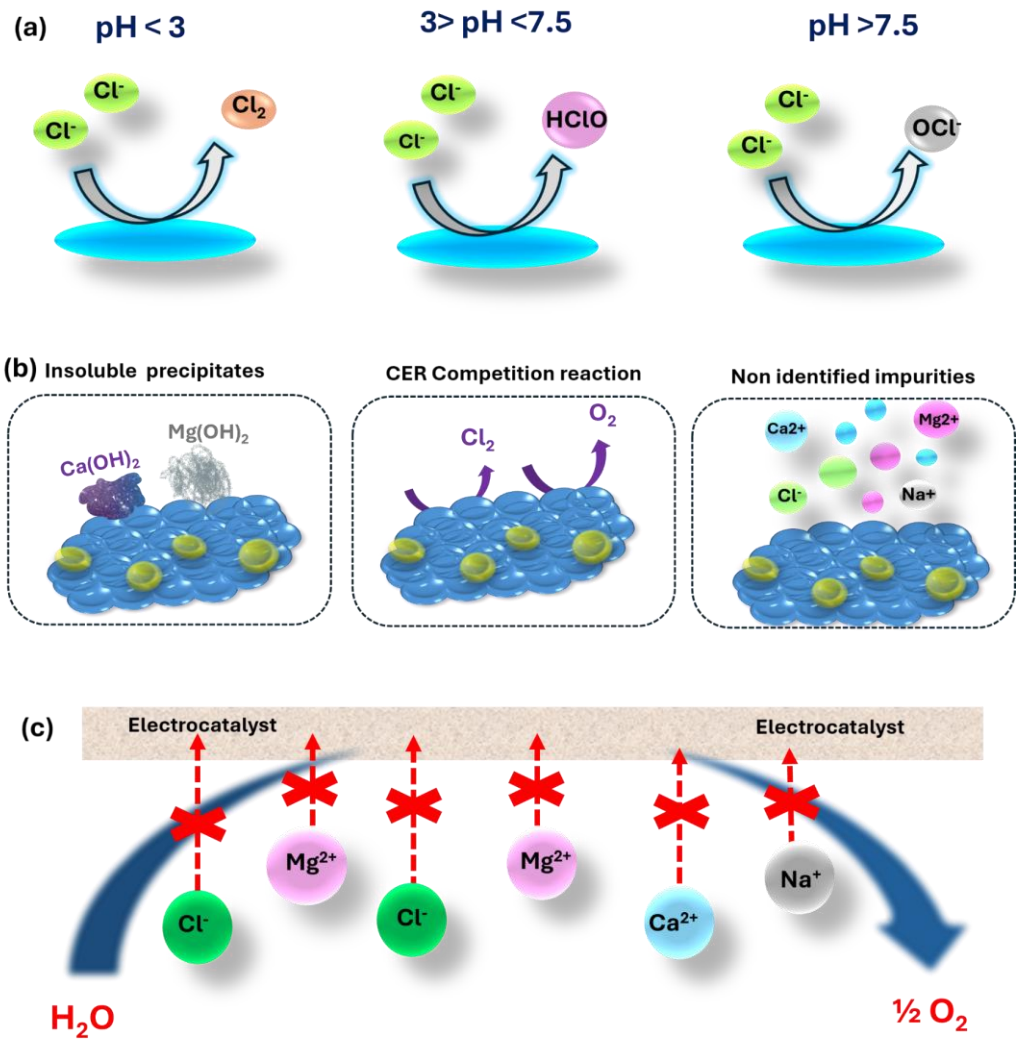

Figure 1.9 (a) stable chlorine species at different pH range (b) Challenges with seawater electrolysis (c) Ideal OER electrode for seawater splitting.

1.4.2.3 Mechanism of the Chloride Corrosion

The Cl^- ion undergoes a complex sequence of electrochemical transformations influenced by factors such as pH, electric potential, and ion concentration. Depending on the pH, various chlorine-containing species can form such as Cl_2 which dominates at pH < 3.0, hypochlorous acid (HClO) that is formed between pH 3.0 and 7.5, and hypochlorite ions (ClO^-) which forms at pH > 7.5, as shown in **Figure 1.9a**. These reactive intermediates

interfere with the OER by promoting side reactions [36]. Corrosion in the presence of chloride ions proceeds through three main stages: polarization, dissolution, and hydroxide formation. Initially, an external electric field polarizes the metal surface, promoting Cl^- adsorption. These ions form coordination bonds with the surface, leading to the dissolution of metal chlorides. Subsequently, these metal chlorides hydrolyze into metal hydroxides. This corrosion process consumes local hydroxide ions, lowering the pH and accelerating further degradation. Over time, chloride-induced corrosion damages transition-metal-based catalysts, resulting in catalyst poisoning and reduced durability. This mechanism can be summarized by three key reactions given below:

Adsorption:

$$M + Cl^- = MCl_{ads} + e^-$$

Dissolution:

$$MCl_{ads} + xCl^- = MCl_x^-$$

Hydroxide Formation:

$$MCl_x^- + xOH^- = M(OH)_x + xCl^-$$

Hence, to ensure stable seawater electrolysis, it is essential to design OER-selective electrocatalysts that suppress CER and hypochlorite formation. Catalysts with inherent corrosion resistance or selective surface chemistry (**Figure 1.9c**) offer a promising path to improve long-term OER stability.

1.4.3 Electrolyzer design for water splitting

Electrolyzer design for water splitting focuses on maximizing efficiency, durability, and scalability for hydrogen production. Key components include the anode, cathode, and electrolyte, all housed within a cell structure that supports ion transport and gas separation.

Designs vary based on electrolyte type such as alkaline, PEM (proton exchange membrane), or solid oxide, with each offering trade-offs in cost, performance, and operational conditions. The schematic diagrams of conventional alkaline water electrolysis cells are illustrated in **Figure 1.10a**. Two metallic electrodes are submerged in an alkaline aqueous electrolyte. Generally, aqueous solution of potassium hydroxide (KOH) is used with a concentration of 20-30 wt.% [38].

Water reduction takes place at the cathode according to:

$$4H_2O + 4e^- = 2H_2 + 4OH^- \qquad E = -0.83\,V \quad (1.3)$$

and the oxidation of hydroxyl ions takes place at the anode according to:

$$2H_2O + O_2 + 4e^- = 4OH^- \qquad E = 0.402\,V \quad (1.4)$$

The overall reaction is:

$$2H_2O(liq) = 2H_2(g) + O_2\,(g) \qquad (1.5)$$

As highlighted in Fig. 1.10, conventional alkaline water electrolysis employs asbestos-based diaphragms, which act as simple physical separators preventing gas crossover while allowing hydroxide ion transport. However, these diaphragms typically suffer from lower ionic conductivity and limited chemical stability. In contrast, modern AEM-based electrolyzers replace diaphragms with ion-conducting membranes that provide selective hydroxide ion transport with significantly higher conductivity, better chemical/mechanical stability, and improved gas separation efficiency (**Figure 1.10b**) [39,40].

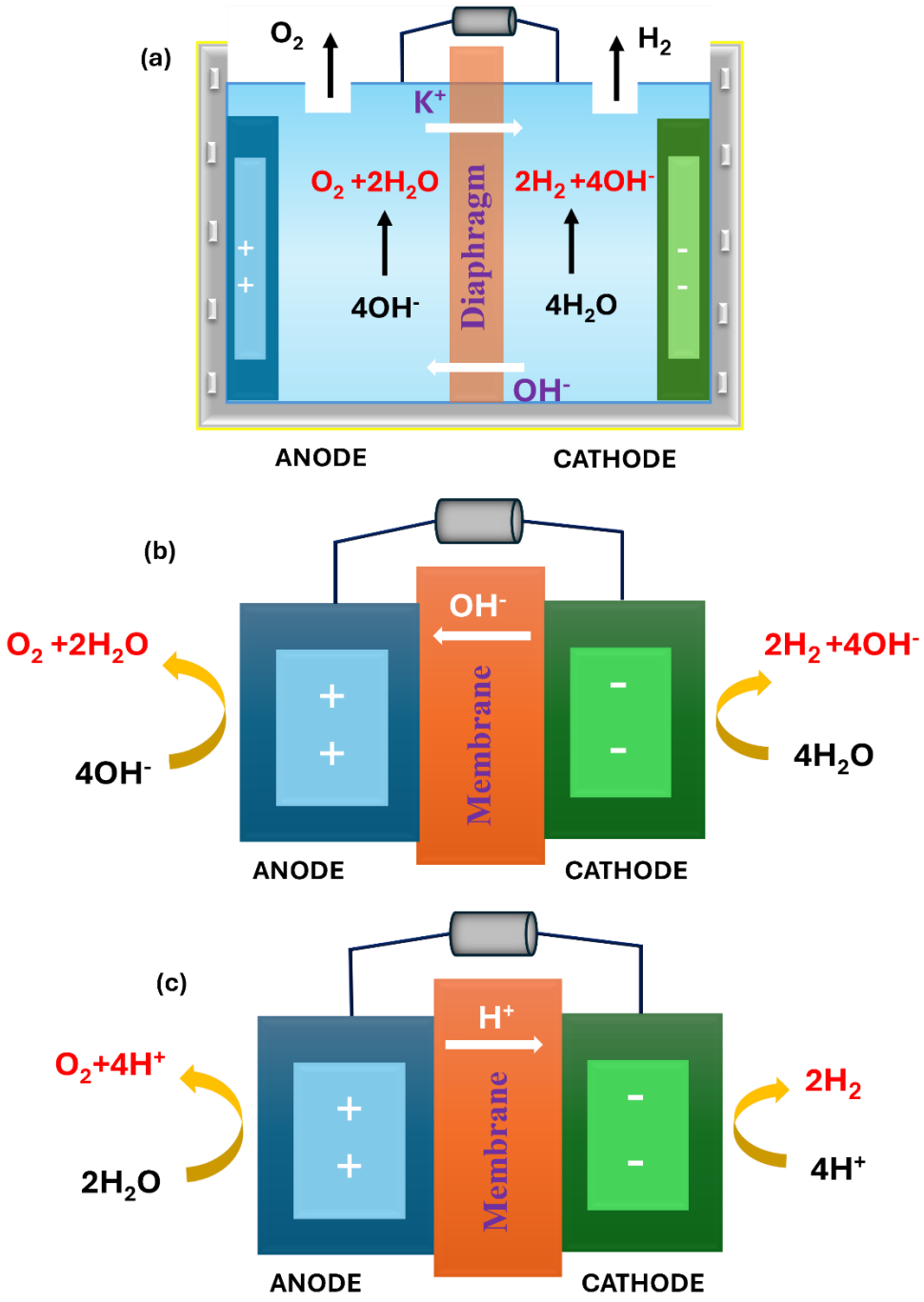

Figure 1.10 Schematic diagrams of electrolyzer (a) Conventional alkaline electrolyzers (b) anion exchange membrane (AEM) electrolyzer (c) proton exchange membrane (PEM) electrolyzer.

However, alkaline water electrolyzers (AWEs) still face key challenges, including enhancing electrode porosity and catalyst layers for better mass transport and bubble

removal, improving cathode durability, and developing better separators for higher gas purity [41]. Proton exchange membrane (PEM) electrolyzers (**Figure 1.10c**) offer advantages such as lower ohmic loss, lower overpotentials, higher current densities, faster response, and greater gas purity in a compact design. Nevertheless, PEM electrolyzers require costly noble metal anode catalysts due to the highly corrosive environment and high electrode potentials, demanding durable materials. Catalysts like Ru, Ir, Rh, Pt, and Au are commonly used, with activity following the order Ru > Ir > Rh > Pt > Au [42], contributing to high system costs. Reducing these expenses while maintaining efficiency remains a key challenge for PEM systems. In contrast, AWEs though slightly less energy-efficient, offer better durability, reliability, and safety, fueling growing interest in AWE technology.

1.4.4 H_2S Splitting

Water splitting is a widely accepted method for producing green hydrogen, but its efficiency is hampered by the sluggish OER at the anode, which has high thermodynamic demands ($\Delta G° = 237.19$ kJ mol^{-1} or >1.23 V) with slow kinetics [43]. In contrast, the electrochemical sulfide oxidation reaction (SOR) offers significant thermodynamic and kinetic advantages. When combined with the HER, hydrogen sulfide (H_2S) splitting can generate green hydrogen while reducing energy input, recovering valuable sulfur compounds (**Figure 1.11**), and mitigating environmental pollution. Thermodynamically, SOR requires much less energy ($\Delta G° = 33.44$ kJ mol^{-1} or >0.17 V) and proceeds faster than OER, making H_2S and related sulfide species effective electron donors [44,45]. Additionally, unlike OER, SOR does not produce gas bubbles, avoiding issues such as electrode surface blockage, mass transport limitations, and the formation of potentially

explosive gas mixtures [46]. In summary, integrating HER with SOR avoids the kinetic limitations posed by the sluggish OER, allowing the naturally faster HER to proceed more efficiently. Sulfide, particularly in its aqueous form, is abundant in natural anaerobic environments like the Black Sea, which holds an estimated 4×10^9 tons of buried H_2S and produces around 10,000 tons daily [47]. However, H_2S primarily originates from anthropogenic industrial activities such as oil.

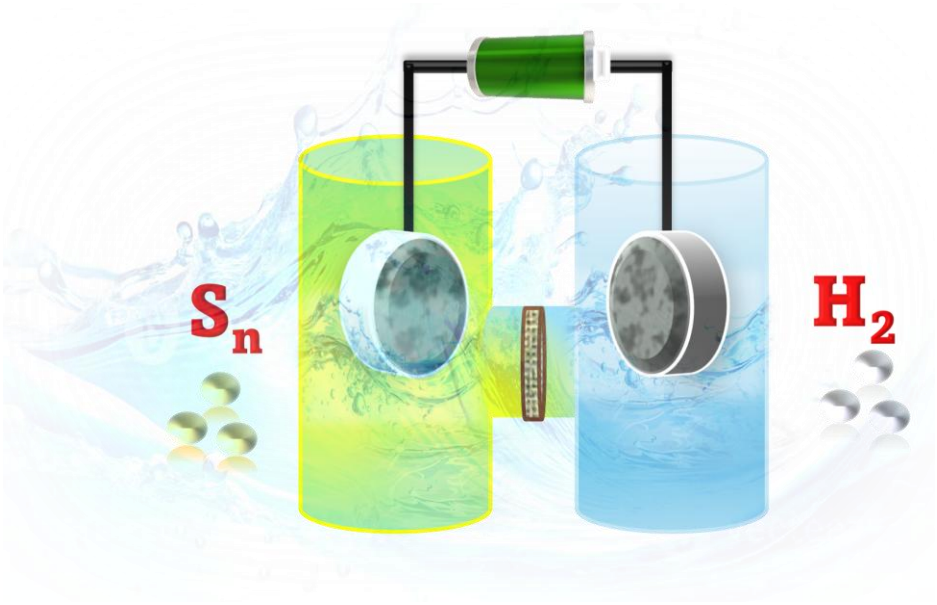

Figure 1.11 Electrochemical H_2S splitting.

The success of coupling the sulfide oxidation reaction (SOR) with the hydrogen evolution reaction (HER) hinges on efficient electron transfer from sulfide to the anode, either directly or indirectly. Although sulfide is electrochemically active, enhancing electron transfer is essential for practical, industrial-scale applications [48]. SOR generates a variety of oxidation products such as polysulfides (0/–1), elemental sulfur (0), sulfite (+4), thiosulfate (–1/+5), and sulfate (+6), reflecting its complex redox behavior. Among these, elemental sulfur poses a major challenge due to its insolubility in water and tendency to

form a high-resistivity (~10^{15} Ω·m) passivation layer on the anode. This layer severely impedes catalytic activity during continuous operation unless electrode–sulfur interfacial chemistry is carefully controlled. Moreover, the dynamic buildup of sulfur complicates the interpretation of SOR kinetics by introducing time-dependent increases in ohmic resistance. Thus, developing electrocatalysts with high activity, sulfur tolerance, and long-term stability is critical for achieving efficient desulfurization and sustainable sulfur valorization

1.4.4.1 Sulfide Oxidation Dynamics and Electrode Passivation by Sulfur

The SOR in aqueous electrolytes is complicated owing to the potential existence of several oxidation species; nevertheless, the primary reactions occurring in the SOR are as follows (**eq 1.8-1.10**) [49]:

$$2HS^- \rightarrow S + H_2S + 2e^- \qquad E^0 = -0.065 \text{ V vs. SHE} \quad (1.8)$$

$$HS^- + OH^- \rightarrow S + 2H_2O + 2e^- \qquad E^0 = -0.478 \text{ V vs. SHE} \quad (1.9)$$

$$S_2^- \rightarrow S + 2e^- \qquad E^0 = -0.508 \text{ V vs. SHE} \quad (1.10)$$

In aqueous alkaline sulfide solutions, elemental sulfur can react with sulfide or polysulfide ions to form extended-chain polysulfides (**eq 1.11-1.12**) [49].

$$HS^- + (n-1)S^0 + OH^- \rightarrow S_n^{2-} + H_2O \; ; n = 2-5 \quad (1.11)$$

$$S^0 + S_n^{2-} \rightarrow S_{n+1}^{2-} \; ; n = 2-4 \quad (1.12)$$

Moreover, sulfur oxyanions can form through the oxidation of sulfide, polysulfide ions, or elemental sulfur (**eq 1.13-1.15**) [49,50].

$$S_2^- + 6OH^- \rightarrow SO_3^{2-} + H_2O + 6e^- \qquad E^0 = -0.597 \text{ V vs. SHE} \quad (1.13)$$

$$S_n^{2-} + 6OH^- \rightarrow S_2O_3^{2-} + 3H_2O + (n-2)S + 6e^-;\ n = 2-5 \qquad E^0 = -0.647\ \text{V vs. SHE} \qquad (1.14)$$

$$S + 4H_2O \rightarrow SO_4^{2-} + 8H^+ + 6e^- \qquad E^0 = 0.357\ \text{V vs. SHE} \qquad (1.15)$$

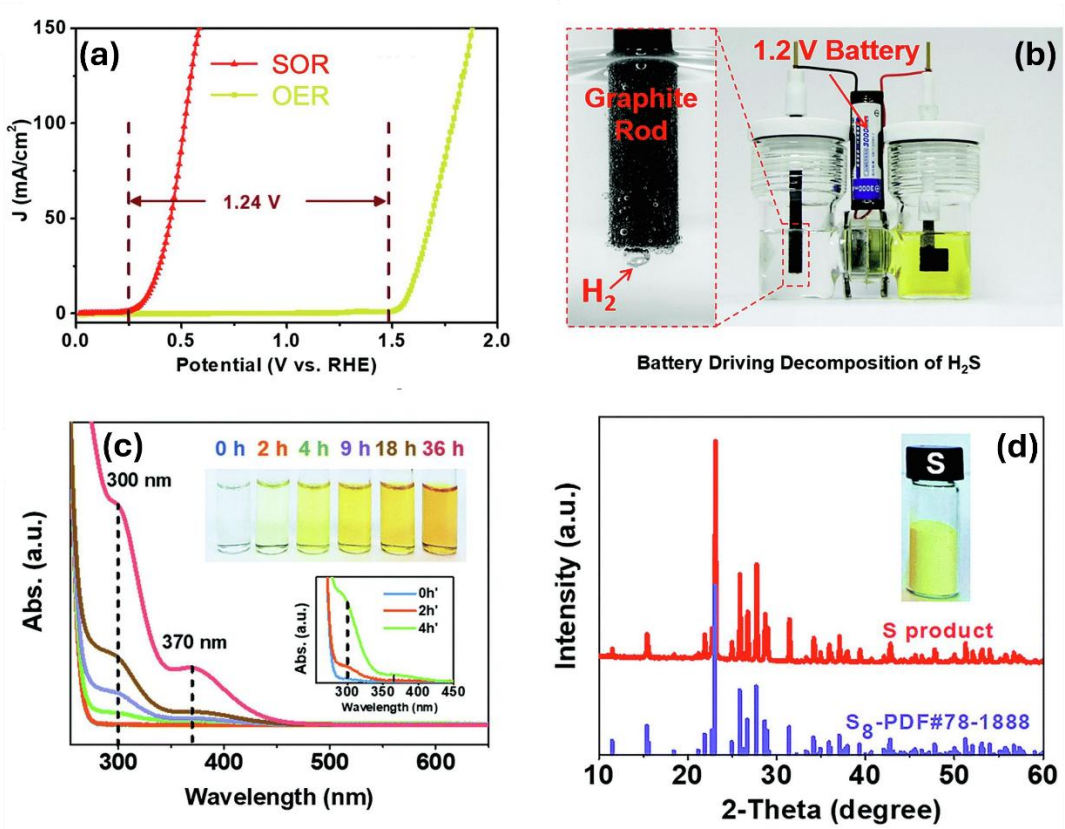

Figure 1.12 (a) Comparison of the electrochemical performance of synthesized catalysts (CoNi@NGs) during the SOR in 1 M Na_2S and 1 M NaOH and during the OER in 1 M NaOH (b) Image of a H_2S-splitting device powered by a commercial 1.2 V battery (c) UV–vis spectra of 250-times-diluted electrolyte samples and images of the corresponding electrolytes collected during a galvanostatic SOR in 1 M Na_2S and 1 M NaOH at 100 mA cm^{-2}, Inset graph shows the UV–vis spectra of electrolytes that were diluted 50 times (d) X-ray diffraction pattern and photograph of the harvested elemental sulfur. [Reproduced with permission from ref. 51, 2020, Royal Society of Chemistry]

Recent advances have led to the development of electrocatalysts capable of oxidizing sulfides in alkaline media while minimizing sulfur passivation. Typically, their performance is assessed using linear sweep voltammetry (LSV) with and without sodium sulfide (Na_2S), a common sulfide source. The addition of Na_2S notably shifts the onset

potential to lower values compared to OER, reflecting the greater thermodynamic favorability of the SOR (**Figure 1.12a**) [51]. Replacing OER with SOR in a water-splitting system reduces the required cell voltage by 2-3 times, with some studies demonstrating successful hydrogen production using a 1.2 V battery (**Figure 1.12b**).During SOR, the formation of yellow/orange polysulfides in the anolyte can be tracked using UV-vis spectroscopy, with peaks around 300 and 370 nm indicating short-chain polysulfides (S_2^{2-} - S_4^{2-}) (**Figure 1.12c**). These are produced by oxidation of sulfides to elemental sulfur, which then reacts with additional sulfide or polysulfides. Upon acidification with sulfuric acid, elemental sulfur precipitates out and is confirmed by X-ray diffraction (XRD) (**Figure 1.12d**). Stability and durability of the catalysts are further verified through chronoamperometry, chronopotentiometry, and repeated LSV or cyclic voltammetry. Recent studies have focused on developing catalysts for direct SOR in alkaline electrolytes to retain volatile H_2S and its products in the aqueous phase. As a result, catalyst design has shifted toward enhancing resistance to sulfur-induced degradation. Unlike conventional catalysts prone to sulfur passivation, sulfur-tolerant materials enable stable and efficient H_2S splitting by maintaining consistent SOR performance.

1.4.5 Evaluation parameters for electrochemical H_2O/H_2S splitting

To compare various electrocatalysts, it is essential to evaluate their performance in HER, OER, and overall water splitting. This is typically done by assessing three key parameters: activity, selectivity, and stability. Catalyst activity is gauged using overpotential, exchange current density, and Tafel slope; stability is assessed through changes in potential or current over time; and efficiency is measured via Faradaic efficiency and turnover frequency (TOF). The different evaluation metrics are briefly illustrated in **Figure 1.13**.

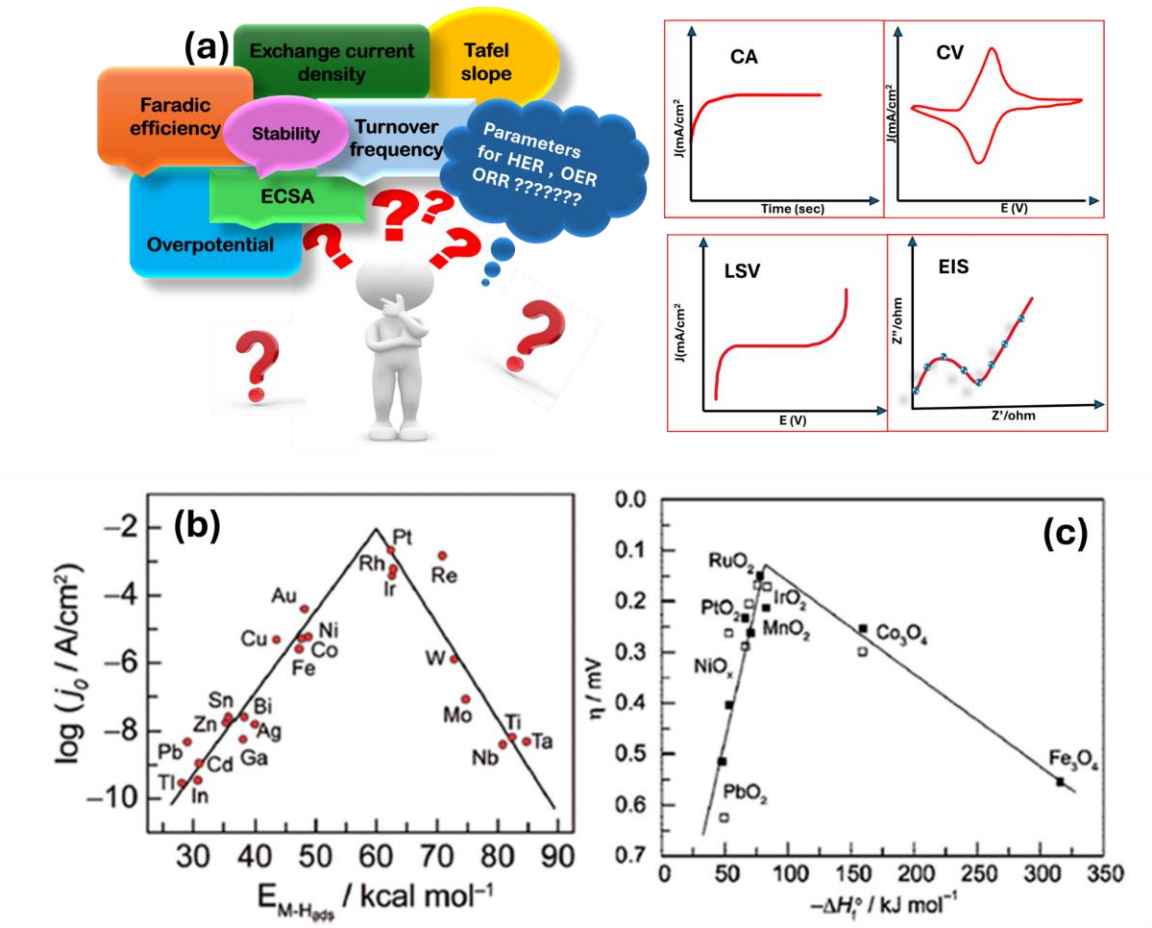

Figure 1.13 (a) Electrochemical evaluation parameters of HER/OER/ORR (b) (HE) volcano plot on metal electrodes under low pH environment (c) Volcano plot demonstrates the relationship between the rate of O_2 oxidation on transition metal oxide surfaces and change in enthalpy in acidic and basic media [Reprinted with permission from ref.70, Copyright 2022 Royal Society of Chemistry 2023]

1.4.5.1 Overpotential

As mentioned early, the thermodynamic equilibrium potentials for HER and OER are 0 V and 1.23 V vs. the RHE, respectively. However, due to inherent kinetic barriers, an additional potential known as the overpotential (η) is required to drive these reactions efficiently [52,53]. Three main types of overpotentials influence water splitting performance: activation, ohmic (resistance), and concentration overpotentials [54]. Activation overpotential refers to the extra energy needed to initiate the electrochemical

reactions and can be reduced by optimizing the catalyst material and surface structure. Ohmic overpotential arises from ionic resistance in the electrolyte and can be minimized using IR compensation. Concentration overpotential results from the accumulation of reaction products near the electrode surface, which can hinder further reaction and is mitigated by enhancing mass transport through nanostructured electrodes or conductive sublayers. In the case of HER, activation overpotential is also called onset overpotential and is the most significant, as HER generally proceeds with faster kinetics than OER. Electrocatalytic performance is commonly assessed using polarization curves, which plot current density against overpotential; a lower overpotential at a given current density indicates superior catalytic activity.

1.4.5.2 Tafel slopes

Tafel slopes are analyzed to gain insight into both the kinetics and the reaction mechanism of the electrocatalytic process. Represented in millivolts per decade (mV dec^{-1}), the Tafel slope indicates the voltage required to increase the current by a factor of 10. Accurate analysis requires linear fitting within the linear region of the Tafel plot, typically using the Tafel equation (**eq 1.16-1.18**) [55]:

$$\Upsilon = a + b\log j \tag{1.16}$$

Here a and b are:

$$a = \frac{2.303\ RT}{\alpha F}\log\left(j_0\right) \tag{1.17}$$

$$b = \frac{-2.303\ RT}{\alpha F} \tag{1.18}$$

In the Tafel equation, γ, b, and j represent the overpotential, Tafel slope, and current density, respectively. This equation provides two key parameters: the Tafel slope (b) and the exchange current density (j_0). While smaller Tafel slopes generally indicate that higher current densities can be achieved with lower overpotentials, the Tafel slope primarily reflects the rate-determining step (RDS) of the reaction rather than serving solely as a measure of kinetics. For the hydrogen evolution reaction (HER), assuming a charge transfer coefficient (α) of 0.5, typical values of ~120, 40, and 30 mV dec^{-1} correspond to the Volmer, Heyrovsky, and Tafel steps, respectively[56–58].

1.4.5.3 Turn over frequency (TOF)

TOF is a key metric for evaluating electrocatalytic performance, reflecting the intrinsic activity of a catalyst. It quantifies the number of hydrogen (H_2), or oxygen (O_2) molecules produced per active site per unit time and is expressed in S^{-1} [59]. While TOF is not influenced by the catalyst's overall quality, it is affected by the extent of active site exposure. A higher TOF indicates greater catalytic efficiency. However, accurate TOF determination depends on reliably identifying the number of active sites.

The equation of TOF is as follows (**eq 1.19**) [60]:

$$TOF = jA/\alpha Fn \quad (1.19)$$

For HER and OER, the TOF formula respectively are given in **eq 1.20-1.21** below

$$TOF_{HER} = jA/2Fn \quad (1.20)$$

$$TOF_{OER} = jA/4Fn \quad (1.21)$$

It is calculated using the current density (j) at a fixed overpotential, the electrode surface area (A), the number of electrons transferred (α = 2 for HER, 4 for OER), Faraday's

constant (F), and the number of moles of active material (n) on the electrode. However, accurately determining TOF for solid-state catalysts is difficult due to uneven active site distribution and accessibility. Despite its limitations, estimated TOF remains a useful comparative metric for evaluating catalytic activity within similar systems.

1.4.5.4 Faradaic efficiency (FE)

FE is a key metric for assessing a catalyst's selectivity toward HER or OER. It measures how effectively electrons from an external circuit are used to produce the target product [61]. For HER, many catalysts show near 100% FE, while OER catalysts often fall below 100% due to side reactions and heat loss. FE is calculated as the ratio of the experimentally measured hydrogen (nH_2) to the theoretically expected amount based on the total charge passed (Q), using the equation below. Q is obtained by integrating current over time, and nH_2 is typically measured via gas chromatography or water displacement. It is calculated using **eq 1.22** [62] :

$$FE = \frac{nH_2O}{Q/_{2F}} \tag{1.22}$$

F is the Faraday constant ≅ 96500 C/mol.

A widely used method to determine the FE of OER catalysts involves the rotating ring-disk electrode (RRDE) setup, which allows for real-time detection of oxygen evolution using a known collection efficiency. The FE for OER is commonly calculated using the **eq 1.23** [63]:

$$FE = \frac{I_R n_D}{I_D n_R N_{CL}} \tag{1.23}$$

Where I_R and n_R are the ring current value and number of transferred electrons at the ring, I_D and n_D are at the disc current value and the corresponding number of electrons transferred at the same and N_{CL} is RRDE collection efficiency, which is obtained by ferrous/ferric redox system response at different rotation rates. For OER, $n_D = n_R = 4$, so the electron-number ratio is unity. This method is highly effective for evaluating the true activity of an OER catalyst. However, potential losses in Faradaic efficiency may arise from redox peaks within the applied potential range, undesired side reactions, or heat dissipation during electrocatalysis [64].

1.4.5.5 Electrochemical Active Surface Area (ECSA)

ECSA refers to the portion of an electrode material that is accessible to the electrolyte, serving as a key indicator of the number of available active sites for electrocatalysis [65]. ECSA is commonly estimated by measuring the electrochemical double-layer capacitance (C_{dl}) using the **equation 1.24** below:

$$\mathrm{ECSA} = \frac{C_{dl}}{C_s} \tag{1.24}$$

Here, C_s is the specific capacitance of a smooth surface of the same material. C_{dl} is typically extracted from cyclic voltammetry (CV) curves recorded at varying scan rates within the non-faradaic potential region. Since ECSA is directly proportional to C_{dl}, a higher C_{dl} implies enhanced water and intermediate adsorption, improved electrolyte contact, and a greater number of active sites [66].

1.4.5.6 Electrochemical impedance spectroscopy (EIS)

Electrochemical Impedance Spectroscopy (EIS) is a valuable technique for probing the kinetics of electrode–electrolyte interactions. It can be performed under open-circuit

conditions or at defined potentials or currents. EIS data are typically analyzed using Nyquist plots fitted to an equivalent circuit model [67]. In these plots, high-frequency resistance (R_s) reflects the intrinsic and contact resistance between the electrode and substrate, while low-frequency resistance corresponds to charge transfer resistance (R_{ct}), indicating the ease of electron transfer. A larger semicircle in the Nyquist plot denotes higher R_{ct} and slower kinetics; a smaller semicircle implies lower R_{ct} and faster kinetics. Additionally, a semicircle in the low-frequency region may indicate adsorption resistance (R_{ad}), with lower R_{ad} values associated with more favorable onset potentials [68].

1.4.5.7 Stability

Stability is crucial for assessing electrocatalyst performance in practical applications. It is commonly evaluated using chronoamperometry/chronopotentiometry and cyclic voltammetry (CV)/linear sweep voltammetry (LSV) [69]. In chronoamperometry or chronopotentiometry, the current or potential is monitored over time at a fixed value, with minimal change indicating strong stability. In CV or LSV, changes in overpotential before and after multiple cycles (e.g., 10,000) are compared; a small shift suggests good catalytic durability.

1.4.5.8 Hydrogen Bonding Energy (HBE)

An ideal HER electrocatalyst should exhibit a hydrogen binding energy (HBE) that is balanced, neither too weak nor too strong. In the HER process, protons first adsorb onto the catalyst surface and are then reduced to form molecular H_2. If the HBE is too weak, proton adsorption is insufficient; if too strong, adsorbed hydrogen atoms (H*) remain bound to the surface, blocking active sites and deactivating the catalyst. Therefore, the

optimal Gibbs free energy for hydrogen adsorption (ΔG_{H^*}) should be close to zero, aligning with the standard hydrogen electrode potential defined as zero [70].

Volcano plots for the HER provide a unifying framework to understand catalytic trends across different pH environments. In acidic media (Figure 1.13b), the classic volcano curve correlates exchange current densities with HBE, with platinum located at the apex due to its nearly optimal H adsorption strength, giving negligible overpotential. In alkaline media, (Figure 1.13b), the volcano relationship is preserved but shifted toward higher overpotentials, as the additional water dissociation step introduces a kinetic barrier, making HER intrinsically slower. Nevertheless, hydrogen binding energy still serves as a reliable descriptor in both cases, allowing meaningful comparison across catalysts. Interestingly, surface oxidation and electrolyte composition can distort or even shift the volcano apex: for instance, Ni and Co show enhanced activity in alkaline solutions after oxidative treatment due to favorable metal oxide interfaces that accelerate water dissociation, while Pt activity diminishes in chloride-containing environments. Thus, while Pt remains the benchmark in both acidic and alkaline solutions on clean surfaces, volcano analysis reveals pathways to promote non-noble catalysts, particularly through interface engineering in alkaline media. Volcano plots have become a central tool to rationalize electrocatalyst activity for the OER in both acidic and alkaline environments (Figure 1.13c). In acidic media, only a few oxides such as RuO_2 and IrO_2 sit near the top of the volcano, combining reasonable activity with stability, whereas most transition-metal oxides dissolve rapidly. In alkaline media, the activity trends extend to a broader class of earth-abundant oxides (Ni-, Co-, Fe-based), and the volcano relationship reveals that either *OH or *OOH adsorption is the limiting step at the volcano legs. The universality of the *OH–*OOH scaling relation

displaces the theoretical "ideal" catalyst by ~0.37 V from zero overpotential, which explains why all known OER catalysts require significant overpotentials. Thus, volcano plots provide a unifying framework to compare OER activity across acidic and alkaline conditions, while also highlighting the intrinsic trade-offs between activity, stability, and mechanism that dictate catalyst performance.

1.4.6 Oxygen reduction reaction (ORR)

ORR has been extensively studied due to its critical role in energy conversion, particularly in fuel cells and metal–air batteries [71,72]. In polymer electrolyte membrane fuel cells (PEMFCs), ORR is the key cathodic process. ORR proceeds via two main pathways: a preferred 4-electron reduction to water (H_2O or OH^-), and a 2-electron reduction to peroxide species (H_2O_2 or HO_2^-), depending on the medium (**Figure 1.14a, Table 1.2**). Mechanistically, ORR can follow a dissociative or associative pathway, influenced by oxygen adsorption modes and the catalyst's O_2 dissociation barrier [73]. Two main adsorption types are observed: bidentate (Yeager model), leading to the 4-electron pathway, and end-on (monodentate), favoring the 2-electron route (**Figure 1.14b**) [74,75]. For practical applications, the 4-electron pathway is preferred to minimize peroxide formation and catalyst degradation.

For the associative mechanism in alkaline media, the ORR begins with the molecular adsorption of O_2 on a catalyst surface. The overall pathway can be summarized as follows, where * denotes a free active site on the catalyst:

$$O_2 + * = O_{2(ads)}$$

$$O_{2(ads)} + H_2O + e^- \rightarrow OOH_{(ads)} + OH^-$$

$$OOH_{(ads)} + e^- \rightarrow O_{(ads)} + OH^-$$

$$O_{(ads)} + H_2O + e^- \rightarrow OH_{(ads)} + OH^-$$

$$OH_{(ads)} + e^- \rightarrow OH^- + *$$

Table 1.2 The thermodynamic reaction potentials for ORR pathways.

Electrolyte	Reaction pathway	Reaction potential (V vs. NHE)
Alkaline electrolyte	$4e^-$ pathway: $O_2 + 2H_2O + 4e^- \rightarrow 4OH^-$	+ 0.401
	Peroxide pathway: $O_2 + H_2O + 2e^- \rightarrow HO_2^- + OH^-$	− 0.065
	$HO_2^- + H_2O + 2e^- \rightarrow 3OH^-$	+ 0.867
	Or	Decomposition
Acidic electrolyte	$4e^-$ pathway: $O_2 + 4H^+ + 4e^- \rightarrow 2H_2O$	+ 1.229
	Peroxide pathway: $O_2 + 2H^+ + 2e^- \rightarrow H_2O_2$	+ 0.67
	$H_2O_2 + 2H^+ + 2e^- \rightarrow 2H_2O$	+ 1.77
	Or	Decomposition

Here, four electrons in total are accepted by O_2, resulting in 4 OH^- ions being produced to complete a 4-electron ORR.

Alternatively, if adsorbed OOH_{ads} accepts an electron and desorbs from the catalyst surface, it leads to the formation of peroxide ions (HO_2^-), terminating the reaction chain and resulting in a 2-electron ORR pathway, as shown below:

$$OOH_{(ads)} + e^- \rightarrow OOH^- + *$$

In the dissociative mechanism under alkaline conditions, O_2 molecules adsorb onto the catalyst surface and directly dissociate into two adsorbed oxygen atoms (O_{ads}). This pathway proceeds via a complete 4-electron reduction, as represented by the following steps:

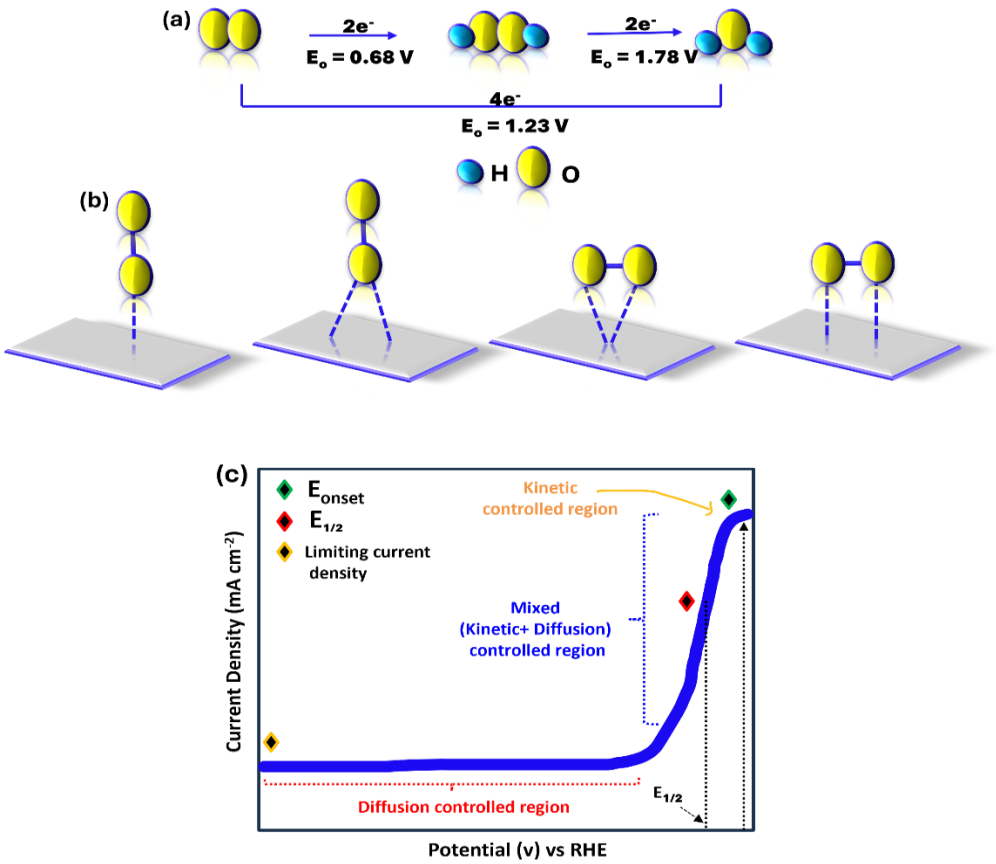

Figure 1.14 Scheme of the ORR mechanism by direct pathway and indirect pathway (b) The schematic illustration of various modes of O adsorption on catalyst surfaces [From left to right: on top end-on; bridge end-on; bridge side-on one site; and bridge side-on two sites] (c) Typical LSV polarization curve for ORR with different regions.

$$\frac{1}{2}O_2 + * \rightarrow O_{(ads)}$$

$$O_{(ads)} + H_2O + e^- \rightarrow OH_{(ads)} + OH^-$$

$$OH_{(ads)} + e^- \rightarrow OH^- + *$$

As for acidic electrolytes, a similar reaction mechanism occurs in which in the presence of protons, the reaction route will change to:

$$O_{2(ads)} + H^+ + e^- \rightarrow OOH_{(ads)}$$

$$OOH_{(ads)} + \ H^+ + e^- \ \rightarrow O_{(ads)} + H_2O$$

$$O_{(ads)} + \ H^+ + e^- \rightarrow OH_{(ads)}$$

$$OH_{(ads)} + \ H^+ + e^- \rightarrow H_2O \ + *$$

Here, four protons and four electrons are consumed and O_2 is completely reduced into two H_2O.In addition, $OOH_{(ads)} + e^- \rightarrow OOH^- + *$ will also change to $OOH_{(ads)} + \ H^+ + e^- \ \rightarrow H_2O_2 + *$

And based on these mechanisms, improving ORR kinetics and reducing overpotentials in both acidic and alkaline media require minimizing the formation of H_2O_2 or HO_2^- to favor the more efficient 4-electron pathway. As discussed earlier, the choice of electrocatalyst plays a critical role in steering the reaction toward this preferred pathway by influencing adsorption behavior and lowering the energy barriers of key steps.

1.4.7 Basic Parameters to Evaluate ORR Catalysts

Since Levich's introduction of the rotating disk electrode (RDE) in 1944, it has become a key tool for analyzing ORR kinetics via polarization curves [76]. These curves are typically divided into three regions: kinetic, mixed (kinetic + diffusion), and diffusion-limited, each reflecting different rate-controlling factors. Key parameters such as onset potential (E_{onset}), half-wave potential ($E_{1/2}$), and diffusion-limited current density (J_l) are derived from these curves to assess electrocatalyst performance. Generally, a more positive E_{onset} and $E_{1/2}$, along with a higher J_l, indicate better ORR activity. In the kinetic region, ORR is slow, and current density rises gradually with decreasing potential (**Figure 1.14c**). In the mixed (kinetic and diffusion-controlled) region, the reaction rate increases with decreasing

potential, leading to a sharp rise in current density, which becomes inversely related to the applied potential. In the diffusion-controlled zone, which is the plateau region of the curve, the current density is governed primarily by mass transport through convection and stabilizes at a value determined by the electrode's rotation speed.

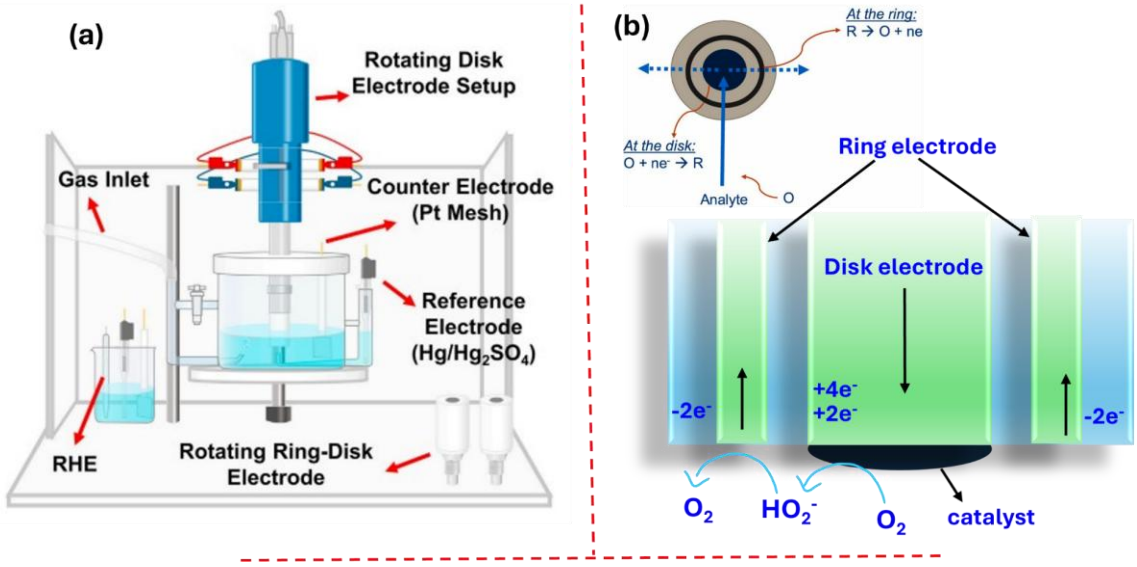

Figure 1.15 Schematic of a RRDE set-up [Reprinted with permission from ref. 77, Copyright 2021 Cell Press] (b) Reactions at the disk and ring electrodes.

1.4.7.1 Onset Potential and Half-Wave Potential

The definition of onset potential (E_{onset}) varies across the literature, and its experimental determination can be somewhat arbitrary. Typically, E_{onset} is identified as the potential where the current first deviates from the baseline, often determined by the intersection of tangents drawn along the baseline and the rising portion of the polarization curve [**Figure 1.14c**]. Another key parameter, the half-wave potential ($E_{1/2}$), is more straightforward and it is the potential at which the current reaches half of the diffusion-limited current density, usually determined from the LSV curve recorded at 1600 rpm.

1.4.7.2 Kinetic Current Density

The kinetic current density (I_k) is a crucial parameter for evaluating the catalytic activity of an ORR catalyst. It can be determined by correcting the polarization curve for mass transport limitations. This correction is performed using the Koutecky–Levich (K–L) equation, as shown in **Equation 1.25** below. The K–L analysis helps isolate the intrinsic kinetic behavior of the catalyst by separating it from diffusion-related effects.

$$\frac{1}{I} = \frac{1}{I_{\mathrm{L}}} + \frac{1}{I_{\mathrm{K}}} = \frac{1}{B\omega^{0.5}} + \frac{1}{I_K} \qquad (1.25)$$

where I is the measured current density, I_L is the diffusion-limiting current density, and I_k is the kinetic current density. The term w represents the electrode rotation rate, while B is the Levich constant that accounts for diffusion-related contributions. The Levich constant is defined as

$$B = 0.62\, nFD^{2/3}\, \nu^{-1/6}\, C$$

where n is the number of electrons transferred per molecule, F is the Faraday constant (96,485 C mol^{-1}), D is the diffusion coefficient of the reactant, ν\nuν is the kinematic viscosity of the electrolyte, and C is the bulk concentration of the reactant. To minimize errors associated with mass transport corrections, catalysts are typically compared based on their I_k values at higher potential regions, where diffusion limitations are minimal and kinetic effects dominate.

1.4.7.3 Electron Transfer Number and H_2O_2 % yield

The number of electrons transferred (n) and the percentage of H_2O_2 intermediates are fundamental parameters for evaluating ORR kinetics. These can be determined using

rotating disk electrode (RDE) or rotating ring-disk electrode (RRDE) techniques, which are highly effective for probing multistep charge transfer reactions. RRDE enables real-time detection of intermediates or products formed at the disk and captured at the ring electrode. By applying an appropriate potential to the ring, species like hydrogen peroxide (H_2O_2) generated at the disk can be precisely quantified. The RRDE setup and corresponding reactions at the disk and ring electrodes are illustrated in **Figure 1.15a, b** [77]. The Koutecky–Levich (K–L) equation is typically used to calculate the n value by plotting $1/I_l$ against the square root of the rotation rate ($\omega^{-1/2}$), forming the well-known K-L plot (**Equations 1.26 and 1.27**).

$$I_L = B\omega^{1/2} \tag{1.26}$$

$$\text{here, } B = 0.62\, nFC_0\, (D_0)^{2/3}\, \nu^{-1/6} \tag{1.27}$$

where, ω is the electrode rotating rate (rad s^{-1}), n is the number of electrons, F is the Faraday constant (F = 96485 C mol^{-1}), C_0 and D_0 are the concentration and diffusion coefficients of O_2, υ is the kinematic viscosity of the electrolyte, and k is the electron transfer rate constant [77]. The "n" value can also be calculated from the RRDE technique by using the following **eq 1.28** given below

$$n = 4 \times \frac{I_D}{I_D + I_R/N} \tag{1.28}$$

where I_D is the disc current density, I_R is the ring current density, and N is the RRDE collection efficiency, n is the number of electron transfers during the reaction.The percentage of intermediate species for ORR is calculated by the **eq 1.29** given below:

$$\%\, H_2O_2 = 200 \times \frac{\frac{I_R}{N}}{I_D + \frac{I_R}{N}} \tag{1.29}$$

1.5 Transition Metal Compounds in the Electrochemical Era: Diversity, Design, and Direction

Precious metals like Pt, Ir, and Ru, along with their alloys, are considered benchmark electrocatalysts due to their exceptional activity and stability. However, their scarcity and high cost hinder large-scale industrial applications. To address this, intensive research has focused on developing non-precious metal-based electrocatalysts for various electrochemical processes.

Among these, transition metal compounds (TMCs) have drawn significant attention due to their unique crystal structures, abundant redox-active sites, tunable electronic properties, and relatively high conductivity. Compared to conventional anode materials like graphite in lithium-ion batteries (LIBs), TMCs often exhibit higher theoretical specific capacities [80,81]. In metal-air batteries, TMCs used as air electrode materials have shown excellent catalytic performance for both the ORR and the (OER, rivaling that of noble metal catalysts [82].

Transition metal oxides and hydroxides are particularly effective for OER due to their favorable electronic structures and oxygen binding affinities. Their performance can be significantly enhanced through strategies such as morphological tuning, heteroatom doping, vacancy engineering, and integration with conductive substrates. These approaches improve charge transfer, expose more active sites, and optimize the binding energies of reaction intermediates, thereby boosting both OER and hydrogen evolution reaction (HER) activities [83].

Transition metal sulfides and selenides are also prominent HER catalysts, valued for their layered structures, abundant active sites, and suitable hydrogen adsorption energies. They

function well in both acidic and alkaline media [84]. Incorporating multiple metals into bimetallic or multimetallic systems (e.g., Ni-Co-C/NF, 2D VSe_2, NiSe/NF, NiCu-MoS_2) further enhances catalytic performance through synergistic effects, electronic structure modulation, and improved conductivity. These Transition metals (TM) also demonstrate excellent activity for H_2S splitting, benefiting from enhanced sulfur adsorption and resistance to sulfur-induced deactivation [85]. Despite these advantages, TMCs still face challenges such as low specific surface area, limited reactivity, poor charge transfer rates, and rapid electron-hole recombination [86]. A promising strategy to overcome these limitations is the integration of TMCs with carbon-based substrates. Constructing strong interfacial adhesion between TMCs and conductive carbon skeletons promotes uniform dispersion, enhances stability, and facilitates efficient electron transport, making these composites more viable for practical energy applications [86].

1.6 Conductive Carbon Skeletons: The Backbone of Advanced Electrochemical Systems

As mentioned earlier, the high-power output of TM-based electrodes is often constrained by their inherently low electrical conductivity and sluggish redox reaction kinetics. To overcome these limitations, TMCs are typically integrated with carbon-based skeletons, which not only construct efficient electron and ion transport channels but also enhance the structural stability of the electrodes. In recent years, carbon skeletons with various dimensionalities, ranging from 0D to 3D, have been successfully designed and incorporated into TM composites [87-90]. Among the different carbon supports, graphene has attracted particular interest due to its unique combination of advantageous properties. These include its intrinsic catalytic activity that enables co-catalytic functions, its ability to

enhance the performance of supported metals, and its capacity for chemical functionalization to fine-tune catalytic behavior [91-93]. Additionally, graphene possesses a robust lattice structure, excellent electrical conductivity, and a distinctive ability to modulate the electron donor/acceptor properties of the metal components it supports. This carbon framework often exhibits a hierarchical porous architecture and extremely high surface area, which together provide abundant pathways for electrolyte ion and electron transport as well as ample space for the uniform and stable growth of nanoscale TMCs [94].

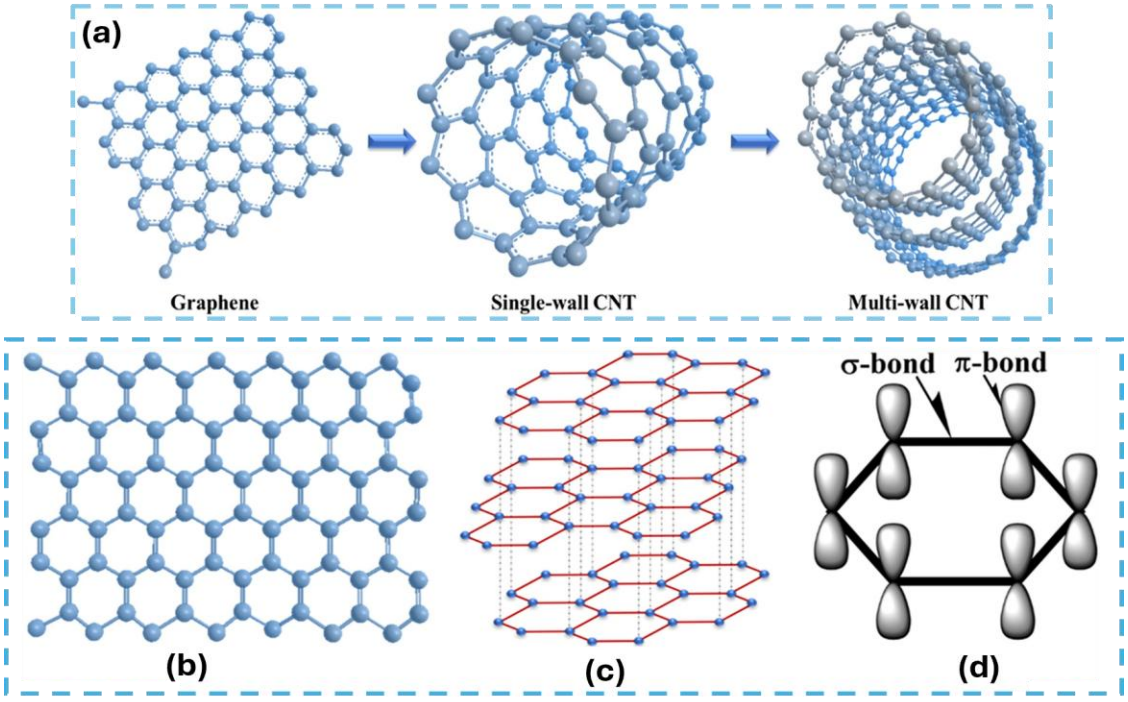

Figure 1.16* (a) *Rolling of graphene into SWCNTs and stacking within MWCNTs (b) Hexagonal honeycomb structure of graphene (c) stacked graphene layer, and (d) distribution of σ and π bonds on the graphene structure. [Reprinted with permission from ref. 95, Copyright 2022 Elsevier]

Graphene is a two-dimensional allotrope of carbon composed of sp^2-hybridized carbon atoms arranged in a hexagonal honeycomb lattice. Each carbon atom forms three strong

covalent σ-bonds, separated by 0.142 nm, contributing to graphene's remarkable mechanical strength. The fourth valence electron forms a π-bond, oriented perpendicular to the σ-plane, which enables efficient electron delocalization and contributes to graphene's exceptional electronic properties [95]. These structural features are visually represented in **Figures 1.16a–d**, which show both 2D and 3D configurations of graphene derived from its hybridized carbon bonding.

Table 1.3 Physical property characteristics of common carbon support materials [95].

Carbon materials	Specific surface area (m^2/g)	Pore volume (cm^3/g)	Density (g/cm^3)	Electric conductivity(S/cm)
Graphite	10–100	0.01–0.1	2.26	10^4
Activated carbon	1000–3500	0.6–2	0.4–0.7	0.1–1
Carbon fibers	1000–3000	0.3–0.7	0.3–0.8	5–10
carbon aerogels	400–1000	2–6	0.5–0.7	1–10
CNTs	120–500	2.5	0.6	10^4 –10^5
Graphene	1500–2500	2–3.5	> 1	10^4

Like graphene, carbon nanotubes (CNTs) are essentially rolled graphene sheets. They exist as either single-walled carbon nanotubes (SWCNTs), which consist of a single cylindrical graphene layer, or multi-walled carbon nanotubes (MWCNTs), which are composed of multiple concentric graphene cylinders. **Table 1.3** summarizes the key physical properties of various carbon-based supports. Of all, Graphene materials, have demonstrated remarkable performance as electrocatalysts for the ORR, OER, and HER due to its exceptional properties (**Figure 1.17**) [96]. A wide variety of graphene-based materials such as reduced graphene oxide (rGO), graphene quantum dots (GQD) and doped graphene

have shown their applications as electrocatalysts. While pristine graphene has shown limited intrinsic catalytic activity for HER and overall water splitting (OWS), significant improvements have been achieved through nanoscale structuring and chemical modifications in graphene's electronic configuration and surface reactivity, thereby boosting its catalytic efficiency for HER and OWS applications.

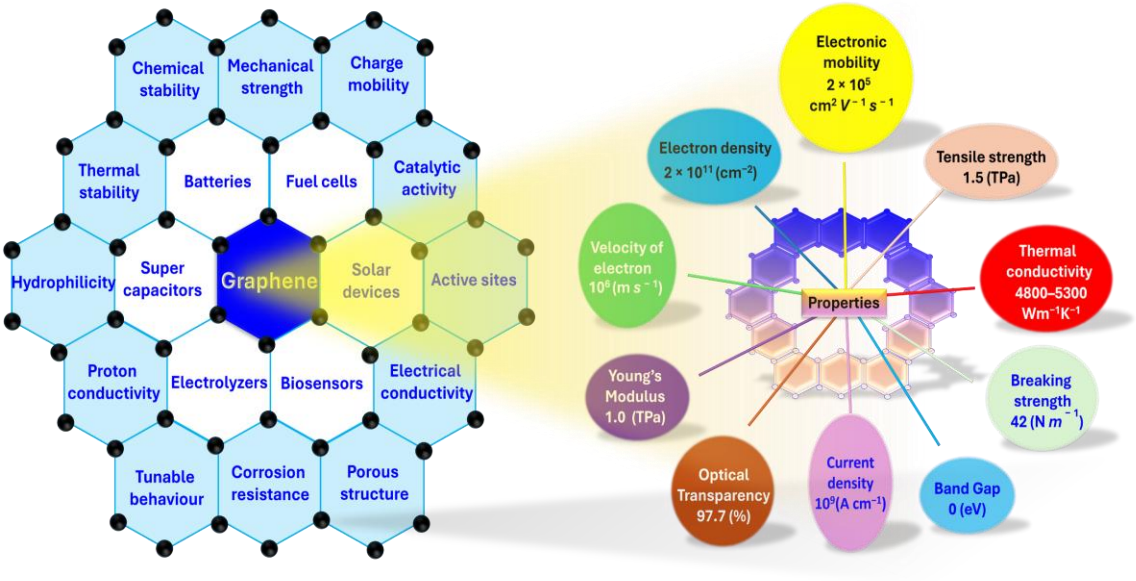

Figure 1.17 Material properties of graphene.

1.7 Strategic Manipulation of Graphene's Properties for Enhanced Electrocatalytic Performance

Pristine graphene, with its zero bandgap, allows excellent electron flow but is challenging to preserve during synthesis. As mentioned earlier, Modified graphene, featuring defects, functional groups, or dopants, offers tunable catalytic properties by altering the π-electron network and band structure. Defects enhance metal ion affinity and nucleation, while

dopants enable precise control of electronic and active site characteristics. These modifications make graphene an ideal support for optimizing heterogeneous catalysis.

1.7.1 Defect and Edge Tailoring

Metastable states in materials, often formed by defects, display unique properties distinct from thermodynamically stable phases. In graphene, such defects like vacancies, intrusions, and grain boundary shifts arise from applied stresses and enable property tuning for specific applications. The behavior of these defects depends on the type of stress and graphene's ability to re-hybridize for self-repair [97,98]. Graphene is commonly synthesized via chemical vapor deposition or graphite exfoliation [95], producing either pristine or defective forms based on the carbon source, synthesis conditions, and mechanical forces. Defects in graphene are typically classified as point, line, or interlayer types (**Figure 1.18**). Defects play a crucial role in enhancing the electrochemical performance of catalysts in HER, ORR, and OER. Kinetically, defect sites can serve as active centers for hydrogen evolution, and their presence helps optimize the electronic structure to accelerate the HER process [99]. Heteroatom doping is an effective strategy to increase defect density, enabling precise tuning of the band structure and electrical properties of 2D materials.

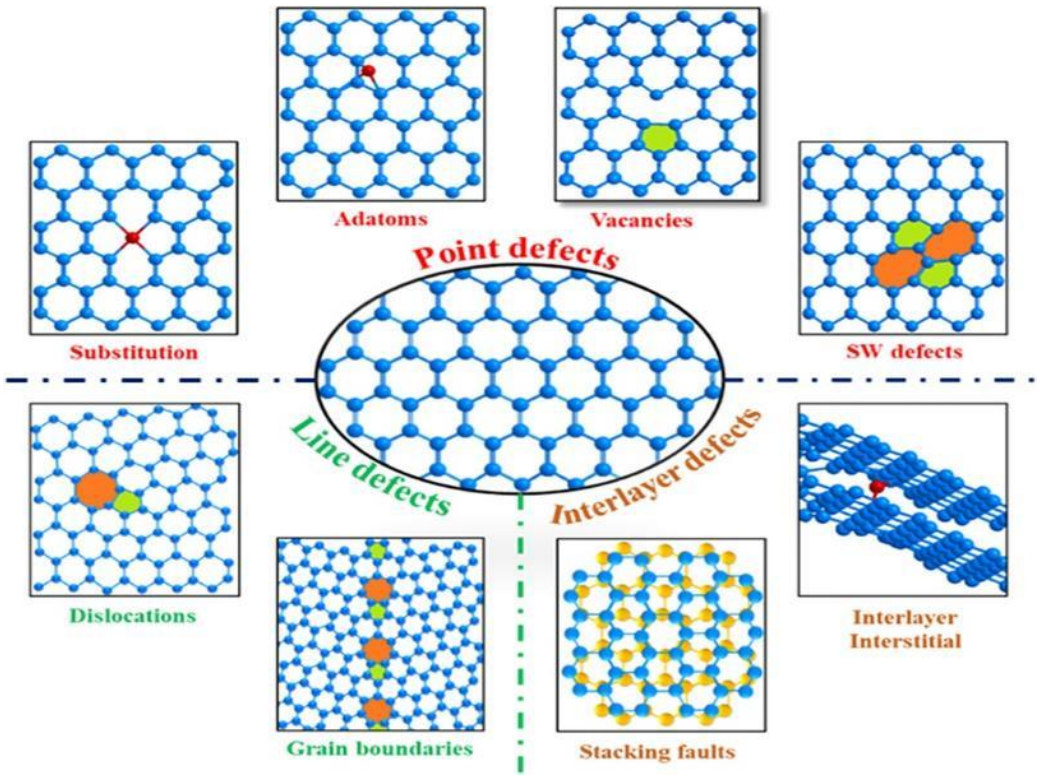

Figure 1.18 Structural defects in graphene [Reprinted with permission from ref.95, Copyright 2022 Elsevier]

Additionally, edge modulation is vital for catalytic activity; edge sites are far more reactive than the basal plane and strongly influence the electronic behavior and surface reactivity of graphene-based materials [100,101].

1.7.2 Graphene functionalization

Graphene-based nanomaterials are classified based on the number of layers, sheet dimensions, surface modifications, and defect density. Common forms include single-layer graphene, few-layer graphene, graphene oxide (GO), and reduced graphene oxide (rGO), as illustrated in **Figure 1.19** [102]. A key challenge in their use as electrocatalysts is their inherent hydrophobicity, which limits electrolyte dispersion. Surface functionalization, particularly heteroatom doping with elements like N, B, O, and S, enhances wettability and catalytic activity by introducing oxygen-containing groups (e.g., hydroxyl, epoxy,

carboxyl) or generating defects through lattice oxidation [103,104]. In GO, peripheral regions are typically modified with carboxylic acids and phenols, while the basal plane contains epoxy and hydroxyl groups. Although this disrupts the sp^2 hybridization and planarity, it increases the number of active sites and enhances catalytic performance [105]. The catalytic efficiency of modified graphene depends on the type and density of these functional groups. Furthermore, graphene's tunable structure makes it an excellent platform for functionalization, particularly as a support for metal dopants that can serve as catalysts or co-catalysts in various reactions.

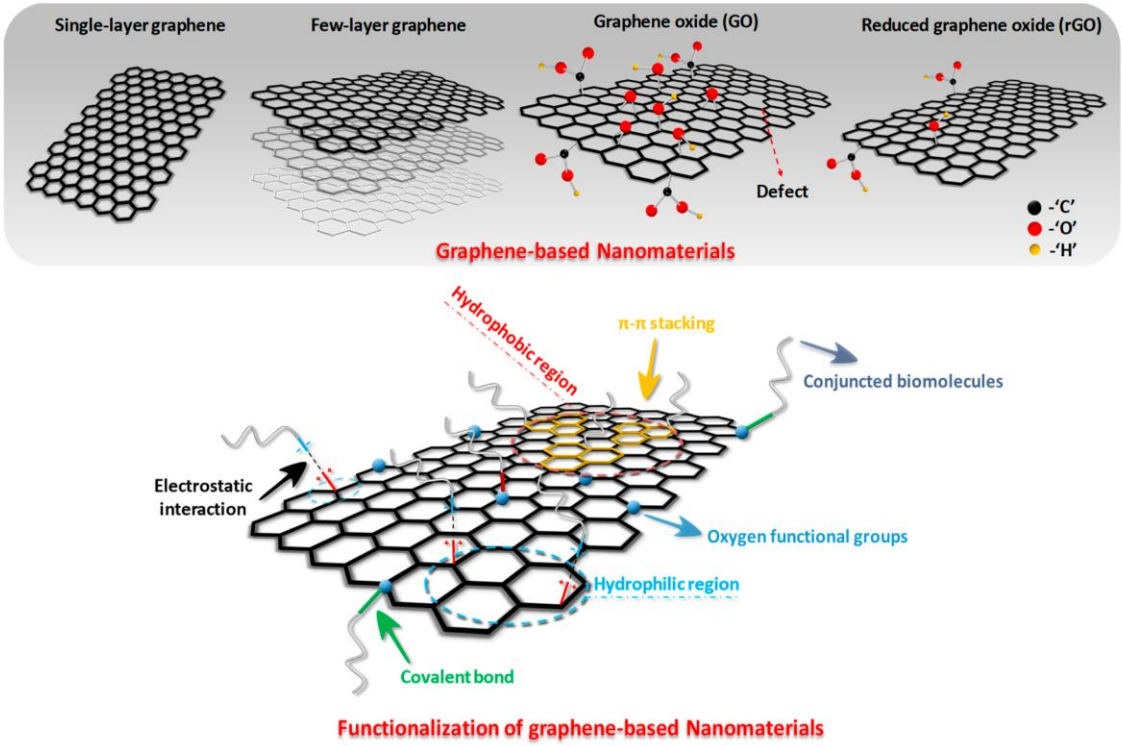

Figure 1.19 Overview of the various structures of graphene-based nanomaterials (GNs) and the illustration of covalent/non-covalent functionalization of these nanomaterials. [Reprinted with permission from ref. 102, Copyright 2019 MDPI]

Metals are highly effective catalysts, and single-atom catalysis has emerged as a promising alternative to traditional nanoparticle-based systems due to its potential for material

efficiency and maximized atom utilization. In this context, doping graphene has opened exciting avenues for energy-related applications by significantly enhancing its catalytic properties. However, several challenges remain. A deeper mechanistic understanding of how doping improves graphene's performance is still needed, along with methods to introduce dopants without compromising graphene's intrinsic physical properties. Additionally, insights into the nature of dopant-graphene bonding are crucial for rational catalyst design. To address these gaps, the development of innovative doping strategies will be essential for advancing the electrochemical performance of graphene-based materials.

1.7.3 Porous Structure and Morphology Engineering

Nano-engineered 3D porous materials have emerged as next-generation electrocatalysts for efficient water splitting, offering superior physicochemical properties over bulk materials [106,107]. Their high surface area, improved mass transport, and abundant active sites enhance both HER and OER performance. In particular, micropores (<2 nm) increase active site density, mesopores (2-50 nm) improve connectivity, and macropores (>50 nm) facilitate reactant diffusion [108]. In graphene-based systems, tuning pore size, shape, and distribution enhances conductivity, electron transport, and prevents nanoparticle aggregation. These advantages make porous graphene-based catalysts highly active, durable, and cost-effective alternatives to noble-metal catalysts for sustainable energy applications.

1.8 Synergizing Strengths: Enhanced Performance via TMC-Carbon Nanomaterial Integration

As discussed earlier, TMCs are excellent electrocatalysts for electrochemical reactions due to their tunable electronic structures and rich active sites. Meanwhile, carbon-based

nanomaterials, particularly graphene and its derivatives, offer high electrical conductivity, structural stability, and large surface area. The strategic integration of TMCs with graphene creates a promising class of hybrid electrocatalysts for various reactions including HER, OER, ORR, and SOR [109-111].

These hybrids form heterointerfaces that enable strong electronic coupling and intimate contact between TMCs and carbon supports. This synergy increases the density of exposed active sites, enhances surface area, and improves reactant accessibility. As a result, the kinetics of HER and OER are significantly improved, leading to greater water-splitting efficiency [112-114]. The carbon support also prevents TM nanoparticle aggregation and oxidation, ensuring long-term structural and electrochemical stability. Graphene's exceptional conductivity enables rapid electron transfer to active sites, especially critical for sluggish ORR processes. Moreover, the electronic interaction at the TMC/graphene interface can modulate local electronic environments, optimizing intermediate adsorption (*O, *OH, *OOH) and promoting efficient four-electron ORR pathways, yielding improved onset and half-wave potentials [115].

Beyond water splitting, TMC/graphene hybrids show promise in hydrogen sulfide (H_2S) electrolysis, a growing area in industries dealing with H_2S as a hazardous by-product. In sulfur-rich electrolytes like Na_2S, TMC sulfides and selenides often favor the HER + SOR pathway due to favorable thermodynamics and faster kinetics. However, sulfur accumulation on the anode surface remains a challenge, deactivating the catalyst by blocking active sites [116,117]. This issue can be mitigated by tuning the sulfiphilicity of catalysts through heterojunction formation with conductive supports like graphene or

reduced graphene oxide (RGO), which resist sulfur poisoning and enhance long-term durability [51,85,118].

In summary, TMC/graphene composites offer synergistically enhanced activity, stability, and charge transfer efficiency across a broad range of electrochemical reactions. Their versatility and performance make them strong candidates for energy conversion and environmental remediation. However, further research is needed to address remaining challenges, including catalyst degradation, active site optimization, scalable synthesis, and integration into practical devices to fully realize their potential in next-generation sustainable technologies.

1.9 Recent advances in Graphene-Transition metal based electrocatalysts for various electrochemical reactions

Over the last several years, many graphene-TM based electrocatalysts which mainly include transition metal alloys, oxides, hydroxides, chalcogenides, phosphides, nitrides, carbides and borides, etc. have been developed as efficient electrocatalysts for various electrochemical applications like water splitting, hydrogen sulfide splitting, oxygen reduction reactions etc. [119,120]. Several literature reports have highlighted the mutual benefits of integrating TMCs with graphene-based materials in electrocatalysis, as summarized below:

Liu et al. synthesized 3D flower-like $MoSe_2$ nanostructures on graphene via a simple wet-chemical method (**Figure 1.20a**), where graphene improved $MoSe_2$ dispersion and prevented leaching, leading to enhanced HER activity with a low onset potential of 125 mV, Tafel slope of 67 mV dec^{-1}, and stable performance over 6000 s in 0.5 M H_2SO_4

(**Figure 1.20b, c**) [121]. Zhang et al. prepared FeP nanoparticles on graphene nanosheets via thermal phosphidation, achieving a low onset potential of 30 mV and a Tafel slope of 50 mV dec^{-1} in acidic media, highlighting improved durability and efficiency for water splitting [122]. Similarly, MoO_2@PC-rGO, derived from carbonizing a polyoxometalate-based MOF and GO, featured MoO_2 embedded in phosphorus-doped porous carbon on rGO (**Figure 1.20d**). It exhibited outstanding HER performance with a Tafel slope of 41 mV dec^{-1}, overpotential of 64 mV at 10 mA cm^{-2}, and superior electrochemical surface area (C_{dl} = 131.2 mF cm^{-2}), significantly outperforming MoO_2@PC (C_{dl} = 19.2 mF cm^{-2}) (**Figure 1.20e, f**) [123]. MoO_2@PC-RGO exhibits enhanced HER activity due to synergistic effects between highly dispersed MoO_2 particles, phosphorus-doped porous carbon, and RGO, which expose more active edge sites. Zhang et al. synthesized 3D mesoporous van der Waals heterostructures of graphene and N-doped MoS_2 using a two-step CVD process. This hybrid showed significantly improved HER, OER, and ORR performance in 0.1 M KOH due to better conductivity, accessible active sites, and optimized intermediate adsorption (**Figure 1.20g-i**) [124]. Specifically, N-MoS_2 delivered a low HER overpotential of 243 mV at 10 mA cm^{-2}, while graphene boosted ORR and OER with a potential gap of ~0.90 V, indicating promising trifunctional activity. The electron transfer mechanism in the G@N-MoS_2 heterostructure is illustrated in **Figure 1.20j.**

Xu et al. fabricated Ni nanoparticles encapsulated in few-layer N-doped graphene (Ni@NC) via high-temperature annealing of a Ni-MOF. Ni@NC achieved 10 mA cm^{-2} at 1.60 V in 1 M KOH, attributed to the synergistic interaction between Ni cores and N-doped graphene shells [125]. Yan et al. developed a freestanding 3DCNT/rGO heterostructure film (CGHF), named Ni@N-HCGHF, based on interfacial interactions between MOFs and

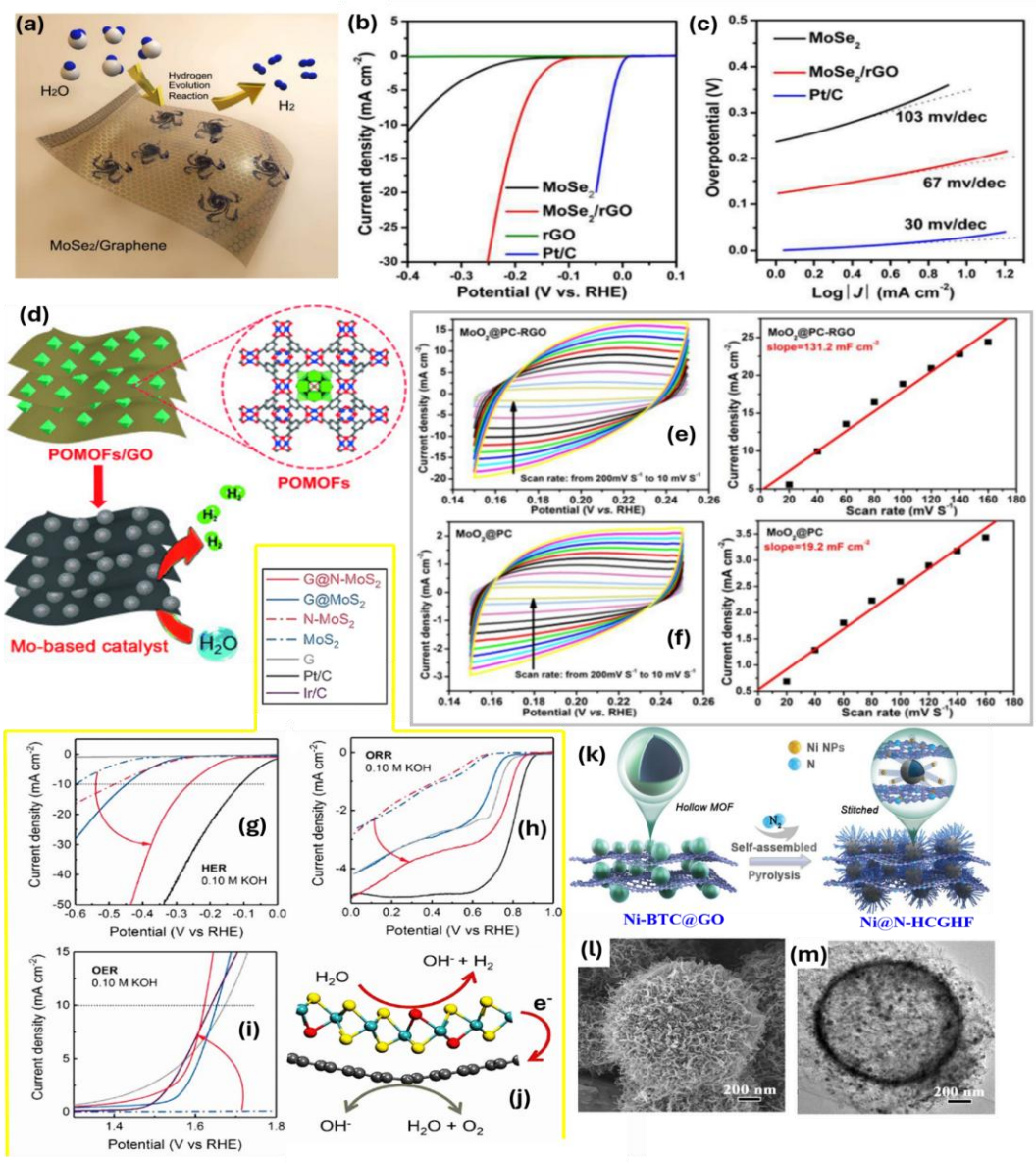

Figure 1.20 (a) Schematic illustration of uniform 3D $MoSe_2$ nanoflowers anchored on graphene nanosheets (b) Polarization curves of $MoSe_2$, $MoSe_2$ -rGO hybrid nanostructures, rGO and Pt/C (15%) for comparison (c) The corresponding Tafel curves [Reproduced with permission from ref. 121, Copyright 2015 Royal Society of Chemistry] (d)MoO_2@PC-RGO nanocomposite used as electrocatalyst for the HER Cyclic voltammograms ; CV curves for (e) MoO_2@PC-RGO (f) MoO_2@PC in the region of 0.15~0.25 V vs. RHE at various scan rates and the corresponding electrochemical double-layer capacitances (C_{dl}) measurements; Trifunctional electrocatalytic activity [Reproduced with permission from ref. 123, Copyright 2015 Wiley-VCH] (g) HER (h) ORR (i) OER of 3D G@N-MoS_2 in 0.1 M KOH solution (j) Schematic representation of the electron transfer effects in G@N-MoS_2 heterostructures toward improved electrocatalytic activities for ORR, OER, and HER [Reproduced with permission from ref. 124, Copyright 2018 Wiley-VCH] (k)Schematic of the preparation of Ni@N-HCGHF (l) SEM and (m) TEM images of Ni@N-HCGHF. [Reproduced with permission from ref. 126, Copyright 2020 Wiley-VCH]

the graphene framework (**Figure 1.20k**), enabling improved electrocatalytic performance. The MOF-derived N-doped CNT-HM superstructure (**Figure 1.20l, m**) prevents rGO aggregation, offers a large surface area, and generates abundant active sites, significantly boosting electrocatalytic performance. DFT calculations and experimental data confirm that the synergistic interaction between Ni nanoparticles and the N-doped carbon shell leads to optimized films exhibiting outstanding trifunctional catalytic activity. This includes low overpotentials of 95 mV for HER, 260 mV for OER at 10 mA cm^{-2}, and an ORR half-wave potential of 0.875 V in alkaline media [126].

Despite promising advances in graphene-TM based electrocatalysts, most studies emphasize material design over real-world performance and long-term stability in practical electrolyzer systems [127]. Moreover, the mechanistic understanding of the enhanced activity remains limited, raising concerns about operational stability. Bridging this gap requires developing next generation electrocatalysts through strategies such as constructing freestanding hierarchical architectures, elemental doping, morphological tuning, and engineering superhydrophilic/superaerophobic surfaces.

A comprehensive grasp of synthesis methods, DFT modeling, and structure–property relationships is crucial for optimizing catalysts for HER and OER. In this context, our group has published two review articles [86,127] focusing on graphene–transition metal-based electrodes for water and seawater splitting. These works emphasize how the hybrid material's architecture, electrical framework, and surface engineering influence catalytic efficiency. They also highlight the importance of in situ characterization and theoretical modeling in guiding catalyst design and performance enhancement. Few new age designed electrocatalysts for various electrochemical reactions have been mentioned below:

Hybrid materials with heterogeneous interfaces often exhibit enhanced electrocatalytic activity compared to single-component systems due to electron reconfiguration and the generation of additional defect sites [128,129]. Yan et al. developed an in situ electrocatalytic etching strategy to construct a Mo_2N–Mo_2C/holey reduced graphene (HGr) heterostructure [130]. The process began with the immobilization of $H_3PMo_{12}O_{40}$ (PMo_{12}) clusters on graphite oxide, followed by calcination in air and NH_3. PMo_{12} not only acted as the Mo source but also catalyzed the formation of HGr during GO reduction. Concurrently, released CO and NH_3 reacted with Mo species to form the Mo_2N–Mo_2C heterojunction on HGr (**Figure 1.21a**). The resulting hybrid showed excellent HER performance, with low onset potentials of 11 mV in 0.5 M H_2SO_4 and 18 mV in 1 M KOH, along with outstanding stability. Hybrid materials featuring distinct heterogeneous structures show a synergistic increase in activity when compared to their single-component counterparts. This is due to the formation of an electron reconfiguration structure and the establishment of additional defect sites at the interfaces [128,129]. At high current densities(>88 mA cm^{-2}), the Mo_2N–Mo_2C/HGr catalyst outperforms Pt/C in alkaline media. Its enhanced activity stems from the synergistic Mo_2N–Mo_2C heterojunction, efficient charge/mass transport of holey graphene (HGr), and compact morphology, as supported by experimental and theoretical studies. Stability tests via 2000 cyclic voltammetry cycles in both H_2SO_4 and 1 M KOH at 100 mV s^{-1} showed negligible changes in polarization curves, confirming excellent durability (**Figure 1.21b, c**).

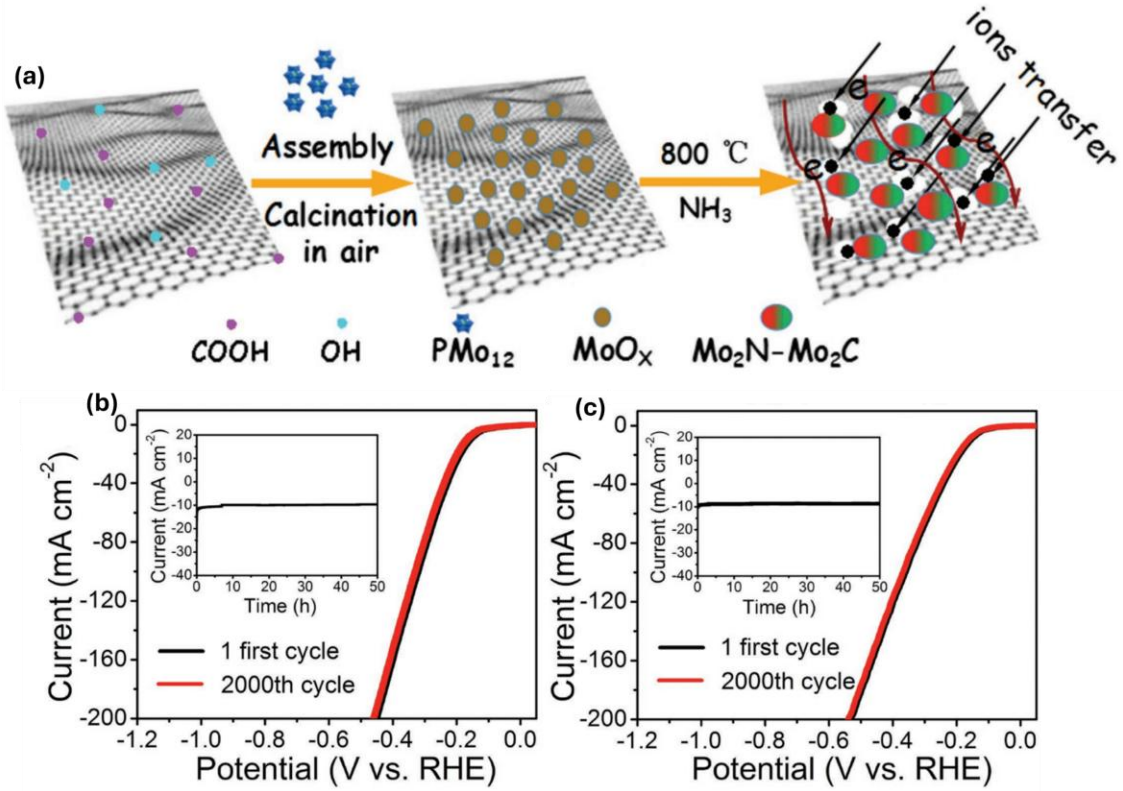

Figure 1.21 (a) Schematic illustration for the preparation of the Mo_2N–Mo_2C/HGr hybrid through three steps including assembly and calcination in air and an NH_3 atmosphere; Polarization curves for Mo_2N–Mo_2C/HGr-3 in (b) 0.5 M H_2SO_4 and (c) 1 M KOH with a scan rate of 5 mV s^{-1} before and after 2000 cycles at a scan rate of 100 mV s^{-1}, Inset: current–time (I–t) curves of Mo_2N–Mo_2C/HGr-3 under the temporal evolution of the potential required to maintain 10 mA cm^{-2} for 50 h. [Reproduced with permission from ref. 130, Copyright 2018 WILEY-VCH]

To date, Heteroatom doping is a widely adopted strategy to tailor the electronic structure of metal compounds and graphene, offering substantial potential for enhancing electrocatalytic performance [131]. Recent studies reveal that co-doping graphene with nitrogen and sulfur increases electron density in the lattice, favoring H^+ and H_2O adsorption by optimizing Gibbs free energy [132]. These defect-rich N/S co-doped graphene structures serve as efficient catalytic sites for both HER and OER.

In this context, Lai et al. synthesized a sulfur-modulated Ni_3FeN catalyst supported on N/S co-doped graphene (S-Ni_3FeN/NSG) by controlling the nitriding of NiFe disulfides. The

process involved hydrothermal synthesis of NiFe-LDH on N-doped graphene, conversion to NiFeS using thioacetamide, and subsequent nitridation under NH_3/Ar to yield Ni_3FeN while simultaneously doping N and S into the graphene framework (**Figure 1.22a**). The resulting S-Ni_3FeN/NSG-700 exhibited excellent OER performance, with a low overpotential of 260 mV at 10 mA cm^{-2} in 1 M KOH. This enhanced activity is attributed to residual sulfur in the Ni_3FeN nanoparticles and the conductive doped carbon support, which together facilitate efficient charge transfer and active site exposure. DFT calculations further confirmed that sulfur decoration in S-Ni_3FeN/NSG-700 promotes the formation of OOH* intermediates and significantly lowers the Gibbs free energy barriers for the four key OER steps (**Figure 1.22b**), validating its superior catalytic efficiency for OER [133].

The nanoscale morphological modulation has been shown to be quite advantageous at improving the effectiveness of catalysts. Several 1D (nanorods, nanowires, nanoribbons, nanochains, nanotubes, etc.) and 2D (nanosheets, nanoplates, nanorings, nanodisks, etc.) structures have been developed in this regard [134]. Three-dimensional (3D) nano-porous materials are emerging as next-generation electrocatalysts for efficient water splitting. Liu et al. reported a straightforward synthesis strategy for dual-atom transition metal (Fe, Co) co-doped graphene-like catalysts using $CaCl_2$ and $ZnCl_2$ as dual templates, sodium lignosulfonate as the carbon/sulfur source, and low-polymerized urea-formaldehyde resin as the nitrogen source (**Figure 1.23a**). $CaCl_2$ assisted in precursor formation, while $ZnCl_2$ promoted carbon etching at high temperatures, yielding a 3D multilevel porous structure. The resulting FeCo-N, S-G catalyst, rich in Fe-N_x and Co-N_x active sites, showed excellent electrocatalytic performance.

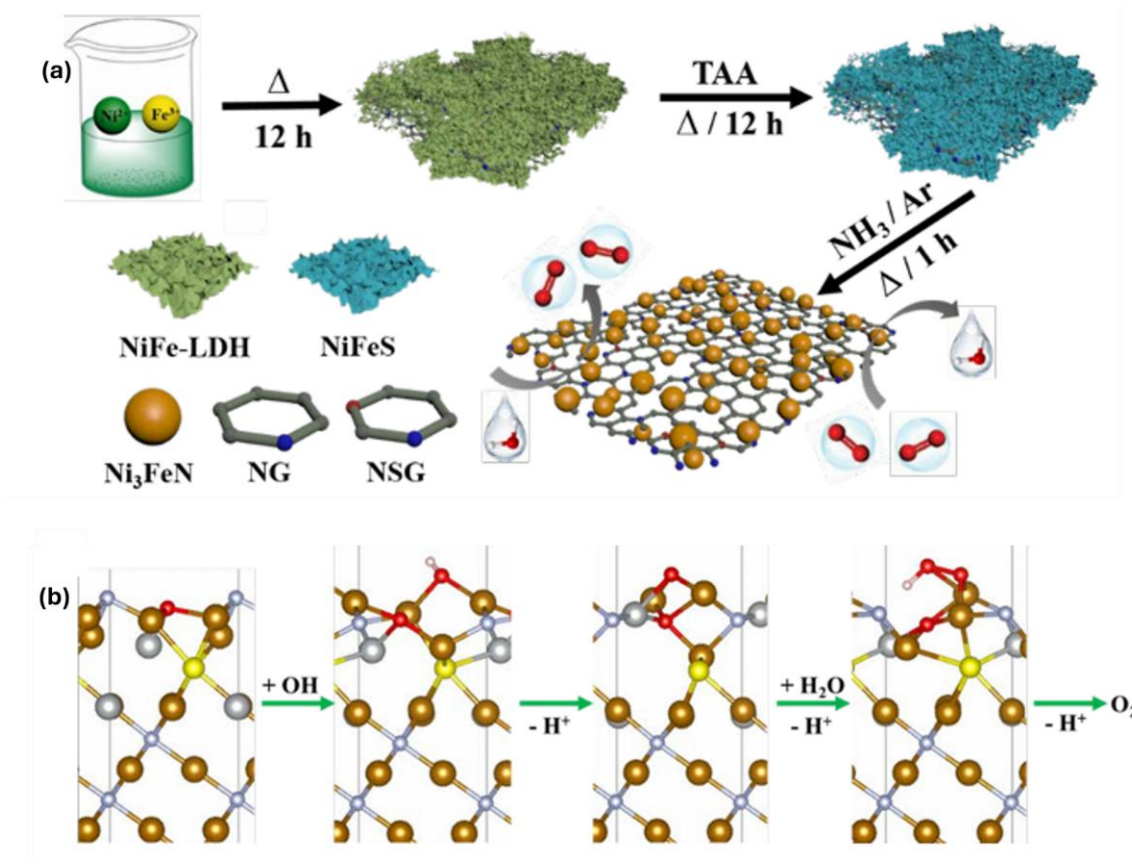

Figure 1.22 (a) Schematic illustration for the synthesis of S-Ni₃FeN/NSG-700 as bifunctional oxygen electrocatalyst (b) The four primitive steps of OER on the surface of S-Ni₃FeN/NSG-700. [Reproduced with permission from ref. 133, Copyright 2020 Elsevier]

BET analysis (**Figure 1.23b**) reveals that the dual-template strategy significantly enhances the microporosity and specific surface area of the FeCo-N, S-G catalyst, thereby facilitating the formation of a well-developed porous structure and improving mass transport. The S 2p XPS spectra (**Figure 1.23c**) showed peaks for C-S-C, C=S, and S_x species, indicating successful sulfur doping. The weaker C–S bonds, which are more reactive than C-C bonds, contribute significantly to catalytic activity. The incorporation of quaternary nitrogen further boosted OER performance [135]. Our group developed a self-assembled 3D hybrid of tungsten trioxide and reduced graphene oxide (SA-GWO) and proved that two distinct morphologies of WO_3 are separately accountable for the HER and the OER in acidic

electrolysis [136]. A voltage of 1.9 V is necessary to simultaneously carry out the electrode processes of HER and OER at a current density of 10 $mAcm^{-2}$ under standard conditions (1 M H_2SO_4, 50ºC).

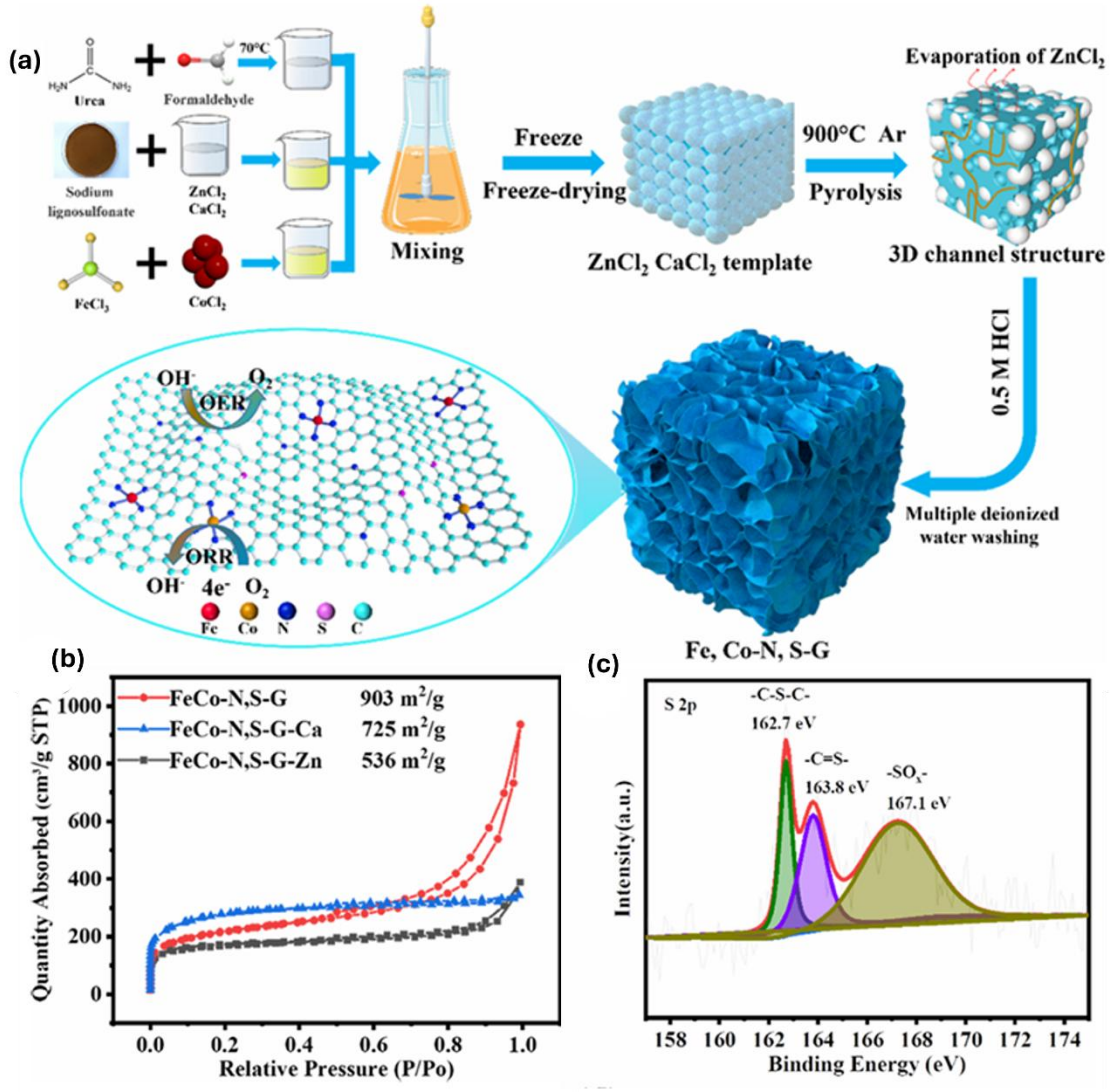

Figure 1.23 (a) Preparation scheme of Fe, Co-N, S-G. (b) N_2 Article adsorption-desorption information, XPS survey spectra (c) S 2p spectra of FeCo-N, S-G. [Reproduced with permission from ref. 135, Copyright 2023 American Chemical Society]

The development of various polymorphs is strongly influenced by the potential. The 2D W-O framework, which consists of empty hexagonal and original nanochannels (referred

to as 2D NS WO_3), plays a key role in the HER electrode process. On the other hand, the oxygen deficient vacancy found inside the matrix of 3D monoclinic WO_3 is responsible for the OER, as shown in **Figure 1.24**.

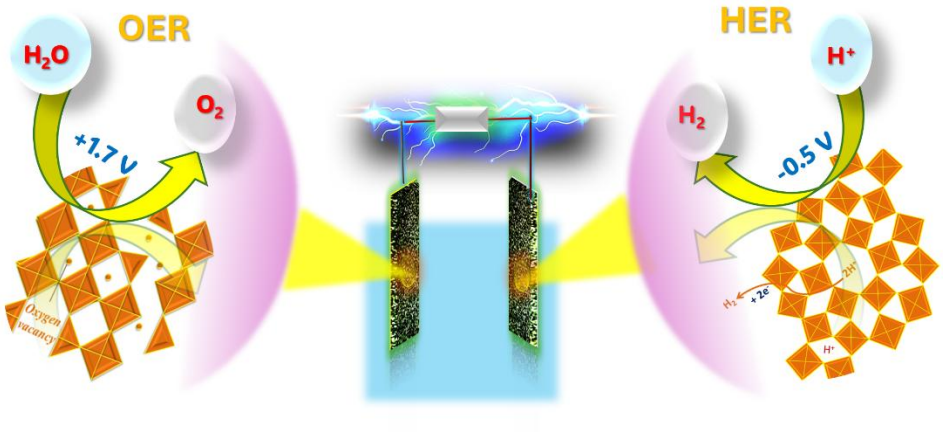

Figure 1.24 Distinct morphologies of WO_3 responsible separately for HER and OER.

Typically, electrocatalysts require a polymeric binder to adhere to the working electrode; however, the binder's limited cohesive strength often results in catalyst detachment, thereby undermining long-term stability. In contrast, graphene provided a robust platform for fabricating binder-free 3D SA-GWO electrodes via a simple self-assembly method, enhancing durability, reducing cost, and ensuring mechanical integrity under harsh conditions.

So far, Various TM based compounds such as transition metal oxides, hydroxides, phosphides, and nitrides have been explored as OER electrocatalysts for seawater electrolysis, where OER is challenged by competing CER. Qi et al. developed NiFe phosphide arrays on P-doped reduced graphene oxide supported on nickel foam (NiFeP/P-rGO/NF) [137]. The hydrophobic P-rGO layer formed a tight interface with the substrate, improving corrosion resistance and electrical conductivity. This, along with the ultrathin

NiFeP arrays and rGO network, delivered excellent performance with overpotentials of 290 and 340 mV at 100 and 400 mA cm^{-2} in seawater. Jadhav et al. reported a catalyst comprising FeOOH-coated Ni-Co hydroxide with a graphene oxide (GO) protective shell [138]. Gas chromatography confirmed exclusive O_2 evolution, while o-tolidine tests detected no Cl-based oxidants, highlighting the role of GO's oxygen groups in enhancing corrosion resistance and stability. Jia et al. synthesized a heterostructured V-doped Co_2P catalyst anchored on N,P-doped covalently cross-linked 3D graphene (V-Co_2P@NPPC/3DG) using V-doped ZIF-67 and a controlled phosphidation process [139]. The optimized V-Co_2P@NPPC/3DG-1:5 showed low overpotentials of 98.3 mV in alkaline water and 88.3 mV in artificial seawater at 10 mA cm^{-2}, with Tafel slopes of 56.4 and 51.0 mV dec^{-1}, respectively. In a flow-type electrolyzer using artificial seawater, the catalyst paired with RuO_2 achieved a cell voltage of 1.54 V at 10 mA cm^{-2} comparable to Pt/C||RuO_2 (1.52 V). At higher current densities (>58 mA cm^{-2}), it even outperformed Pt/C in terms of voltage and stability. V doping improved the intrinsic activity of Co_2P, while the NPPC/3DG support facilitated full active site exposure and enhanced charge transfer during HER.

Recently, transition metal cores encapsulated by protective layers have shown promise for enhancing catalyst durability in harsh environments. Zhang et al. developed a cobalt–nickel nanoalloy encapsulated in nitrogen-doped graphene (CoNi@NGs) for anodic sulfide oxidation in alkaline media [51]. Nanoparticles of size 4-6 nm were wrapped in a ~3.4 Å graphene shell, delivering a stable current density of 30 mA cm^{-2} over 500 h and maintaining performance during a 1200 h test at 20 mA cm^{-2}. The catalyst exhibited a low onset potential of 0.25 V vs. RHE in 1 M Na_2S and 1 M NaOH ,1.24 V lower than typical

OER onset potential hence, demonstrating its efficiency for H_2S splitting. In oxygen electrocatalysis, to prevent nanoparticle dissolution or agglomeration during the ORR, graphene supports are widely used [140]. Wang et al. synthesized a $Co_{1-x}S$/rGO catalyst via a two-step method, which showed a strong four-electron ORR pathway based on RDE/RRDE analysis [141]. Liu et al. prepared $NiCo_2S_4$ nanoparticles on graphene via solvothermal synthesis, achieving bifunctional ORR/OER activity in 0.1 M KOH. This catalyst had a half-wave potential just 47 mV below that of Pt/C, outperforming Co_3S_4-based systems and highlighting Ni's beneficial role. Although transition metal chalcogenides still lag behind Pt-based catalysts, doping and graphene support can significantly narrow the gap.

Moghaddam et al. synthesized molybdenum disulfide/reduced graphene oxide (MoS_2/rGO) nanosheets via a hydrothermal method, followed by the uniform deposition of iron-nickel (FeNi) bimetallic nanoparticles using a simple ethylene glycol reduction process (**Figure 1.25a**). The resulting FeNi-MoS_2/rGO nanocomposite exhibited excellent ORR activity in alkaline media (**Figure 1.25b**), attributed to the synergistic interaction between the FeNi alloy and the MoS_2/rGO substrate. The catalyst delivered a high current density of 6.10 mA cm^{-2}, a half-wave potential of 0.895 V, and an onset potential of 0.988 V vs. RHE [143].TEM analysis displays the uniformity and distribution of FeNi nanoparticles onto the surface of catalyst's support, respectively (**Figure 1.25c**).In the CV cycle and LSV polarization curve,the cathodic reduction peak potential of FeNi-MoS_2/rGO moved to a positive potential than that of MoS_2/rGO and even Pt/C which indicates a quick reduction of FeNi-O and better ORR activity (**Figure 1.25d,e**).The synergetic effects of the excellent conductivity and high aspect ratio of rGO, as well as

high catalytic activity and role of susbtrate-like such as MoS_2, along with the use of the FeNi transition bimetallic hybrid, resulted in the FeNi-MoS_2/rGO electrode to become a suitable candidate for high performance electrocatalytic applications.

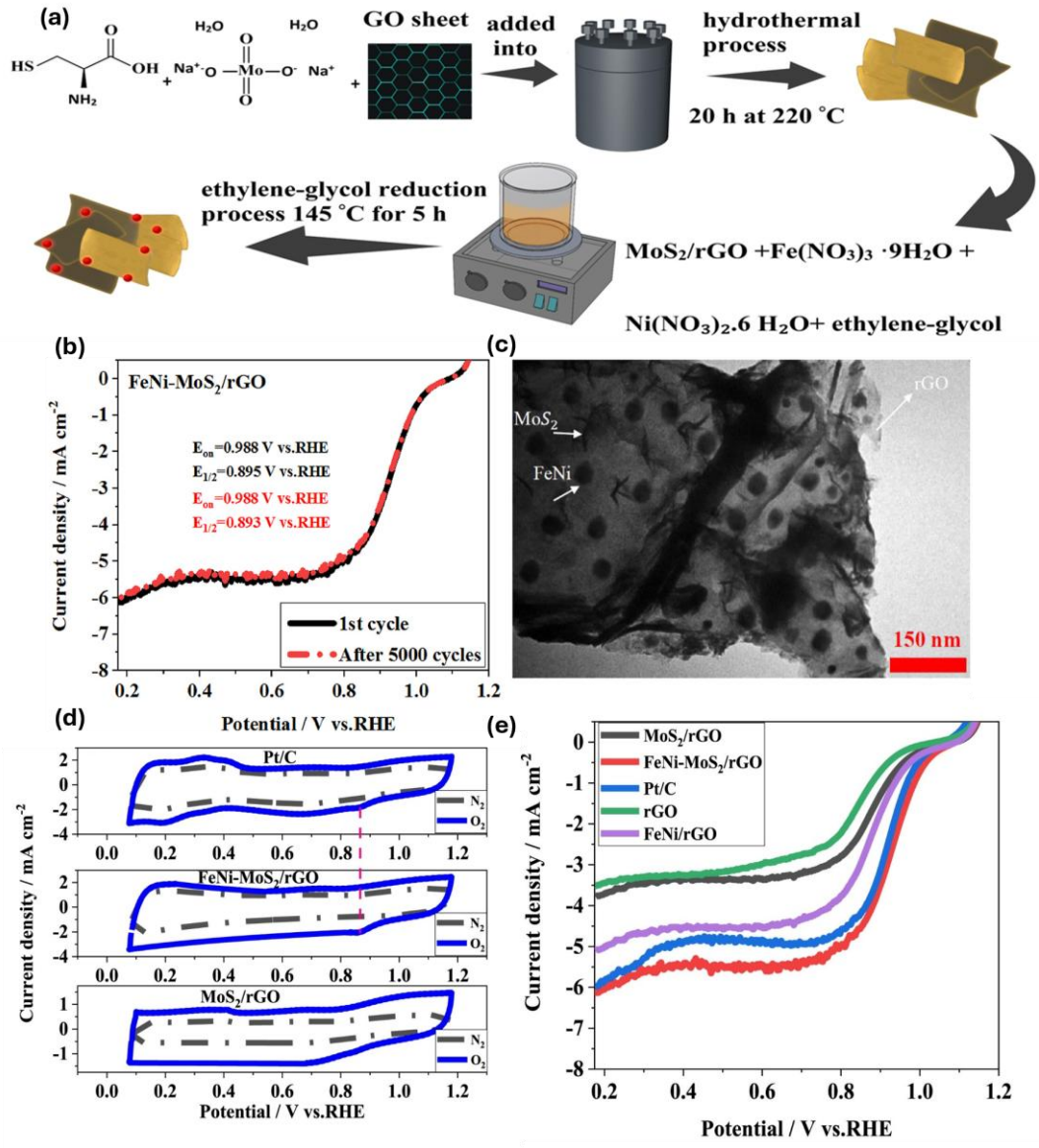

Figure 1.25 (a) Schematic of the developing procedure of the FeNi-MoS_2/rGO nanocomposite (b) CV stability of the FeNi-MoS_2/rGO nanocomposite for 5000 cycles in O_2-purged 0.1 M KOHF(c) TEM image of FeNi-MoS_2/rGO nanocomposit (d) CV curves of the MoS_2/rGO, FeNi-MoS_2/rGO nanocomposite, and Pt/C in N_2 and O_2-saturated 0.1 M KOH solution at a scan rate of 50 mV/s (e) O_2 reduction polarization curves of different materials at 1600 rpm [Reprinted with permission from ref. 143, Copyright 2023 Elsevier].

1.10 Research Hypothesis and Objectives

Catalysts for electrocatalytic reactions, including hydrogen evolution reaction (HER), oxygen evolution reaction (OER), oxygen reduction reactions (ORR), hydrogen peroxide oxidation reaction (H_2O_2OR), Sulphur oxidation reaction (SOR), hydrazine reduction reaction (HzRR), hydrogen peroxide reduction reaction (H_2O_2RR) play a significant role in the advanced electrochemical technologies, such as water splitting devices, fuel cells, rechargeable metal-air batteries, and sensing. Transition metal compounds (TMCs) are potentially fruitful substitutes for noble metals for various electrochemical reactions due to their intrinsic electrocatalytic activity, modifiable morphology, tunable electronic structure and their earth-abundance. The combination of TMCs with graphene improves the dispersion of loaded catalysts, providing more catalytic active sites, enhancing the conductivity of hybrids, affording accelerated charge-transfer kinetics, and minimizing catalyst bleaching, aggregation, and sintering under harsh reaction conditions (**Figure 1.26**). Additionally, graphene incorporation into TMCs modulates the electronic structure of active centers because of the synergistic interaction between them, thereby improving their catalytic performance. Although there have been many studies on the high current density capabilities of graphene-TMC electrocatalysts for various HER/OER or ORR reactions, most of these studies have mainly focused on the material's design rather than its actual performance and stability in practical electrolyzer or Fuel cell systems. Furthermore, there is a lack of thorough understanding of the underlying mechanism which raises concerns about the stability of the process during electro-chemical reactions. In general, there is still a significant gap between the progress made in developing materials and their actual implementation as electrocatalysts for water splitting.

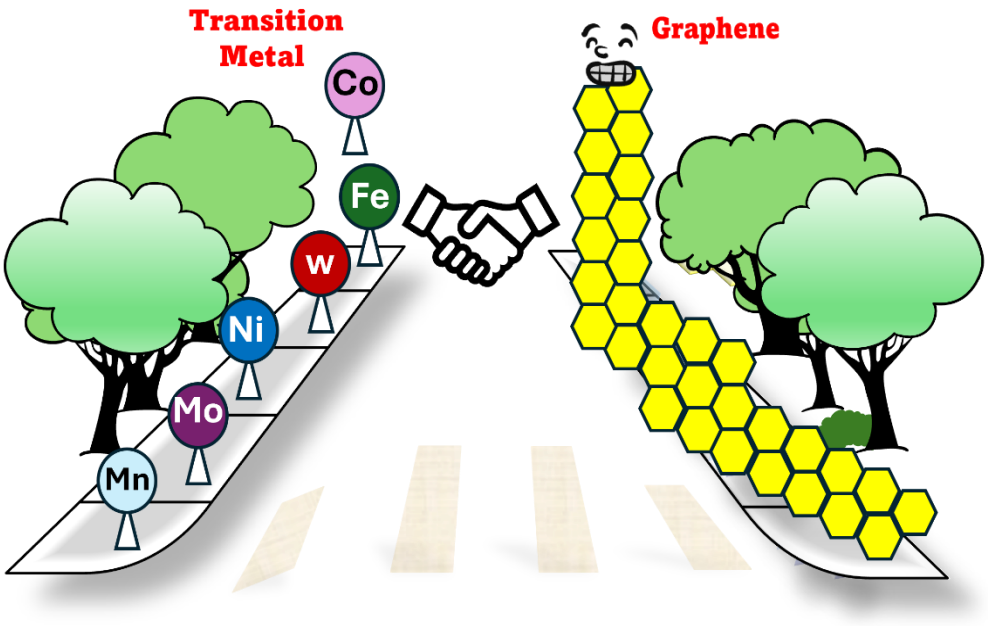

Figure 1.26 Graphene-Transition metal integration for a better electrocatalysis future.

So, there is a need to design new age electrocatalysts based on advanced strategies like building free standing hierarchical assemblies, elemental doping, morphological tuning, and incorporating superhydrophilic/superaerophobic properties. Additionally, a thorough understanding of the catalysis mechanisms via Density Functional Theory (DFT) and in situ characterization techniques is essential for the development of the most effective electrocatalyst and their implementation in energy conversion and storage systems. Based on the literature analysis, following objectives are proposed:

a) **Development of multifunctional low-cost, graphene–transition metal-based multifunctional electrocatalysts** with high tolerance to harsh reaction environments having exceptional electrocatalytic activity and long-term stability across a wide pH range.

b) These catalysts would go beyond traditional materials (e.g., bulk platinum or nickel) and incorporate **innovative nanostructuring, compositional tuning, or hybrid architectures** to achieve superior performance in applications like water splitting, fuel cells, metal–air batteries, and electrochemical sensors.

c) **To understand the reaction mechanisms and active sites** using theoretical calculations (e.g., Density Functional Theory, DFT) and correlate these findings with experimental observations.

d) **To assess the scalability and practical feasibility** by addressing key challenges, including large-scale material synthesis, long-term operational stability, and seamless integration into functional devices. Moving beyond laboratory-scale catalyst powders, it is crucial to design and fabricate scalable, durable structures that can operate efficiently under industrial conditions and in real-world electrochemical systems.

Chapter 2: Design and assessment of a Freestanding rGO–WO_3 electrode for bifunctional water electrolysis under acidic conditions

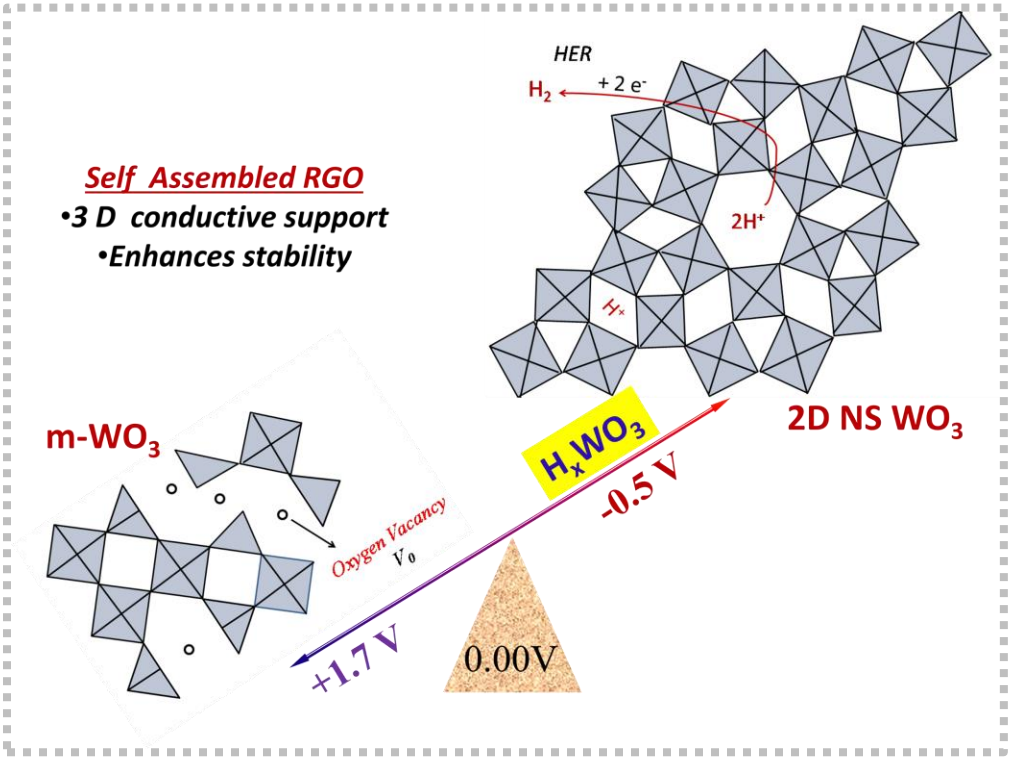

Water splitting in acidic media remains a significant challenge due to electrode instability and sluggish kinetics. Here, we present a highly efficient, self-architectured SA-GWO electrode that overcomes these limitations, enabling stable and bifunctional hydrogen and oxygen evolution in acidic media.

(Adapted from International Journal of Hydrogen Energy, 47, 86, 2022, 36381 – 36396)

2.1 Abstract

Efficient and sustained hydrogen production via acidic water splitting is critically important for advancing electrolyzer technologies. In this study, we have designed and synthesized a self-assembled, freestanding, three-dimensional (3D) reduced graphene–tungsten oxide hybrid electrode (SA-GWO) that demonstrates exceptional overall performance in acidic electrolysis. The electrode exhibits bifunctional catalytic activity for both the HER and OER, operating at a combined cell voltage of 1.9 V to achieve the benchmark current density of 10 mA cm^{-2} in 1 M H_2SO_4 at 28 °C. Notably, the SA-GWO electrode shows significant OER activity in acidic media which is a challenging and relatively rare feature. For HER, a Tafel slope of 117 mV dec^{-1} and an exchange current density of 1.73 × 10^{-3} mA cm^{-2} were observed at 28 °C, indicating favorable kinetics. Hydrogen production rates increase with temperature, and mechanistic analysis suggests that HER proceeds predominantly via the Volmer step. Gas chromatography (GC) confirms the evolved gases and validates the faradaic efficiencies of 73% for HER and 52% for OER. SEM analysis after HER operation (-0.5 V vs RHE in 1 M H_2SO_4) reveals structural transformation, including the disintegration of 3D monoclinic WO_3 into 2D nanochannel-like features. This morphological evolution correlates with enhanced catalytic performance. Importantly, the specific WO_3 polymorph responsible for the distinct HER and OER mechanisms in acidic media has been clearly identified. The SA-GWO electrode also demonstrates excellent durability and long-term stability for HER under acidic conditions, highlighting its potential for practical water electrolyzer applications.

2.2 Introduction

With the rapid depletion of fossil fuels, renewable energy sources such as solar, hydropower, wind, and tidal energy have emerged as promising alternatives. Although technologies like photovoltaics, batteries, and wind turbines are advancing, their cost, intermittency, and seasonal dependence limit widespread adoption. To address these limitations, researchers are turning to electrolyzer technologies for green hydrogen production [39], as hydrogen offers high energy density, environmental compatibility, and the ability to balance daily and seasonal energy fluctuations. Hydrogen produced via electrocatalytic water splitting is especially attractive due to its sustainability, recyclability, and zero carbon emissions [144,145]. However, practical application is hindered by the high overpotential of the hydrogen evolution reaction (HER) and low production rates, leading to energy losses and elevated costs. While platinum remains the benchmark catalyst for hydrogen and oxygen evolution [146,147], its high cost and scarcity restrict large-scale use. Consequently, there is an urgent need for cost-effective, non-noble metal alternatives. In this regard, a range of transition metal-based electrocatalysts such as oxides [148], selenides [149], sulfides [150], phosphides [151], and single-atom catalysts [152] have been explored to enhance water-splitting efficiency.

Recently, tungsten oxide (WO_3)-based materials have attracted growing attention as promising electrocatalysts for the HER and OER, owing to their natural abundance, low cost, favorable reaction kinetics, and good chemical stability [153,154]. A key advantage lies in their ability to form hydrogen tungsten bronzes (H_xWO_3), which accelerate various electrocatalytic processes [155]. As a result, WO_3-based systems are being increasingly explored for electrocatalytic applications.

Despite this interest, pristine WO_3 nanostructures often suffer from poor kinetics, limited active surface area, and inadequate electronic conductivity, which hinder their catalytic efficiency. To address these limitations, strategies such as incorporating transition metals, metal oxides [156,157], or conductive carbon-based materials including graphene, carbon nanotubes, reduced graphene oxide, and carbon quantum dots, have been employed to enhance their performance [158-160]. The choice of support material plays a crucial role, as it directly affects charge and proton transfer, particle dispersion, and the overall conductivity of the composite, thereby significantly boosting HER activity [161]. However, most reported WO_3-based electrocatalysts (**Table A1**, **Appendix information**) involve complex and expensive synthesis methods requiring high temperatures, costly precursors, or sacrificial templates [162-172]. Additionally, the common use of polymer binders like Nafion to immobilize electrocatalysts on electrodes can reduce catalytic efficiency by blocking active sites and limiting gas permeability [173]. Moreover, the HER performance of current WO_3-based catalysts remains substantially inferior to that of Pt-based benchmarks, with poor long-term durability and a noticeable drop-in activity after prolonged cycling. Therefore, there is an urgent need to develop economically viable and scalable methods for synthesizing WO_3 nanomaterials with enhanced catalytic activity and durability.

To reduce costs and enhance performance, the development of advanced, freestanding, low-cost electrode materials is essential. Graphene, a renowned two-dimensional carbon allotrope, holds immense promise across a wide range of applications, including solar cells, light-emitting diodes (LEDs), touch panels, smartphones, transistors, photovoltaics, sensors, and electroactive electrodes [174-179]. In this context, the emergence of next-

generation three-dimensional (3D) self-assembled graphene-based electrodes offers significant potential and will be explored in this article.

Self-assembly is the process by which reactive components spontaneously organize into ordered structures due to specific physical interactions and has proven effective in constructing such materials [181,182]. Various techniques have been developed for assembling 2D graphene building blocks into well-defined architectures, including layer-by-layer assembly, flow-directed assembly, evaporation-induced methods, interface-induced techniques, and template- or space-confined strategies. These methods yield diverse morphologies ranging from 1D fibers and 2D films to 3D porous networks, characterized by high surface area, high aspect ratio, and tunable microstructure and surface chemistry [174-179].

Furthermore, these architectures offer broad opportunities for hybridization with both inorganic and organic components, expanding their applicability [180,181]. The properties of reduced graphene oxide such as high surface area, prevention of agglomeration, and rich surface functionality make it particularly suitable for developing multifunctional materials. These materials have significant potential in fields like energy storage and conversion, catalysis, electronics, optoelectronics, and water treatment.

In this study, we report a low-cost, freestanding 3D electrode fabricated through a simple self-assembly approach using only graphene oxide (GO) and tungstic acid as precursors. During the process, oxygen-deficient tungsten oxide (WO_{3-x}) uniformly integrates with GO sheets, resulting in the formation of a stable, gel-like composite that solidifies into a robust electrode architecture. These self-assembled graphene-WO_3 (SA-GWO) electrodes serve as efficient bifunctional electrocatalysts, enabling both the hydrogen evolution reaction

(HER) and oxygen evolution reaction (OER) in acidic media. Remarkably, the electrodes exhibit full water splitting at a cell voltage of 1.90 V at 10 mA cm^{-2} in 1 M H_2SO_4.The ability to catalyze both HER and OER under acidic conditions is especially significant, as most bifunctional catalysts in such media rely heavily on noble metals and remain scarce [182]. The HER mechanism follows the Volmer pathway, while the OER is characterized by a steep Tafel slope, indicating sluggish kinetics. Interestingly, under cathodic HER conditions (-0.5 V vs. RHE), a clear structural transformation from 3D monoclinic WO_3 to 2D nanostructures is observed, suggesting dynamic morphological adaptability. Most notably, two distinct WO_3 morphologies appear to be selectively active toward HER and OER, respectively, highlighting a unique structure-function relationship within the SA-GWO catalyst that enables its bifunctional performance.

2.3 Experimental Section

2.3.1 Materials

Graphite powder (Qualikems fine chem Pvt. Ltd), Sulphuric acid (H_2SO_4) [Merck life science Private Limited], Ortho-phosphoric acid (H_3PO_4) [Merck life science Pvt. Ltd], Potassium permanganate ($KMnO_4$) [Quicklimes fine Chem Pvt. Ltd], Hydrogen peroxide (H_2O_2) [Merck life science Private Limited], Tungstic acid (H_2WO_4) [Hi Media Lab. Pvt. Ltd], Hydrochloric acid (HCl) SDFCL [s d fine-Chem Limited], Acetone (C_3H_6O) [s d fine-Chem Limited] , Methanol (CH_3OH) SRL [Sisco Research Laboratories Pvt. Ltd], Potassium hydroxide (KOH) [s d fine-Chem Limited], Sodium sulphate (Na_2SO_4)[Sisco Research Laboratories Pvt. Ltd], araldite standard epoxy resin (Huntsman International Pvt. Ltd., India), double distilled water (DDW) prepared by redistillation of distilled water in glass distillation apparatus were used during the work.

2.3.2 Material Characterizations

The UV-Vis spectra of composites were recorded on the SHIMADZU UV-1700 Pharma spectrophotometer. Raman spectra were obtained using a Renishaw RM 1000 Raman spectrophotometer with an Argon ion (Ar^+) laser source of 514.5 nm. X-ray diffraction measurements of the samples were carried out using the Rigaku Mini Flex II. Samples were ground well before measurement and the diffractograms were recorded with 2θ ranging from 5º to 40º using CuKα radiation. Thermogravimetric analyses (TGA) were performed using a Mettler TGA thermo gravimetric analyzer in the temperature range of 40600 ºC with a heating rate of 10 ºC/min under N_2 atmosphere. Morphology studies were performed using a scanning electron microscope (SEM) (EVO 18 Research, Zeiss) along with an energy dispersive X-ray diffractogram Oxford instrument (Xact) and TEM (Technai G2 20 twin, FEI, U.S.A.). To examine the morphology using TEM, the self-assembled SA-GWO solid architecture was disintegrated into fine powder *via* sonication, then dropped on to TEM copper grids and examined under microscopes. In contrast, for SEM characterization, the electrode extracted from 3D SA-GWO was used directly for surface characterization.

2.3.3 Electrochemical measurements

Electrochemical measurements were carried out using a computer-controlled μ-Autolab III potentiostat/galvanostat in a standard three-electrode configuration (Metrohm), with a Pt disc as the counter electrode, Ag/AgCl (3 M KCl) as the reference, and SA-GWO as the working electrode. All potentials were calibrated to the reversible hydrogen electrode (RHE) using the formula:

$$E\ (\text{vs. RHE}) = E\ (\text{vs. Ag/AgCl}) + 0.210\ \text{V} + 0.059 \times \text{pH}.$$

Linear sweep voltammetry (LSV) was conducted from -0.7 to +1.5 V (vs. Ag/AgCl) at a scan rate of 1 mV s^{-1} for HER and OER studies in electrolytes of varying pH: 1 M H_2SO_4 (pH 0), 1 M Na_2SO_4 (pH 5.6), and 1 M KOH (pH 13). Chronoamperometry was performed at -0.5 V and 1.7 V (vs. RHE) for HER and OER, respectively, in 1 M H_2SO_4 (250 mL). Prior to measurements, CV/LSV scans were repeated until consistent curves were obtained. Temperature effects on HER/OER performance were also assessed in 1 M H_2SO_4. Electrochemical impedance spectroscopy (EIS) was conducted over a frequency range of 0.1 Hz to 100 kHz with a 10 mV AC perturbation at 28 ± 2 °C in 0.5 and 1 M H_2SO_4 using the same three-electrode setup. Current densities were normalized to the planar geometric area of the SA-GWO electrode.

2.3.4 Product Gas Analysis

Gas chromatography (GC) was employed to analyze the gaseous products generated at the cathodic and anodic sites of SA-GWO. Gases were collected via the water displacement method using an inverted graduated burette. GC analysis was performed using a Centurion Scientific 5800 system equipped with a 3 m stainless steel 5A molecular sieve column (60–80 mesh, 2 mm I.D.) and a thermal conductivity detector. The column was maintained at 50 °C, with Ar as the carrier gas. The instrument was pre-calibrated using standard gases (H_2, O_2, N_2), yielding retention times of 1.03 min for H_2 and 1.44 min for O_2.

2.4 Electrocatalyst synthesis

2.4.1 Fabrication of self-assembled SA-GWO electrodes

Self-assembled graphene–tungsten oxide (SA-GWO) architecture was synthesized via a hydrothermal self-assembly method using tungstic acid (H_2WO_4) and graphene oxide (GO)

[183]. Typically, 250 mg of H_2WO_4 was refluxed in methanol at 105 °C for several hours, followed by the addition of 750 mg GO suspension after cooling. The mixture was stirred for 1 h and transferred to a 100 mL Teflon-lined autoclave for hydrothermal treatment at 180 °C for 24 h. The resulting SA-GWO was washed thoroughly with water and ethanol. Control experiments with GO or H_2WO_4 alone confirmed the necessity of both components, with the optimal architecture forming at a 1:2.5 weight ratio (H_2WO_4: GO; see **Table A1, Appendix information**). The 3D SA-GWO structure was dried and cut into freestanding electrodes. A copper wire was affixed with silver paste on the back, and epoxy resin was applied to insulate all edges, ensuring electrochemical activity was confined to the catalyst surface (**Figure A1, Appendix information**).

2.5 Result and Discussions

2.5.1 Microstructural characterization of SA-GWO electrode

The XRD patterns of GO, RGO, WO_3, and SA-GWO are presented in **Figure 2.1a**. GO was synthesized via the improved Hummer's method, showing a characteristic peak at ~12.48° (2θ), indicating oxygenated groups on graphite. Upon hydrothermal treatment at 180 °C without any tungsten precursors (a blank test), GO converted to RGO, displaying a broad (002) diffraction peak at 24.56°. This step helped assess the structural changes during self-assembly. WO_3 showed distinct diffraction peaks at 2θ values of 23.12°, 23.59°, 24.38°, 26.55°, 28.87°, 33.24°, 34.22°, 41.87°, 47.24°, 49.88°, 55.90°, 61.95°, and 76.69°, corresponding to various planes of monoclinic WO_3 (JCPDS 01-072-1465). These peaks were retained in the SA-GWO sample, confirming the formation of monoclinic WO_3 (see **Table A2, Appendix information**), with major reflections at 23.12°, 23.59°, and 24.38° corresponding to the (002), (020), and (200) planes. In XRD analysis, characteristic peaks

of graphene-based materials are often masked by signals from associated nanomaterials [183,184], as observed in the SA-GWO spectrum. Despite GO being used in a higher weight ratio (2.5:1) compared to H_2WO_4, distinct graphene-related peaks were not clearly visible. This obscuration is likely due to the effective prevention of RGO sheet restacking within the 3D architecture, which weakens its diffraction signals. Nevertheless, the prominent reflections corresponding to monoclinic WO_3 confirm its dominant and uniform presence within the self-assembled SA-GWO framework.

Raman spectroscopy was employed to obtain structural insights into the SA-GWO composite, as shown in **Figure 2.1b**. Two well-defined peaks were observed in the 600–900 cm^{-1} range, corresponding to the O-W-O stretching vibrations characteristic of monoclinic WO_3 [185–188]. The primary bands of monoclinic WO_3, typically located at 716 and 806 cm^{-1}, were red-shifted to 704 and 801 cm^{-1}, respectively, indicating the presence of oxygen vacancies or a sub-stoichiometric WO_{3-x} phase within the 3D SA-GWO structure [185,188]. Additionally, the D and G bands of graphene were clearly visible at 1340 and 1585 cm^{-1}, respectively. The intensity ratio (I_D/I_G) was calculated to be 1.04, suggesting a significant degree of disorder and the presence of oxygen-containing functional groups in the graphene framework [189].

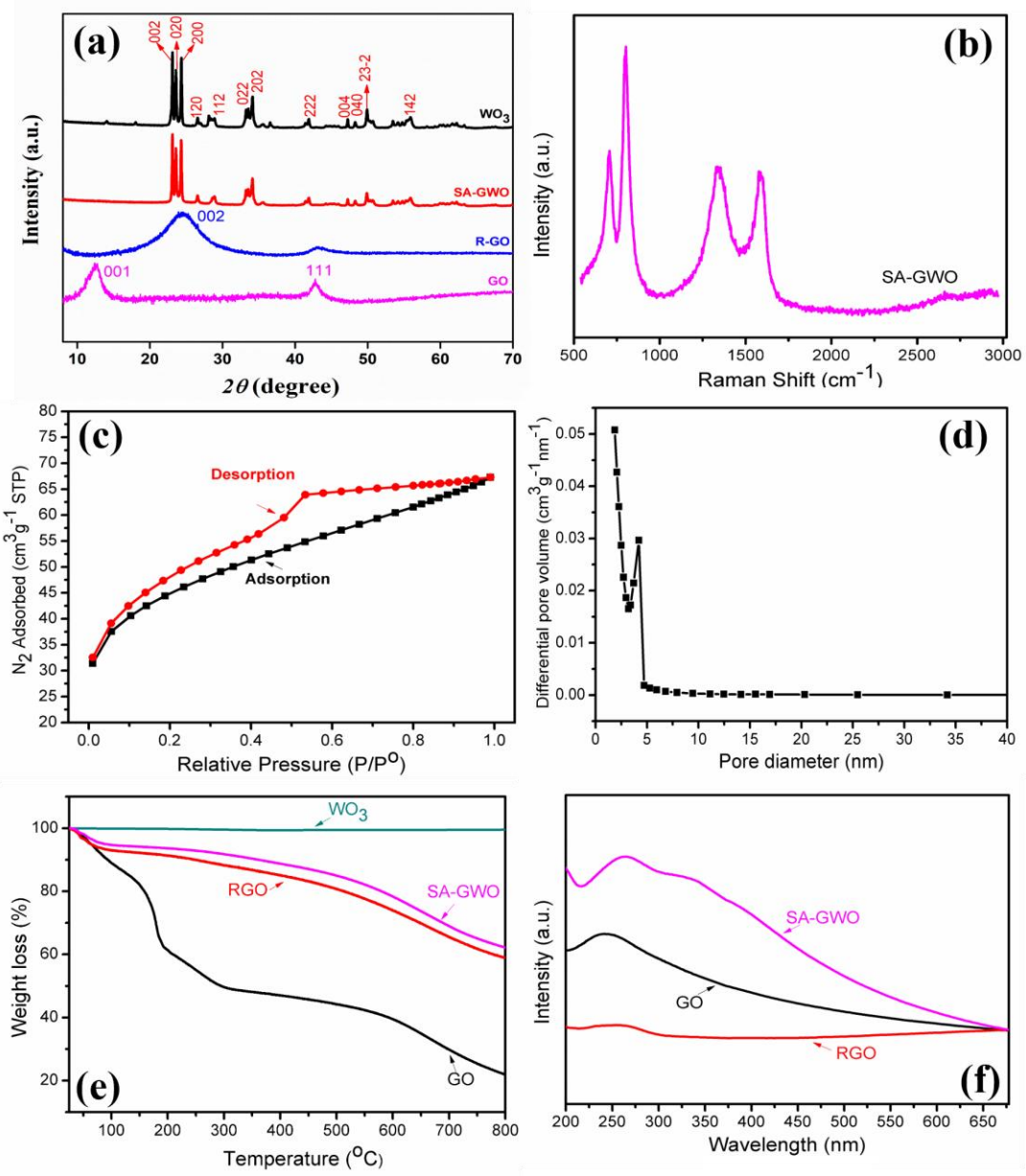

Figure 2.1 (a) XRD pattern of the samples GO, RGO, WO_3, and SA-GWO (b) Raman spectrum of SA-GWO (c) BET adsorption desorption curve (d) the corresponding pore-size distribution of SA-GWO (e) TGA spectra of samples GO, RGO, WO_3 and SA-GWO (f) UV-Visible spectra of samples GO, RGO and SA-GWO.

The porous structure of SA-GWO was characterized using nitrogen sorption analysis (**Figure 2.1c, d**). The Brunauer-Emmett-Teller (BET) surface area was found to be 152 m^2/g. The isotherm exhibited a typical type IV profile with H4-type hysteresis,

indicative of capillary condensation and consistent with mesoporous carbon materials featuring medium-sized pores (<50 nm) [190-192]. The Barrett-Joyner-Halenda (BJH) pore size distribution (**Figure 2.1d**) confirmed mesoporosity, with pore diameters ranging from 3 to 5 nm. Thermal stability was assessed via DT-TGA analysis (**Figure 2.1e**). As expected, the profile reflected the decomposition of oxygen-containing groups in RGO, accounting for a ~25% weight loss. WO_3, known for its thermal robustness [193], remained stable throughout. Electronic interactions within the 3D SA-GWO framework were examined using UV-Vis spectroscopy in the 200-700 nm range (**Figure 2.1f**). An absorption peak at 270 nm corresponds to π–π* transitions of aromatic domains, while a peak at 350 nm is attributed to electronic transitions from the oxygen 2p valence band to the tungsten 5d conduction band [194].

High-resolution transmission electron microscopy (HR-TEM) further revealed the structural features of SA-GWO (**Figure 2.2a-e**). The TEM micrographs (**Figure 2.2a,b)** displayed a nanolamellar morphology, with tungsten oxide domains predominantly located along the sheet edges (**Figure 2.2a-c**).

These findings confirm the formation of a robust 3D architecture resulting from strong interactions between WO_3 nanolamellae and the edge functionalities of RGO sheets [186]. The selected area electron diffraction (SAED) pattern of SA-GWO exhibited distinct bright spots corresponding to the crystalline monoclinic WO_3, while diffuse diffraction rings were attributed to the RGO component [195–198]. Specifically, the SAED revealed the (002) and (531) planes of WO_3 and the (002) and (100) planes of RGO (**Figure 2.2d**). The corresponding interplanar d-spacing values are listed in **Table A3** of the **Appendix information.**

These structural features are further corroborated by XRD analysis. The (002) plane observed in the XRD pattern aligns well with high-resolution TEM results, where clear lattice fringes with an interplanar spacing of 0.38 nm were resolved (**Figure 2.2c-e**), confirming the presence of well-defined monoclinic WO_3.

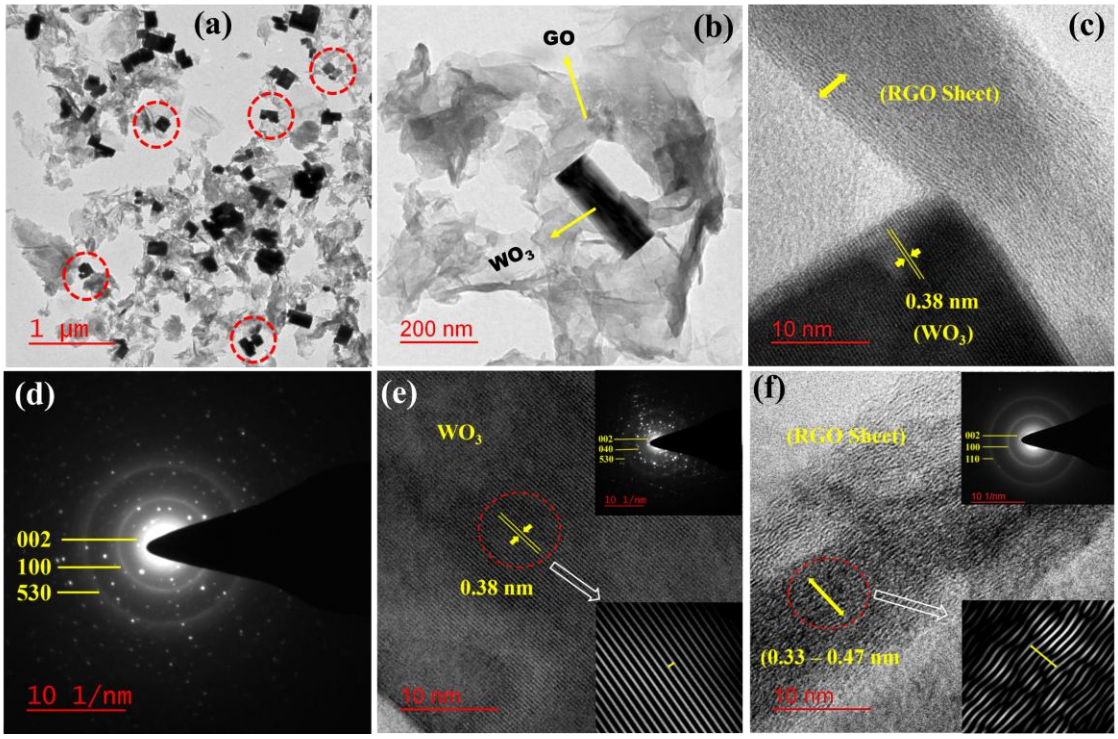

Figure 2.2 TEM images of SA-GWO at (a) 1 μm (b) 200 nm (c) 10 nm showing WO_3 dispersed on RGO (d) SAED pattern from overlapped WO_3-RGO region (e) Lattice fringes of WO_3 (f) TEM image of RGO with the corresponding SAED pattern inset.

The low-resolution TEM image of RGO (**Figure 2.2b, f**) reveals its characteristic corrugated morphology and confirms the presence of multilayer graphene. The interlayer d-spacing of RGO, measured at various points, ranges from 0.33 to 0.47 nm (**Figure A2, Appendix information**). Overall, HR-TEM analysis supports the formation of an

interconnected network within the SA-GWO architecture, consistent with the self-assembly mechanism.

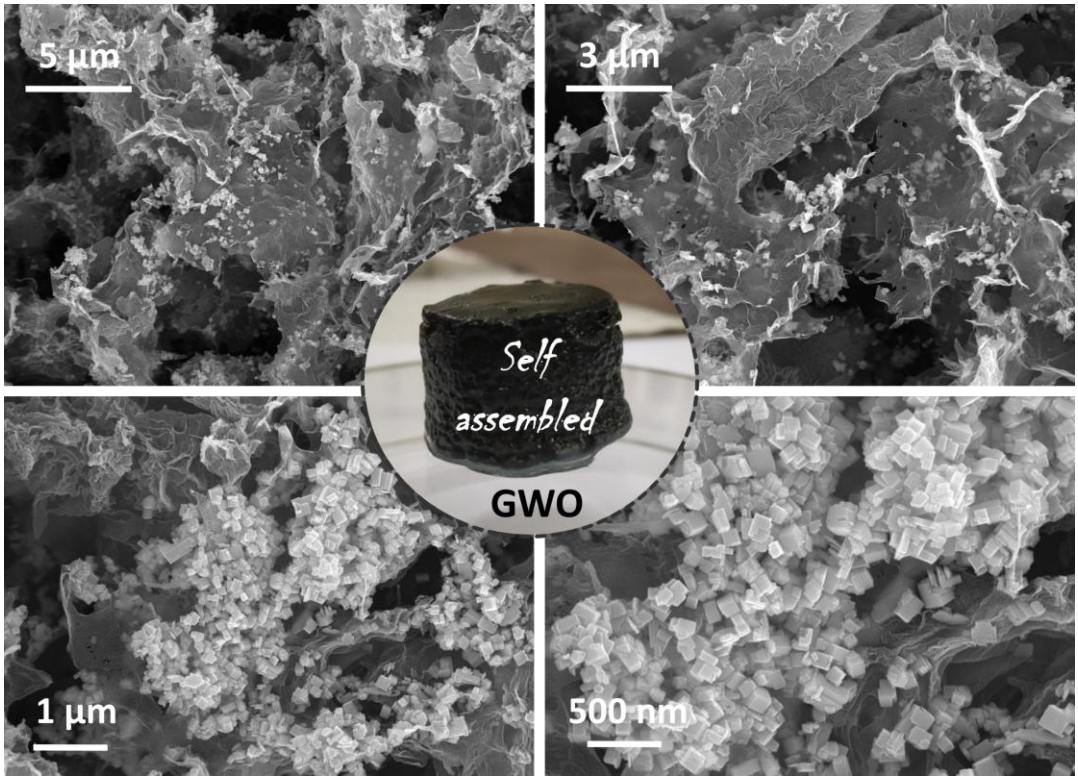

Figure 2.3 SEM images of 3D self-assembled nanostructure of SA-GWO electrode.

High-resolution scanning electron microscopy (SEM) at various magnifications (**Figure 2.3**) reveals the uniform distribution of nanoparticles throughout the 3D self-assembled SA-GWO architecture. Low-resolution SEM images (**Figure A3, Appendix information**) show square-shaped nanoplates with side lengths of 100-200 nm distributed above and beneath the structure. These images, taken from cross-sections of SA-GWO (**Figure A1, Appendix information**), highlight the hierarchical design that provides ample void spaces between WO_3 and RGO components which is an advantageous feature for enhancing electrocatalytic performance.

2.5.2 Electrochemical properties of SA-GWO electrode.

The electrochemical properties of SA-GWO electrodes were initially assessed through open circuit potential (OCP) measurements in various electrolytes. The OCP remained stable in both acidic and neutral media (**Table 2.1**), indicating good electrode stability. However, in alkaline media, SA-GWO disintegrated within 5 minutes (Table 2.1; **Figure A4, Appendix information**), likely due to the formation of soluble tungstate species (WO_4^{2-}, HWO_4^-) from the deprotonation of acidic surface sites (**Equation 2.1**) [199,200]. Additionally, SA-GWO exhibited excellent thermal stability in acidic conditions, remaining stable up to 60 °C (**Table A4, Appendix information**).

$$WO_3 + H_2O \rightarrow HWO_4^- \; or \; WO_4^- + H^+ \; or \; 2H^+ \qquad (2.1)$$

Electrochemical impedance spectroscopy (EIS) was conducted to gain further insights into the electrochemical behavior of SA-GWO in 0.5 and 1 M H_2SO_4. The impedance data were analyzed using ZSimpWin 3.1 software, and the spectra were best fitted with an equivalent circuit comprising four elements: R_1 (solution resistance), Q (constant phase element representing the double-layer behavior typical of porous electrodes) [201], R_2 (charge transfer resistance), and W (Warburg element related to ion diffusion) (**Figure 2.4a, b; Table A5 of Appendix information**).

Table 2.1 Stability of SA-GWO in different electrolyte: Measured OCP potential of SA-GWO in different electrolyte media vs. Time (*study performed @ fixed temperature of 36 °C).

Electrolyte (1 M)	@pH		Time (min)							
			0	5	15	30	60	240	1440	10080
H_2SO_4	0.00	OCP (V)*	0.47	0.47	0.47	0.47	0.47	0.47	0.47	0.47
Na_2SO_4	5.60		0.33	0.34	0.34	0.34	0.34	0.34	0.34	0.34
KOH	13.00		0.90	0.43	0.04	0.02	0.003	0.000		

A notable reduction in both solution resistance (from 18.70 to 5.31 Ω) and charge transfer resistance (from 33.20 to 25.78 Ω) were observed as the H_2SO_4 concentration increased from 0.5 M to 1 M. This decrease is likely attributed to enhanced ion mobility and a higher number of effective charge carriers at higher acid concentration. It is well established that increased electrolyte concentration significantly lowers electrode overpotentials [202,203] (**Figure A5, A6, Appendix information**).

2.5.3 Acidic electrolysis performance of SA-GWO electrode

The HER activity of the SA-GWO electrode was systematically evaluated (**Figure 2.5a-d**). Linear sweep voltammetry (LSV) was performed in the potential window of 0.3 to -0.5 V vs RHE. The HER overpotentials (η_{HER}) required to reach a current density of 10 mA cm^{-2} were 0.44 V, 0.35 V, and 0.25 V at 25, 50, and 70 °C, respectively, in 1 M H_2SO_4. The observed decrease in overpotential with increasing temperature likely reflects an increase in the exchange current density of SA-GWO (**Figure 2.5a; Table A6 of Appendix information**).

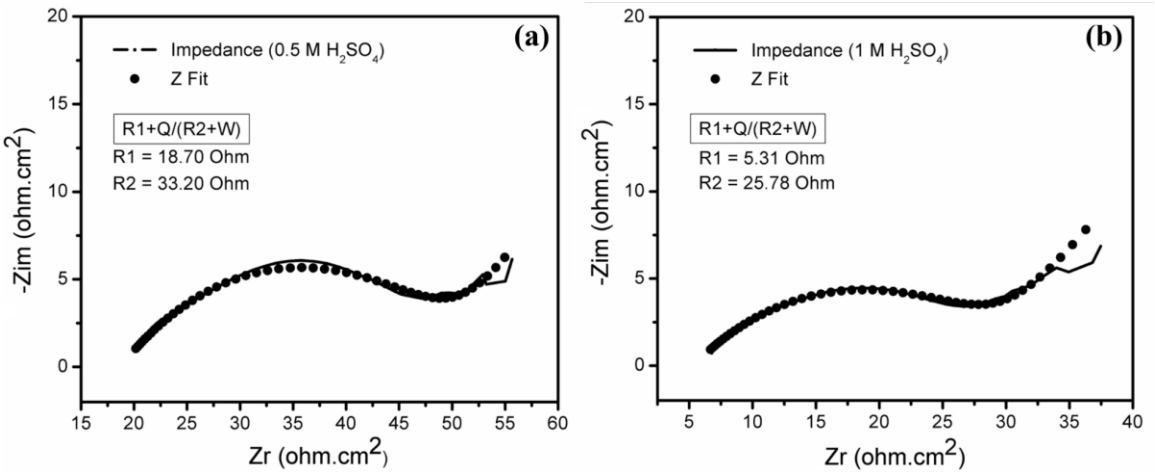

Figure 2.4 Fitted EIS spectrum (a) 0.5 H_2SO_4 (b) 1 M H_2SO_4 of SA-GWO at constant temperature of 28 ^oC (R1 is solution or ohmic resistance, Q constant phase element, R2 Charge transfer resistance and W Warburg impedance).

Tafel slopes were derived from LSV curves recorded at 28, 50, and 70 °C (Figure 2.5b) using the Tafel equation (**Equation 2.2**):

$$\eta = b \log j + a \qquad (2.2)$$

where η is the overpotential, j is the current density, and a and b represent the Tafel intercept and slope, respectively. At both 28 and 50 °C, the Tafel slope was 117 mV dec^{-1}, indicating that the Volmer step where proton adsorption is the rate-determining step in the HER process on SA-GWO [205]. This behavior may be attributed to the partial reduction and structural transformation of oxygen-deficient WO_3 into 2D nanochannel-like WO_3 nanostructures (2D NS-WO_3) [206–208].

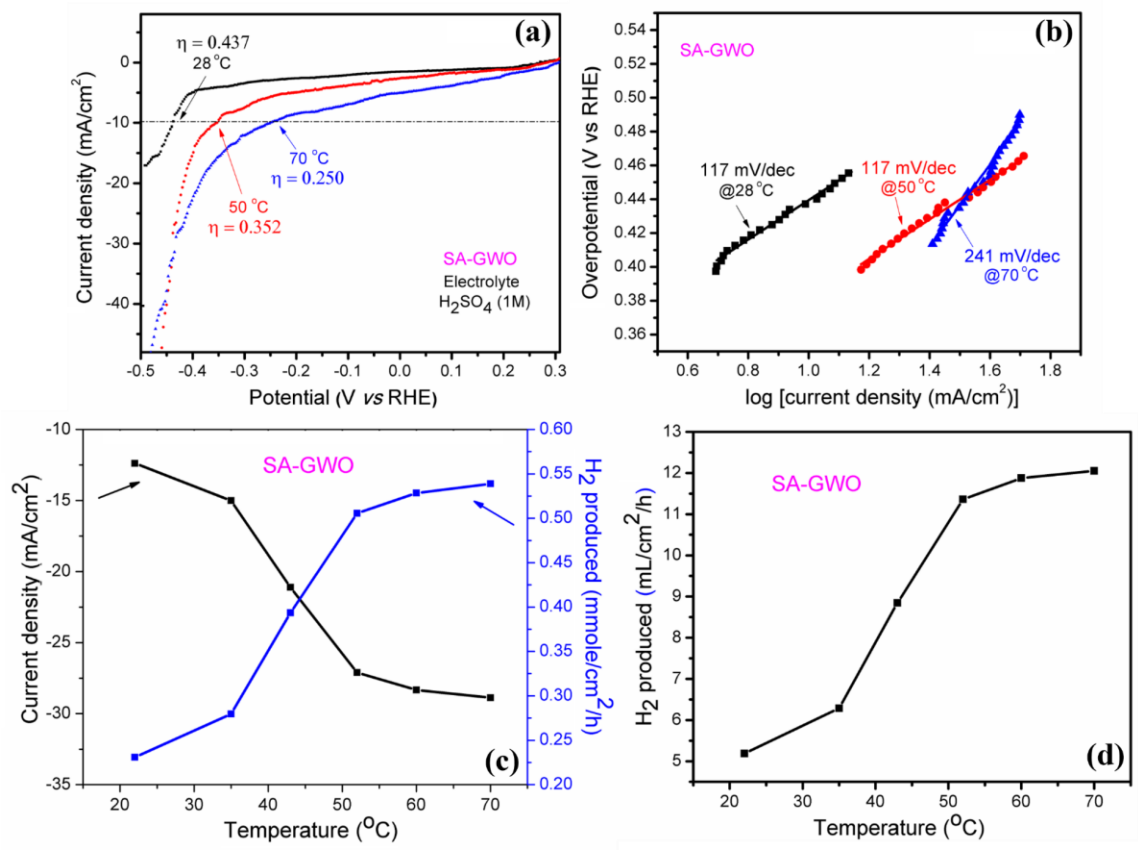

Figure 2.5 HER electrode reaction (a) LSV curves recorded at the scan rate of 5 mV/s (b) corresponding Tafel analysis (c) temperature dependent HER activity measured at fixed potential of -0.5 V in 1M H_2SO_4 (d) corresponding theoretically calculated H_2 (mL) at six different temperatures.

Detailed justification is provided in the mechanism section. The increase in Tafel slope at elevated temperatures likely arises from weakened interactions between hydrogen ions and the WO_3 component of SA-GWO [209,210]. Current density measurements at a fixed cathodic potential of -0.5 V demonstrated a notable enhancement in HER activity with increasing temperature. At 50 °C, approximately 11 mL H_2 cm^{-2} h^{-1} was theoretically generated (**Figure 2.5c, d**). The evolved gas, collected via inverted burette, was confirmed as hydrogen by GC analysis through comparison with standard H_2 retention times.

For benchmarking, bare WO_3-coated FTO electrodes (**Fabrication details in E1, Appendix information**) were tested under identical conditions. They showed inferior performance with a current density of just 2 mA cm^{-2} at -0.5 V, high overpotential, and substantial degradation after 20 cycles due to leaching from the FTO substrate (**Figure A7**, **Appendix information**). This underscores the stabilizing role of RGO in the SA-GWO composite, which greatly enhances both HER and OER performance.

SA-GWO was also evaluated for OER in the potential window up to 1.9 V vs RHE. Overpotentials (η_{OER}) of 1.58, 1.54, and 1.43 V were recorded at 28, 50, and 70 °C, respectively (**Figure 2.6a**), indicating improved kinetics at higher temperatures. The Tafel slopes (**Figure 2.6b**) remained high, consistent with the complex, multistep OER mechanism involving W(V/VI) disproportionation and terminal oxygen coupling [211,212]. A significant decrease in slope from 759 to 460 mV dec^{-1} was observed with increasing temperature, reinforcing the temperature-enhanced reaction kinetics. The full potential required to reach 10 mA cm^{-2} was 1.9 V at 50 °C (**Figure 2.6c**).

Durability and faradaic efficiency (FE) of SA-GWO were assessed by chronoamperometry at 50 °C (**Figure 2.7a, b**). Under a constant potential of -0.5 V, SA-GWO maintained a

stable HER current density of ~25 mA cm^{-2} over 25 hours, confirming its robustness and high FE in acidic media.

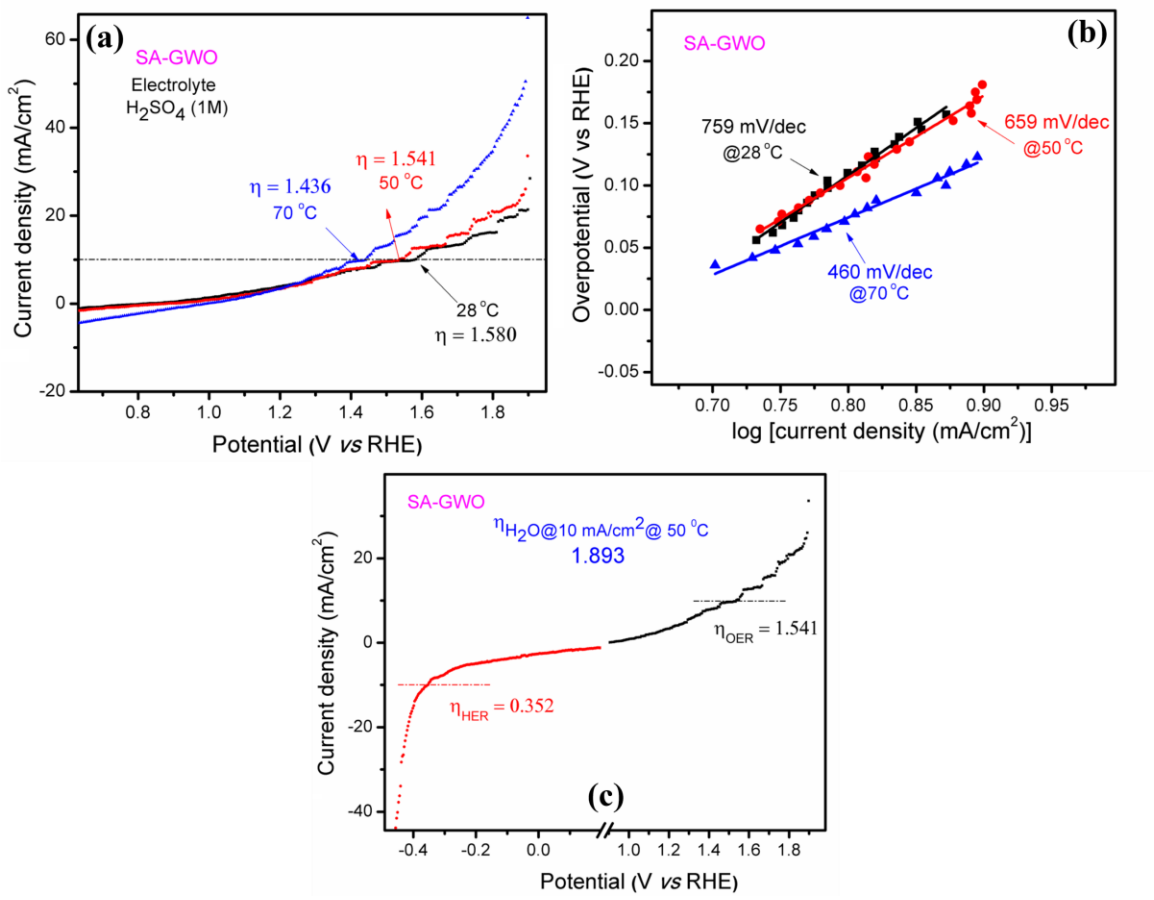

Figure 2.6 OER electrode reaction (a) LSV curves at the scan rate of 5 mV/s (b) corresponding Tafel analysis and (c) bi-functional activity marked at standard 10 mA cm^{-2} in 1M H_2SO_4 and at the temperature 50 °C.

Under HER conditions (-0.5 V, 1 M H_2SO_4, 50 °C), the experimentally collected hydrogen volume was approximately 8 mL after 1 hour, compared to the theoretically calculated value of 10.97 mL based on the current–voltage relationship (**Figure 2.5d and 2.7a**). This corresponds to a faradaic efficiency (FE) of 73%, suggesting the occurrence of side reactions alongside HER at -0.5 V. Notably, a delay of approximately 600 seconds was observed before visible gas evolution began from the SA-GWO surface and a stable current

was established. Literature reports indicate that at potentials ≤ -0.5 V, the conversion of oxygen-deficient WO_3 [W(VI/V)] to hydrogen tungsten bronze can occur [206-208], which could account for the observed side reactions and reduced FE.

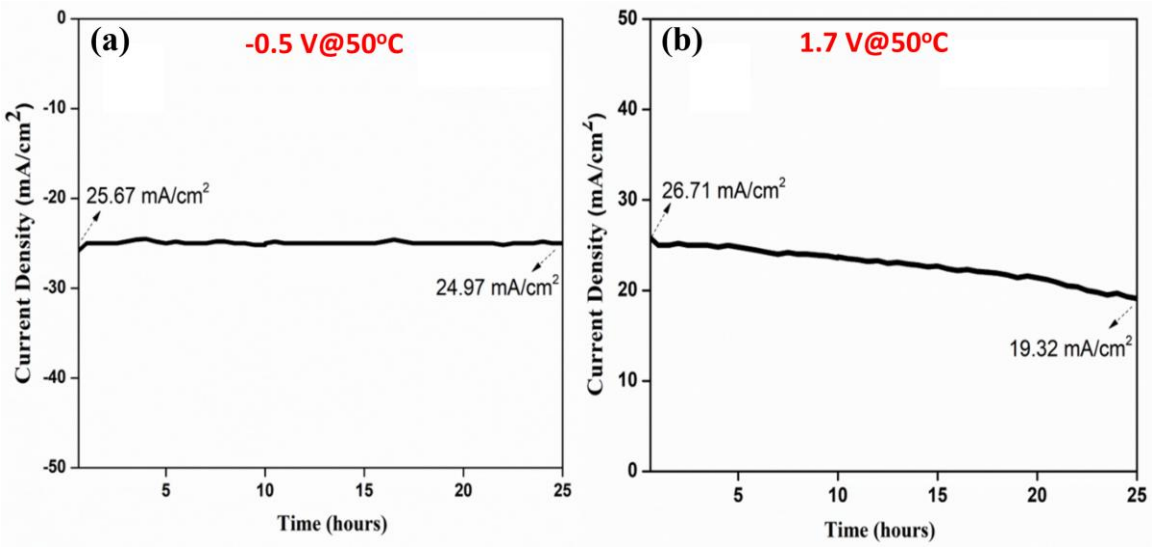

Figure 2.7 Stability study for the duration of 25 h in (a) -0.5 V vs RHE (b) +1.7 V vs RHE at 50 °C and 1M H_2SO_4 condition.

Similarly, the faradaic efficiency (FE) for OER activity at +1.7 V in 1 M H_2SO_4 was evaluated. Approximately 61,200 coulombs of charge generated 1.8 mL of pure O_2 in 1 hour, corresponding to an FE of 52%. Notably, a significant decline in OER current density was observed over time, from 26.71 to 19.32 mA cm^{-2} at 50 °C (**Figure 2.7b**). This performance loss can be attributed to the inherently sluggish kinetics of the OER on the SA-GWO surface, as indicated by the high Tafel slope values (**Figure 2.6b**). Overall, SA-GWO exhibited superior electrocatalytic performance and long-term durability for HER compared to OER, along with excellent stability in acidic media [213,214]. Remarkably, the same batch of SA-GWO, stored under ambient conditions for several months, consistently delivered a stable HER current density of ~25 mA cm^{-2} under identical test

conditions (-0.5 V, 1 M H_2SO_4, 50 °C), confirming its outstanding long-term electrochemical robustness (**Figure A8, Appendix information**).

2.5.4 Proposed Mechanism for Acidic Water Electrolysis

This section presents a detailed discussion on the mechanistic aspects of the HER and OER on the SA-GWO electrode (**Figure 2.8-2.11; Figure A9, Appendix information**). As a first step, morphological changes in SA-GWO following electrocatalytic activity were examined and compared to the pristine electrode. SEM analysis revealed a distinct distortion in the monoclinic WO_3 nanoplates (square-like structures) after HER testing at -0.5 V in 1 M H_2SO_4, indicating structural transformation induced under cathodic conditions (**Figure 2.8a, 2.9**). In contrast, no significant morphological changes were observed when the electrode was subjected to OER at +1.7 V in 1 M H_2SO_4, suggesting greater structural stability of SA-GWO under anodic conditions.

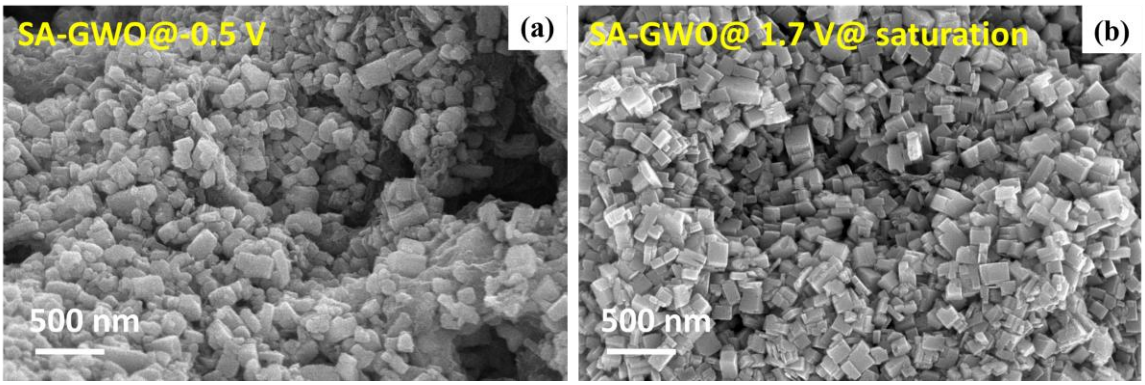

Figure 2.8 SEM images of SA-GWO during acidic electrolysis (1M H_2SO_4, 28°C) at respective potential (a) -0.5 V (b) +1.7 V.

The impact of prolonged cathodic polarization (-0.5 V, 1 M H_2SO_4) on the morphological evolution of SA-GWO was systematically investigated (**Figure 2.9a-d**). SEM images were captured at time intervals of 15 minutes, 30 minutes, 1 hour, and 2 hours. Notably,

significant deformation of the WO_3 nanoplatelet structures was evident within just 15 minutes. After 1 hour, the nanoplatelets were almost completely disintegrated, giving rise to a transformed two-dimensional nanostructure characterized by well-defined nanochannels and nanopores. Among all images, **Figure 2.9d** (after 2 hours of cathodic treatment) best illustrates this transition, displaying a saturated and uniform surface entirely composed of 2D nanoporous and nanotunnel-like architectures.

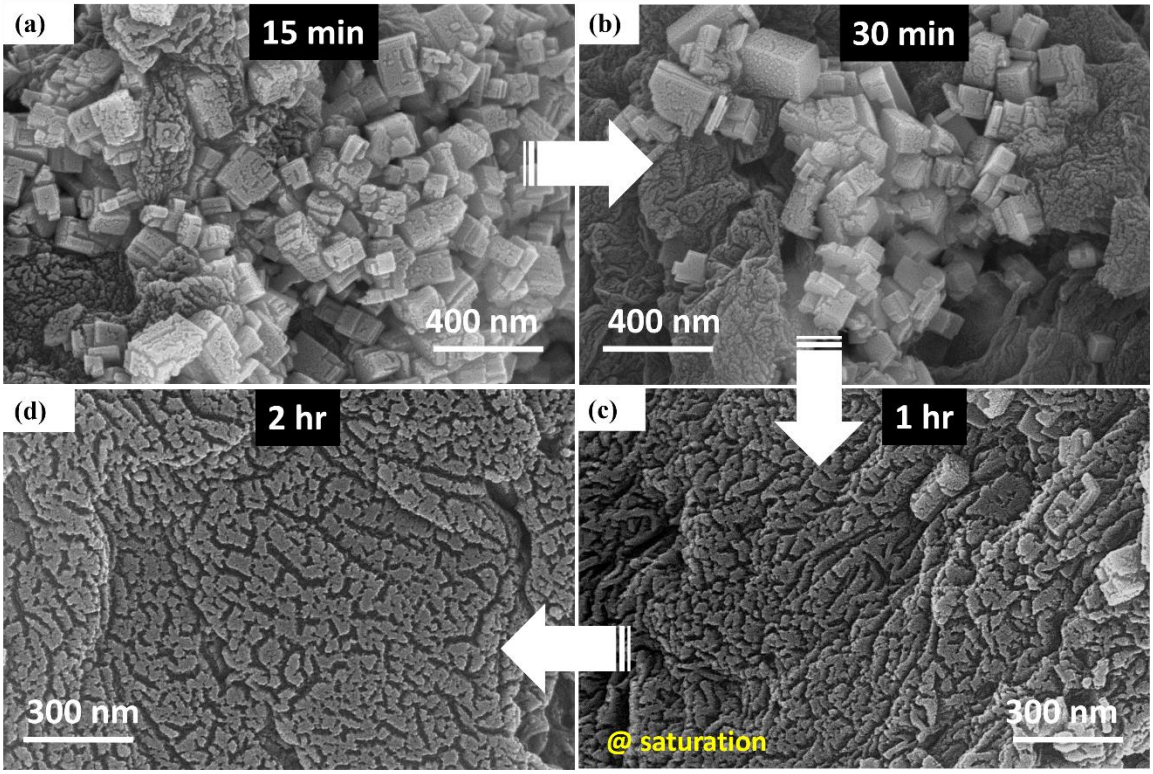

Figure 2.9 SEM images of SA-GWO electrode subjected to cathodic polarizations (-0.5 V, 1M H_2SO_4, 28°C) for duration (a) 15 min (b) ~0.5 h (c) ~1 h (d) ~2 h (saturation).

Furthermore, the structural transformation of SA-GWO was found to be strongly influenced by the applied potential. Upon cathodic polarization, a rapid morphological transition was observed from 3D square-like WO_3 nanoplatelets to a 2D nanostructure composed of interconnected nanopores, nanotunnels, and nanochannels (**Figure A9,**

Appendix Information). This distinct structural reconfiguration suggests a potential correlation with enhanced electrochemical performance. While these observations are promising, gaining a comprehensive understanding of the underlying conversion mechanisms and long-term stability will require further experimental and theoretical investigations. Nonetheless, our study clearly demonstrates a sharp and well-defined structural transition, which appears to be a key feature contributing to the electrode's functional efficiency. To further probe the chemical composition and changes at the molecular level, X-ray photoelectron spectroscopy (XPS) was conducted on both the fresh

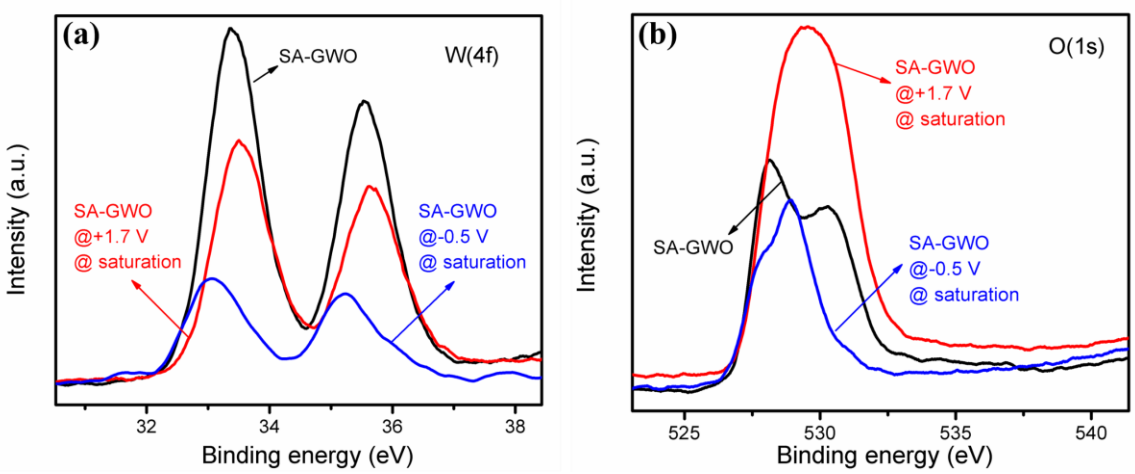

Figure 2.10 XPS (a) W (4f) and (b) O (1s) spectra of SA-GWO electrode subjected to set potential of + 1.7 V and - 0.5 V, for duration ≥ 1 h in H_2SO_4.

Figures 2.10 and 2.11 present the XPS analysis of both pristine (untreated) SA-GWO and SA-GWO subjected to acidic electrolysis. The survey spectra confirmed the presence of only W, O, and C elements in all samples (**Figure A10, Appendix Information**). Notably, significant differences were observed in the high-resolution W 4f spectra between the fresh and HER-tested SA-GWO electrodes (**Figure 2.10a**). For the untreated sample, the W 4f peaks appeared at binding energies (BEs) of 35.55 eV and 33.38 eV, corresponding to W^{5+}

species (W $4f_{5/2}$ and W $4f_{7/2}$, respectively) [215-217]. These features are characteristic of oxygen-deficient monoclinic WO_3, indicating the presence of intrinsic oxygen vacancies. Upon subjecting the electrode to hydrogen evolution conditions (-0.5 V, 1 M H_2SO_4), the W 4f peaks exhibited a noticeable shift (~0.33 eV) toward lower binding energies, suggesting a partial reduction of tungsten species and the possible formation of hydrogen tungsten bronzes (H_xWO_3) during HER [215]. In contrast, the W 4f spectrum of the OER-tested SA-GWO electrode closely resembled that of the fresh electrode, indicating minimal structural or oxidation state changes under anodic conditions.

The O 1s spectra also provided insightful information regarding the bonding environment of oxygen in SA-GWO (**Figure 2.10b**). For WO_3, two distinct peaks at 529.5 and 531.0 eV are commonly attributed to lattice oxygen (O^{2-}) and oxygen in oxygen-deficient regions (WO_{3-x}), respectively [218,219]. In the fresh SA-GWO, similar peaks were observed, though with a slight shift (to 528.16 and 530.15 eV), which can be attributed to strong interfacial interactions between WO_3 and RGO. These W-O-C interactions likely arise from electron redistribution due to the difference in electronegativity between oxygen and carbon, leading to polarization of the C-O bond ($^{\delta+}C\text{-}O^{\delta-}$). The previously discussed TEM images (**Figure 2.2**) further support the existence of strong interfacial contact between RGO and WO_3, which contributes to enhanced electrical conductivity and catalytic performance.

Further comparison of the O 1s spectra revealed the disappearance of the 530.15 eV peak in the HER-tested SA-GWO sample (**Figure 2.11c**). This change suggests a possible phase transformation from monoclinic WO_3 to a hexagonal form (h-WO_3), associated with the formation of 2D nanostructures (NS-WO_3) [217,220]. Such structural evolution is

consistent with the morphological changes observed during cathodic treatment and is indicative of dynamic phase and oxidation state transitions that occur during the HER process.

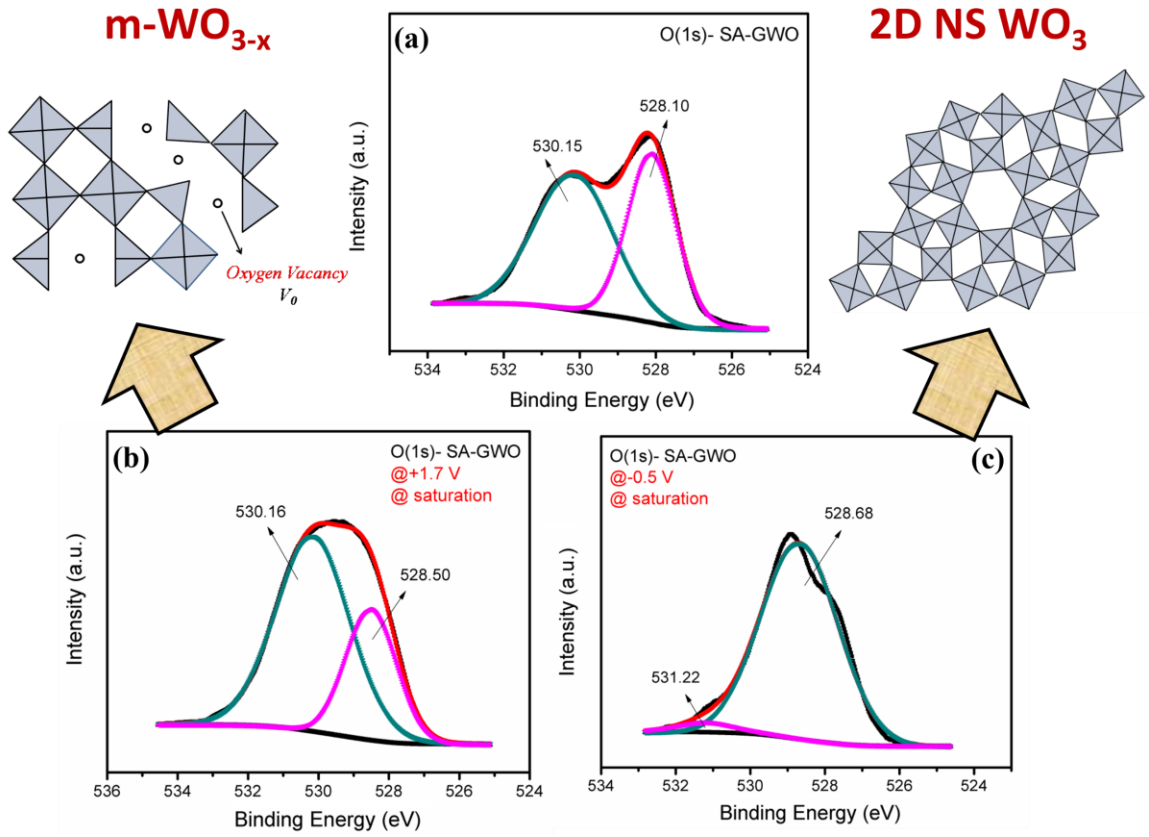

Figure 2.11 (a) Deconvoluted O (1s) spectra of untreated SA-GWO and the same subjected to acidic electrolysis at (b) +1.7 V and (c) -0.5 V electrode, for duration ≥ 1 h in H_2SO_4.

The crystal structure of hexagonal tungsten trioxide (h-WO_3), also referred to as 2D NS-WO_3, shares chemical similarity with the monoclinic phase but exhibits a distinct arrangement characterized by empty hexagonal or trigonal nanochannels within a W-O framework [207,208]. This framework presents a hybrid structural configuration comprising one-dimensional (1D) chains and two-dimensional (2D) nanostructural features, which gives rise to hexagonally aligned channels capable of hosting intercalated

protons (H^+). These nanochannels serve as potential binding sites, making h-WO_3 a highly efficient intercalation oxide host for the formation of hydrogen tungsten bronzes (H_xWO_3) during reductive electrochemical processes [220].

In contrast, the O 1s XPS spectrum of the SA-GWO electrode subjected to anodic conditions (+1.7 V, 1 M H_2SO_4) remained largely unchanged compared to the fresh sample. The two characteristic oxygen peaks persisted, with only a minor variation in peak intensity (**Figure 2.11b**), which is likely attributed to the adsorption of molecular oxygen or hydroxyl species at surface defect sites on WO_3 [218,219]. This observation suggests that the anodic electrochemical environment does not significantly alter the oxidation state or structural integrity of the WO_3 component within SA-GWO.

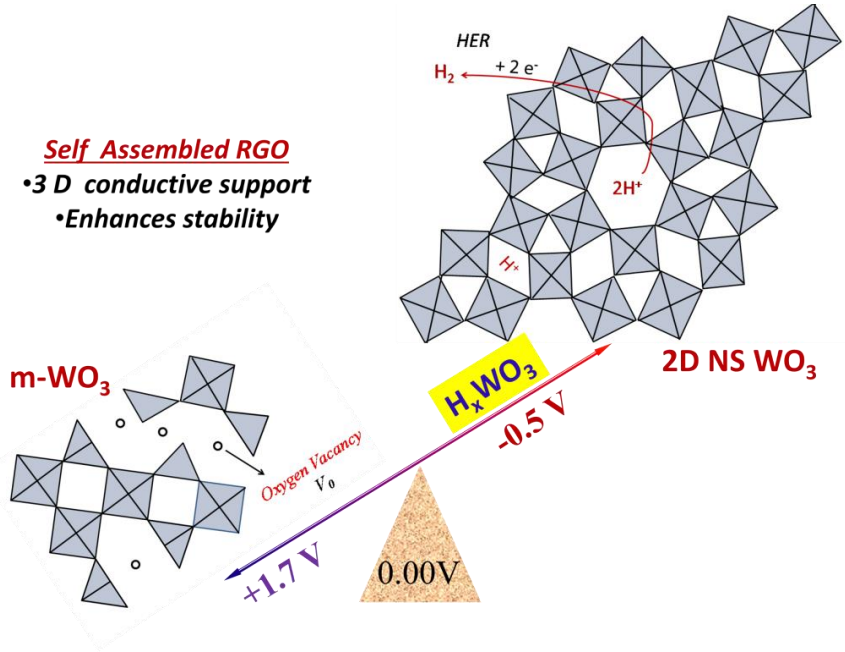

Figure 2.12 Plausible mechanism underlying the bifunctional HER and OER activities of SA-GWO, as deduced from SEM and XPS analysis.

Overall, this study reveals the emergence of two distinct morphologies of WO_3, each playing a pivotal role in driving either the hydrogen or oxygen evolution reactions under

acidic electrolysis conditions (**Figure 2.12**). The formation of these polymorphic structures is strongly governed by the applied electrochemical potential. During cathodic operation (-0.5 V, 1 M H_2SO_4), a transformation occurs, leading to the generation of a hexagonal WO_3 phase (h-WO_3) characterized by a 2D nanostructured framework with empty hexagonal and trigonal nanochannels. This phase is primarily responsible for the HER. The HER mechanism is closely linked to the simultaneous insertion of protons (H^+) and electrons into the nanochannels of h-WO_3, resulting in the formation of hydrogen tungsten bronzes (H_xWO_3) and the subsequent release of H_2 via a reversible insertion/de-insertion pathway. RGO plays a critical supporting role by providing a highly conductive substrate that enhances charge transfer kinetics and increases the electrochemically active surface area of WO_3 [221-224]. Furthermore, RGO significantly improves the structural and electrochemical stability of WO_3, enabling prolonged operation under harsh acidic conditions.

In contrast, during anodic polarization (+1.7 V, 1 M H_2SO_4), the pristine 3D monoclinic WO_3, retaining its inherent oxygen-deficient sites, remains the active phase responsible for driving the OER. These oxygen vacancies facilitate the multi-step oxidative transformation processes essential for O_2 evolution, without necessitating major morphological changes.

2.6 Conclusions

We demonstrated the effective application of self-architectured SA-GWO as a freestanding, bifunctional electrode for acidic water electrolysis, enabling simultaneous hydrogen and oxygen generation. In situ formation and uniform integration of WO_3 and RGO within the 3D SA-GWO framework were confirmed by XPS, UV-Vis, Raman, and SEM analyses. SA-GWO exhibited superior electrocatalytic performance for HER over OER, requiring a full cell voltage of 1.9 V to achieve 10 mA cm^{-2} in 1 M H_2SO_4 at 50 °C. Faradaic efficiencies of 73% for HER and 52% for OER were achieved, along with excellent long-term stability in acidic media. Mechanistic studies revealed two distinct WO_3 morphologies: a 2D nanosheet structure with hexagonal channels responsible for efficient HER, and oxygen-deficient 3D monoclinic WO_3 active toward OER. This work highlights the promise of self-assembled graphene–metal oxide composites as next-generation electrocatalysts for water splitting.

Chapter 3: MoS_2/Sulfonated Reduced Graphene Oxide as an activity and durability booster for prolonged seawater electrolysis

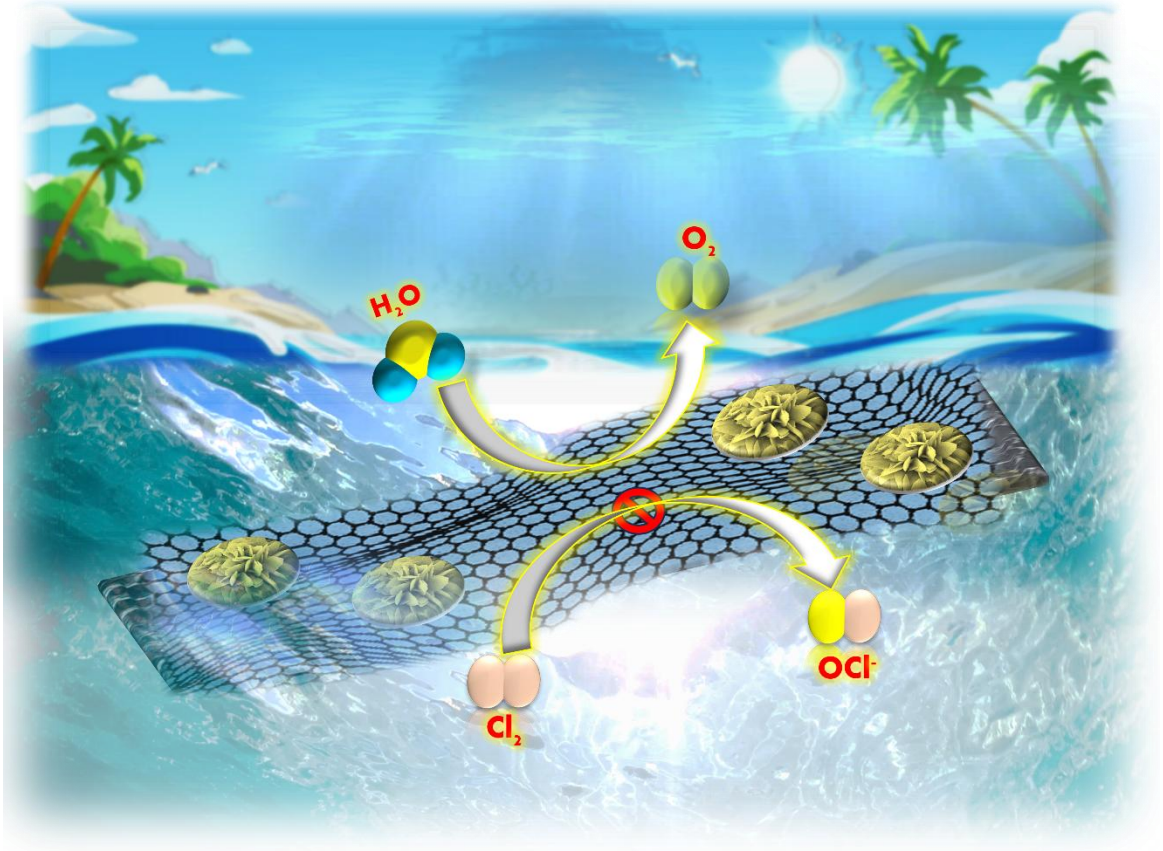

Seawater is a more sustainable alternative to freshwater for electrolysis, but its high chloride content poses significant challenges. We address this by developing a chloride-resistant GNiMoOS electrode that enables efficient and selective seawater electrolysis.

(Adapted from RSC Sustainable Energy & Fuels, 2025, https://doi.org/10.1039/D5SE00541H).

3.1 Abstract

The advancement of electrolyzer technology increasingly demands the use of seawater over freshwater to ensure a sustainable and economically viable clean energy supply. However, the presence of chloride ions (Cl^-), which aggressively corrode metal surfaces, presents a major challenge for seawater electrolysis. Thus, designing chloride-resistant electrodes is critical for enabling efficient and durable seawater electrolyzers. In this work, we report a bifunctional, chloride-resistant double-layer electrode (GNiMoOS), consisting of molybdenum sulfide (MoS_2) nanostructures uniformly deposited on sulfonated graphene sheets over Ni foam. This architecture effectively enables selective water splitting producing H_2 and O_2, while suppressing undesired chloride oxidation (Cl^- to ClO^-) under seawater conditions. The chromogenic substrate 3,3′,5,5′-tetramethylbenzidine (TMB) confirmed the Cl^--blocking ability of the GNiMoOS catalyst by showing negligible ClO^- formation. Furthermore, density functional theory (DFT) calculations revealed a strong preferential interaction of sulfonic groups ($-SO_3H$) with OH^- over Cl^-, validating the chlorine-repelling properties of the electrode. Comprehensive material characterization using XPS, Raman, SEM, TEM, and FT-IR confirmed the successful in situ functionalization of sulfonic moieties into the RGO skeleton and the simultaneous growth of flower-like MoS_2 nanostructures. The GNiMoOS electrode demonstrated outstanding bifunctional performance with current densities of 100 mA cm^{-2} for both HER and OER at room temperature, requiring overpotentials as low as 180 mV and 165 mV, respectively. At industrially relevant current densities (400-600 mA cm^{-2}), the combined overpotentials remained below 600 mV. The unique MoS_2 morphology ensures abundant catalytic sites, while sulfonated RGO imparts excellent anti-corrosion properties. Additionally, the strong

electronic coupling between MoS_2 and RGO enhances charge transfer, and the synergistic interaction among MoS_2, $-SO_3H$, and RGO collectively drives high catalytic activity and long-term stability in harsh seawater environments.

3.2 Introduction

Water electrolysis offers a sustainable and eco-friendly approach to hydrogen (H_2) production, playing a crucial role in the future of renewable energy [225]. Utilizing abundantly available seawater rather than limited freshwater resources for electrolysis presents a promising pathway for generating clean hydrogen fuel. However, the major obstacle in seawater electrolysis is the chlorine evolution reaction (CER), which occurs on the anode due to the existence of chloride anions (~0.5 M) in seawater that competes with the oxygen evolution reaction (OER) [127]. Although the equilibrium potential of oxygen evolution is lower than that of chlorine evolution, the chlorine evolution is kinetically favored. Hence, the formation of toxic chlorine on the anode is generally unavoidable in seawater electrolysis. The fundamental understanding of seawater splitting indicates that, whereas CER predominates at low pH, OER and hypochlorite production compete at high pH at the anode [226]. These aggressive chloride/hypochlorite ions in seawater damage the electrodes, severely impeding the growth of seawater splitting. Moreover, the presence of various elements in seawater and their interference with electrochemistry make the OER in seawater extremely challenging [227]. Although Pt-based catalysts and iridium/ruthenium oxides (IrO_2/RuO_2) are most effective for the electrochemical HER and OER respectively, their high cost and limited supply makes it impossible to be used commercially [228]. Therefore, finding some robust electrocatalysts that can sustain seawater splitting without chlorine corrosion could address the issue of freshwater scarcity

on earth [127]. In this direction, Vos and co-workers [229] proved that putting MnO_x layer on the surface of IrO_2 could effectively improve the efficiency of OER over CER. The MnO_x layer acted as a sieve that disfavors the transport of chloride ions. However, such materials are unable to generate high current densities at low cell voltage, leading to a decrease in electrolyzer efficiency. Kuang et al. [230] developed a multilayer electrode which, when activated, produced a polyanion sulphate/carbonate-passivated NiFe/NiS_x-Ni anode with OER high activity and resilience to corrosion for chlorides in saline electrolytes. The enhanced corrosion resistance in seawater was accomplished by negatively charged polyanions that were integrated into the anode through anodization of the underlying nickel sulfide layer and carbonate ions in the alkaline solution. When the activated polyanion sulphate/carbonate-passivated NiFe/NiS_x-Ni anode was paired with Ni-NiO-Cr_2O_3 cathode, a current density of 400 mA cm^{-2} was achieved at a potential of 1.72 volt in 6 M KOH + 1.5 M NaCl electrolyte at 80 °C. This being the first and last report till date which proved the implications of sulfonated and carbonated moieties in imparting corrosion resistance and acting as chloride ions repellent. However, no specific explanation for the CER/hypo oxychloride reaction's inhibition was given in the study. Yu.et al [231] reported a S doped Ni/Fe hydroxide catalyst S-(Ni, Fe)OOH which exhibited extraordinary OER performance in both alkaline brine and seawater electrolyte. In the seawater electrolyte with 1 M KOH, the overpotentials of S-(Ni, Fe)OOH were 300 and 398 mV at of 100 and 500 mA cm^{-2} current densities respectively. In another report, Feng et al. [232] have reported that the sulfonate functional groups on carbon related materials particularly graphene can capture H^+ from *OH or *OOH during OER catalysis, thus significantly reducing OER overpotential due to the numerous advantages associated with doping inside

graphene matrix [86, 232-236]. In this direction, Zhu et al. [233]. used Electrical-field polarization to cause the enrichment of the sulfonated group on the surface nickel–iron layered double hydroxide (NiFe LDH)/carbon dots (CDs) composite catalysts. The polarized-SO_3-CDs/NiFe LDH could be used as a highly efficient OER electrocatalyst with a low overpotential of 200 mV at the current density of 10 mA cm^{-2}. So, from the above reports, it is concluded that sulfur and its associated anionic forms have a good adjusting property for working in saline water conditions. In the past, several methods, including chemical functionalization of graphene oxide (GO) [237], hydrothermal sulfonation of GO [238] and edge sulfonic acid functionalized graphene via ball-milling of graphite powder [239] have been utilized to generate sulfur moieties into graphene matrix for developing an efficient electrocatalyst. Despite their conductivity and stability, functionalized graphene systems alone lack the intrinsic catalytic activity and fail to reduce activation energy effectively for HER/OER. But when these sulfur rich graphene or Sulfonated graphene systems are coupled with transition metals or their sulfides/oxides/phosphides, a stable, conductive, high-performing hybrid catalyst can be developed where, the transition metals provide the actual catalytic active sites enhancing the activity and the functionalized sheets brings stability and conductivity. Molybdenum sulfides with different stoichiometries and polymorphs have been intensively investigated as efficient electrocatalyst material alternative to noble metals for water splitting applications [240-252]. However, it has predominantly been employed as a HER catalyst due to its inherent activity and has rarely been explored for OER applications. So, in order to transform MoS_2 it into an efficient and robust OER electrocatalyst for seawater splitting, we started the present work on MoS_2 by coupling it with functionalized (S doped) reduced graphene oxide

(RGO). Previous reports [7–9] highlighting the effectiveness of sulfur or sulfonic moieties in developing anode materials for seawater splitting guided the incorporation of -SO_3H functional groups to combat the harsh chloride environment in seawater and enhance system efficiency. So, the polyanion rich RGO layer was expected to improve the hydrophilicity and introduce a negative surface charge to repel Cl^- ions (especially relevant for seawater electrolysis) which would not only resist corrosion but also compensate for MoS_2's inherent limitations in OER activity, thereby boosting both the stability and overall electrocatalytic performance of the developed electrode. We chose Ni foam as our base substrate to grow our electrocatalyst due to its numerous advantages [251,252]. All the previously reported papers utilizing MoS_2 and RGO over Ni foam as electrocatalyst material, [246-250] have accounted the synergistic effects between MoS_2 and GO/RGO to be accountable for the enhanced electrochemical activity obtained with the respective systems. While synergy between MoS_2 and RGO plays a central role, in complex multi-component systems for instance, in our present system where we are utilizing Ni foam, MoS_2 and RGO (which integrates Mo, Ni, S, and GO), potential combinations like Mo-S, Ni-S, or their interactions with GO introduces ambiguity in mechanistic understanding. This raises an important question regarding material attribution and mechanistic clarity in catalyst design for such multi-component systems. None of the previously reported studies have accurately elucidated the formation of the target electrocatalyst will full accuracy while systematically ruling out the possible formation of other undesired species that may arise in complex multicomponent systems. Keeping all this in mind, we moved forward towards the fabrication of a target specific catalyst utilizing the state-of-the-art MoS_2 along with polyanion functionalized graphene *via* simply one-step hydrothermal approach,

wherein oxidized sulfur moieties are in-situ generated without the use of any sophisticated techniques which usually requires multiple steps. Sulfur is simultaneously introduced on the surface of reduced graphene oxide and in the lattice of Mo catalyst during the reaction. Importantly, the developed sulfonic functionalized reduced graphene oxide supported over Ni introduces two essentials features inside catalyst system, first is the mechanical integrity and second the specificity for electrode process typically OER over CER. Thus, we present a double layer electrode (GNiMoOS) consisting of a molybdenum sulfide electrocatalyst layer uniformly deposited sulfonated graphene-Ni foam electrode offering superior catalytic activity and corrosion resistance properties in alkaline seawater electrolysis. The GNiMoOS electrode exhibits outstanding OER and HER activities in simulated seawater requiring a very low overpotential of 180 and 165 mV, respectively, to reach current densities of 100 mA cm^{-2} at room temperature. When GNiMoOS was employed as both the cathode and anode in a two-electrode setup, it achieved current densities of 100 mA cm^{-2} and 500 mA cm^{-2} at low overall cell voltages of just 1.58 V and 1.80 V, respectively, at room temperature, demonstrating its exceptional bifunctional activity and long-term stability in simulated seawater. All the spectroscopic techniques such as RAMAN, SEM, TEM and XPS and FT-IR confirm the 100% formation of MoS_2 along with the abundance of oxidized sulfur moieties doped inside reduced graphene oxide in the GNiMoOS electrode which were responsible for the excellent performance of the electrode towards seawater splitting. In addition , DFT studies also validated the role of sulfonated graphene towards imparting stability to the GNiMoOS system during seawater electrolysis. So, a facile hydrothermal method to steer commercial Ni foam into robust novel electrode having superior catalytic activity for oxygen evolution and corrosion resistance properties for

seawater electrolysis, which has important implications for both the hydrogen economy and environmental remediation by allowing direct splitting of seawater into renewable fuels without desalination is hence developed.

3.3 Experimental Section

3.3.1 Materials

Graphite powder [Qualikems Fine ChemPvt. Ltd],Sulfuric acid (H_2SO_4) [Finar Ltd],Ortho-phosphoric acid (H_3PO_4)[Merck life science Pvt. Ltd],Potassium permanganate ($KMnO_4$)[Sisco Research Laboratories Pvt. Ltd], Hydrogen peroxide (H_2O_2) [Merck life science Private Limited],Thiourea (CH_4N_2S)[Merck Pvt. Ltd],Molybdic Acid (H_2MoO_4) [Spectrochem Pvt.Ltd], ($Na_2S.9H_2O$) [Avantor Performance Materials India Limited], Ethanol (C_2H_5OH)[Changshu Hongsheng Fine Chemical Co. Ltd], Acetone (C_3H_6O) SDFCL [S D Fine-Chem Limited], Methanol (CH_3OH) SDFCL[S D fine-Chem Limited], Potassium hydroxide (KOH) [Finar Ltd], Sodium Chloride (NaCl) [Finar Ltd], Nickel foam (Sigma Aldrich-GF28024657-5EA) , Ni plate (Sigma Aldrich- GF86063654-1EA**)** were used as received. Deionized water (DDW) was prepared by redistillation of the double distilled water in a glass distillation apparatus. All reactants were of analytical purity and used as received. Doubly distilled Deionized water was used throughout the experiments.

3.3.2 Material Characterizations

Functional group identification was done by Thermo Electron Scientific Instruments LLC, Nicolet iS20, Fourier Transform Infrared Spectrometer (FTIR) in the spectral range of 350 cm^{-1} to 11000 cm^{-1}. Raman spectra of the samples were recorded in a Jasco NRS-5500 Laser Confocal Raman Spectrophotometer equipped with 1200 grooves per mm gratings,

and laser spot intensity 0.0001% of microscope with objective. The samples were excited with a 532 nm wavelength laser from an Ar^+ laser with fluorescent correction. The XPS measurements were recorded in the Thermo Fisher Scientific K-Alpha X-ray Photoelectron Spectrometer, which was outfitted with Al-Kα X-ray (1486.6 eV) as a primary excitation and an auto-firing, 3 filament TSP software. The curve fitting of the high-resolution spectra was performed with combined Gaussian−Lorentzian functions. Elemental analysis (% of Nitrogen, sulfur, hydrogen and carbon) of the material was estimated by Elementar Unicube CHNS instrument, which ensured a complete combustion at 1200°C. The surface morphology was recorded using a Field Emission Scanning Electron Microscopy (FESEM) JSM-7900F (Jeol Ltd.), and the elemental distribution was analyzed by the energy dispersive X-ray spectroscopic technique (EDS). The particle morphology was characterized by transmission electron microscope (TEM) imaging using a JEOL JEM-F200. The UV−vis measurements were carried out using a Cary 5000 (Agilent Technology). The Multi Autolab M 204 from Metrohm Autolab was used to record impedance studies (Serial number: MAC90581). Further, the electrochemical characterizations were performed using μ-AUTOLAB type-III (Serial number: μ3AUT70731).

3.3.3 Electrochemical Measurements

The electrochemical performance of the electrocatalysts were evaluated using MULTI AUTOLAB M204 involving three electrode configurations with platinum mesh as counter electrode and Ag/AgCl as reference electrode. The Reference electrode was well saturated with 3 M KCl and to ensure the reliability of our reference electrode. Before all our experimental tests, we used $[Fe(CN)_6]^{3-/4-}$ as a non-reactive redox probe to monitor

reference electrode drift and negligible drift was noted making is feasible for use. All the electrochemical measurements were carried out in harsh simulated seawater (0.1 M KOH and 0.5 M NaCl) and alkaline seawater electrolyte (2M KOH + 0.5 M NaCl). The catalyst was first stabilized by cyclic voltammetry (CV) at a 30-mV s^{-1} scan rate in the potential window of -1.5 to 0.7 V vs. Ag/AgCl. All the LSV experiments were conducted at a scan rate 5 mV s^{-1}. Chronoamperometry studies were carried out to check the stability and the durability of the working electrode with time. For prolonged stability tests, a two-compartment cell with Nafion membrane, between the working and counter electrode compartments was used to prevent migration of dissolved Pt (if any) to the working electrode area and get the desired current response solely from the electrocatalyst! The current density was calculated considering the planar geometry surface area of all the electrodes. All the potential in this study were adjusted to the reversible hydrogen electrode (RHE) reference scale using the formula equation

E (*vs.* RHE) = applied potential (*vs*. Ag/AgCl) + E^0 [Ag/AgCl (3M KCl)] + 0.059 V (pH)**.**

The electrochemical impedance experiment was carried out over the frequency range of 0.1 Hz to 1 x 10^5 Hz at the OCP potential in 2 M KOH + 0.5 M NaCl. The present study is dedicated to understanding the phenomenon associated with the electrode during OER in harsh medium and understanding the principle behind the remarkable stability of the working electrode in such a harsh medium.

3.3.4 Spin-polarized density functional theory (DFT)

Spin-polarized density functional theory (DFT) calculations were performed using the Vienna Ab initio Simulation Package (VASP). The exchange-correlation energy was

evaluated using the generalized gradient approximation (GGA) with the Perdew-Burke-Ernzerhof (PBE) functional, while the projector-augmented wave (PAW) method was employed to describe electron-ion interactions [253-254]. The energy cutoff for plane wave expansion was set to 500 eV, and the convergence threshold was set as 10-6 eV in energy and 0.01 eV/Å in force. To describe the van der Waals interaction, we used the DFT-D3 correction in the Grimme Scheme.

For ribbon model calculations, a 20 Å vacuum layer was added to prevent interactions between periodic images. Graphene ribbons with zigzag edge morphology were modeled, saturated with hydrogen atoms to satisfy all in-plane carbon bonds (32 carbon and 4 hydrogen atoms). Separate calculations were performed for MoS_2 and SO_3H-decorated ribbons to reduce the computational costs. A Monkhorst-Pack mesh with a 1 × 4 × 1 k-point grid was used for Brillouin zone sampling during geometry optimizations and subsequent calculations.

Gibbs free energy variations for electron transfer reactions were computed using the computational hydrogen electrode (CHE) model developed by Nørskov et al [73]. The Gibbs free energy was defined as:

$$\Delta G = \Delta H + \Delta ZPE - T\Delta S$$

where, ΔH denote the change in enthalpy from the DFT calculation, T is the temperature, ΔS is the change in entropy, and ΔZPE represents the change in zero-point energy of the reaction. The entropy values for free gas molecules were obtained from the NIST database, while for adsorbed species, entropy was calculated based on the vibrational frequencies of the adsorbed intermediates, considering only vibrational entropy in the calculation of SSS

for these species. The theoretical onset potential (U_{Min}) is defined as the minimum potential required to make the entire reaction pathway thermodynamically favorable (downhill) in the Gibbs free energy diagram, calculated using U_{Min} = -Maximum(ΔG)/e.

The adsorption energies (E_{ad}) of ions on active site, were calculated by $E_{ad} = E_{ion@site} - E_{site} - E_{(ion)}$

Where E_{ion}@site represents the total energy of an ion adsorbed on active site, E_{site} is the total energy of either MoS_2@Gr or SO_3H@Gr and E_{ion} is the energy of an isolated OH or Cl molecule.

3.4 Electrocatalyst Synthesis

3.4.1 Synthesis of graphene oxide (GO)

GO was synthesized by modified Hummer's method. Typically, 3 g of natural graphite flakes were added into 9:1 mixture of concentrated H_2SO_4: H_3PO_4 (360:40 mL). After that, 18 g of $KMnO_4$ was added very slowly and the reaction was put to heat at 55 °C and stirred for 12 hrs. The resultant solution mixture was poured to ice-cold water containing 3 mL 10% H_2O_2. Thereafter, the resultant product was repeatedly washed with excess of DI water by centrifugation at 10000 rpm for 30 minutes and the process was repeated until pH of solution reaches 7. Finally, it was washed with absolute ethanol to dissolve organic debris, if any! Then **GO** was collected and stored at room temperature for use.

3.4.2 Synthesis of RGO/NF electrocatalyst

Ni foam (NF) (foam, 20 x 20 mm, thickness 1.6 mm) was carefully cleaned with concentrated HCl solution (37 wt. %) in an ultrasound bath for 5 min to remove the surface oxide layer. Then the process was repeated with deionized water and absolute ethanol for

5 min each, to ensure the surface of Ni foam was well cleaned. The foams were fully dried in air at 60°C.These electrodes were then dip coated in graphene oxide multiple times in order to develop an even layer of graphene oxide all around the Ni foam electrode [GO coated Nickel foam; GO thickness (0.67 mm)] and subsequently, the electrodes were dried at room temperature before use. The following electrodes obtained were placed inside a 100 ml Teflon-lined stainless autoclave containing 30 ml of water and 10 ml methanol and heated at 180°C in an electric oven for 24 hours. The electrodes obtained after washing with water and ethanol followed by drying were named as **RGO-NF.**

3.4.3 Synthesis of MoS_2 Powder

MoS_2 Powder was prepared hydrothermally by taking molybdic acid for '**M**' along with the thiourea for '**S'** in the molar ratio of 1:2. This powder mixture was dissolved in 30 ml of water and 10 ml methanol and transferred into a 100 ml Teflon-lined stainless autoclave. The autoclave was heated at 180°C in an electric oven and maintained for 24 hours. The following MoS_2 powder obtained after washing with water and ethanol followed by drying.

3.4.4 Synthesis of NiMoOS electrocatalyst

NiMoOS electrocatalyst was prepared hydrothermally by taking molybdic acid (source of Mo) and thiourea (source of S) in the molar ratio of 1:2. The cleaned Ni foam (foam, 20 x 20 mm, thickness 1.6 mm) along with powder mixture were transferred into a 100 ml Teflon-lined stainless autoclave that consisted of 30 ml of water and 10 ml methanol. The autoclave was heated at 180°C in an electric oven for 24 hours. The following electrodes was washed with water and ethanol followed by drying and named as **NiMoOS.**

3.4.5 Synthesis of NiS electrocatalyst

Ni foam was carefully cleaned with concentrated HCl solution (37 wt. %) in an ultrasound bath for 5 min to remove the surface oxide layer followed by washing with deionized water and absolute ethanol. The following electrodes along with thiourea were put inside a 100 ml Teflon-lined stainless autoclave containing 30 ml of water and 10 ml methanol and heated at 180°C in an electric oven for 24 hours. The following electrode obtained after washing with water and ethanol followed by drying was named as **NiS**. This catalyst precursor was prepared to check the role of sulfur in imparting durability and activity to the electrode.

3.4.6 Synthesis of GNiS electrocatalyst

Thiourea was in-situ deposited over RGO/NF electrode *via* the hydrothermal route following the same above-mentioned operating parameters. The electrodes were washed properly with distilled water followed by drying. The resulting electrodes were named **GNiS**. The deposition of graphene over Ni-foam followed by the in-situ formation of abundant sulphonated graphene or sulphonic groups over graphene is highly advantageous in defending component against chloride ions.

3.4.7 Synthesis of GNiMoOS electrocatalyst

GNiMoOS electrocatalyst was prepared hydrothermally by taking GO coated Nickel foam (GO-Ni foam, 20 x 20 mm, thickness 2.27 mm), molybdic acid (source of Mo) and thiourea (source of S) in the molar ratio of 1:2. The GO coated Ni foam and powder mixture were transferred into a 100 ml Teflon-lined stainless autoclave that consisted of 30 ml of water and 10 ml methanol. The autoclave was heated at 180°C in an electric oven for 24 hours.

The resulting electrodes obtained after washing with water and ethanol followed by drying were labelled as **GNiMoOS**. The synthesis scheme is shown in **Figure 3.1**.

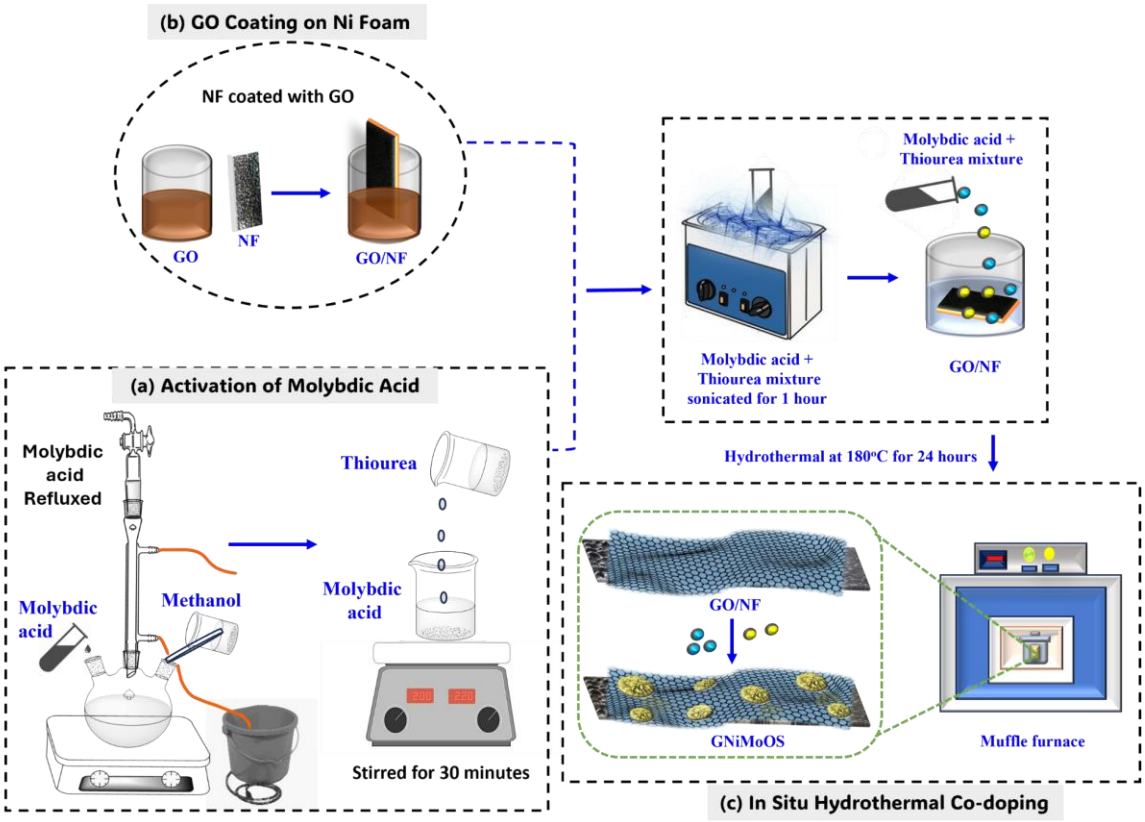

Figure 3.1 Synthesis scheme of GNiMoOS.

3.4.8 Synthesis of RGO/Nip electrocatalyst

Ni plate (foil, 20 x 20 mm) was carefully cleaned with concentrated HCl solution (37 wt. %) in an ultrasound bath for 5 min to remove the surface oxide layer followed by washing with deionized water and absolute ethanol. These electrodes were then dip coated in graphene oxide multiple times to develop an even layer of graphene oxide all around the Ni plate and the electrodes were dried at room temperature completely before put to use. The following electrodes obtained were placed inside a 100 ml Teflon-lined stainless

autoclave containing 30 ml of water and 10 ml methanol and heated at 180°C in an electric oven for 24 hours. The electrodes obtained after washing with water and ethanol followed by drying were named as **RGO/Nip**

3.4.9 Synthesis of RGO/S/Nip electrocatalyst

Thiourea was in-situ deposited over RGO/NiP electrode via the hydrothermal route following the same above-mentioned operating parameters. The electrodes were washed properly with distilled water followed by drying. The resulting electrodes were named **RGO/S/Nip.**

3.5 Results and discussions

Electrochemical studies were conducted to evaluate the electrocatalytic performance of five distinct electrode materials namely RGO/NF (hydrothermally treated GO coated Ni foam), NiS (S doped over Ni foam), NiMoOS (Mo and S codoped over Ni foam), GNiS (S doped over GO coated Ni foam), and GNiMoOS (Mo and S codoped over GO coated Ni foam) along with bare Ni foam (NF) for comparison to check their performance as an electrocatalyst in harsh simulated seawater.This medium was more favourable for CER than OER, as Cl^- ion were in abundance as compared to OH^- ions. The electrochemical performance of NF, RGO/NF, NiMoOS, NiS, GNiS and GNiMoOS electrodes were firstly evaluated by linear sweep voltammetry (LSV) and the corresponding polarization curves are presented in **Figure 3.2a**. It is noticeable to see that the GNiMoOS catalyst exhibits the lowest overpotential amongst all, requiring only 56 mV to achieve a current density of 10 mA cm^{-2} in comparison to GNiS, NiMoOS, NiS, RGO/NF and bare NF, which showed overpotentials of 89, 101, 199, 237 and 246 mV respectively, at a current density of 10

mAcm^{-2} in the same media. GNiMoOS catalyst exhibited lower overpotential 40 mV and 52 mV in simulated seawater and real seawater media respectively, at a current density of 10 mAcm^{-2},which were lower than even the recently reported CA-1T-MoS_2/rGO (466 mV) [255];rGO/MnO_2/MoS_2(205mV)[256];MoS_2/rGOhybrids(242mV)[257];MoS_2/$NiSe_2$/rgO (127mV)[258] and 2H-1TMoS_2/rGOhybrid (71mV)[259] electrocatalysts for simulated/seawater media.

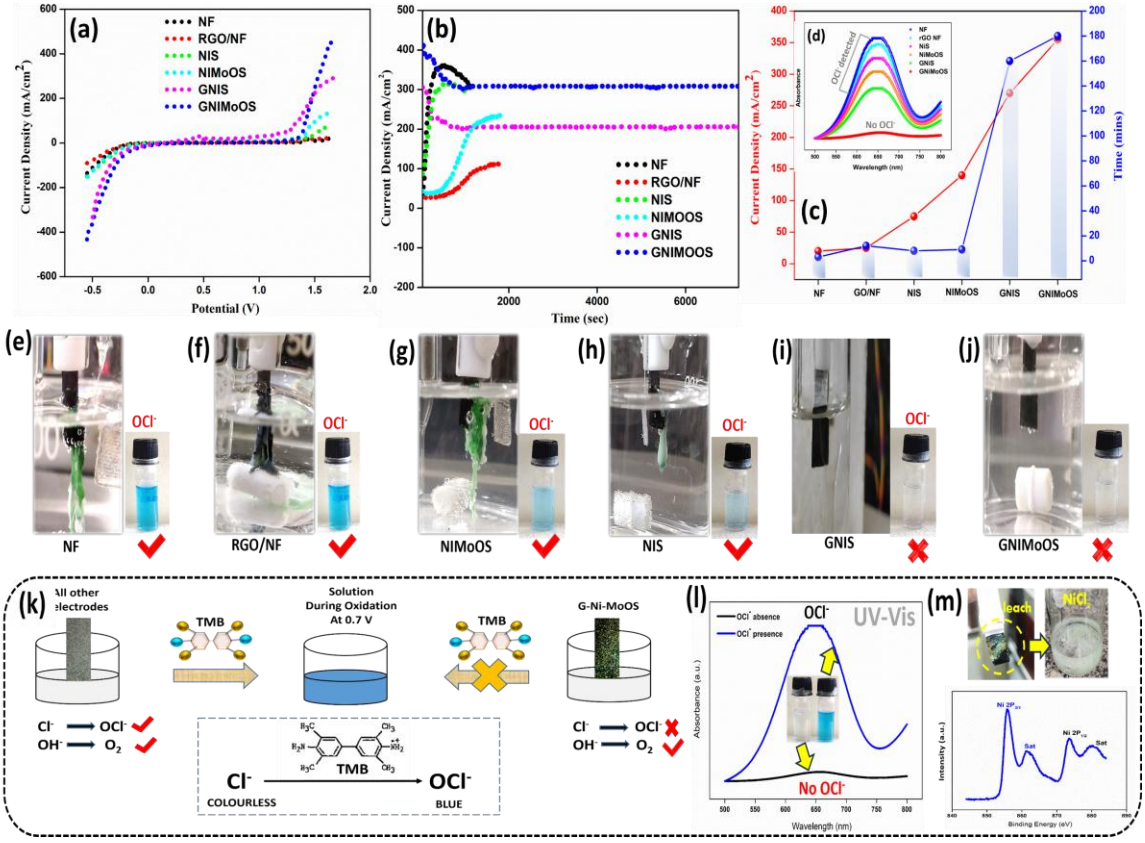

Figure 3.2 (a) Linear sweep voltammetry (LSV) profiles of various electrodes recorded from -0.5 V to 1.7 V vs. RHE in 0.1 M KOH + 0.5 M NaCl electrolyte (b) Chronoamperometry curves of the electrodes during the OER at a fixed potential of 0.7 V in the same electrolyte (c) Long-term stability profiles of the catalysts, showing current density variations with time (d) UV-Visible spectra of the electrolyte post-electrolysis, indicating oxidation products (e-j) Photographic images of the electrodes bare Ni foam (NF), RGO/NF, NiMoOS, NiS, GNiS, and GNiMoOS before and after anodic polarization/oxidation in the same electrolyte, alongside images of their respective electrolytes post-OER using TMB dye for the qualitative detection of hypochlorite ions (OCl⁻) (k-l) Schematic illustration of the hypochlorite (OCl⁻) detection mechanism using TMB dye (m) Analysis of species leached into the electrolyte after electrolysis.

This remarkable HER activity is obvious considering literature reports [255-262] stating MoS_2/RGO as an efficient HER catalyst in alkaline medium. However, rare reports sighting MoS_2/RGO as an efficient OER electrocatalyst or a robust bifunctional electrode which could stand seawater oxidation for long are available. The LSV polarization curve (**Figure 3.2a**) demonstrates promising OER activity for the prepared electrodes. However, when assessing the long-term sustainability of these electrodes in the harsh medium, several important conclusions were drawn. Initially, the stability of the electrodes was observed to be limited, with Ni foam lasting no more than a minute and NiMoOS less than 10 minutes in the harsh medium. This highlighted the significant challenge of ensuring the sustainability of the electrode material in the harsh environment (0.1 M KOH + 0.5 M salt) without material degradation. To address this, a GO/NF composite was developed by dip-coating Ni foam multiple times in graphene oxide to enhance the mechanical strength of the substrate and form a uniform coating on the Ni surface, followed by air drying. Unlike the bare Ni foam, which degraded within 90 seconds, the GO-coated Ni foam demonstrated improved durability. However, after extended exposure, exfoliation of the graphene sheets began, leading to material degradation over time. The same electrode was then hydrothermally treated to convert the GO coating into reduced graphene oxide (RGO) on the Ni foam. The increase in conductivity was immediately evident from the higher current values, as RGO is known for its significantly higher electrical conductivity compared to GO, which has relatively low conductivity [263]. This RGO-coated Ni foam electrode demonstrated improved stability, withstanding the anodic environment for approximately 400 seconds before the electrode began to leach out. A nearly fourfold increase in durability observed for the RGO/NF electrode compared to bare Ni foam prompted us to extend the

same strategy of providing a solid carbon support to the NiMoOS electrode as well, anticipating a similar enhancement in durability. So, initially, an inner layer of graphene oxide (GO) was coated onto a conductive nickel foam (NF) substrate, forming a GO/NF composite. Subsequently, a uniform outer layer of molybdenum sulfide (MoS_2) was hydrothermally deposited onto the GO/NF surface, resulting in the final electrocatalyst, GNiMoOS, a robust and high-performance anodic electrode material. Surprisingly, the GNiMoOS electrode demonstrated a remarkable durability and activity during the OER in a harsh simulated seawater environment. The enhanced conductivity, coupled with newly imparted resistance to corrosive chloride ions, enabled the electrode to withstand chlorine-rich conditions for up to three hours of testing, significantly outperforming its counterparts, which degraded within minutes as seen in **Figure 3.2b**. The current densities and corresponding survival times of all the electrodes under anodic polarization is shown in **Figure 3.2c**. Notably, GNiS and GNiMoOS both exhibit highest OER current densities and enhanced durability in a harsh seawater media. Furthermore, UV-visible spectroscopic analysis showed the presence a of a sharp peak at 650 nm which revealed the presence of hypochlorite ions OCl^-(a byproduct of chloride ion oxidation) post electrolysis in the electrolytes used with the less stable electrodes like RGO/NF, NiS and NiMoOS (**Figure 3.2d**).The degradation of all electrodes, except GNiS and GNiMoOS, due to chlorine corrosion is clearly evident in **Figure 3.2e-j**. The figures attached adjacent to each of the **Figures 3.2e-j** shows the presence of hypochlorite ions in the electrolyte solutions post electrolysis, as detected using a dye detection method. The whole mechanism of thorough identification of OCl^- ions is depicted in **Figure 3.2k-l**. With the electrolyte solution of the respective electrodes after OER reaction, 10µm of the electrolyte solution post electrolysis

was taken out and mixed with a dye solution made with 3,3',5,5'-Tetramethylbenzidine (TMB) dye and a buffer solution to check for its colour in presence of oxidized species OCl^-, if formed [176,264]. A change in the colour of the electrolyte from colourless (TMB) to blue (Oxy-TMB; 3,3',5,5'-tetramethylbenzidine diamine) indicated the presence of these harsh ions, which oxidize the TMB dye, resulting in the blue colour. As expected, the electrolyte bearing GNiS and GNiMoOS electrode remained colourless after dye addition whereas the electrolytes bearing the other electrocatalysts immediately turned blue. This indicates that chlorine oxidation reactions were negligible with the GNiS and GNiMoOS electrodes. These OCl^- species were also identified with the help of UV-Visible analysis (**Figure 3.2l**), where the presence of a sharp peak at 650 nm corresponds to oxy TMB formed by the oxidation of TMB by oxidizing OCl^- ions. The green-colored leached product from the electrodes during anodic polarizations is supposed to be a corrosion product as a result of the undesired reaction of Cl^- ions with Ni metal resulting in the formation of $NiCl_2$ as confirmed by the XPS analysis (**Figure 3.2m**) where the Ni 2p spectrum contains two main peaks, which are attributed to $2p_{3/2}$ and $2p_{1/2}$ centered at 853.8 eV and 871.9 eV respectively which is in good agreement with the Ni^{2+} oxidation state [265]. Notably, the GNiS and GNiMoOS catalyst exhibited exceptional stability, showing no signs of leaching even under prolonged anodic polarization in harsh electrolytic conditions. Furthermore, this solid electrode effectively suppressed the formation of chlorine and hypochlorite ions as no such formation was detected post electrolysis in the electrolytes using dye detection and UV-visible analysis. These observations suggest that chloride ions were somehow unable to penetrate the Ni foam surface to initiate corrosion and oxidation processes [266]. This again highlighted the fact

that Sulfur along with RGO has imparted some anticorrosive and resistant features to these electrodes that were accountable for their remarkable stabilities. The functionalization of the reduced graphene oxides embedded with sulfonated moieties (which are validated in the subsequent sections) benefitted the system with superior specificity for OER over CER reactions.

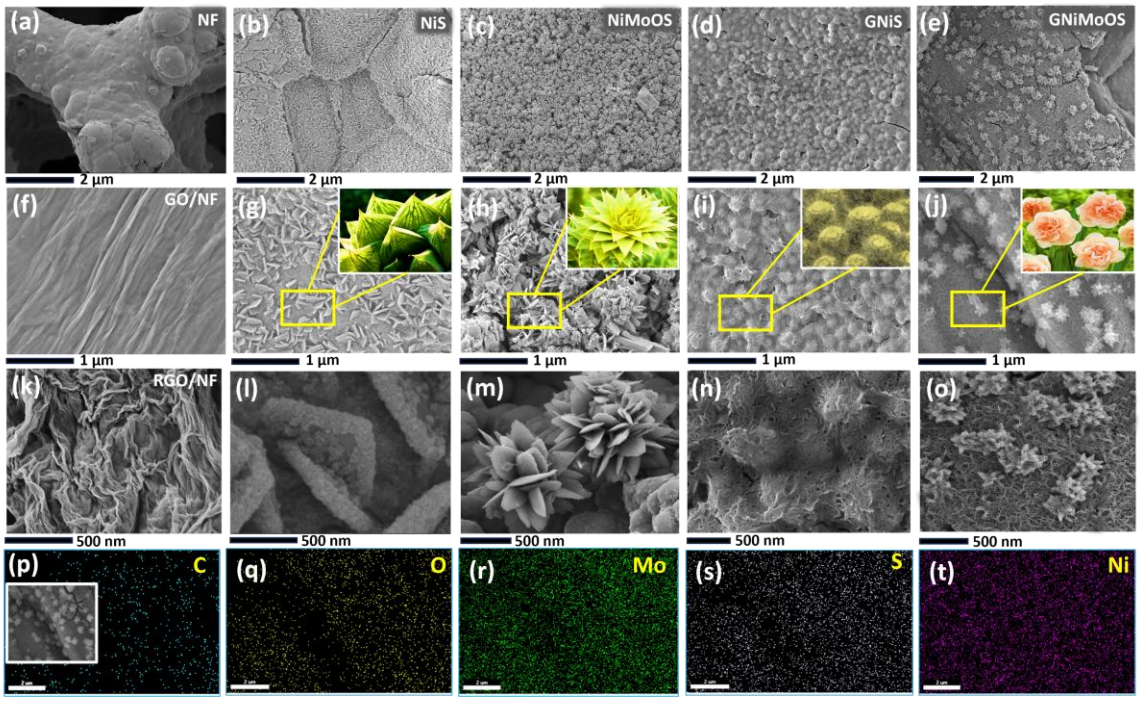

Figure 3.3 SEM images of (a) bare Ni foam (b) GO/NF (c) RGO/NF (d-f) NiS (g-i) NiMoOS (j-l) GNi, (m-o) GNiMoOS electrodes respectively (p-t) the corresponding elemental mapping of the GNiMoOS electrode.

The morphology and microstructure of the prepared electrodes i.e. RGO coated Ni foam, NiMoOS, GNiMoOS, GNiS, NiS along with of Bare Ni foam were characterized with scanning electron microscope (SEM). The SEM images of Ni foam before hydrothermal growth (**Figure 3.3a**) show a smooth metallic surface with minimal micro- or nano-scale roughness. Upon GO coating, large, flat sheets with few wrinkles are observed (**Figure**

3.3b) When GO is converted to RGO (**Figure 3.3c**), the surface exhibits a typical crumpled and rippled sheet-like morphology, with clearly visible twisted graphene sheets. SEM images of the thiourea-treated Ni foam surface (NiS) reveal the growth of inverted wedge-shaped flakes, pointed at the center and firmly adhered to the base material. These flakes appear uniformly across the entire surface and cross-sectional area, indicating homogeneous NiS wedge formation throughout (**Figure 3.3d-f**) [267]. However, despite this well-distributed flaky structure, it contributes little to long-term stability, as the electrode shows poor durability under applied oxidation potentials. X-ray diffraction (XRD) profiles of the NiS taken using longer scan times and narrow step sizes (**Figure A1**,**Appendix information**) exhibits peaks at 22.45°, 38.26°, 50.0° and 55.6°, which are indexed to the (101), (003), (211) and (122) planes of hexagonal Ni_3S_2 (JCPDS no:44-1418), respectively [267].The other two strong peaks at 45.° and 52.0° and peak at 76.0° are assigned to cubic Ni of Ni foam (JCPDS no:04-0850) [268].Upon in situ deposition of Mo along with S precursors over the Ni foam surface solvothermally, characteristic flower like features of MoS_2 were visible and these flowers were clinged to the surface of base foam as seen in **Figure 3.3g-i**. But the flower pattern was not uniform everywhere and observed only at fewer locations leaving the bare foam surface exposed to the harsh electrolyte during oxidation resulting in structure collapse during harsh simulated seawater electrolysis with time. So, with inclusion of Mo and S, enhanced OER activity compared to bare Ni foam material could be observed but stability of the developed electrode with time was still a challenge. The SEM images of GNiS shown in **Figure 3.3j-l**, shows that the NiS nanoparticles are not able to grow and come up on the surface because of the RGO coating which is acting as a barrier and preventing the direct exposure of Ni with sulfur

component which can be a probable reason for the enhanced mechanical strength of GNiS compared to NiS.This observation is further supported by the XRD spectrum of GNiS (**Figure A11**, **Appendix information**), where the absence of any characteristic NiS peaks indicates negligible formation of the NiS phase. **Figure 3.3m–o** presents the SEM images of our active catalyst, GNiMoOS, showing folded, flower-like nanostructures composed of petal-like MoS_2 lamellae densely clustered together.

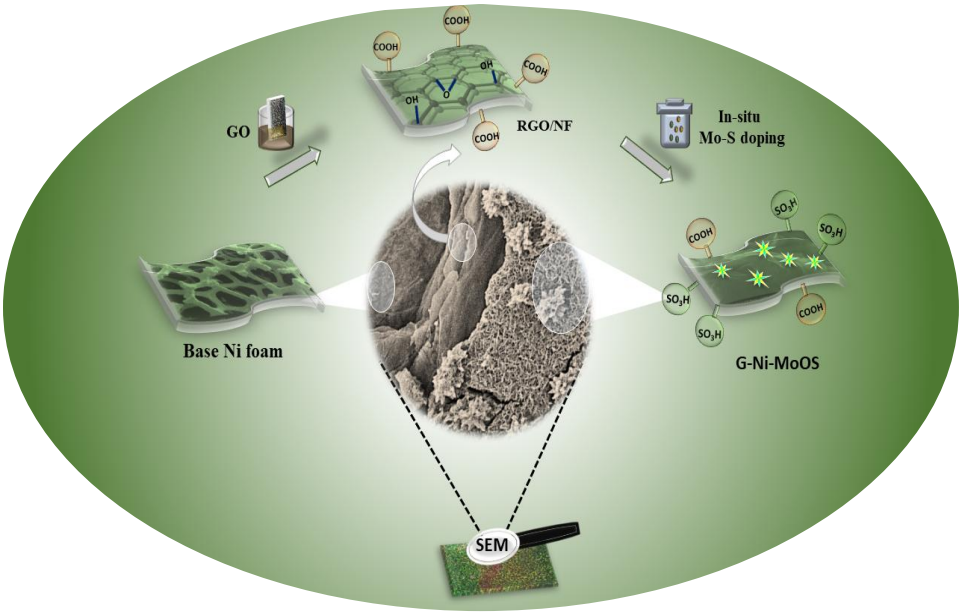

Figure 3.4 Cross-sectional SEM image of GNiMoOS electrocatalyst

These structures closely resemble marigold-like formations, with an average diameter of approximately 200-300 nm, anchored onto the underlying graphene sheet [268]. The Raman spectrum of GNiMoOS also confirmed the presence of MoS_2(discussed later in details). The elemental mappings of C, N, Mo and S elements taken by Energy-Dispersive X-ray Spectroscopy **(**EDX**)** reveal that Mo, S, C and O elements were distributed uniformly throughout the whole GNiMoOS structure (**Figure 3.3p-t**). The absence of inverted wedge-

shaped NiS patterns confirms that only MoS_2 structures are present in GNiMoOS, with no indication of NiS formation.

Figure 3.4 highlights the cross-sectional SEM image of active electrocatalyst GNiMoOS electrode in the center which is validating the double layer characteristics of our active electrode. The porous foam surface is loaded with sulfonated graphene sheets above which the MoS_2 nanoflower like structure are adhered following the hydrothermal deposition of active components thereafter (nanoparticles catalyst over to GO coated foam).

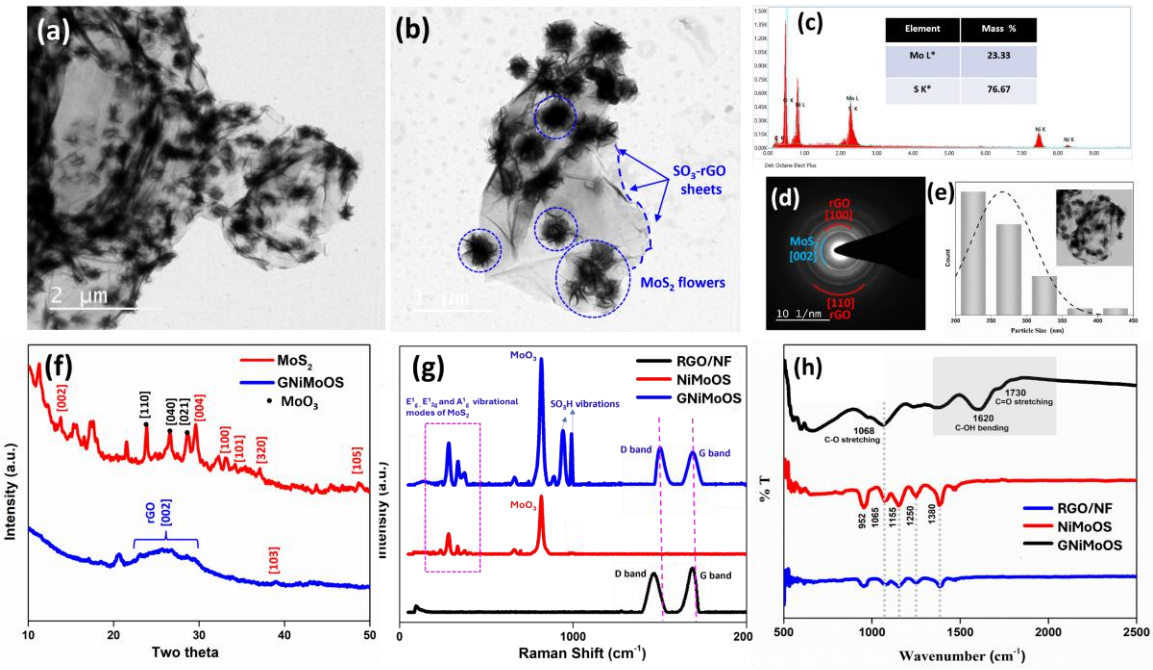

Figure 3.5 (a, b)TEM images of the GNiMoOS electrode (c) EDAX spectrum (d) SAED pattern, and (e) particle size distribution of GNiMoOS (f) XRD pattern of MoS_2 and GNiMoOS (g) Raman spectra of RGO/NF , NiMoOS and GNiMoOS electrodes (h) FT-IR spectra of GNiMoOS, RGO/NF, and GNiS {Note: MoS_2 powder was synthesized in-lab}.

The TEM image of GNiMoOS is shown in **Figure 3.5a, b** where, many MoS_2 nanoflowers with diameter in 250-300 nm range were homogeneously incorporated over the RGO sheets suggesting that the MoS_2 nanospheres tended to nucleate and grow over the RGO

sheets. The EDX and element mappings reveal that the nanocomposite contains C, O, Mo, and S as the main components and confirms the uniform distribution of each element (**Figure 3.5c**). The atomic percentages of Mo and S atoms are 23.33 and 76.6 % respectively confirming the formations of MoS_2. Selected area diffraction pattern (SAED) of GNiMoOS displayed diffraction rings of MoS_2 and RGO corresponding to 002 [MoS_2], 100 (rGO) and 110 (rGO) planes (**Figure 3.5d**). The d-spacing value of MoS_2 nanosheets was calculated to be 0.26 nm, which was ascribed to the (100) plane of MoS_2. The d-spacing values for the other two 100 (rGO) and 110 (rGO) planes were 0.208 and 0.122 nm respectively. **Figure 3.5e** shows the particle size distribution of the GNiMoOS where the maximum number of MoS_2 flowers are within the diameter range 250-350 nm, homogeneously adhered over the RGO sheets as verified by SEM earlier. To further garner the structural information of the samples, X-ray diffraction (XRD) and Raman analysis were carried out (**Figure 3.5f, g**). MoS_2 powder synthesized hydrothermally under same mimicking condition to GNiMoOS was taken as reference to see the changes incorporated in the active catalyst GNiMoOS. As shown in **Figure 3.5f**, no sharp peaks were observed for the free MoS_2, indicative of the poorly crystallized MoS_2 powder synthesized by the solvothermal method. All the XRD diffraction peaks were matched to the JCPDS Card No. 65-1951, which confirmed the formation of the pure hexagonal crystal phase of the MoS_2 nanosheets [269]. Diffraction peaks detected at $2\theta \sim 13.8°$, 32.8°, 39.5°, and 58.3° can be assigned to (002), (100), (103), and (110) atomic planes of MoS_2 nanosheets, respectively [270,271]. Other peaks at $2\theta = 29°$, 39.6° and 49.8° corresponding to the planes (004), (103) and (105) of bulk MoS_2 faces were detected, respectively (JCPDF 37-1492) [272]. The other peaks at $2\theta = 23.3°$, 25.7° and 27.3° can be attributed to the (110), (040) and

(021) crystal planes of molybdenum trioxide (MoO_3) due to the oxidation Mo atoms [273,274]. The XRD pattern of RGO/NF, NiS, NiMoOS, GNiS and GNiMoOS electrodes are shown in **Figure A12** of **Appendix information**. It was very difficult to get any clue about the material phase in any of the electrodes from XRD as Nickel foam is a highly crystalline material with strong, sharp diffraction peaks and hence these Ni peaks typically at 44.5°, 51.8°, and 76.4° 2θ, corresponding to (111), (200), and (220) Ni planes dominate the XRD patterns. Also, the NiS or the MoS_2 might have formed amorphous phases during hydrothermal synthesis and amorphous materials yield broad humps or weaker peaks, so they do not appear distinctly in XRD.So, the GNiMoOS layer was scraped off from the GNiMoOS electrode and grind it into fine powder. The XRD results with this powder (**Figure 3.5f**) showed the appearance of a broad peak centered at around 26.5° which was associated with a graphitic crystal structure, implying that the GO was efficiently deoxidized (reduced) during the hydrothermal process [275].The decreased intensity of the diffraction peaks of MoS_2 in the composite indicates that the incorporation of graphene considerably restrains the aggregation of layered MoS_2 during the solvothermal process, which leads to the growth of few-layered MoS_2 nanosheets of poor crystallinity [276]. Recently, it has been demonstrated that amorphous MoS_2 exhibits higher HER activity than crystalline MoS_2 as the amorphous structure affords a higher number of exposed edges [277]. The Raman spectrum of RGO/NF, NiMoOS and GNiMoOS samples in the frequency range of 100-1800 cm^{-1} is presented it in Figure 5G.Generally in carbon based samples like graphene, the peak at about 1580 cm^{-1} (G band), assigned to an E_{2g} mode of graphite, is related to the vibration of the sp^2 bonded carbon atoms in a two-dimensional hexagonal lattice, while the peak at about 1350 cm^{-1} (D band) is easily influenced by the

lattice distortion (defects) in the hexagonal graphitic layers or atomic substitution (doping) [278]. More functional groups or defect sites can increase D band intensity and shifts the bands slightly, depending on local bonding environments. As seen in Figure 5G, The D and the G bands in GNiMoOS have shifted significantly towards higher wavenumbers indicating oxidation or functionalization in the graphene moieties. Also, the doping with sulfur moieties have increased the D band intensity in comparison to the G band in GNiMoOS which is consistent with our proposed conclusion that sulfonic moieties are embedded into the graphene matrix. The characteristic peaks of MoS_2, specifically the E_1g and $E^1{}_2g$ (in-plane) and A_1g (out-of-plane) modes, around 289 cm^{-1},385 cm^{-1} and 405cm^{-1}, respectively are clearly identified in both the NiMoOS and GNiMoOS electrode [279]. Besides, two new peaks resulting from sulfur oxidation is observed around 900 -950 cm^{-1} range which is due to the SO symmetric stretching vibration suggesting prominent presence of the oxidized sulfur moieties in the catalyst which could be possibly due to the sulfonation of graphene sheets [280]. The lack of other ionizable groups on the surfaces of graphene nanosheets was confirmed by the IR analysis (**Figure 3.5h**) wherein, all the labile groups i.e. the OH and the carbonyl groups were found to be absent at 1620 cm^{-1} and 1730 cm^{-1} in GNiMoOS and the presence of sulfonic groups and oxidized sulfur moieties was seen in abundance as S=O stretching vibrations at 1188 cm^{-1}, 1107 cm^{-1} and 1051 cm^{-1} were recorded [281].These results clearly give solid evidence of the formation of sulfonate graphene as abundant sulfonic groups were detected. For further information regarding the elements present and its chemical composition, XPS measurement was performed. **Figure 3.6a-c** displays the XPS spectra of the GNiMoOS electrode. In **Figure A13** of **Appendix information**, the full spectrum shows C 1s peak at 284 eV, a strong O 1s peak at 532 eV,

an N 1s peak at 402 eV, S 2p peak at 168.7 and the peak for Mo at 233.8 and 235.6 eV, confirming the presence of MoS_2 and SO_3H group over graphene coated Ni foam.

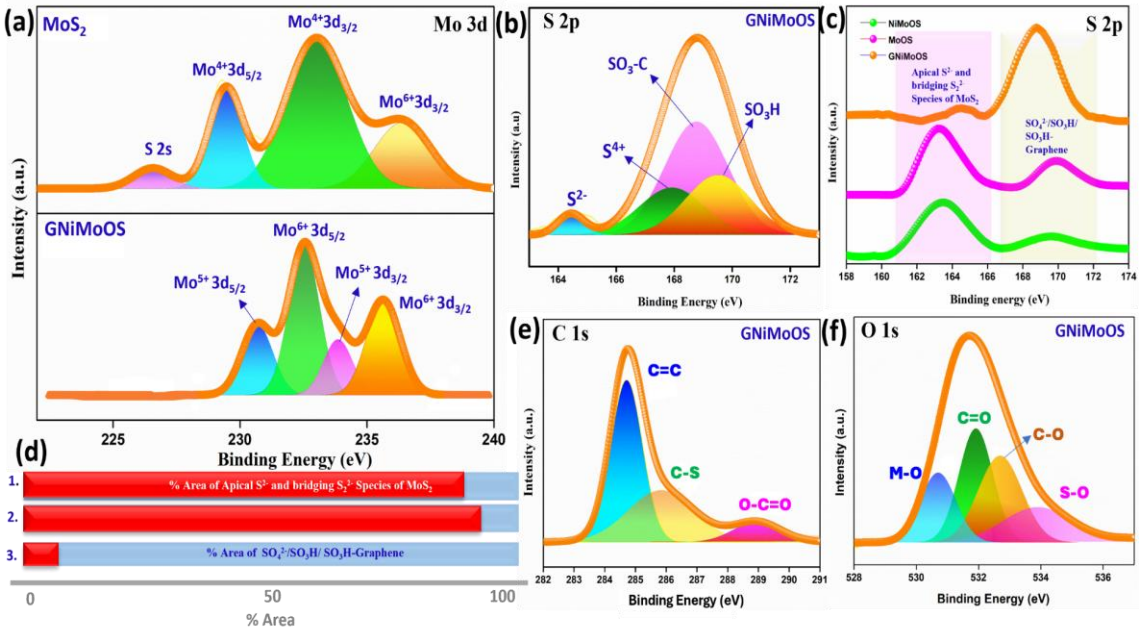

Figure 3.6 (a) Deconvoluted Mo 3d XPS spectra of GNiMoOS, NiMoOS, and MoOS electrodes (b) Deconvoluted S 2p XPS spectrum of the GNiMoOS electrode (c) Overlay of S 2p XPS spectra for GNiMoOS, NiMoOS, and MoS_2 precursor powder for comparison (d) Bar graph showing the percentage area of peaks A and B, corresponding to different sulfur species in MoS_2 (1), NiMoOS (2), and GNiMoOS (3) (e) Deconvoluted C 1s XPS spectrum of GNiMoOS (f) Deconvoluted O 1s XPS spectrum of GNiMoOS.

In **Figure 3.6a**, the deconvolution of the Mo 3d spectrum of GNiMoOS and the bare MoS_2 compounds in powderous state (excluding graphene oxide) are compared. In the Mo 3d spectrum of MoS_2 powder (similar to the Mo 3d spectrum of NiMoOS), two peaks located at the binding energy (BE) values of 229.5 and 232.3 eV can be assigned to the Mo $3d_{5/2}$ and Mo $3d_{3/2}$ core levels, respectively; while the peak at 226.5 eV is associated with the S 2s core level ,which confirms the Mo^{4+} and S^{2-} charge states due to Mo-S charge transfer [282]. Another peak located at 235.4 eV is also ascribed to the Mo $3d_{3/2}$, indicative of an oxidation state of 6^{+}. These peaks were attributed to molybdenum trioxide (MoO_3) due to

the oxidation of low-oxidation-state Mo atoms [274]. GNiMoOS displayed two broad peaks representing two set of doublets one being ascribed to Mo VI (235.6 and 232.2 eV corresponding to $3d_{3/2}$ and $3d_{5/2}$ of Mo VI), the other to Mo V (233.8 and 230.6 eV corresponding to $3d_{3/2}$ and $3d_{5/2}$ of Mo V) [283]. It is worth noting that the deconvolution of the Mo 3d spectrum (**Figure 3.6a**) for NiMoOS and GNiMoOS correlates well with the SEM observations. The shift in the oxidation state of molybdenum from Mo^{4+} to higher states (Mo^{5+} and Mo^{6+}) in the MoS_2-based structures likely contributes to the morphological transformation from lotus-like flower patterns composed of assembled MoS_2 petals in NiMoOS, to marigold-like MoS_2 nanostructures anchored over graphene sheets in GNiMoOS. Besides, the coexisting oxidation states of Mo (V) and (VI) indicates that the oxidation state of Mo is affected by the presence of sulfonic acid moieties which is the key component in enhancing the absorption of OH^- anions over chloride ions leading to a faster OER kinetics and this has been proven by DFT studies (shown in the later sections). However, the peak of Mo (V) might also result from the oxidation of the catalyst in air to form MoO_3 or MoO_4^{2-} which is inevitable to happen with these kind of species [284]. **Figure 3.6b** shows the deconvoluted S(2p) XPS spectrum of GNiMoOS where the peak at 169.63 eV corresponds to S^{6+} and S^{4+} species in oxides form i.e. SO_3^{2-} and SO_4^{2-} and these groups could locate at edges of graphene layers [285,286]. The peaks at 169.84 eV (S $2p_{1/2}$) and 168.85 eV(S $2p_{3/2}$) typically correspond to sulfonic acid groups [287]. It might be attributed to the consumption of sulfur for formation of sulfonated graphene over the graphene substrate. So, the abundant species that could be thought of responsible in imparting commendable strength to the GNiMoOS electrode is sulfonated graphene which is the major species present in the electrode of interest alongside the MoS_2 flowers which

are embedded uniformly over its surface. The successful doping of Sulfonic groups into carbon skeleton of the GNiMoOS electrode compared to the other electrode materials is clearly depicted in **Figure 3.6c**, where it is seen that the peak responsible for the apical S^{2-} and bridging S_2^{2-} sulfide groups is negligible in comparison to the prominent peak representing the oxidized sulfur moieties around 168 eV in the S 2p XPS spectrum of GNiMoOS. However, in the base precursor MoS_2 and the NiMoOS electrode, the peaks at 162-164 eV denoting S^{2-} groups were intense and majorly present in comparison to the less abundant sulfonic peaks. The ratio of the peak corresponding to the oxidized sulfonic acid species were estimated from the respective integrated peak area of XPS spectra (**Figure 3.6d**) and it was found that 93 percent of the total area corresponds to the abundant sulfonic acid groups present on the catalyst surfaces (**Table A7**, **Appendix information**). The deconvolution of C 1s and O 1s XPS spectrum of GNiMoOS gives additional support to the proposed sulfonic group abundance (**Figure 3.6e, f)**. The main peak of C 1s at 284.7 eV is related to the graphitic carbon (C=C linkage). The peaks at 285.6 and 288.6 eV were assigned to the C-S linkage and O-C=O moiety, respectively [288-289]. Besides, the O1s core level of GNiMoOS could be deconvoluted into two curves at 532.5 (O-C) and 533.9 eV (O–S) confirming the sulfur-oxygen bonds [289]. The in-situ hydrothermal deposition results in the incorporation of sulfonated functional groups over graphene imparting the much-needed anti repelling properties. The MoS_2 nanoparticles are dispersed on the RGO due to the large surface of graphene oxide and this structure not only provides sufficient void space between the neighboring MoS_2 nanosheets but also more catalytic edge sites on the RGO. Meantime, the electrical coupling between MoS_2 and RGO can make easier the electrons transfer to RGO. Overall, the novel aspects are the formation of a layer of Mo-S

catalyst formed over graphene supported Nickel foam, with abundant sulfonic functionalized graphene which is altogether responsible for the high HER/OER activity and repulsiveness to chloride anions in seawater.

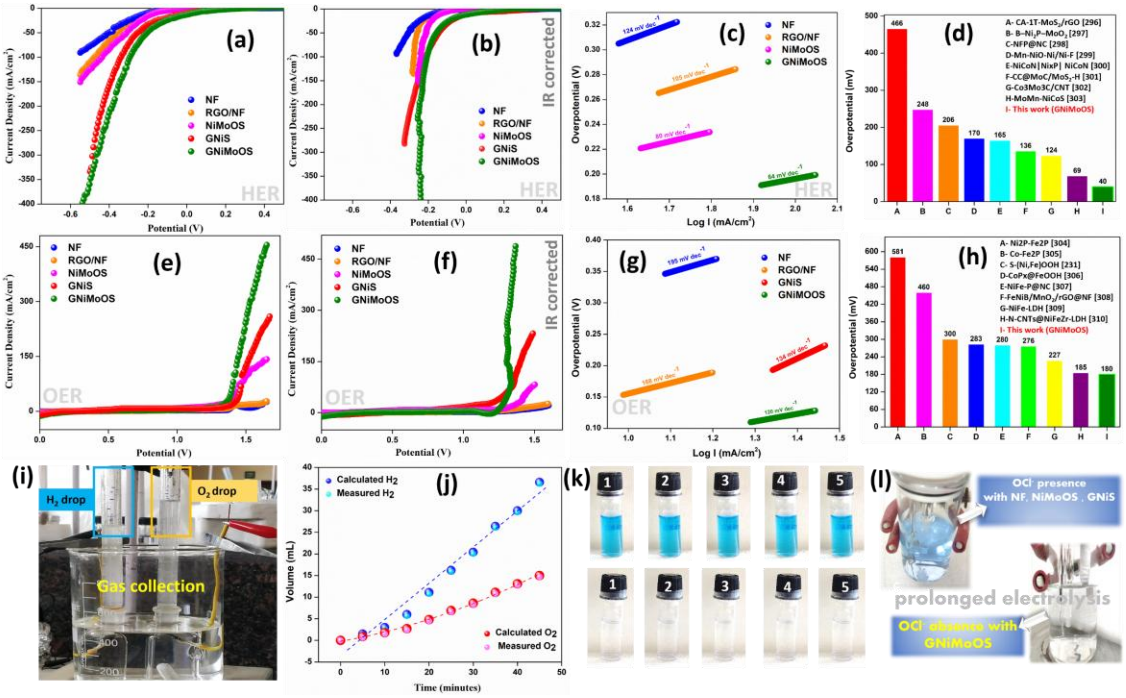

Figure 3.7 (a-b) LSV spectra of electrodes showing HER activity before and after IR correction respectively in harsh KOH (0.1 M) + NaCl (0.5 M) media from 0 to -0.5 V vs. RHE (c) corresponding Tafel plots for HER (d) Electrocatalyst comparison data for HER @ 10 mA cm^{-2} current density (e-f) LSV spectra of electrodes showing OER activity before and after IR correction respectively in harsh media from 0 to 1.7 V vs. RHE (g) corresponding Tafel plots for OER (h) Electrocatalyst comparison data for OER @ 100 mA cm^{-2} current density (i) gas collection setup for calculating faradic efficiency (j) volume of H_2 and O_2 produced by GNiMoOS electrode during water splitting (k) images showing OER selectivity of the electrodes over CER at frequent time intervals (l) images showing OER selectivity of the electrodes over CER during prolonged electrolysis at the fixed potential 0.7 V in the medium of KOH (0.1 M) + NaCl (0.5 M) at Room temperature.

In **Figure 3.7a, b**, the polarization curves before and after iR correction for HER in 0.1 M KOH + 0.5 M NaCl media are compared. From the LSV data in Figure 3.7a, the overpotentials required to reach a current density of 100 mA cm^{-2} follow the trend:

GNiMoOS (256 mV) < GNiS (340 mV) < NiMoOS (436 mV) < RGO/NF (472 mV) < NF (550 mV). After iR correction (**Figure 3.7b and E2, Appendix information**), GNiMoOS demonstrates the best HER performance, requiring only 201 mV to achieve 100 mA cm^{-2} , significantly outperforming GNiS (210 mV), NiMoOS (236 mV), RGO/NF (276 mV), and bare NF electrodes (371 mV).The LSV results demonstrated that GNiMoOS hybrid exhibited the best electrocatalytic activity for HER among all the other electrodes compared. The comparisons of the overpotentials before and after iR correction at 100 mA cm^{-2} current density is shown in **Figure A14** of **Appendix information**. Notably, the overpotentials required to deliver the current densities of 200, 300, 400 and 500 mA cm^{-2} were 238, 241, 245 and 252 mV respectively for GNiMoOS in harsh alkaline media after iR corrections (**Figure A15, Appendix information**). To have a better understanding of the HER mechanism of these samples, Tafel plots were analyzed. It is well known that the HER process could be divided into three possible reactions, namely Tafel reaction (30 mV dec^{-1}), Heyrovsky reaction (40 mV dec^{-1}), and Volmer reaction (120 mV dec^{-1}). According to the kinetic model, an inherent index Tafel slope of 120, 40 or 30 mV dec^{-1} signifies the Volmer, Heyrovsky or Tafel reaction as the rate-determining step, respectively [290]. To investigate the rate-determining step of GNiMoOS electrode, the Tafel plots were derived from the LSV curve by fitting the linear regions according to the Tafel equation (**eq 3.1**):

$$\mathrm{Y} = a + b\log j \qquad (3.1)$$

where γ, b, and j denote overpotential, Tafel slope, and current density, respectively. As shown in **Figure 3.7c**, the Tafel slope value for GNiMoOS was 64 mV dec^{-1}, whereas the Tafel slope of the NF, RGO/NF and NiMoOS catalysts were 124, 105 and 80 mV dec^{-1}, respectively. The GNiMoOS catalyst exhibited a lower Tafel slope when compared to the

other prepared catalysts, due to the strong electronic and chemical interaction between the anionic doped RGO and MoS_2 which provides more catalytic edge sites, hence speeding up the rate. The Tafel slope of GNiMoOS catalyst falls within the range of 40 - 120 mV dec^{-1}, which indicate that the electrochemical HER reaction proceeds through the Volmer-Heyrovsky mechanism. The CV with different scan rate (20 mV sec^{-1} to 100 mV sec^{-1}) at non-faradic current region was conducted to estimate electrochemically active surface areas (ECSA) for GNiMoOS (**E3, Appendix information**). ECSA of GNiMoOS was calculated to be 55.55 cm^2 (**Figure A16, Appendix information**). **Figure 3.7d** shows the comparison of the HER overpotential values at 10 mA cm^{-2} current density of some recently reported electrocatalysts with GNiMoOS and GNiMoOS requires much lower overpotential to reach the current density (10 mA cm^{-2}) than any of the recently reported HER electrocatalysts for simulated seawater/real seawater systems and is among the most efficient electrocatalysts reported for overall seawater splitting.

OER is known to be bottleneck of overall water splitting owing to large overpotential for driving the half reaction. As shown in **Figure 3.7e**, GNiMoOS exhibited the lowest overpotentials of 90 and 180 mV at the current density of 10 and 100 mA cm^{-2} during OER in simulated seawater media. For instance, the overpotentials of NF, RGO/NF, NiMoOS and GNiS at 10 mA cm^{-2} current density were 450, 330, 200 and 150 mV respectively and the overpotentials of NiS, NiMoOS and GNiS at 100 mA cm^{-2} current density were 550, 290 and 250 mV respectively, which are very high compared to that of GNiMoOS, indicating its high electrocatalytic activity toward OER. In **Figures 3.7e and 3.7f**, the polarization curves before and after iR correction for OER were compared. The overpotentials required to deliver a current density of 100 mA cm^{-2} for OER decreases by

110 mV upon iR correction in the active GNiMoOS electrocatalyst. Tafel slope was also used to evaluate the OER activity for these as-prepared samples. The sample with higher OER activity usually presents a lower Tafel slope. As shown in **Figure 3.7g**, the Tafel slope of GNiMoOS for OER is 120 mV dec^{-1}, lower than that of NF (198 mV $dec^{-1)}$, RGO/NF (165 mV dec^{-1}) and GNiS (134 mV dec^{-1}). Compared to the other recently reported OER electrocatalysts for seawater splitting, GNiMoOS stands out, requiring the lowest overpotential to reach the benchmark current density (100 mA cm^{-2}) in simulated/real seawater systems (**Figure 3.7h**).For the calculation of Faradic efficiency, evolved gas was collected through a manual setup as shown in **Figure 3.7i** and measurement of the evolved gases was performed, considering water displacement method. The measured volume ratio of H_2 to O_2 was found close to the theoretical value of 2:1 (**Figure 3.7j**) with the Faradaic efficiency of nearly 94 % and 87.6%, for HER and OER respectively, indicating the good selectivity of GNiMoOS for HER and OER in simulated seawater medium. The faradic efficiency of HER and OER with time is shown in **Figure A17** of **Appendix information**. The selectivity of GNiMoOS towards OER was further monitored hourly by checking the presence of hypochlorite ions formed gradually in the medium during applied anodic potentials. Images after dye test for OCl^- ions every hour are kept in **Figure 3.7k**. Whereas all the other electrodes kept showing hypochlorite presence up to a testing time of 6 hours, GNiMoOS proved to be highly selective for OER compared to CER which can be seen from the images taken post electrolysis. The solution remained colorless from start till the testing hours indicating the sole occurrence of hydroxide ion to oxygen gas transformation with our active catalyst. To further confirm this selectivity, experiments were conducted in a two-compartment electrochemical cell, separating the anodic and cathodic electrolytes.

After prolonged electrolysis lasting several days, the TMB dye test showed that the anodic electrolyte containing the GNiMoOS electrode remained colorless, with no detectable OCl^- (**Figure 3.7l**). This strongly confirms the superior selectivity of GNiMoOS toward OER, even under harsh conditions in 0.1 M KOH + 0.5 M NaCl.

The long-term stability of the GNiMoOS catalyst for the hydrogen evolution reaction was assessed using chronoamperometry (i-t) at a constant potential of 0.354 V for 400 hours in pure alkaline media, as shown in **Figure 3.8a**. The catalyst demonstrated exceptional durability, maintaining a nearly constant current density of 330 mA cm^{-2} with negligible decay in HER activity over the entire testing period. Comparable stability was also observed in simulated seawater and real seawater, where current densities of 350 mA cm^{-2} and 360 mA cm^{-2}, respectively, were recorded (**Figure 3.8a**). Even after 400 hours of continuous operation, negligible decay in current density was observed, highlighting the excellent long-term durability of the GNiMoOS catalyst. Post-stability analysis revealed no significant morphological changes; the MoS_2 flower-like structures remained firmly anchored onto the RGO sheets, and the elemental distribution remained uniform, as evidenced by the SEM images in **Figure A18** of **Appendix information**. These findings confirm the exceptional structural and electrochemical stability of the synthesized GNiMoOS hybrid catalyst under prolonged HER conditions. The HER alkaline stability of the GNiMoOS electrocatalyst was also investigated at current densities of 10, 20, 40, 60, 80, and 100 mA cm^{-2} using a multistep chronopotentiometry method (**Figure 3.8b**). The potential remains steady at each applied current density, but it instantly changes by altering the current density from one value to the another. The symmetry of potential changes during both the increase and decrease of current density further confirms the robust

electrochemical stability and sustained HER performance of the GNiMoOS catalyst under dynamic operating conditions.

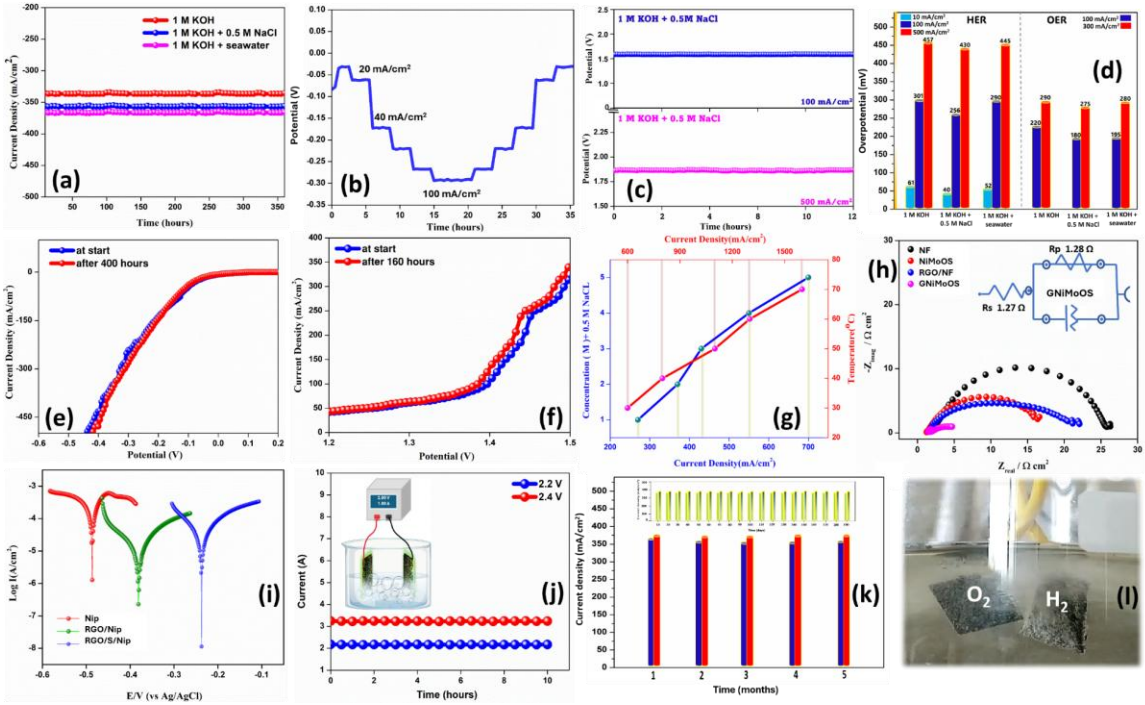

Figure 3.8 (a) chronoamperometry spectra of GNiMoOS during HER at a fixed potential of 0.354 V for 400 h in 1 M KOH, 1 M KOH + 0.5 M NaCl (simulated seawater), and 1 M KOH + seawater, while (b) presents the multistep chronopotentiometry analysis for HER at different current densities (10-100 mA cm⁻²) (c) displays the chronopotentiometry spectra during overall water splitting at fixed current densities of 100 and 500 mA cm⁻² in simulated seawater (d) compares the overpotentials of GNiMoOS in alkaline, simulated seawater, and real seawater media for HER (10, 100, 500 mA cm⁻²) and OER (100, 300 mA cm⁻²) (e) The cathodic polarization curves (LSV) before and after 400 h HER operation (f) the anodic polarization curves before and after 160 h OER operation, both in simulated seawater (g) effect of electrolyte concentration and temperature on current density , using a DC source under 2 M KOH + 0.5 M NaCl in the range of 24-70 (h) Nyquist plots of NF, NiMoOS, RGO/NF, and GNiMoOS electrodes in simulated seawater)(i) shows the Tafel plots of Ni, RGO/Ni, and RGO/S/Ni electrodes in 2 M KOH + 0.5 M NaCl for corrosion resistance analysis (j) The bifunctional activity of a two-electrode GNiMoOS setup for overall water splitting in 2 M KOH + 0.5 M NaCl at 2.2 V and 2.4 V (k) long-term stability of GNiMoOS for HER and OER over ~6 months with measurements at 10-day intervals (l) provides an optical image demonstrating vigorous H_2 and O_2 evolution from the GNiMoOS electrodes during overall water splitting.

Furthermore, the stability of the GNiMoOS catalyst as a bifunctional electrocatalyst was investigated by chronopotentiometry (η-t) measurement at a constant current density of 100 mA cm^{-2} and 500 mA cm^{-2} in simulated seawater media for 12 hours by keeping the same active catalyst as cathode and anode in a two-electrode setup. **Figure 3.8c** showed that the catalyst maintained a constant potential of 1.58 V and 1.8 V at current densities of 100 mA cm^{-2} and 500 mA cm^{-2} for 12 hours respectively, signifying superior stability and excellent bifunctional activity with a slight potential increment of 10 mV. The overpotentials exhibited by GNiMoOS at a current density of 10, 100 and 500 mA cm^{-2} for HER and 100, 300 mA cm^{-2} for OER in alkaline (1 M KOH), simulated seawater (1 M KOH + 0.5 M NaCl) and real seawater (1 M KOH + seawater media) respectively, are collectively summarized in **Figure 3.8d**. After the chronopotentiometry measurement, the polarization curve before and after a time period of 400 hours and 160 hours for both HER and OER in simulated seawater showed a small ignorable shift from the initial one (**Figure 3.8e-f**). These results confirm that the long-term electrochemical stability of the GNiMoOS catalyst during the electrochemical process in the harsh alkaline electrolyte. The effect of the amount of sulfur source as precursor (thiourea) with molybdic acid in the synthesis of GNiMoOS, on the electrocatalytic performance was also investigated. Their corresponding HER electrocatalytic results are presented in **Figure A19** of **Appendix information**. When the molar ratio of Mo to S is 1:2, the GNiMoOS sample has the best HER performance. This can be seen in the **inset image A19**, where no residue precursors are left in the medium after hydrothermal rection. This is unlike the results obtained with 1:1 ratio where excess precursors are left in the solvent medium (**inset image A9**) or 1:3/1:4 ratio where precursor quantity is not optimal for giving a current density better than Ni foam itself. Thus, the

ratio of Mo to S (1:2) exhibits the highest HER and OER activity. The electrode's activity varying the concentration of the electrolyte and the reaction temperature to see the rise in the current value besides the durability of the electrode material when exposed to high concentration of OH^- ions and high temperature is combinedly plotted in **Figure 3.8g**. The conductivity of the electrolyte becomes greater with increased concentration of electrolyte, leading to enhanced current efficiency and, consequently, a higher electrolysis rate. The sharp rise in current value with a 1x1 cm^2 area of the catalyst at room temperature without undergoing any leaching confirms the high anti corrosive nature of the prepared electrode. Further , on increasing the temperature, conductivity of the electrode increases due to the the drop in resistance of electrolytes,increasing the ionic mobility of the ions [291]. The evolution of hydrogen gas becomes very rapid with increasing temperature of electrolyte as high temperature decreases the potential required to rupture the water molecule increasing the mass flow of hydrogen [292]. Besides, some of the energy is supplied as heat, which is cheaper than electricity. The current value increases from 600 mA cm^{-2} to 1.6 A cm^{-2} on increasing the temperature of the electrolyte from 30 to 70ºC in 5 M KOH respectively as seen in **Figure 3.8g**. Electrochemical impedance spectroscopy (EIS) measurements were performed for four electrodes NF, NiMoOS, RGO/NF, and GNiMoOS in simulated seawater media at open circuit potential (OCP).The representative Nyquist plots obtained from EIS measurements are shown in **Figure 3.8h**. Theoretically, a smaller semicircle diameter at high frequencies corresponds to lower charge transfer resistance R_{ct} ,indicating faster charge transfer and enhanced electrocatalytic kinetics. As shown in **Figure 3.8h**, the Nyquist plot for GNiMoOS displays the smallest semicircle, signifying the lowest R_{ct} amongst all tested electrodes confirming its superior hydrogen desorption

efficiency and rapid electron transport at the active sites. The fitted EIS spectrum for GNiMoOS is provided in **Figure A20** of **Appendix information**. As already mentioned, Seawater electrodes must be highly stable and corrosion-resistant due to Cl^--induced anodic corrosion and reduced electrode lifespan. So far, many investigations of anticorrosion design have focused on the preparation of a protective layer. Although the physical protective layer can prevent the corrosion and improve the stability of the electrode, active sites may be corroded or blocked at the electrochemical reaction due to complex ions in seawater. To avoid this problem, the insertion of a polyanion layer as an electrostatic repulsion layer into the interior of the active material can effectively prevent the adsorption of Cl^- [293]. In our system, we have proposed the presence of abundant sulfonic moieties over the graphene sheets and this anion insertion has imparted anticorrosion properties to our system towards chloride ions. To validate our findings, we carried out corrosion experiments with Bare Ni plate (Nip) modified with GO treated hydrothermally (RGO/Nip) and RGO/Nip treated with thiourea hydrothermally (RGO/S/Nip), to confirm the importance of sulfonic functionalities in minimizing corrosion of the surface in simulated seawater. The Tafel plots of pure Nip, RGO-Nip and RGO/S/Nip in 2 M KOH +0.5 M NaCl are presented in **Figure 3.8i**, from which the corrosion potential (E_{corr}) and corrosion current density (I_{corr}) have been calculated. Generally, higher E_{corr} and lower I_{corr} indicate a better corrosion resistance performance [294]. E_{corr} values of Nip, RGO-Nip and RGO/S/Nip were reported to be -0.486 V, -0.381 V and -0.236 V respectively. The I_{corr} values were 1.52×10^{-6} A cm^{-2}, 2.2×10^{-7} A cm^{-2} and 1.19×10^{-8} A cm^{-2} for Nip, RGO-Nip and RGO/S/Nip, respectively. Although severe corrosion existed in high salinity electrolytes, difference of E_{corr} and I_{corr} were still

observed. E_{corr} became more positive and I_{corr} became smaller in the sulfonic groups-modified reduced graphene oxide nickel plates compared to bare graphene oxide coated plates, indicating a much weaker corrosion tendency of the surface. The above results demonstrated that corrosion was inhibited by the formation of SO_3-C/SO_3H/SO_4^{2-} kind of moieties into the graphene matrix which re-confirmed our suggested findings.

Encouraged by high catalytic activity of GNiMoOS for OER and HER in simulated seawater media, an electrolyzer was assembled by integrating GNiMoOS electrodes as the cathode and anode for overall water splitting in 2.0 M KOH + 0.5 M NaCl media with a DC source operating at 2 to 2.5 V. The assembled electrolyzer with the symmetrical electrodes could drive the current densities of 2.2 A and 3.1 A at a combined overpotential of 2.2 V and 2.4 V respectively (**Figure 3.8j**), which are greater than the state-of-the-art catalyst reported. Further the electrode was tested for its activity at regular intervals of 10 days (**inset of Figure 3.8k**) for a period of nearly 6 months (**Figure 3.8k**) and nearly same current density was obtained for HER and OER in each trial with negligible current decay. The vigorous hydrogen and oxygen evolution activity of the GNiMoOS electrode is shown in **Figure 3.8l**.

3.6 Decoding Functionality and Synergy in GNiMoOS Electrocatalyst

Based on all the above discussions, GNiMoOS emerges as the most active and durable electrode for both simulated and real seawater, delivering industrial-scale current densities with remarkable long-term stability. This outstanding performance is largely attributed to the in-situ formation of abundant sulfonic moieties and MoS_2 nanostructures over the graphene matrix during synthesis. However, in complex multi-component systems

involving various metals and nonmetals, it becomes inherently difficult to attribute the observed functionality to a single moiety with complete certainty. Multiple moieties can either contribute synergistically or serve overlapping roles. In the case of GNiMoOS, which integrates Mo, Ni, S, and GO, potential combinations like Mo-S, Ni-S, or their interactions with GO introduce ambiguity in mechanistic understanding. This raises an important question regarding material attribution and mechanistic clarity in catalyst design for such multi-component systems. To provide a clearer understanding, we have summarized all key findings below to support and validate our proposed rationale.

To clearly isolate and quantify the role of SO_3H-GO (sulfonated GO) ,all the prepared electrodes namely Bare Ni-foam, RGO/NF (to see the role of RGO), NiS (to see the role of S), NiMoOS (to see the individual role of MoS_2 developed in-situ over Ni foam), GNiS (to see the individual role of sulfonated graphene developed in-situ), and GNiMoOS (to see the combined role of MoS_2 and sulfonated graphene developed in-situ over Ni foam) were taken and few tests were performed. The following activity and stability results were obtained:

Activity order [OER] - NF<RGO/NF<NiS< GNiS < NiMoOS <GNiMoOS **[0.5 M KOH]**

Activity order [OER] – NF<NiS<NiMoOS<RGO/NF <GNiS<GNiMoOS **[0.5 M NaCl]**

Activity order [OER]- NF<RGO/NF~NiS< NiMoOS< GNiS <GNiMoOS **[0.1 M KOH + 0.5 M NaCl]**

In pure KOH media (free of any harsh Cl^- ions), the activity of NiMoOS > GNiS which means that MoS_2 [MoS_2 flowers developed over Ni foam in NiMoOS] has a role in the enhanced activity but in 0.5 M NaCl, this trend is inverse, and the activity follows GNiS > NiMoOS .Also the sulfur doped RGO coated electrodes were the most stable amongst

all in 0.5 M NaCl compared to the bare electrodes devoid of any RGO coatings. Our hypothesis that sulfur and RGO i.e. in-situ developed sulfonated graphene play a significant role in imparting stability to the electrode in harsh environments explains why GNiS and GNiMoOS were stable in 0.5 M NaCl, while NiMoOS, which doesn't appear to contain any sulfonated graphene, was unstable in the same media. However, it is still more active than GNiS in KOH media (but less active than GNiMoOS). To validate the trend observed and the conclusions proposed, we put forward some important findings supporting our proposed finding which are mentioned below:

The Raman spectra of GNiMoOS clearly indicated the characteristic peaks of MoS_2 and the SO_3H related vibrations in the 1000–1200 cm^{-1} region. The functionalization in the graphene sheets with sulfonic moieties was well justified due to the shift in the D and G band positions towards higher wavenumbers as well as the increase in the D band intensity compared to the G band. However, the peaks at 182, 199, 221 and 301 cm^{-1} which coincide with the characteristic Raman peaks of Ni_3S_2 were missing in the Raman spectra of GNiMoOS which were present in the Raman spectra of NiS (**Figure 3.9**). The Raman spectra of GNiS (**Figure 3.9**) was similar to the Raman spectra of GNiMoOS where the peaks corresponding to SO_3H vibrations were present. This might be because there is a possibility of the in-situ doping of sulfonic moieties into the graphene matrix like the case of GNiMoOS as the reaction conditions for the synthesis of both GNiS and GNiMoOS were similar, except the use of Molybdic acid in GNiMoOS. However, the peaks at 182, 199, 221 and 301 cm^{-1} which coincide with the characteristic Raman peaks of Ni_3S_2 (which were found in **NiS**) were absent in GNiS in the lower frequency range which confirms any formation of Ni_3S_2 kind of species over the Ni foam in GNiS (**inset of Figure 3.9**). Since

GNiS was equally stable as compared to GNiMoOS in harsh media, this led us to conclude that sulfonic doped graphene is definitely linked to the remarkable stability of the electrode.

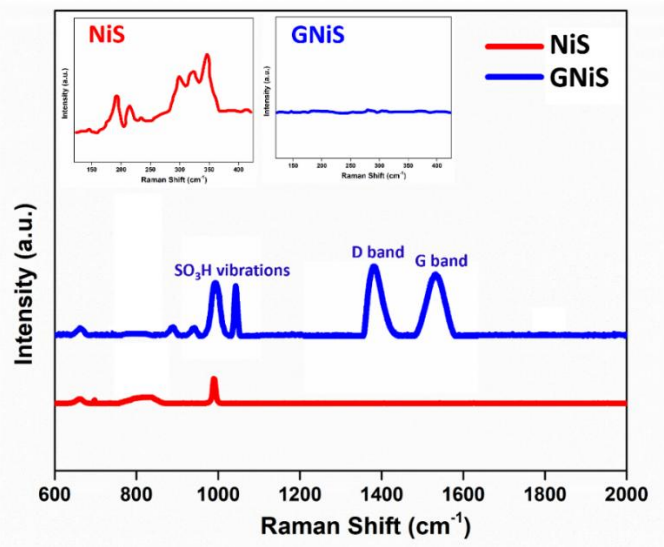

Figure 3.9 Raman spectra of the NiS and GNiS electrode.

Further if we see the XPS spectra of GNiMoOS , the S^{2-} peak around 161.1 to 162.2 eV (attributed to S $2p_{3/2}$) and 162.4 to 163.5 eV (attributed to S $2p_{1/2}$) in the S 2p spectrum , which are found in Ni_3S_2 were absent and the peaks in the region 168-170 eV were majorly present suggesting the abundance of oxidized sulfonic moieties which again confirmed the absence of Ni_3S_2 . Also, in the SEM images of GNiMoOS, any growth of inverted wedge-shaped flakes of Ni_3S_2 which were obtained when S was solely doped over Ni foam in the same operating conditions as GNiMoOS, were nowhere to be seen except for the MoS_2 flowers adhered over Graphene sheets homogeneously suggesting the sole formations of MoS_2 in GNiMoOS. Hence the possibility of any Ni_3S_2 formation during the in-situ development of GNiMoOS was ruled out. Since our active catalyst GNiMoOS exhibits higher activity than GNiS and comparable stability in harsh media, we conclude that both

MoS_2 and sulfonated graphene (SO_3H-GO) contribute synergistically to its high efficiency and chlorine-repelling capability, making it the most effective among the GNiS and NiMoOS electrodes for seawater electrolysis.

So, Raman, SEM, TEM and XPS analysis confirm the 100% possibility of MoS_2 formation along with the abundance of oxidized sulfur moieties doped inside graphene in the GNiMoOS electrode which were responsible for the excellent performance of the electrode towards seawater splitting. In addition , DFT studies also validated the role of sulfonated graphene towards imparting stability to the GNiMoOS system during seawater electrolysis. The details are discussed in the next section.

3.7 Validation of the sulfonic group's repulsive potential by computational analysis

To gain a deeper understanding of the catalytic performance of GNiMoOS, density functional theory (DFT) calculations were performed to examine the mechanism of the OER for these catalysts. To optimize computational efficiency, separate calculations were conducted for MoS_2 and SO_3H -decorated graphene ribbons (SO_3H@Gr). These ribbons were used as theoretical models to represent the edges of the graphene sheet, where MoS_2 typically forms (MoS_2@Gr). A Mo_3S_{12} cluster, consisting of three Mo and twelve S atoms, was used to simulate the flower-like MoS_2 morphology, with the optimized structure shown in **Figure 3.10a, b**. The study first focused on the catalyst's stability in an alkaline medium by examining the interaction between Cl^- ions and the catalyst (**Figure 3.10c-e**). The adsorption energy of Cl^- on MoS_2 was calculated to be slightly positive at 0.045 eV. Meanwhile, Cl^- ions were found to interact with the hydrogen atom of SO_3H @Gr, leading

to deprotonation and the formation of HCl, with a formation energy of -0.34 eV. Further evaluation of Cl^- adsorption on SO_3@Gr, specifically on the SO_3^- ions, yielded an adsorption energy of 0.68 eV, confirming Cl^- repulsion. This suggests that SO_3^- ions remain stable and could potentially participate in the OER process. The interaction between Cl^- and SO_3H creates a localized acidic environment within the alkaline medium, thereby enhancing the catalyst's stability.

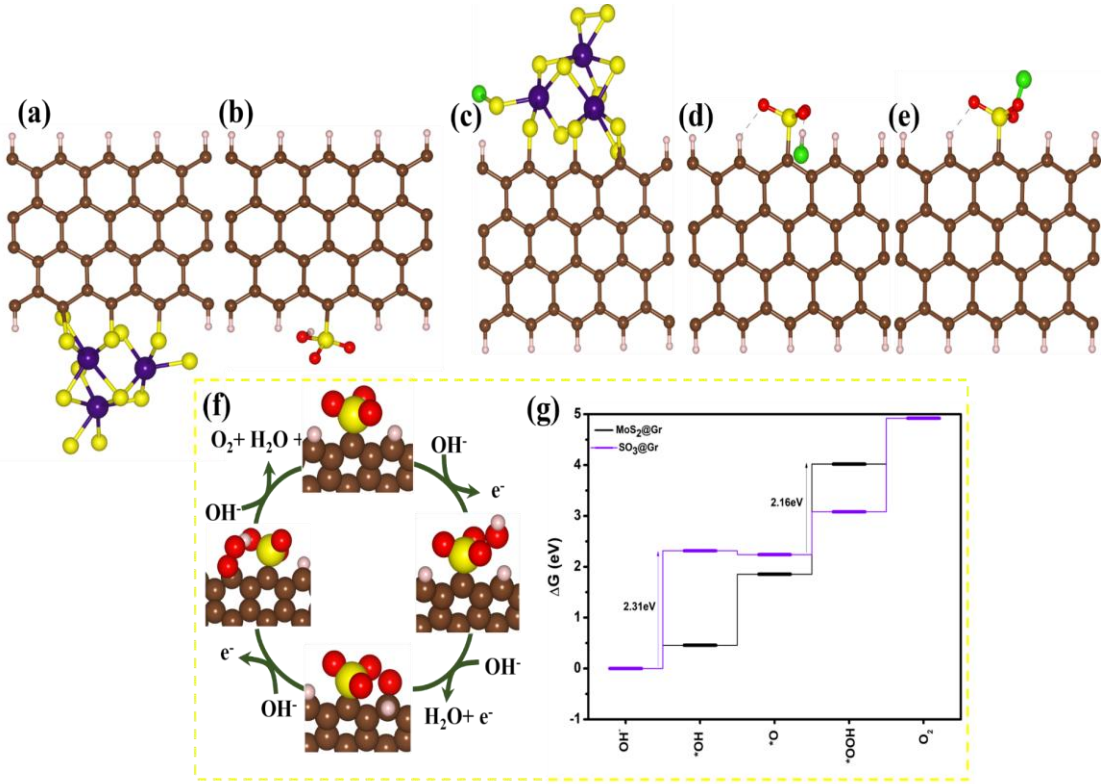

Figure 3.10 DFT optimized structure of (a) MoS_2@Gr (b)SO_3H@Gr. {Color code- C: brown, O: Red, S: Yellow, H: White, and Mo: blue}; DFT optimized structure for adsorption Cl ion on (c) MoS_2@Gr (d) SO_3H@Gr (e) SO_3@Gr {Color code- C: brown, O: Red, S: Yellow, H: White, Mo: blue and Cl: Green} (f) OER reaction mechanism with optimized structure for intermediates adsorbed on SO_3H@Gr (g) Calculated free energy diagram for OER on MoS_2@Gr and SO_3H@Gr {Color code- C: brown, O: Red, S: Yellow and H: White}.

The OER catalytic process in alkaline media can follow two mechanisms: the conventional adsorption evolution mechanism (AEM) and the lattice oxygen participation mechanism

(LOM) [295]. We investigated both mechanisms on SO_3@Gr. For the AEM, as depicted in **Figure 3.10f**, the process begins with OH adsorption at an oxygen site, which then reacts with another OH radical to form *O and a water molecule. This is followed by the reaction of *O with OH^- to form *OOH, eventually leading to O_2 evolution and H_2O production through interactions with OH^-. Gibbs free energy calculations revealed a theoretical onset potential (U_{min}) of 2.31 V, as shown in **Figure 3.10g** with the rate-determining step being the initial adsorption of OH.

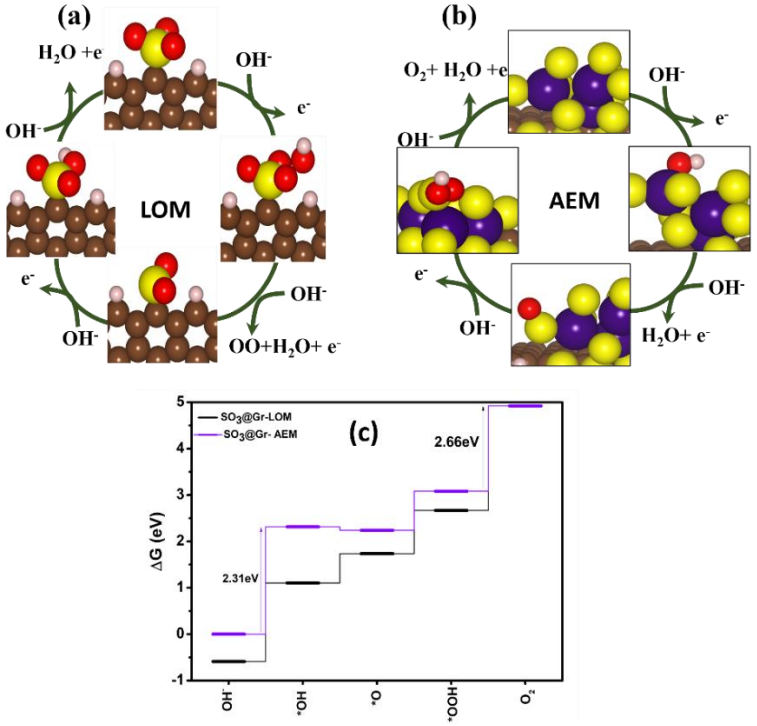

Figure 3.11 (a) OER-LOM reaction mechanism with optimised structure for intermediates adsorbed on SO_3H@Gr (b) OER reaction mechanism with optimised structure for intermediates adsorbed on MoS_2@Gr {Colour code- C: brown, O: Red, S: Yellow, Mo: Blue and H:White} (c) Calculated free energy diagram for AEM and LOM mechanism on SO_3H@Gr {Colour code- C: brown, O: Red, S: Yellow, and H: White}.

Next, we studied the LOM mechanism shown in **Figure 3.11a,** where OH adsorbs onto SO_3 and reacts with an oxygen atom from SO_3 to form OOH (SO_3H-OOH). This is followed by an interaction between OH and OOH, resulting in O_2 evolution and H_2O

formation. Subsequently, OH adsorbs onto SO_2, and further interaction with OH releases H_2O, regenerating SO_3. The free energy diagram in **Figure 3.11c** indicates U_{min} of 2.66 V, with the rate-determining step identified as the final step in the process.

Additionally, the OER activity of MoS_2@Gr was investigated using AEM. As depicted in **Figure 3.11b**, various intermediate structures were identified throughout the reaction process. Initially, the Mo atom in MoS_2@Gr adsorbs an OH radical, which then reacts with another OH radical to form *O and a water molecule. The *O species subsequently desorbs from the Mo atom and adsorbs onto a neighboring S atom. This process continues as *O reacts with OH^- to form *OOH, eventually leading to O_2 evolution while producing H_2O through interactions with OH^-. Gibbs free energy calculations determined Umin of 2.16 V, as shown in **Figure 3.10g**. The rate-determining step was identified as the formation of the OOH intermediate. Both MoS_2 and SO_3 follow the AEM mechanism, with theoretical overpotentials of 0.93 V and 1.08 V, respectively. Although MoS_2 has a lower overpotential than SO_3, SO_3 is expected to be more available and stable, as Cl^- could adsorb at the MoS_2 site.

3.8 Conclusion

In summary, a robust and efficient GNiMoOS electrode has been developed for selective seawater electrolysis, favoring H_2O oxidation to O_2 over Cl^- oxidation to ClO^-. The formation of a protective sulfonated graphene layer on Ni foam enables prolonged operation by repelling Cl^- ions, as confirmed by TMB dye tests and DFT studies. The in-situ integration of sulfonic groups and flower-like MoS_2 into reduced graphene oxide was verified via XPS, Raman, SEM, TEM, and FT-IR analyses. GNiMoOS showed superior bifunctional activity and stability compared to bare NiMoOS or RGO/NF, due to the synergistic interplay of Ni foam, sulfonated graphene, and MoS_2. These results highlight the importance of electrode and electrolyte design in overcoming chloride corrosion, enabling direct seawater splitting for sustainable fuel generation.

Chapter 4: A trifunctional, freestanding, 3D self-assembled Graphene-MoS electrode for green electrode reactions

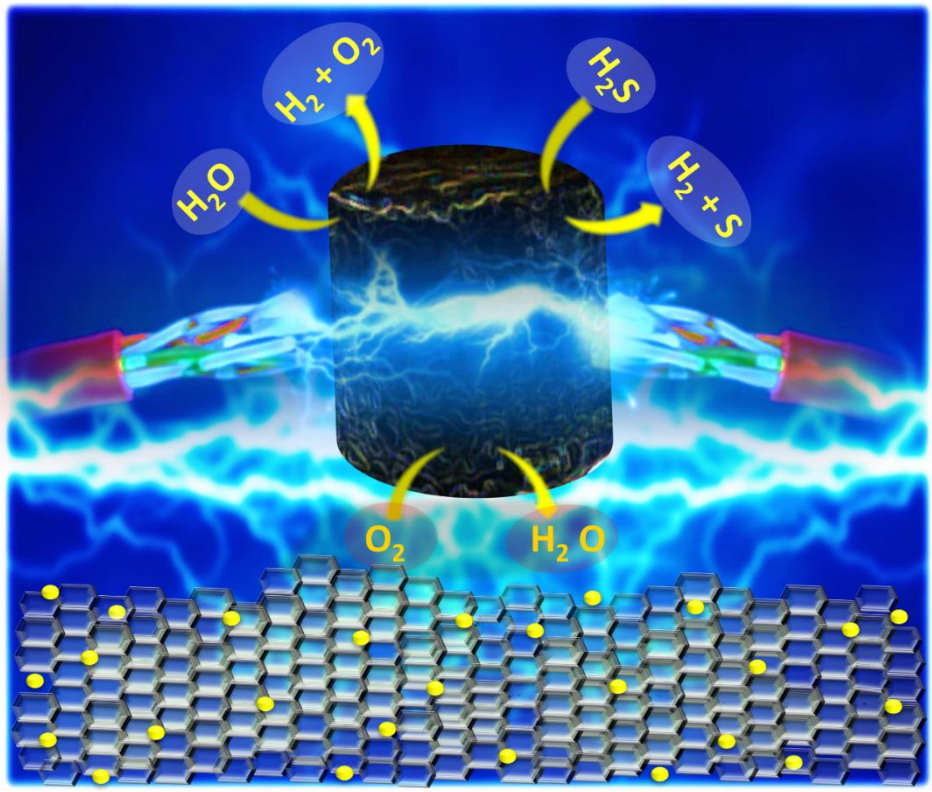

Multifunctional catalysts are urgently needed to meet diverse electrochemical demands. We developed a 3D self-assembled MoOS-G nanocomposites as a versatile electrode-efficient for HER from H_2O/H_2S in alkaline Na_2S media, bifunctional HER/OER in acidic media, and promising for ORR activity.

(This work is published in RSC New Journal of Chemistry, 2025, https://doi.org/10.1039/D5NJ02817E).

4.1 Abstract

Development of multifunctional catalysts is highly desired for the production of green energy and next-generation technologies but, is a challenging task. Under this report, we have tried to develop a novel three-dimensional (3D) self-assembled, freestanding defensible, graphene- molybdenum sulfide (MoOS-G), graphene-molybdenum selenide (MoOSe-G) and graphene- molybdenum oxide (MoO-G) by a simple one step hydrothermal approach. All three transition metal chalcogenide composites function as efficient bifunctional electrocatalysts for overall water splitting in acidic media, showing electrocatalytic activity in the order: MoOS-G > MoO-G > MoOSe-G. Of all the three, MoOS-G exhibits the lowest overpotential, requiring only 280 mV to achieve a current density of 10 mA cm^{-2} in comparison to MoO-G and MoOSe-G which showed overpotentials of 390 and 540 mV respectively. Interestingly, the sulfide- and selenide-based catalysts demonstrated good activity and stability toward hydrogen sulfide (H_2S) splitting in Na_2S + NaCl (simulated seawater) media, producing hydrogen at the cathode via hydrogen evolution reaction and elemental sulfur at the anode via sulfion oxidation reaction. Current density of 35 mA cm^{-2} at 350 mV at room temperature were obtained with the self-assembled sulfide systems and it outperformed the MoOSe-G and the widely used bare graphite electrodes in both catalytic efficiency and long-term stability. The superior activity of MoOS-G in both the medias was thoroughly correlated with structural and compositional insights obtained from XRD, Raman, SEM, TEM, and XPS analysis. Additionally, MoOS-G was found to catalyze the four-electron oxygen reduction reaction (ORR) pathway with an onset potential of 0.97 V in alkaline KOH solution, a highly desirable trait for fuel cell applications. So overall, this study aimed to design a robust,

low-energy, multifunctional electrode capable of operating across a wide pH range for diverse electrochemical processes. Notably, the sulfide-based systems demonstrated enhanced surface area, high electrocatalytic activity, and excellent durability, positioning MoOS-G as a versatile and sustainable electrocatalyst for various green energy technologies. The enhanced performance is attributed to efficient electron transport and the synergistic effects between Mo–S moieties and sulfonated graphene support.

4.2 Introduction

The development of electrochemical energy conversion and storage devices (e.g., fuel cells, metal–air batteries, and water splitting) offers new opportunities to address global energy challenges. However, their development is limited by the lack of suitable electrocatalysts to drive electrode reactions. To overcome the limitations associated with current electrocatalysts, extensive scientific and engineering efforts have been dedicated to developing highly functional systems for electrochemical energy conversion processes, such as the oxygen reduction reaction (ORR), oxygen evolution reaction (OER), hydrogen evolution reaction (HER), sulfur oxidation reactions (SOR) etc. While these heterogeneous electrochemical reactions follow distinct mechanistic pathways, they share common features: occurring at the solid–liquid interface and involving multistep proton/electron-coupled electron transfer processes. These characteristics contribute to inherently sluggish reaction kinetics, necessitating the use of highly active electrocatalysts [311,312].

However, the widespread adoption of these technologies is hindered by their reliance on scarce and costly noble metal catalysts, such as platinum, iridium, and ruthenium oxides [311,313]. Therefore, the design and development of efficient, robust, and nanostructured bifunctional or trifunctional electrocatalysts capable of driving both oxygen and hydrogen-

related reactions is both highly desirable and technically challenging for the commercialization of renewable energy systems. Although many catalysts have shown potential for facilitating multiple reactions, most research to date has primarily focused on enhancing the performance of a single reaction, often overlooking the development of multifunctional catalysts that combine high activity with long-term durability. Despite significant advances in recent decades [314-318], achieving optimal adsorption and desorption energies for multiple reaction intermediates on a single catalyst surface remains a critical bottleneck.

Transition metal-based chalcogenides including oxides, sulfides, and selenides have emerged as promising electrocatalysts for electrochemical water (H_2O) and hydrogen sulfide (H_2S) splitting, as well as fuel cell applications. Their appeal lies in their diverse morphologies, abundant active sites, structural tunability, and cost-effectiveness, which have collectively attracted significant research attention in recent years [319,320]. These materials exhibit a range of functional properties, including magnetism, high optical response, and catalytic activity, stemming from the covalent bonding between transition metals and chalcogen elements (O, S, Se) that contributes to their unique structural characteristics [321]. Among them, transition metal oxides have been more extensively investigated as electrocatalysts for water splitting due to their low cost, ease of synthesis, and controllable morphologies [322]. However, transition metal sulfides have also gained increasing interest, owing to their layered and non-layered architectures, and despite their relatively lower intrinsic electrical conductivity, they have shown considerable potential as electrocatalysts for water and H_2S splitting, as well as in a variety of other electrochemical applications [323,324].

In addition to transition metal sulfides, the selenides for instance, molybdenum selenide ($MoSe_2$) has emerged as an intriguing narrow-band-gap semiconductor with a layered Se-Mo-Se sandwich structure that is isostructural with MoS_2. Theoretical band structure calculations, corroborated by photoelectron spectroscopy, indicate that $MoSe_2$ has a band gap of approximately 1.4 eV, nearly similar to that of MoS_2 [325], making both materials versatile for photoelectrochemical and electrocatalytic applications. MoS_2 has been extensively used in water splitting applications. Though MoS_2 is less naturally active for OER compared to HER, its sulfiphilic nature allows strong interaction with sulfur species, making it an excellent candidate for H_2S splitting where both HER and sulfur oxidation are involved. The preference for HER + SOR (H_2S splitting) over HER + OER (H_2O splitting) in some systems comes down to a combination of thermodynamics, kinetics, sustainability, and economic viability, especially in industries where H_2S is a problematic waste product. For example, the aqueous form of sulfide can be found in natural anaerobic environments such as the Black Sea, where the amount of H_2S buried is estimated at over 4×10^9 tons. As an important resource, directly converting H_2S into H_2 and S is highly desirable [326,327]. Thermodynamically, the Gibbs free energy required for H_2S splitting reaction is 34 kJ mol^{-1}, which is only one-seventh of that required for H_2O splitting (237 kJ mol^{-1}) [328]. Also, considering H_2S splitting, the thermodynamic potential for the SOR is -0.48 V vs SHE, which is much lower compared to that of the OER (1.23 V vs RHE) [329]. In an alkaline aqueous solution with suitable pH conditions, the conversion of sulfide ions to elemental sulfur and polysulfides predominates as the primary process in the SOR. However, the electro-oxidized product sulfur produced at the anode tends to adhere to the catalyst's surface in SOR, deactivating the catalyst's active sites [117,329]. While the

inherent sulfiphilicity of transition metal sulfides and selenides facilitates their catalytic activity toward sulfur-involving reactions, excessive sulfur binding leads to surface passivation [330]. This challenge can be very well addressed by tuning their sulfiphilicity through combining sulfides/selenides with conductive supports like graphene or RGO to create heterojunctions [331,332]. This promotes charge delocalization, speeds up electron transfer, and changes adsorption behavior by altering surface polarity which can enhance selectivity, adsorption properties, and charge transfer processes at the catalyst-electrolyte interface. Alongside being an effective water splitting catalyst, Metal sulfides (MoS_2) are popular candidates for use in fuel cell cathodes for ORR and known as active catalysts toward ORR activity in literature [333,334]. In most of the previous reports, MoS_2 nanoflowers, prepared by hydrothermal synthesis route, results in the formation of MoS_2 with particle size ranges between 500 nm to 3μm with lattice fringes thickness ≥12nm [335-338]. Therefore, it is obvious that for any electrochemical application, those bigger particles will significantly increase the ion diffusion path and will suffer from more internal strain during reaction, leading to cracking of material, hence poor electrochemical performance. The electrocatalytic activity of nanoscale materials is heavily influenced by their special shape and structure, tunable electronic together with crystal morphologies [339]. As a result, selecting an appropriate synthesis process (e.g., ball milling, hydrothermal approach, solvothermal procedure, chemical vapor overthrow, etc.) and optimizing porosity are significant steps in the design and development of transition metal chalcogenides electrocatalysts for various electrochemical applications.

Besides, all transition metal-based chalcogenide catalysts face common challenges, including low intrinsic electrical conductivity, limited surface area, a scarcity of exposed

active sites, and poor long-term stability [136,86]. To overcome these limitations, a practical strategy involves integrating these materials with conductive matrices to enhance their structural integrity and electrical performance. In this context, both two-dimensional (2D) and three-dimensional (3D) nanocarbon materials have been employed to address conductivity issues and to increase the number of exposed active sites and surface area [86]. Among various nanocarbon supports, reduced graphene oxide (RGO) stands out as an ideal matrix due to its unique electronic structure, abundance of defects, excellent electrical conductivity, and mechanical flexibility. Graphene-supported catalysts are considered highly synergistic multi-composite systems for diverse electrocatalytic applications. They not only serve as a robust support for metal nanoparticles (NPs) but also enhance charge/mass transport and overall catalyst stability through strong metal–support interactions [340,341]. While these hybrid systems have demonstrated effectiveness in catalyzing individual reactions in both acidic and alkaline media, they rarely exhibit high activity across all these key reactions HER, OER, SOR and ORR simultaneously and it remains challenging to achieve such multifunctionality on a single catalyst, although many systems can exhibit either one or two activities.

Single material for multiple reactions reduces the need for multiple catalyst layers or distinct electrode compositions, saving on synthesis and manufacturing. Also, they are useful in simplifying device architecture and lowering material diversity, which helps with recycling and scale-up. Also, electrocatalysts that can operate in a wide pH range further reduce the need for harsh or environmentally damaging conditions. Therefore, researchers have endeavored to develop efficient, novel, robust, and durable trifunctional or

multifunctional electrocatalytic materials for the production of green energy and next-generation technologies [314-318].

Herein, the synthesis of three-dimensional (3D), self-assembled and freestanding graphene-transition metal-based sulfide (MoOS-G), selenide (MoOSe-G), and oxide (MoO-G) electrodes for different electrochemical reactions under H_2SO_4, KOH, and H_2S medium has been reported. All the self-assembled electrode systems were found active in H_2SO_4 media for HER, with sulfide electrode (MoOS-G) being the most active of all, serving as a bifunctional electrode showing a current density of 25 mA cm^{-2} at 350 mV at room temperature. Except the sulfides, all the electrodes were unstable under alkaline KOH media and underwent dissolution with time during anodic polarizations. However, the electrochemical HER and OER activity was not noteworthy in the KOH media. Interestingly, the self-assembled sulfide and selenide systems were found to be active under Na_2S + NaCl (alkaline) media with the sulfide system being the most active and stable delivering HER current density of 35 mA cm^{-2} at an overpotential of 350 mV in Na_2S +NaCl media at room temperature. Sulfur as a byproduct was obtained at the counter electrode via SOR by the selective electrolysis of H_2S. Besides HER/OER, the electrochemical reduction of oxygen on MoOS-G catalyst in alkaline solutions, along with its detailed mechanism has been investigated using the rotating ring-disk electrode (RRDE) method. The RRDE results indicated that MoOS-G catalyzes a 4-electron reduction of oxygen with an onset potential of 0.97 V. The developed 3D electrodes have been well characterised by TEM, SEM-EDAX, RAMAN, and XRD techniques.

4.3 Experimental section

4.3.1 Materials

Graphite powder [Qualikems Fine ChemPvt. Ltd], Sulphuric acid (H_2SO_4) [Finar Ltd], Ortho-phosphoric acid (H_3PO_4) [Merck life science Pvt. Ltd], Potassium permanganate ($KMnO_4$) [Sisco Research Laboratories Pvt. Ltd],Hydrogen peroxide (H_2O_2) [Merck life science Private Limited], Thiourea (CH_4N_2S)[Merck Pvt. Ltd], Molybdic Acid (H_2MoO_4) [SpectrochemPvt.Ltd], Disodium Sulphide Nonahydrate Flakes($Na_2S.9H_2O$)[Avantor Performance Materials India Limited], Ethanol (C_2H_5OH)[Changshu Hongsheng Fine Chemical Co. Ltd], Acetone (C_3H_6O) SDFCL [S D Fine-Chem Limited], Methanol (CH_3OH) SDFCL[S D fine-Chem Limited], Potassium hydroxide (KOH) [Finar Ltd], Sodium Chloride (NaCl) [Finar Ltd], Selenium powder(Sigma Aldrich-209651-50G), Nickel foam (Sigma Aldrich-GF28024657-5EA) were used as received. Deionized water (DDW) was prepared by redistillation of the double distilled water in a glass distillation apparatus.

4.3.2 Material Characterizations

Absorbance spectra of samples were recorded by the Agilent Technologies Cary 5000 DRS 2500 UV-Vis-NIR Spectrophotometer in the spectral range of 175 nm to 2200 nm. Raman spectra of the samples were recorded in a Jasco NRS-5500 Laser Confocal Raman Spectrophotometer equipped with 1200 grooves per mm gratings, and laser spot intensity 0.0001% of microscope with objective. The samples were excited with a 532 nm wavelength laser from an Ar^+ laser with fluorescent correction. The XPS measurements were recorded in the Thermo Fisher Scientific K-Alpha X-ray Photoelectron Spectrometer, which was outfitted with Al-Kα X-ray (1486.6 eV) as a primary excitation and an auto-

firing, 3 filament TSP software. The Jeol, NEOARM/JEM-ARM200F, AMI 300, High Resolution Transmission Electron Microscope (HR-TEM) was used to determine the structural identity, particle size distribution and elemental composition. Furthermore, we performed a JEOL JSM-7900F Field Emission Scanning Electron Microscope (HR-FE-SEM) to determine surface morphology and elemental confirmation. Panalytical X-Ray Diffraction Spectrophotometer with Cu-Kα (λ = 1.540598 Å) and the Rigaku SmartLab 9kW Powder type (without χcradle) were used to find crystallite size, d-spacing, and the lattice constant values. Further, the active sites of the material were analyzed by Temperature Programmed Desorption (TPD) and Temperature Programmed Reduction (TPR) spectra, recorded by Altamira Instruments, AMI 300, Pulse Chemisorption/Desorption system. Elemental analysis (% of Nitrogen, sulfur , hydrogen and carbon) of the material was estimated by Elementar Unicube CHNS instrument, which ensured a complete combustion at 1200°C. The Multi Autolab M 204 from Metrohm Autolab was used to record impedance studies (Serial number: MAC90581). Further, the electrochemical characterizations were performed using μ-AUTOLAB type-III (Serial number: μ3AUT70731).

4.3.3 Electrochemical Measurements

The electrochemical performance of MoOS-G electrode was evaluated using μ-Autolab III potentiostat involving three electrode configurations with platinum metal as counter electrode and Ag/AgCl as reference electrode. The catalytic performances of the electrodes were checked in H_2SO_4(1 M), KOH (1M), pure NaCl (0.5 M) and Na_2S electrolyte (0.1 M) in simulated seawater (0.5 M NaCl).The catalyst was first stabilized by cyclic voltammetry (CV) at a 30 mV s^{-1} scan rate in the potential window of -1.5 to 0.7 V vs. Ag/AgCl, then

the LSV experiments were conducted at a scan rate 5 mV s^{-1}. Chronoamperometry studies were carried out to check the stability and the durability of the working electrode with time. The effect of temperature on the H_2S decomposition and sulfide oxidation reaction on electrodes were also studied. The current density was calculated considering the planar geometry surface area of resulting self-assembled electrodes. All the potential in this study were adjusted to the reversible hydrogen electrode (RHE) reference scale using the formula equation (1). E^o value of Ag/AgCl (3M KCl) is taken 0.205 at the operational temperature of 28 ºC.

E (vs. RHE) = Applied potential (vs. Ag/AgCl) + E^o [Ag/AgCl (3M KCl)] + 0.059 V (pH)

Similarly, EIS were performed in an applied frequency ranging from 0.1 Hz to 1 x 10^5 Hz and an excitation of 10 mV amplitude in electrochemical cell with a three-electrode system compromising the same set-up, at the operational temperature of 28 ± 2 ºC in.

4.4 Material synthesis

4.4.1 Synthesis of MoS_2

MoS_2 was prepared by simple hydrothermal process. In a typical experiment, molybdic acid (250 mg) and thiourea (267 mg) was taken in a two neck round bottom flask containing Teflon coated magnetic bar. To it, methanol was added, and the system was put to reflux for few hours at temperature at 180ºC. Then the resultant mixture was poured into the Teflon lined hydrothermal reactor (100 mL), transferred inside the furnace maintained at 180ºC for 24 hours. The resultant **MoS_2** was washed with water and ethanol to ensure the removal of surface adsorbed impurities.

4.4.2 Synthesis of 3D MoOS-G

MoOS-G was prepared by hydrothermal self-assembly of Molybdic acid and Graphene oxide (GO). GO was synthesized by modified Hummer's method (**E4, Appendix information**). In a typical experiment, molybdic acid (250mg) and thiourea (267 mg) was taken in a two neck round bottom flask containing Teflon coated magnetic bar. To it, methanol was added, and the system was put to reflux for few hours at temperature at 180^{o}C. After cooling at room temperature, 20 mL of stable suspension of GO (15 mg/mL) was added to it and vigorously stirred for 1 h, to ensure proper homogenization. Then the resultant mixture was poured into the Teflon lined hydrothermal reactor (100 mL) and were transferred inside the furnace maintained at 180^{o}C for 24 h. The resultant MoOS-G was washed with water and ethanol to ensure the removal of surface adsorbed impurities. As formed **MoOS-G**, was cut into pieces, subsequently dried at room temperature, resulting in freestanding electrodes. For an ohmic contact, a copper wire was pasted by silver glue on the upper back portion of MoOS-G. Epoxy resin was coated around the wires and edges completely to ensure that the electrochemical reactions obtainable only from the surface containing catalyst. The electrode fabrication is kept in **Figure A 21**.

4.4.3 Synthesis of 3D MoOSe-G

MoOSe-G was prepared by hydrothermal self-assembly of Molybdic acid and Graphene oxide (GO). In a typical experiment, molybdic acid (250mg) and Selenium metal powder (273.2 mg) mg) was taken in a two neck round bottom flask containing Teflon coated magnetic bar. To it, methanol was added, and the system was put to reflux for few hours at temperature at 180^{o}C. After cooling at room temperature, 20 mL of stable suspension of GO (15 mg/mL) was added to it and vigorously stirred for 1 h, to ensure proper

homogenization. Then the resultant mixture was poured into the Teflon lined hydrothermal reactor (100 mL) and were transferred inside the furnace maintained at 180°C for 24 h. The resultant MoOSe-G was washed with water and ethanol to ensure the removal of surface adsorbed impurities. As formed MoOSe-G, was cut into pieces, subsequently dried at room temperature, resulting in freestanding electrodes. For an ohmic contact, a copper wire was pasted by silver glue on the upper back portion of MoOSe-G. Epoxy resin was coated around the wires and edges completely to ensure that the electrochemical reactions obtainable only from the surface containing catalyst.

4.4.4 Synthesis of 3D MoO-G

MoO-G was prepared by similar method as mentioned above with precursors hydrothermal self-assembly of Molybdic acid (250mg) and Graphene oxide (15 mg/mL).

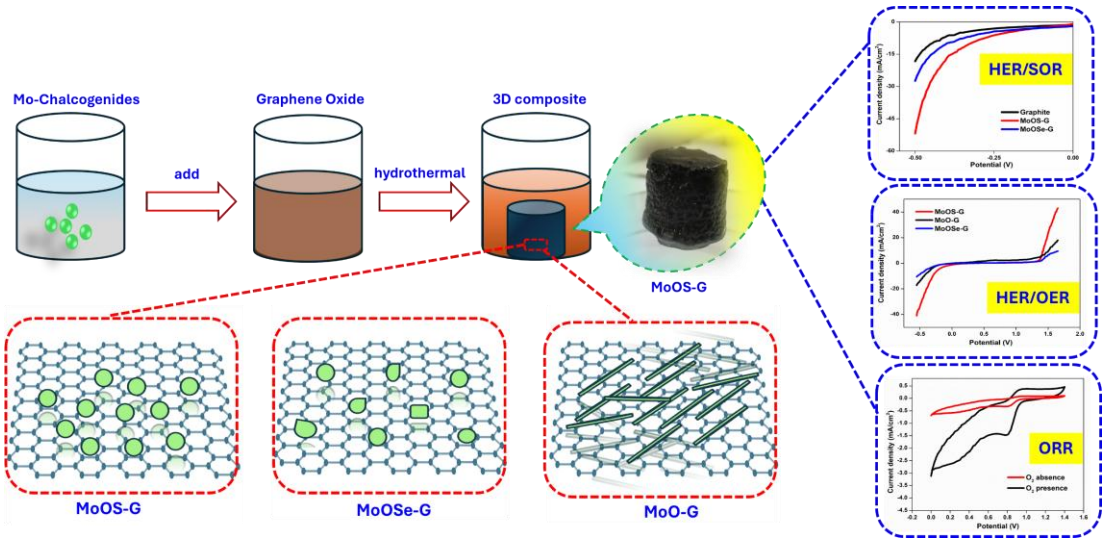

Figure 4.1 Synthesis scheme of the self-assembled electrodes.

4.5 Results and Discussion

The MoOS-G 3D architecture was prepared by simple one step hydrothermal heating of a homogenous aqueous dispersion containing liquid paste of graphene oxide, molybdenum precursor and thiourea at 180 ºC for 24 h. The formed MoOS-G was cut into pieces, subsequently dried at room temperature, thereafter, resulting in the freestanding electrodes. The selenides and the oxides were prepared likewise. The electrocatalyst synthesis scheme has been presented in **Figure 4.1**.

The Electrocatalytic water splitting performances (HER/OER) of all the three prepared electrodes MoOS-G, MoOSe-G and MoO-G were checked in different mediums including neutral (NaCl), basic (KOH), acidic (H_2SO_4), so that an active and a durable electrode could be developed that would serve the purpose of a Bifunctional Electrocatalyst for water splitting. To get a clear idea of the ongoing process near the electrodes in the different mediums, a dilute universal indicator solution (a few drops in 100 mL of electrolyte) was used with negligible change the ionic strength or conductivity of the electrolyte. Using a universal indicator during electrocatalytic HER and OER is a clever visual way to monitor local pH changes around the working electrode in different media (acidic, neutral, and basic). It gives a colour change indicating local proton (H^+) or hydroxide (OH^-) production or consumption thus helping in observing acidification or basification near the electrodes. The colours from yellow to red indicate an acidic solution, colours blue to violet indicate alkali and green colour indicates that a solution is neutral [342].

Taking all the three electrodes one by one in a two-electrode setup, their HER and the OER activity was checked in pure NaCl electrolyte. In neutral media, water undergoes oxidation at the anode to produce oxygen and H^+ ions, while at the cathode, it is reduced to hydrogen

gas and OH^- ions. In 0.5 M NaCl solution, no gas evolution or color change near either electrode was observed at -0.5 V(cathodic) or 1.8 V (anodic) vs RHE, indicating restricted HER and OER activity. The absence of a blue/purple zone near the cathode suggests minimal HER and OH^- production, while no yellow/red zone near the anode suggests suppressed OER and H^+ production. However, the gradual shift of the bulk electrolyte to purple indicates the formation of acidic oxidative chlorine species, such as HOCl, under anodic conditions in chloride-containing media (**Figure A22a, Appendix information**). In the basic KOH medium, MoO-G or MoOSe-G were unstable and degraded due to the following **eq 4.1**:[343]

$$MoSe_2 + OH^- \rightarrow MoO_X + SeO_y^{2-} \quad (4.1)$$

Hydrolysis of MoO_3 and $MoSe_2$ resulted in the formation of soluble molybdates (MoO_4^{2-}) and selenites (SeO_3^{2-}), leading to material dissolution and instability of the following systems in KOH media. However, the MoOS-G system was quite stable, the reason being, the oxidation of MoS_2 to molybdate (MoO_4^{2-}) species is much slower in alkaline conditions i.e. MoS_2 can remain stable for longer periods [344]. Also, RGO acts as a protective barrier, reducing direct exposure of MoS_2 to OH^- attack. So, we proceeded with MoOS-G and checked its activity in KOH media with the addition of 0.5 M salt (NaCl) to mimic seawater. Upon applying a cathodic potential of -0.5 V vs RHE, no noticeable gas evolution or color change was observed near the cathode, indicating minimal hydrogen evolution over an extended period. In contrast, a slight blue color change was observed near the anode at 1.8 V vs RHE, suggesting weak OER activity accompanied by a modest increase in current density [**Figure A22b, Appendix information**] However, during prolonged operation, visible degradation of the anodic electrode occurred, as evidenced by the dark

brown coloration of the electrolyte attributed to the leaching of molybdenum and sulfur species into the solution. This degradation likely stems from the formation of strong oxidizing species, such as hypochlorite or oxyanions, generated under oxidative conditions in the highly alkaline medium (0.1 M KOH), which destabilize the MoOS-G structure. Due to the limited HER/OER electrocatalytic activity and stability in both neutral and alkaline media, further investigations were pursued in Na_2S electrolyte, leveraging the enhanced chemical stability of sulfide and selenide-based electrodes in sulfur-rich environments [**Figure A22c, Appendix information**]. In Na_2S solution, S^{2-} ions act as a mild reducing agent and prevent MoS_2/$MoSe_2$ oxidation, thereby stabilizing the structure as per **eq 4.2**:[330].

$$MoX_2 + S^{2-} \rightarrow (MoX_2 - S^{2-})_{stabilized} \ (X = S, Se) \quad (4.2)$$

MoX_2 may form transient solid solutions or undergo surface sulfidation in the presence of Na_2S, which reinforces the catalyst surface. This passivates defect sites and inhibits leaching of Mo and S making it more stable in Na_2S compared to NaOH/KOH. In addition, as per Le Châtelier's Principle, the presence of excess S^{2-} shifts the equilibrium, preventing the release of sulfur from MoS_2 preventing its dissolution in sulfur rich Na_2S media.

However, the story is different for the self-assembled oxide systems. Since, Na_2S is a reducing agent, it reduces MoO_3 to MoS_2, breaking down the oxide structure. The reduction reaction in alkaline Na_2S solution follows **eq 4.3**:[345]

$$MoO_3 + S^{2-} + H_2O \rightarrow MoS_2 + OH^- \quad (4.3)$$

Hence, the MoO_3 loses oxygen and converts into MoS_2 or other Mo sulfides and dissolves in alkaline Na_2S, forming molybdate ions which further reacts with sulfide ions to form

thiomolybdate species (MoS_4^{2-}), which are highly soluble in alkaline media leads to its complete dissolution. The stability data of the three electrodes in terms of stable current in the 0.1 M Na_2S and 0.5 M NaCl medium is kept in [**Figure A23, Appendix information**]. So, we proceeded with the two self-assembled sulfides and the selenides electrodes along with graphite rod (standard for comparison), which has been widely used for H_2O splitting in literature [346] to see the enhancement in current of the two self-assembled electrodes in comparison to the standard graphite rod.

4.5.1 Electrochemical HER Studies in Na_2S+NaCl media

Firstly, all the three electrodes were checked for their HER activity in Na_2S medium with and without 0.5 M NaCl to see the enhancement in current and the durability in the media. The electrolyte solution was divided into two experimental sets of which the first was a 0.1 M pure Na_2S solution and the second was a solution of 0.1 M Na_2S and 0.5 M NaCl (futile seawater). **Figure 4.2a** represents the polarization curves of the MoOS-G catalyst which has a decent HER activity in Na_2S medium, while its activity got tripled in Na_2S+NaCl medium due to the enhanced conductivity provided by the ions added. Interestingly, MoOS-G exhibited higher HER activity in Na_2S+NaCl medium, outperforming both the selenide and graphite rod, as evidenced by the LSV polarization curve shown in Figure 2b. However, the oxygen evolution reaction (OER) activity under the same conditions was relatively lower, with a maximum current density of 10 mA cm^{-2} at 1.8 V vs RHE. The colourless solution could be seen turning yellow with time due to the formation of elemental sulphur or oxidized sulphur species near the anode. The LSV polarization curve (**Figure 4.2b**) clearly shows that MoOS-G has the highest HER activity in Na_2S saltwater

medium compared to the MoOSe-G and Graphite rod. Tafel plots were derived from the LSV curve by fitting the linear regions according to the Tafel equation (**eq 4.4**): [86].

$$\gamma = a + blogj \quad (4.4)$$

where γ, b, and j denote overpotential, Tafel slope, and current density, respectively. The catalyst with higher HER activity usually presents a lower Tafel slope. As shown in **Figure 4.2c**, the Tafel slope of MoOS-G was 171 mV dec^{-1} compared to the Tafel slope of the MoOSe-G and Graphite rod which were 182 and 201 mV dec^{-1} respectively. The MoOS-G catalyst exhibits a lower Tafel slope when compared to the other catalysts which might be due to the strong electronic and chemical interaction between the anionic doped RGO and MoS_2 and it provides more catalytic edge sites during HER [proven later]. The long-term stability of catalysts during HER was investigated by chronoamperometry (i-t) measurement with constant potential of 0.354 V for 1000 seconds (**Figure 4.2d**) and 500 hours (**Figure A24a, Appendix information**). MoOS-G showed a negligible decay in HER activity maintaining a constant current of 35 mA cm^{-2} throughout the runtime. The selenide system showed a constant current density of 15 mA cm^{-2} for the said time and. After the chronopotentiometry measurement, the polarization curve before and after a time period of 500 hours for MoOS-G is shown in **Figure A24b of Appendix information** , where a small ignorable shift from the initial curve could be seen with the MoOS-G catalyst confirming its long-term electrochemical stability during the electrochemical hydrogen evolution process. **Figure 4.2e** represents a comparison of the overpotential and stable current densities of all the three electrodes. It is noticeable to see that in Na_2S + NaCl media, the MoOS-G exhibits the lowest overpotential amongst all, requiring only 290 mV to achieve a current density of 10 mA cm^{-2} in comparison to MoOS-G and Graphite rod

which required overpotentials of 405 and 445 mV respectively, at a current density of 10 mA cm^{-2} in the same media. Electrochemical impedance spectroscopy (EIS) was employed to evaluate the internal resistance and investigate the charge transfer kinetics of the electrodes.

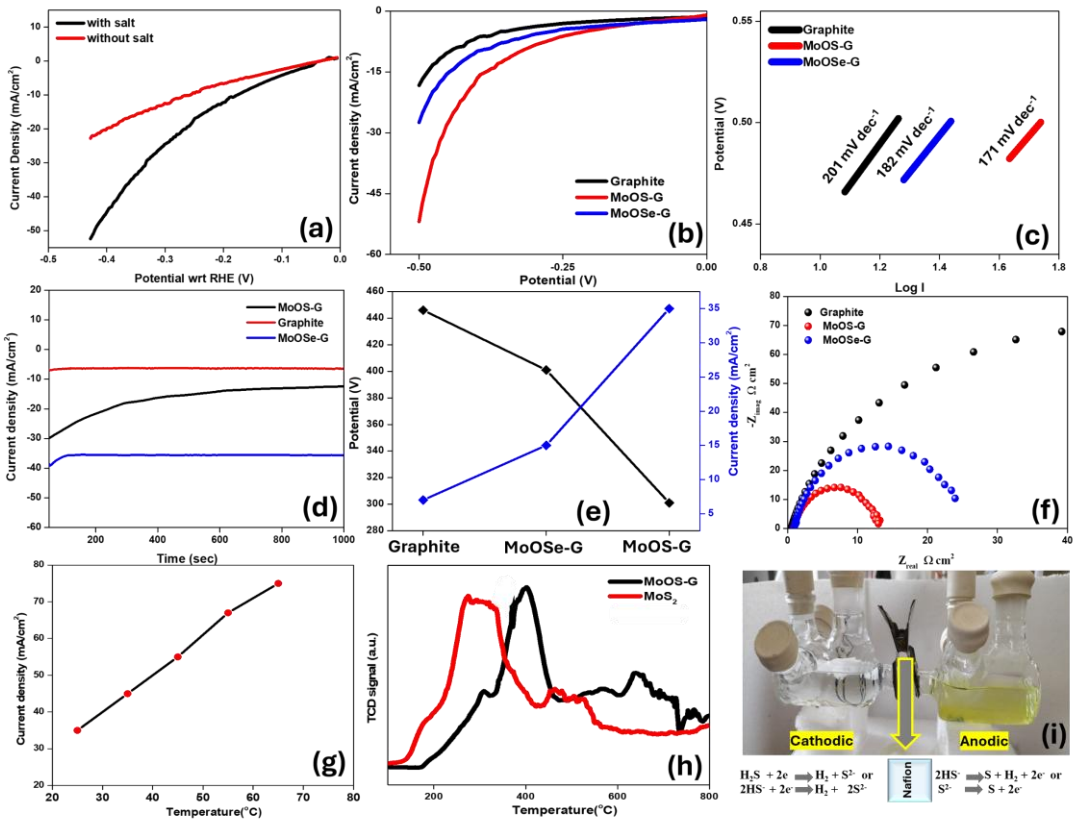

Figure 4.2 (a) LSV curves of MoOS-G electrode between the potential value of to -0.5 V to 1.7 V vs RHE in two electrolyte mediums of Na_2S (0.1 M) and Na_2S (0.1 M)+NaCl (0.5 M) (b) LSV curves of the three electrodes showing HER activity Na_2S (0.1 M)+NaCl (0.5 M) (c) corresponding Tafel plots of the electrodes during HER (d) Stability of the catalysts with time and the corresponding current densities of the electrodes in same media (e)summary plot of Overpotential and current density of all the three electrodes for HER (f) Nyquist plots of the electrodes (g) DC Source study of current dependency on temperature of the electrolyte (h) NH_3-TPD profile of the MoOS-G catalyst (i) schematic representation of the reaction setup in the Na_2S + NaCl electrolyte illustrates the H_2S splitting process, highlighting the spatial separation of anodic and cathodic reactions with a Nafion membrane.

EIS Measurements were conducted for all three electrodes in a mixed electrolyte containing 1.0 M Na_2S and 0.5 M NaCl at open circuit potential, and the corresponding

Nyquist plots are shown in **Figure 4.2f**. Theoretically, a smaller semicircle diameter at high frequency indicates lower charge transfer resistance and consequently, more efficient electrocatalytic performance [86]. Among the tested electrodes, MoOS-G exhibits the smallest semicircle radius, signifying the lowest charge transfer resistance and thus superior HER activity. To further assess the catalytic behavior, the temperature-dependent activity of the MoOS-G electrode was examined. As illustrated in **Figure 4.2g**, the current density increased markedly from 35 mA cm^{-2} to 80 mA cm^{-2} as the temperature of the electrolyte was raised from 30 °C to 70 °C in the same Na_2S + NaCl medium. This enhancement is attributed to intensified hydrogen evolution at elevated temperatures, where thermal energy facilitates the rupture of water molecules and lowers the overpotential for HER [292]. To further probe the chemical environment and surface properties of the as-synthesized MoOS-G catalyst in comparison to its precursor MoS_2 powder, the surface acidity was analyzed using ammonia temperature-programmed desorption (NH_3-TPD). As shown in **Figure 4.2h**, the two catalysts displayed distinct acidity profiles, corresponding to the amount of chemisorbed ammonia quantified by thermal conductivity detection (TCD). Integration of the desorption curves revealed that MoOS-G possesses a significantly broader peak in the 300–500 °C range, indicative of a higher density of strong acid sites [347]. In contrast, the MoS_2 precursor exhibited desorption features associated with moderate acidity [348,349]. The presence of strong acid sites in MoOS-G is beneficial, as they are known to enhance hydrogenation activity and facilitate more efficient conversion to hydrogen [350].

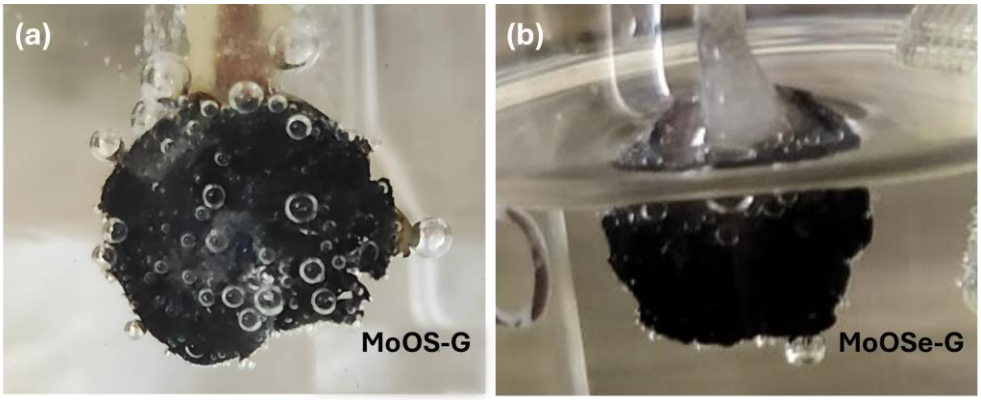

Figure 4.3 (a) Massive evolution of Hydrogen gas over MoOS-G with respect to (b) MoOSe-G in 0.1 M Na_2S + 0.5 M salt at 0.8 V with DC source.

The proposed mechanism for hydrogen sulfide splitting in the dual-compartment H-cell system is depicted in **Figure 4.2i**. The electrolysis involves sulfide oxidation at the anode and concurrent hydrogen evolution at the cathode, separated by a Nafion membrane. Under an applied potential of 0.8 V from a DC source, the MoOS-G electrode sustained a stable current density of 35 mA cm^{-2} over 10 hours, with visible and vigorous hydrogen evolution across the entire electrode surface. In comparison, the MoOSe-G electrode demonstrated significantly lower hydrogen production as shown in **Figure 4.3a and b** under the same conditions reinforcing the superior catalytic performance of MoOS-G (For activity data refer **Figure 4.2b, d**). The stability of the MoOS-G electrode was checked in the medium for over a month and the electrode came out as a robust and a durable electrode unlike the instability issues reported in KOH medium. Next, reactions at the counter Pt electrodes were monitored with time. For a clear understanding the electrolysis was performed in a two compartment H-cell.

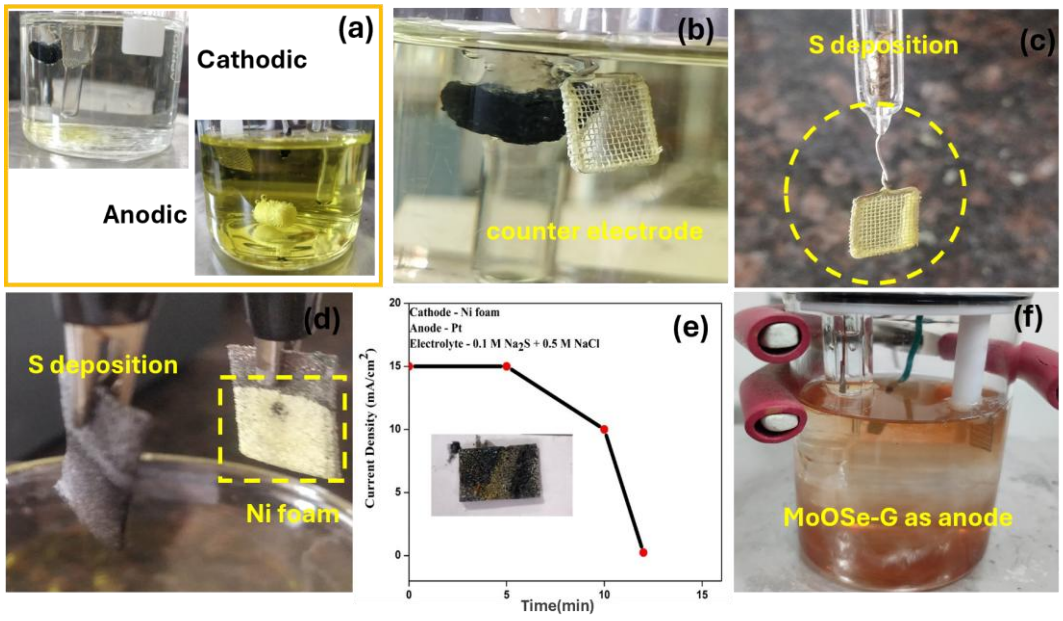

Figure 4.4 (a) Cathodic and Anodic compartments during prolonged Na_2S electrolysis (b,c) Sulfur deposition over Pt counter electrode during oxidation reaction (d-e) H_2S electrolysis with Ni foam (f) MoOSe-G electrode detoriation as anodic electrode.

Figure 4.4a shows the two anodic and cathodic compartments separately after H_2S electrolysis with MoOS-G as working electrode and Pt mesh as counter electrode. The H_2 production from H_2S splitting at the cathode along with sulfion oxidation at the anodes were the probable proposed reactions in both the compartments. Elemental sulfur deposition was the prominent activity over the counter electrode alongside HER (**Figure 4.4b, c)** which was confirmed through UV-Vis spectroscopy, CHNS analysis, and acidification tests (discussed in later sections). Over time, the deposited sulfur gradually converted into polysulfide species in the Na_2S-rich medium. This transformation led to a visible color change in the anodic compartment from colorless to Yellow with time, indicating dissolution of elemental sulfur into the electrolyte. This dynamic equilibrium between sulfur deposition and dissolution effectively prevented persistent electrode passivation, allowing the anodic sulfide oxidation and cathodic hydrogen evolution to

proceed steadily over long durations without significant current degradation, further validating the cyclic sulfur redox mechanism in the system.

Since Ni foam is commonly employed as a support for generating free standing electrocatalysts, we used bare Ni foam as the working electrode to compare its HER activity with our free-standing MoOS-G electrode for HER during H_2S electrolysis (**Figure 4.4d, e**). During electrolysis, the counter reaction on Ni foam involved elemental sulfur deposition and subsequent dissolution. However, the Ni foam electrode demonstrated poor activity in the corrosive Na_2S medium and within few minutes of run, the Ni foam turned black and deteriorated structurally. A full window potential of about 2.2 V was required for a current density of 21 mA cm^{-2} clearly indicating a higher overpotential is required for H_2S splitting giving low current as compared to MoOS-G (0.8 V/ 35 mA cm^{-2}). Agitation of the anodic compartment post-electrolysis led to the collapse of the Ni foam, with the previously yellow electrolyte turning black likely due to the formation and leaching of NiS (black) species from the degraded Ni surface. This pronounced instability emphasizes that, unlike Ni foam, the MoOS-G electrode exhibits both superior HER activity and exceptional chemical durability, making it a far more suitable candidate for sustained H_2S electrolysis in alkaline sulfide-rich media. Upon using MoOS-G, MoOSe-G and graphite rod, as anodic electrodes to check their activity for OER above 1.23 V, neither of the electrodes show any significant increment in current up to 1.7 V vs RHE, suggesting minimal water oxidation. Furthermore, these electrodes exhibited poor stability at such high anodic polarizations, with noticeable deterioration and structural degradation observed beyond 1.23 V (**Figure 4.4f, Figure 4.5a**).

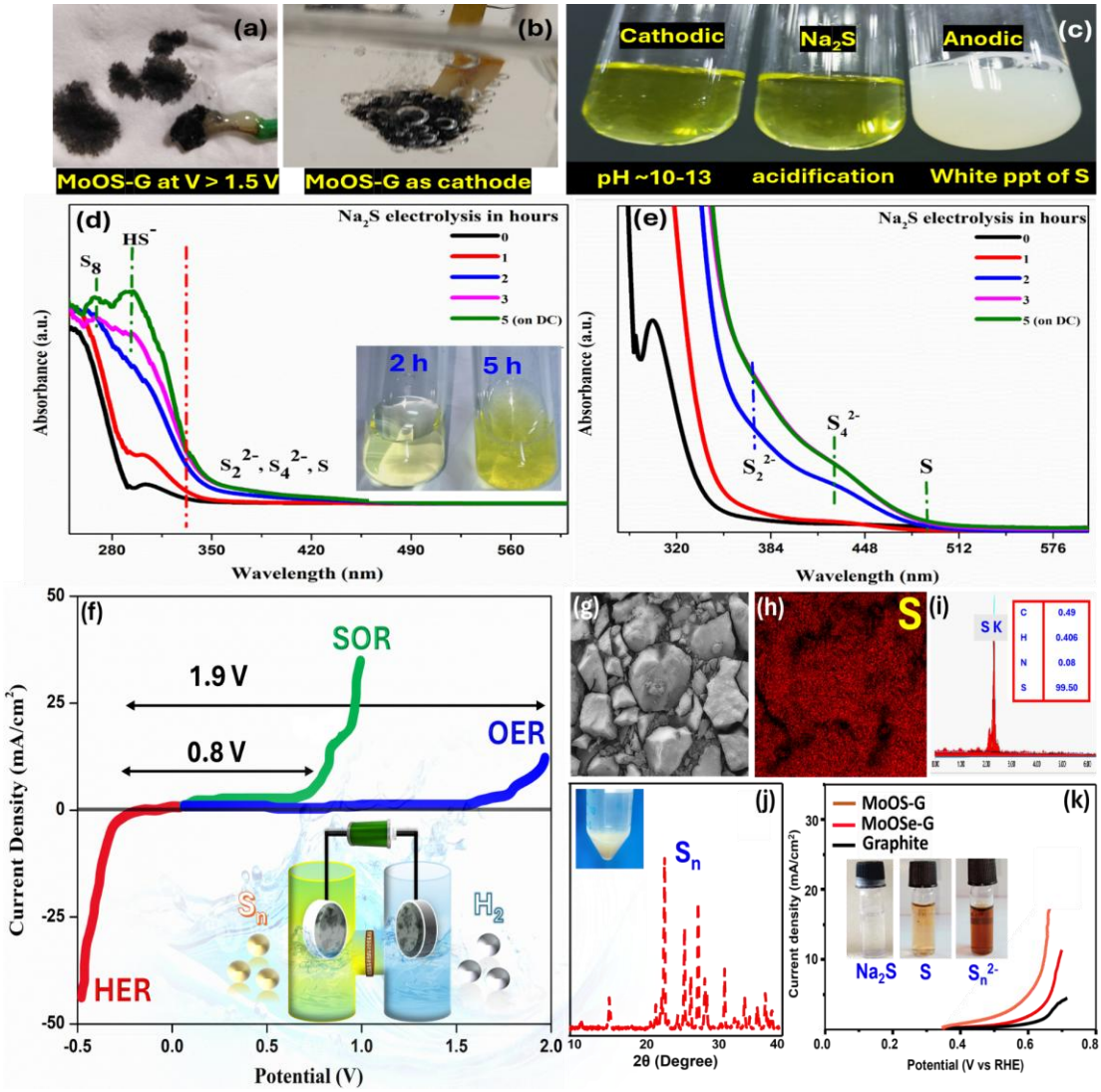

Figure 4.5 (a) The condition of MoOS-G electrode during anodic polarizations > 1.5 V in Na_2S +NaCl medium (b) Vigorous HER activity of MoOS-G in the same medium (c) Acidification of the electrolyte solution post H_2S electrolysis (d, e) UV-Vis spectra of the electrolyte post electrolysis (f) Overall electrocatalytic activity comparison of MoOS-G in Na_2S+NaCl medium (g) FESEM data (h,i) EDX and mapping data (j) XRD data of the Sn collected from the anodic solution after neutralization with H_2SO_4 (k) SOR activity of the three electrodes after 5000 cycles.

Electrochemical oxidation of sulfide to sulfur initiated at around 0.4 V vs RHE on the MoOS-G electrode's surface (**Figure A25, Appendix information**) and this high selectivity towards sulfide oxidation at the anode and the limited water oxidation efficiency is in agreement with the thermodynamically and kinetically (lower over-potential) more favorable oxidation of sulfide over oxygen evolution reaction. It is to be noted that all of

the sulfur is converted to soluble polysulfides, as the electrolyte turned yellowish after extended periods of electrolysis. So, in a nutshell, MoOS-G turned out to be the most effective HER electrocatalyst in Na_2S media and the electrode's vigorous HER activity during cathodic polarization is shown in **Figure 4.5b**.

The mechanism for the electrochemical oxidation of sulfide is complicated since sulfur has a number of different oxidation states such as −2, 0, +4, and +6. Anodic oxidation of sulfide can produce elemental sulfur, polysulfides, or sulfur oxyanions depending on the electrode composition, potential, pH, and temperature of the electrolyte [351]. In general, when hydrogen sulfide is dissolved in aqueous solution, sulfide and hydroxide ion is formed as per **eq 4.5 and 4.6**: [352]

$$Na_2S + H_2O \rightarrow NaOH + H_2S \quad (4.5)$$

$$H_2S + H_2O \rightarrow HS^- + OH^- \quad (4.6)$$

In water H_2S is a weak acid and exists predominantly as hydrogen sulfide anion. The Pk_1 and Pk_2 values of H_2S in 0.1 M KCl at 20^0C are 7 and 17 respectively (**eq 4.7**) [353]

$$H_2S + H_2O \underset{Pk_1}{\leftrightarrow} H_3O^+ + HS^- \underset{Pk_2}{\leftrightarrow} S_2^- \quad (4.7)$$

The extremely low second dissociation constant of H_2S is responsible for the fact that the S_2^- ion is only a minority species in water. Therefore, HS^- is the major sulfur species in alkaline medium prior to oxidation.

Upon H_2S electrolysis, Sulfur is formed at the anode at < 1V and hydrogen is liberated at the cathode according to the following electrochemical reactions (**eq 4.8 to 4.12**): [354]

Cathode-

$$(i) 2HS^- + 2e^- \rightarrow H_2 + S_2^- \quad (4.8)$$

$$(ii) 2H_2O + 2e^- \rightarrow H_2 + OH^- \quad (4.9)$$

Anode-

$$(i) 2HS^- \rightarrow S + H_2S + 2e^- \quad (4.10)$$

$$(ii) S_2^- \rightarrow S + 2e^- \quad (4.11)$$

$$(iii) 4OH^- \rightarrow 2H_2O + O_2 + 4e^- \quad (4.12)$$

Sulfur rapidly dissolves in the alkaline media forming polysulfides as per **eq 4.13** [355]

$$(iv) S + S_{n-1}^{2-} \rightarrow S_n^{2-} + 2e^- \quad (4.13)$$

In the context of sulfur recovery, elemental sulfur was observed to precipitate from thiosulfate decomposition only under acidic conditions, with a threshold pH of less than 4.2 (**eq 4.14**). Conversely, when the system's pH was in the alkaline range (pH 8–10), sulfur was primarily released from polysulfide species (**eq 4.15**). These observations underscore the pH-dependent equilibrium of sulfur species in solution and offer valuable insight into the selective recovery and conversion pathways for sulfur during H_2S electrolysis and related processes [356,357].

$$S_2O_3 + H_2S \rightarrow S + HS^- + HSO_3^- \quad pH < 4.2 \quad (4.14)$$

$$S_2^{2-} + H_2S \rightarrow S + 2HS^- \quad pH < 10 \quad (4.15)$$

Following H_2S electrolysis, the precipitation behavior of sulfur was evaluated by maintaining the anolyte pH at approximately 10. Under these alkaline conditions, the formation of a milky, turbid suspension in the test tube was clearly observed, indicating the presence of polysulfide species in the anolyte from which elemental sulfur precipitated (**Figure 4.5c**). Within 10-20 min this mixture becomes turbid and then looks similar to milk, under the microscope, droplets of liquid sulfur can be observed. On standing of this

sol without further stirring, a slow crystallization is observed: the first crystals occur after 3 days, and after 6 days all droplets usually have crystallized and form conglomerates which slowly settle to the bottom of the vessel. This behavior strongly suggests that the dominant sulfur species near the anode were polysulfides, as precipitation occurred readily at high pH. In contrast, if thiosulfates had been the major products, a significant drop in pH (below 4.2) would have been necessary to induce sulfur precipitation. The absence of such a requirement further confirms that oxidation of sulfur to its higher oxidation state thiosulfates did not occur appreciably during the electrolysis process. Instead, sulfur was selectively converted into polysulfide species, supporting the proposed mechanism of selective sulfide oxidation and underscoring the high selectivity and stability of the MoOS-G electrode in the anolyte compartment. Thus, the Polysulfide formation keeps sulfur in a soluble state, preventing passivation and maintaining electrode performance. This ensures continuous and stable H_2S electrolysis over time.

Ultraviolet-visible (UV-vis) spectroscopy, which is widely used in analysis of polysulfides, was opted to test the UV-vis spectra of the systems at different electrolysis times [358].The electrolyte solutions were collected after different time intervals and were checked for absorption peaks (**Figure 4.5d,e**).The UV bands in the region of 320 to 500 nm are attributed to the polysulfides S_2^{2-}, S_4^{2-},S_8^{2-} species present in the electrolyte which were formed upon sulfur dissolution. These peaks were found to be absent in the electrolyte solution before electrolysis and only the peaks corresponding to HS^- ion could be seen in the UV-Vis spectrum of the solvent. Under the conventional electrolysis pathway via OER and HER activity, the overall potential value required by MoOS-G electrode to reach the current value of 10 mA cm^{-2} was much inferior (1.9 V) suggesting that the electrodes offer

a viable power-saving option with the SOR process where only 0.8 V was required for driving a current density of 35 mA cm^{-2} (**Figure 4.5f**). The FESEM data of the S_n formed after acidification showed granules of varied sizes [359] (**Figure 4.5g**). The EDX and mapping data revealed the presence of S as the only notable constituent (**Figure 4.5h,i**).

Table 4.1 Current density obtained under different pH and electrolyte condition.

Electrode Material (1 cm^2) #	**pH**	**Electrolytes**	**Full potential (V) at which the H_2S splitting by MoOS-G proceed**	**MoOS-G Cathodic Potential (V) evaluated *via* Cathodic polarization curve**	**Cathodic Current density (mA/cm^2) obtained**	**Reference**
MoOS-G	0.00	H_2SO_4 (1 M)	> 2	active -0.35	active 25.00	This work
MoOS-G	13.00	KOH (1 M)	> 2	Insignificant	Insignificant	This work
MoOS-G	6.84	NaCl (0.5 M)	Nil	Inactive	Inactive	This work
MoOS-G	13.11	Na_2S (0.1 M)	1.2	-0.35	20	This work
MoOS-G	12.96	Na_2S (0.1 M) + NaCl (0.5 M)	0.8	-0.35	35.00	This work
MoOS-G	12.96	Na_2S (0.1 M) + NaCl (0.5 M)	0.8	-0352	71.00@	This work
Pyrolytic graphite	0.00	Na_2S (0.1 M) + NaCl (0.5 M)	>1.2	-0.5	2.25	This work
Graphite rod	12.17	Na_2S (1 M) + NaOH (1 M)	>1.2	-0.7	~11 - 15.00**	[394]

@ At the temperature of 55 degree Celsius.
** N doped graphene encapsulating Co-Ni nanoalloy as counter for SOR.
# for present work pt mesh has been used as counter electrode.

The elemental analysis also revealed the presence of '**S**' in ~99.50% in the sample supporting the above (inset of figure 4d). The XRD data of S_n extracted from the solution using H_2SO_4 matched with that of S_8 available in JCPDS 08-0247 (**Figure 4.5j**) [360] indicating elemental sulfur formation. However, our electrode MoOS-G showed decreasing SOR current density after prolonged use as an anode material (**Figure 4.6k**).

Hence the three-dimensional, self-standing MoOS-G can be effectively utilized as an efficient HER electrode alongside any stable SOR active electrode in Na_2S+NaCl medium for H_2S splitting. The electrocatalytic activity of MoOS-G across various electrolyte media has been summarized in **Table 4.1**.

The X-ray diffraction (XRD) spectrum of the MoOSe-G composite reveals four characteristic diffraction peaks at 13.70°, 31.42°, 37.88°, and 55.92°, corresponding to the (002), (100), (103), and (110) planes of $MoSe_2$, respectively, consistent with the hexagonal 2H-$MoSe_2$ phase (JCPDS No. 29-0914) [361,362] (**Figure 4.6a**). Notably, the absence of a peak at 26.62°, which is typically associated with the reduction of graphene oxide (GO) to reduced graphene oxide (RGO) [363], suggests that the reduction of GO is incomplete in MoOSe-G. Furthermore, the presence of a residual peak in the 10-12° range indicates the retention of partially oxidized GO layers. This incomplete reduction allows $MoSe_2$ layers to restack, decreasing the number of accessible catalytic edge sites [364]. Full conversion to RGO would have disrupted this stacking and enhanced exposure of active Mo and Se edge sites, thereby improving HER activity. In contrast, the XRD pattern of MoOS-G displays a broad hump centered around 26°, indicative of disordered or amorphous graphene structures. This suggests that the graphene sheets in MoOS-G are highly exfoliated, and the RGO layers are likely defective, wrinkled, and poorly stacked, which prevents compact stacking. This structural disorder enhances the availability of active edge sites. These observations are further corroborated by SEM images [discussed later], which show highly stacked GO sheets in the selenide-based MoOSe-G composite, whereas the sulfide-based MoOS-G exhibits uniform, monolayer-like exfoliated graphene.

The high degree of exfoliation and reduced restacking in MoOS-G likely contributes to its superior HER activity by increasing the density of exposed active edge sites [365].

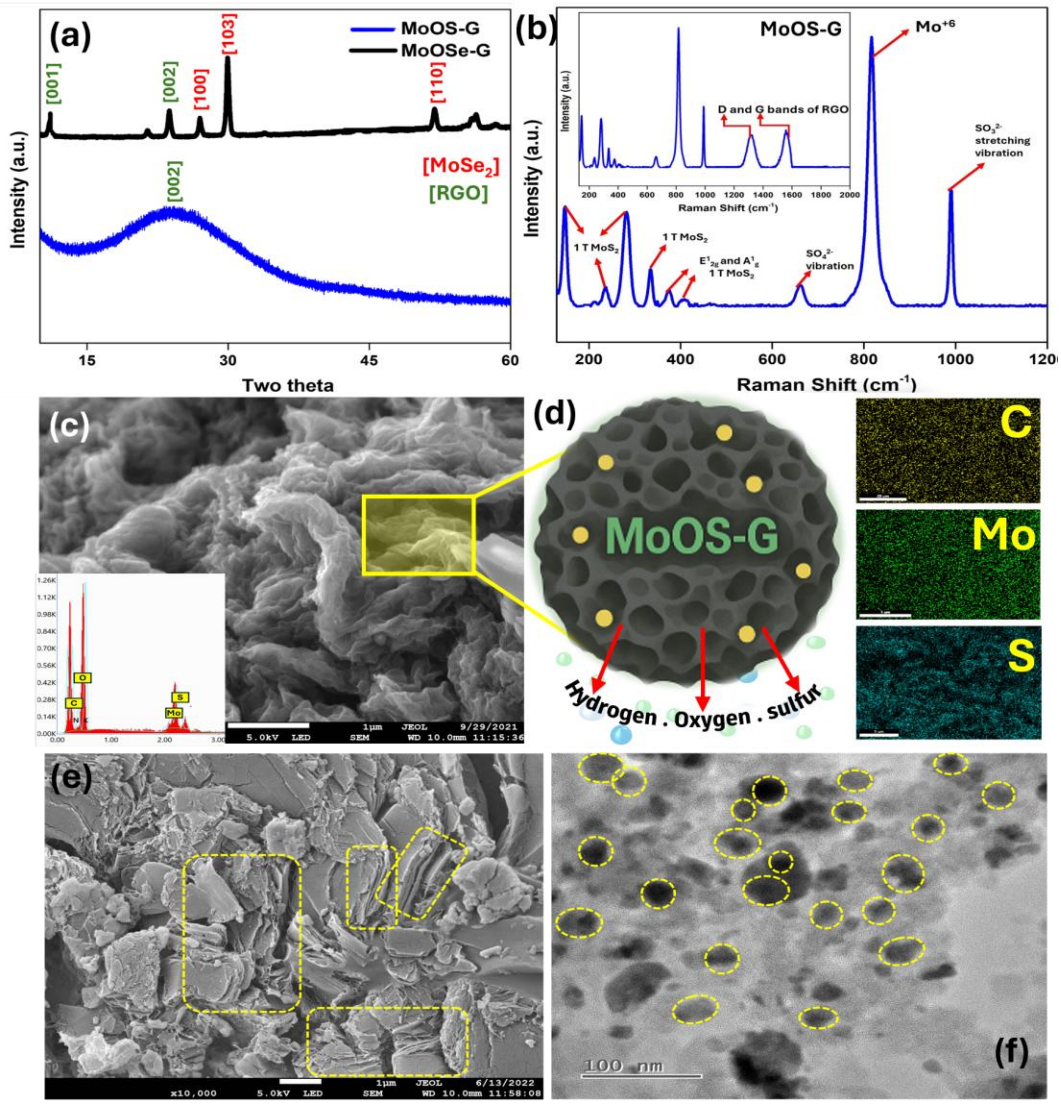

Figure 4.6 (a) XRD pattern of MoOS-G and MoOSe-G (b) RAMAN spectra of MoOS-G (c) Field Emission Scanning Electron Microscopy (FESEM) of MoOS-G , mapping inset (d) Schematic Representation and Elemental Mapping of MoOS-G (e,f) SEM and TEM Image of MoOSe-G composite.

In the MoOS-G hybrid, the intensity of all MoS_2 diffraction peaks is significantly reduced, suggesting a loss of long-range order in the MoS_2 layers. This is accompanied by the emergence of a broad peak centered at ~26.5°, characteristic of disordered or amorphous

graphene structures. This observation indicates that the incorporation of graphene during the solvothermal synthesis effectively suppresses the aggregation of layered MoS_2, leading to the formation of few-layered MoS_2 nanosheets with poor crystallinity [276]. Such nanoscale disorder is advantageous, as it increases the number of exposed active edge sites, thereby enhancing the electrocatalytic performance of the hybrid.

Moreover, the presence of reduced graphene oxide (RGO) provides a highly conductive framework that facilitates efficient charge transfer across the catalyst interface. In contrast, the partial reduction of GO to RGO in the MoOSe-G composite leads to partial restacking of $MoSe_2$ and diminished electrical conductivity, ultimately hampering HER activity compared to the sulfide-based MoOS-G system. This underscores the critical role of graphene exfoliation and reduction in enhancing catalytic performance through improved structural accessibility and electronic transport pathways.

Figure 4.6b shows the enlarged Raman spectra of MoOS-G which consist of the signature peaks attributed to MoS_2. The inset of figure 1b shows enlarged Raman spectra showing peaks at 1341 cm^{-1} and 1582 cm^{-1} attributed to the D and G bands originating from the vibrational modes of sp^3 carbon atoms in the defect sites and the in-plane vibration of sp^2 - bonded carbon atom, respectively [366]. The intensity ratio between the D band and G band (I_D/I_G) is rather large at 1.1, suggesting the high degree of sp^3 defects after the removal of the oxygenated functional groups in the hydrothermal process [367].It is important to note that the E^1_{2g} and A^1_g peaks are situated at ≈ 378.1 and 403.7 cm^{-1} which have shifted to lower wavenumbers as compared to the E^1_{2g} (380 cm^{-1}) and A^1_g (408 cm^{-1}) peaks of 2 H MoS_2. Besides , new distinct peaks are observed at J_1 (147.1 cm^{-1}), J_2 (234.0 cm^{-1}), E^1_g (282.2 cm^{-1}), and J_3(336.2 cm^{-1}), which belong to typical vibrational modes of 1T-MoS_2

, that cannot be found in 2H-MoS_2 [368] .This suggests that metallic 1 T MoS_2 phase has been formed in MoOS-G .Since the 1 T MoS_2 phase is more conductive and active compared to its 2 H phase, thus accounting for the higher HER activity of the sulfide composite compared to the selenide composite where 2H $MoSe_2$ phase is formed [discussed in XPS] which is supposed to be less conducting than the 1 T phase [369,370]. The higher defect densities in MoOS-G are well confirmed by a sharp peak can be seen at 816 cm^{-1} in the Raman spectra of MoOS-G indicating the presence of oxidized Mo in Mo^{+6} state as Defect-rich edges tend to show oxidation due to exposure to air or moisture [371]. Hence MoOS-G exhibits greater HER activity than MoOSe-G in Na_2S media. Additionally, two new peaks resulting from sulfur oxidation is observed around 650 cm^{-1} and 980 cm^{-1} range which is due to the SO symmetric stretching vibration suggesting prominent presence of the oxidized sulfur moieties in the catalyst which could be possibly due to the sulfonation of graphene sheets that accounts for its remarkable stability in Na_2S media [280].

High resolution scanning electron microscopy (SEM) at different magnifications also were employed to investigate the morphology of the obtained 3D MoOS-G electrocatalyst. Typical crumpled and corrugated morphology of twisted graphene sheets were visible as shown in **Figure 4.6c**. Due to the small size of MoS_2 nanospheres [spheres of diameter in the range 2-5 nm, as confirmed by TEM, discussed later] anchored between the graphene layers, it is difficult to see the individual MoS_2 nanoparticles via SEM imaging. Spherical structures tend to have more edge sites and defects, which favor the formation of metallic 1T phase as observed in our case [372]. **Figure 4.6d** is a schematic illustration of MoOSG and it visualizes MoOS-G as a spherical porous framework where the microstructural features indicate self-supported nanostructured frameworks, crucial for eliminating the

need for binders or external substrates. The elemental mapping labels on right show incorporation of Mo, O, S within a carbon (graphene-based) support and the Red arrows highlight the role of MoOS-G as an electrocatalyst for HER, OER, and H2S splitting, emphasizing its multifunctionality. Uniform dispersion indicates strong synergy and homogeneous mixing between MoOS active sites and the conductive graphene matrix, a key factor in enhanced catalytic performance. **Figure 4.6e and Figure A26a-d, (Appendix information)** displays the morphology of the surface of the MoOSe-G sample via SEM analysis. The structure appears non-uniform, with randomly stacked sheet-like features and less porous architecture compared to MoOS-G. The yellow dashed boxes highlight regions of agglomeration and uneven growth, which can Limit electrolyte access, reduce the 180 number of exposed active sites, impair charge transport across the catalyst. This morphology indicates inferior structural characteristics compared to the wrinkled, porous MoOS-G, likely contributing to poorer catalytic performance and reduced multifunctionality. Transmission Electron Microscopy (TEM) image in **Figure 4.6f** provides insight into the nanoscale structure of MoOSe-G. The yellow circles mark the discrete nanoparticles dispersed over the surface However, the particle distribution appears heterogeneous and non-uniform. Such uneven dispersion leads to less effective charge transfer and catalytic activity, reinforcing why MoOS-G outperforms MoOSe-G in multifunctional applications. In contrast, MoOS-G exhibits a uniform, porous, and well integrated structure, contributing to its superior electrocatalytic efficiency.

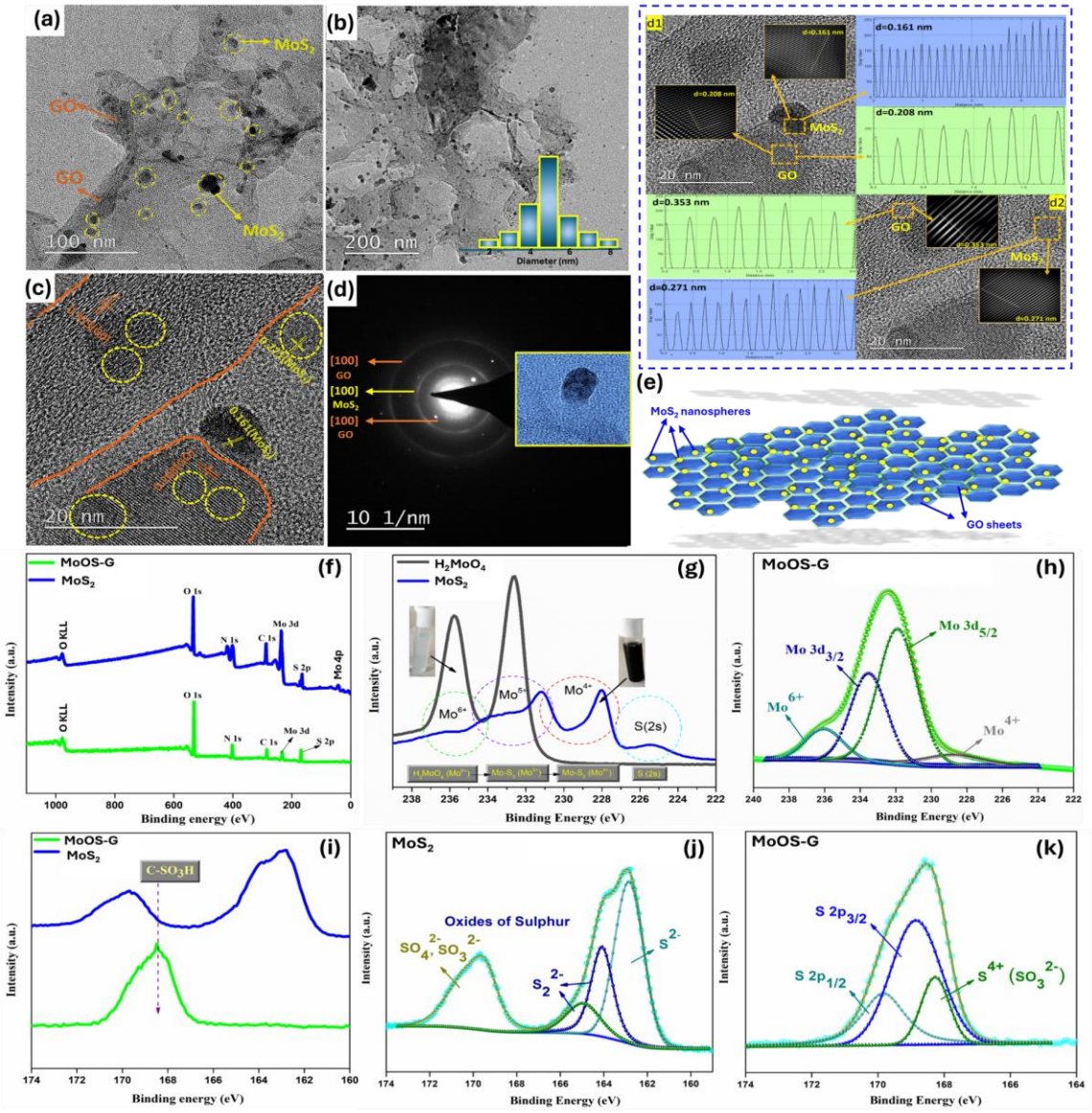

Figure 4.7(a, b) TEM images of MoOS-G electrode with its particle size distribution in inset (c,d) TEM fringes and SAED patterns of MoOS-G (d_1,d_2) plot profiles of MoOS-G (e)schematic representation of the MoOS-G electrode. XPS analysis (f) spectra for Mo-S (powder and MoOS-G (g) Mo 3d combined spectra of molybdic acid and MoOS-G (h) Mo 3d deconvoluted spectra of MoOS-G (i-k) S 2p spectra of MoS_2 powder and MoOS-G (comparison and deconvolution data).

Figure 4.7a and b display the TEM images of MoOS-G, revealing the homogeneous distribution of MoS_2 nanospheres with diameters ranging from 2 to 6 nm embedded within the reduced graphene oxide (RGO) sheets. This uniform dispersion indicates that the MoS_2 nanospheres likely nucleated and grew directly on the RGO surface, promoting intimate

contact between the two components. The spherical morphology and high surface curvature of these nanospheres introduce lattice strain and distortions, which are known to stabilize the metallic 1T phase of MoS_2 by disrupting the regular stacking of the semiconducting 2H structure [373].The measured d-spacing of 0.271 nm, as observed in the high-resolution TEM (**Figure 4.7c**), corresponds to the (100) plane of 1T-MoS_2, thereby confirming the presence of the highly active metallic phase [374]. Additionally, d-spacing values of 0.208 nm were assigned to the (100) and (110) planes of RGO [136].

Selected area diffraction pattern (SAED) of MoOS-G also confirmed the 100 (MoS_2), 100 and 110(RGO) planes of MoOS-G (**Figure 4.7d**). The plot profiles of MoOS-G are provided in **Figure 4.7 d1 and d2**. TEM shows more edge defects and disordered lattice structures in MoS_2/RGO, which explains its superior HER performance compared to MoOSe-G where fewer nanoparticles are seen distributed unevenly over the stacked graphene sheets which is somewhat reducing its activity in comparison to sulfide system (Figure 4.7f) The 3D schematic presentation of the MoOS-G as per the information from TEM is presented in **Figure 4.7e**.

XPS was utilized to further confirm the difference in crystal phases between 1T/2H-MoS_2 and 2H-$MoSe_2$ which have been confirmed so far. **Figure 4.7f** displays the XPS spectra obtained of the MoOS-G electrode which shows C 1s peak at 284 eV, a strong O 1s peak at 532 eV, S 2p peak at 168.7 and the peak for $Mo^{+4/+5}$, confirming the presence of MoS_2 and SO_3H group over MoOS-G. **Figure 4.7g-k** clearly show the predominant formation of sulfonated graphene and Mo-S_2 clusters inside 3-D porous architecture of MoOS-G .In order to understand the chemical composition and atom valence states of the MoOS-G nanocomposites in details, XPS deconvolution was performed. Figure 4.7(g) represents the

high-resolution Mo 3d XPS spectrum of bare MoS_2 (synthesized without graphene oxide for comparison) along with H_2MoO_4 as the precursor reference. The characteristic doublet peaks at 235.78 eV and 232.64 eV corresponds to purely Mo^{6+} species of H_2MoO_4 [378]. In contrast, the deconvoluted Mo 3d spectra of bare MoS_2 reveal the presence of Mo^{5+} and Mo^{4+} states, confirming the reduction of Mo^{6+} to lower oxidation states during sulfide formation. These valence transformations clearly indicate that Mo(V) and Mo(IV) sulfides were derived from the Mo(VI) precursor. The XPS spectra of MoOS-G (**Figure 4.7h**) shows the B.E. of $3d_{5/2}$ peaks at 229.03 eV and $3d_{3/2}$ at ~231.8 eV which can be attributed to the Mo^{4+} composition of MoS_2 in these samples.

It is worth noting that the Mo^{4+} peak slightly shifts to lower binding energy as compared with 2H-MoS_2 suggesting presence of 1T phase due to enhanced electron density [379]. The peaks appearing at 231.92 and 233.54 were related to Mo^{5+} states present in MoOS-G [375]. The Mo (V) has found in about ~82 % of the total Mo compound (**Table 4.2**). Another peak located at 235.4 eV is ascribed to $Mo^{6+.}$ The partial oxidation of unsaturated Mo atoms is responsible for the existence of $Mo^{5+/6+}$. Since Defect-rich edges tend to show oxidation due to exposure to air or moisture, so a higher intensity of oxidized Mo ($Mo^{5+/6+}$) relative to Mo^{4+} suggests more defect sites which were accountable for its noticeable HER activity. The formation of higher oxidation states i.e. MoO_3 also suggests the presence of sulfur vacancy that creates more reactive edge sites resulting in enhanced activity [380]. Similarly, the Mo 3d and Se 3d high-resolution XPS spectra of MoOSe-G showed peaks at 232.1 and 229.2 eV which belong to $3d_{3/2}$ and $3d_{5/2}$ peaks of Mo^{+4} of $MoSe_2$ in MoOSe-G whereas , the peaks situated at 54.5 eV and 55.3 eV are indexed to Se $3d_{5/2}$ & Se $3d_{3/2}$ respectively, (**Figure A26e and f, Appendix information**) indicating a pure 2H phase of

$MoSe_2$ in MoOSe-G [381] which are less active than its 1T phase. Hence the formation of 2 H phase of MoS_2 over the 1T phase of $MoSe_2$ imparts better HER activity to MoOS-G compared to MoOSe-G.

Table 4.2 Elemental composition of MoOS-G determined considering of XPS spectra shown in Figure 4.9c.

Sr. No.	Mo oxidation state	Peak Position (eV)	Area	% Ratio of Mo state
1	**Mo^{6+}**	236.05	20939.38	11
2	**Mo^{5+}**	233.52	56664.83	82
3	**Mo^{5+}**	231.90	96235.00	
4	**Mo^{4+}**	228.82	12948.35	7

In one of our previous works with MoS_2 incorporated over sulfonated RGO sheets, we proved that the sulfonic moieties incorporated in graphene sheets play a key role in providing durability to Ni foam during seawater electrolysis by acting as a chlorine repellant. Layer by layer assembly method was opted for synthesizing the active catalyst wherein MoS_2 flowers were anchored over sulfonated graphene sheets loaded over Ni foam and the 2 H phase of MoS_2 was reported to be formed contrary to the 1 T MoS_2 phase formed in the present work utilizing MoS_2 and RGO by a one-step hydrothermal route. But similar to our previous work, abundant sulfonic moieties were found to be present in our active MoOS-G electrocatalyst as confirmed by Raman earlier. The successful doping of Sulfonic groups into composite of MoOS-G electrode is clearly shown in Figure **4.7i and k**, where it is seen that the peak responsible for the apical $S^{2-}$and bridging S_2^{2-}sulphide groups is negligible in S 2p XPS spectrum of MoOS-G in comparison to the prominent peak representing the oxidized sulphur moieties around 168 eV. However, in the S 2p XPS spectra of the precursor MoS_2 powder from which the MoS_2 and graphene composite were formed, the peaks at 162-164 eV denoting S^{2-} groups were intense and majorly present in

comparison to the less abundant sulfonic peaks (**Figure 4.7j**) . Deconvoluted S(2p) XPS spectrum of MoOS-G (**Figure 4.7k**) showed peaks at 169.84 eV($S2p_{1/2}$) and 168.85 eV($S2p_{3/2}$) which were depicting sulfonic acid groups present in the electrocatalyst system [377,378].Consequently, in-Situ development of sulfonic groups over graphene along with the predominantly formed 1 T Mo-S_2 components in porous architectures of MoOS-G was confirmed which were accountable for the remarked durability as well as hyped activity as compared to the selenide counterpart as well as the bare graphite electrode in futile seawater media.

4.5.2 Electrochemical HER and OER Studies in H_2SO_4 media

Recently, our group published an article on WO_3 based electrode [33], where we reported self-assembled oxides of tungsten (SA-GWO) as an active electrode for water splitting in acidic media. Whereas, in basic media the integrity of the MoO-G (self-assembled oxide electrode) system was challenging, it was stable under acidic medium and stability in acidic media was not an issue with the sulfide/selenide systems either. So, the HER and the OER activities of all the three MoOS-G, MoOSe-G and MoO-G electrodes were evaluated in 1 M H_2SO_4 media. The LSV polarization curve (**Figure 4.8a**) clearly shows that MoOS-G has the highest HER and the OER activity in acidic medium compared to the MoOSe-G and MoO-G electrodes. The stable current density of ~25 mA cm^{-2} (HER) and 30 $mAcm^{-2}$ (OER) was observed at applied potential of -0.45 V and 1.4 V respectively in acidic media. Tafel plots were derived from the HER LSV curves and as shown in **Figure 4.8b**, the Tafel slope of MoOS-G was 222 mV dec^{-1} compared to the Tafel slope of the MoO-G and MoOSe-G which were 228 and 327 mV dec^{-1} respectively. The MoOS-G catalyst exhibits a lower Tafel slope when compared to the other prepared catalysts resulting in a higher

HER activity amongst all. The long-term stability of catalysts during HER was investigated by chronoamperometry (i-t) measurement with constant potential of -0.45 V for 1000 seconds (**Figure 4.8c**) and 500 hours (**Figure A27a, Appendix information**). MoOS-G showed a negligible decay in HER activity maintaining a constant current of 25 mA cm^{-2} for a very long time. The oxide and selenide system showed a constant current density of 17 mA cm^{-2} and 12 mA cm^{-2} respectively for the said time. Compared to our SA-GWO electrode [136], the MoO-G electrodes showed better performance towards HER and OER in acidic medium but was less efficient compared to the MoOS-G electrode in the same media as proven in the present work. After the chronopotentiometry measurement, the polarization curve before and after a time of 500 hours for MoOS-G is shown in **Figure A27b** of **Appendix information** where a small ignorable shift from the initial curve could be seen confirming the long-term electrochemical stability of the MoOS-G catalyst during the electrochemical hydrogen evolution process. **Figure 4.8d** represents a comparison of overpotential and stable current densities of all the three electrodes. It is noticeable to see that in acidic media, the MoOS-G exhibits the lowest overpotential amongst all, requiring only 280 mV to achieve a current density of 10 mA cm^{-2} in comparison to MoO-G and MoOSe-G which showed overpotentials of 390 and 540 mV respectively, at a current density of 10 mA cm^{-2} in the same media. EIS measurement was used to determine the internal resistance and to investigate charge transfer kinetics and ion diffusion process of the electrodes. The EIS measurements were carried out for all the three electrodes in 1.0 M

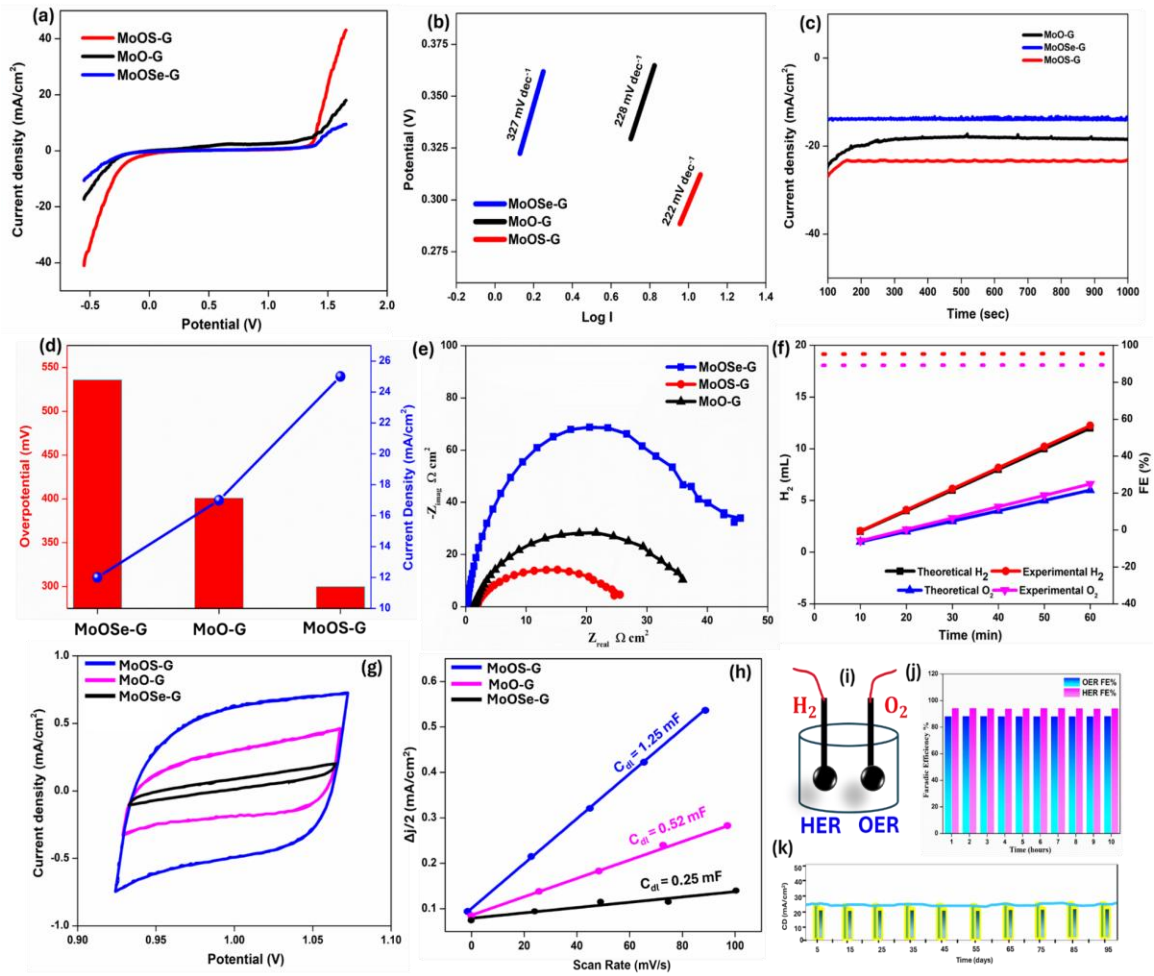

Figure 4.8(a) LSV spectra of MoOS-G, MoOSe-G , MoO-G electrode between the potential value of to -0.5 V to 1.7 V vs RHE in Na_2S (0.1 M) and H_2SO_4 (1 M) (b) corresponding Tafel analysis of the electrodes (c) Chronoamperometry spectra of the electrodes during HER at the fixed potential -0.45 V in the same medium (d) Overpotential and current density comparison data of all the three electrodes for HER (e) Nyquist plots of the electrodes (f) the Gas Evolution (H_2/O_2) and Faradaic Efficiency (FE%) of MoOS-G electrode (g, h) Cyclic Voltammetry (CV) Curves for calculating corresponding Double-Layer Capacitance (C_{dl}) (i) Representation of Bifunctional activity of MoOS-G in acidic media (j) Faradic efficiency reliability (k) MoOS-G Electrode stability data of approx. 4 months.

H_2SO_4 media at an open circuit potential and the representative Nyquist plots were plotted. **Figure 4.8e** shows that the radius of the Nyquist plots of MoOS-G is smaller than that of other two indicating the lowest charge transfer resistance and hence a better HER activity in acidic media. Rct and the solution resistance of the respective electrodes are provided in

Figure A27c of **Appendix information**. MoOS-G's 3D porous morphology and good compositional synergy facilitate rapid charge transfer, which is crucial for high catalytic performance. For the calculation of Faradic efficiency, collection and measurement of the evolved gases was evaluated through a water displacement method , and the Faradaic efficiency approaches 96 % and 87.6%, respectively, for HER and OER indicating the good selectivity of MoOS-G for HER and OER in acidic medium (**Figure 4.8f**). The excellent agreement between theoretical and experimental H_2 and O_2 volumes produced and high FE% (96 % FOR HER and 88 % for OER)without noticeable degradation underscores the superior catalytic activity and selectivity of MoOS-G for overall water splitting. CVs were recorded in a non-Faradaic potential window to calculate the Electrochemical active surface area (ECSA) (**Figure 4.8 g,h** and **Figure A28a-f** in the Appendix information) as the current density in this region is directly proportional to the surface area available for 188 charge accumulation. The graph shows the variation of ΔJ/2 (difference in anodic and cathodic current densities at a fixed potential) with respect to scan rate. The slope of the line Cdl (double-layer capacitance) was calculated to be 1.25 mF , 0.52 mF, and 0.25 mF for MoS-G, MoO-G and MoOSe-G respectively. This demonstrates that MoOS-G has a significantly higher electrochemical surface area due to its porous, well-integrated structure. Further, activity of the active electrode MoOS-G was checked in a two-electrode setup with a DC source and at a combined potential of 1.85 V, current density of 70 mA cm-2 was obtained in acidic media (**Figure A29, Appendix information**). **Figure 4.8i** shows the pictorial representation of the bifunctional activity of the MoOS-G electrode. **Figure 4.8j** displays the Faradaic Efficiency (FE%) for HER and OER across multiple time intervals (e.g., every hour up to 12 h) where both FE values remain consistently high (~98–

100%) without noticeable degradation. The reproducibility in faradic efficiency of HER and OER with time is shown in **Figure 4.8j**.The stability of the electrode was checked in the medium for over 4 months and the electrode came out as a robust and a durable electrode unlike the instability issues reported in KOH medium during anodic polarizations, (**Figure 4.8k**) suggesting great endurance and incomparable stability in the acidic media. To account for the reason behind the observations, information obtained from material characterizations of all the 3D self-assembled systems were corelated with their activity and conclusions were reached as explained in the next section.

4.5.3 Explanation of the observed activity trend

The Raman spectra of MoO_3 (**Figure 4.9a**) shows no Raman peak at around 990 cm^{-1} and 400–700 cm^{-1} due to the absence of Mo=O and Mo_2O_2 entities which suggests the formation of the β-MoO_3 phase [382].Moreover, two intense peaks at 850 and 776 cm^{-1} were identified which correspond to vibrational modes of the monoclinic phase of MoO_3 i.e. β-MoO_3 [383]. Also, at lower frequency, the peaks at 285 cm^{-1} and 330 cm^{-1}, which are usually the Mo-O-Mo deformation modes seen in β -MoO_3 are found to be present confirming β-MoO_3 formation, which are the catalytic active phases of Molybdenum oxides [384,385]. The XRD pattern of MoO-G and its precursor powder MoO_3 is shown in **Figure 4.9b**.A broad diffraction peak centered at 24.56°, corresponds to the (002) plane of RGO, which overlaps with and dominate the weaker MoO_3 peaks [low content of MoO_3] in MoO-G leading to a strong carbon signal. However , the peaks 2θ = 13.3, 23.5, 26.0, 27.6, 34.1, 39.3, 46.4, 49.6, 52.9, 55.6 and 59.0 corresponding to the (001), (101), (022), (011), (111), (033), (112), (020), (121), and (014) crystal planes of the β-MoO_3 phase is identified [385] in the precursor powder MoO_3, which is formed hydrothermally from

molybdic acid in the absence of Graphene oxide , likely suggesting the formation of the active β-MoO_3 phase in MoO-G as well, as, this is prepared likewise in graphene oxide presence. Besides, it is worth mentioning that the HER activity mainly comes from oxygen vacancies and Mo^{6+} reduction in the bare MoO_3 precursor powder to Mo^{5+}/Mo^{4+} in MoO-G , reduces the catalytic edge sites in the case of MoO-G (**Figure 4.9c**),unlike MoOS-G (having Mo as Mo^{5+}/Mo^{6+}) which is rich in edge sites and defect density, possibly accounting for its lower catalytic activity in comparison to MoOS-G. However, when comparing β-MoO_3 (monoclinic molybdenum trioxide) and 1T-MoS_2 (metallic molybdenum disulfide) for Hydrogen Evolution Reaction (HER), 1T-MoS_2 has a Metallic conductivity (~10^3 S/cm), significantly better for electron transfer in HER than β-MoO_3 (~10^{-6} S/cm) due to its semiconductor nature [386]. SEM and TEM images of MoO-G (**Figure 4.9d-f and Figure A30a-c of Appendix information**) shows irregular nanorods or porous networks like structures which are randomly oriented with nanoscale width (80–100 nm) for individual rods and these nanostructures are scattered over the RGO sheets confirming the formations of β-MoO_3 as this form is usually reported in nanorod like morphology [387-389].

The EDX data (**Figure 4.9g,h and Figure A30d of Appendix information**) reveal that Mo and O were uniformly distributed throughout the nanorods, which confirms the Molybdenum oxide nanorod formation and confirms the presence and uniform distribution of these elements.

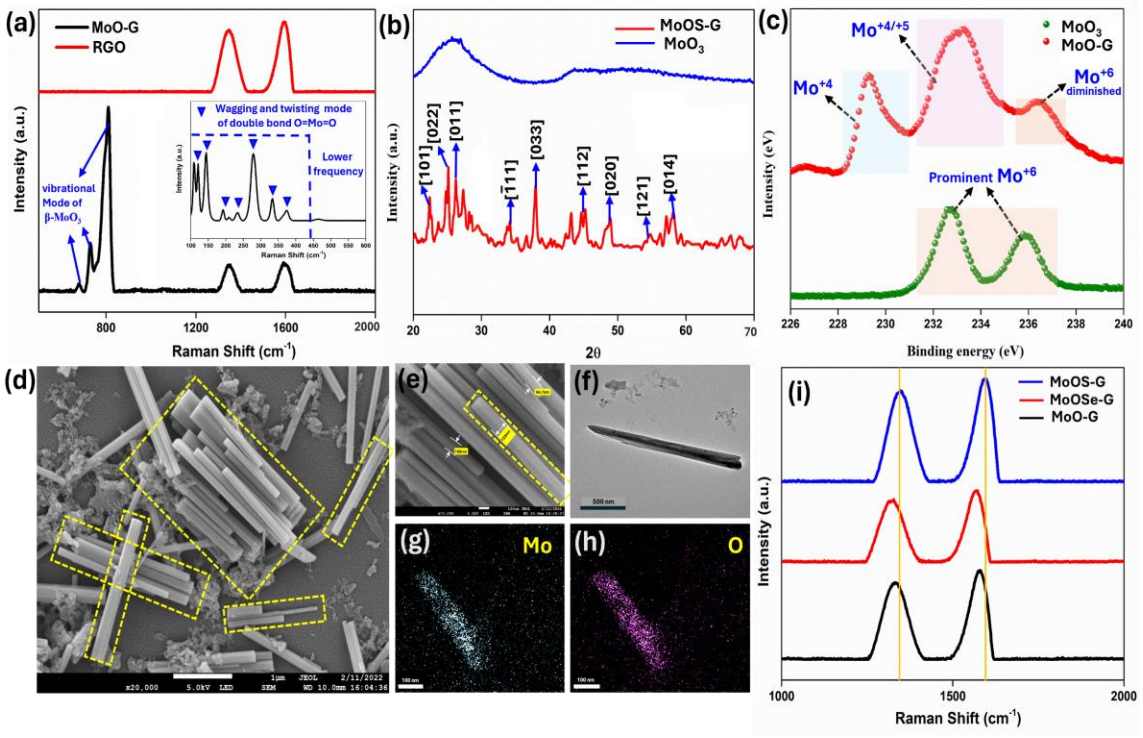

Figure 4.9 (a) XRD pattern of MoO-G (b) RAMAN spectra of MoO-G and MoO_3 powder (c) Mo 3d XPS spectra of MoO-G and MoO_3 powder (d, e) SEM image of MoO-G (f) TEM images of the MoO-G nanorods (g,h) EDAX image of MoO-G (i) RAMAN spectra of the electrodes.

The trend of activity in the acidic media follows MoOS-G>MoO-G>MoOSe-G. This trend is interesting because $MoSe_2$ is generally expected to outperform MoS_2 due to better conductivity and hydrogen adsorption properties. However, in our case the formation of a more conductive and active phase of MoS_2 compared to the formation of a less active phase of $MoSe_2$ has reversed the activity order that can be seen in both the media. The trend observed in our case can be explained by several factors:

First of all, MoS_2 is more stable in acidic conditions compared to $MoSe_2$ and MoO_2. $MoSe_2$ tends to degrade more rapidly in strong acids due to higher susceptibility to hydrolysis, leading to structural deterioration and lower HER activity over time. However, self-assembled MoO-G is less prone to oxidation and dissolution in acidic media, which may

explain its better activity in acidic media compared to MoOSe-G. Previously our group has reported self-assembled transition metal oxide to be extremely stable under acidic conditions. From previous findings , it can be concluded that the presence of oxygen vacancies or active phases (β-MoO_3) can enhance conductivity of MoO-G in comparison to MoOSe-G ,where, fewer Se vacancies were reported alongside lesser edge sites due to the stacked GO sheets accounting for the better activity of MoO-G compared to MoOSe-G. **Figure 4.9i** shows the Raman spectra where ratio of I_D:I_G bands of all the three transition metal chalcogenides during the electrolysis reaction in acidic media are calculated. The ratio was found in the order MoOS-G (1.1> MoO-G (0.93) >MoOSe-G (0.83), reconfirming our observed trend, as, higher the ratio, more the defect density, better the activity! Besides, MoOS-G typically involves the participation of high-valent metal centers (Mo^{6+}) as active species which contrasts with the reduced states ($Mo^{4+/}Mo^{5+}$) commonly observed in Mo oxides (MoO-G) and selenides (MoOSe-G). The presence of Mo^{6+} in MoS_2 facilitates the adsorption and desorption of oxygen intermediates more efficiently, enhancing OER kinetics in acidic media. Moreover, while MoO_3 (in MoO-G) already possesses Mo-O bonds, it exhibits limited ability to further interact with OER intermediates. This inherent Mo-O bonding restricts the dynamic formation and cleavage of oxygen-containing species (e.g., *OOH, O, OH), resulting in lower OER activity whereas, MoS_2 benefits from both higher conductivity and the presence of sulfur vacancies, which serve as additional active sites and promote favorable charge transfer during the reaction. So overall, from a material stability and performance perspective, MoOS-G (sulfide) offers a balanced combination of high conductivity, structural stability in acidic media, and rich surface reactivity due to S-vacancies and high-valent Mo centers. MoO-G

(oxide), while more chemically stable than MoOSe-G (selenide), suffers from poor electrical conductivity and fewer active sites, limiting its OER performance. MoOSe-G, on the other hand, exhibits the lowest OER activity among the three due to its susceptibility to dissolution in acidic conditions, limited active site density, and weaker Mo–O interactions.

4.5.4 Stability and Structural Integrity of MoOS-G Catalyst Post-HER in Na_2S and H_2SO_4 media

The structural and chemical stability of the MoOS-G catalyst after prolonged HER testing in futile seawater and acidic media is clearly evidenced through a combination of XPS, SEM, EDX mapping, and electrochemical analysis after continuous oxidation of 12 h. PostHER high-resolution XPS spectra reveals that the oxidation state of Mo remains almost unchanged, indicating the structural robustness of the Mo-containing active sites. Similarly, sulfur species remain intact, particularly the sulfonic-type S moieties, which are still prominently visible with the binding energy of S 2p is shifted toward a lower energy direction, revealing the reduction and oxidation process. This again contrasts starkly with commercial MoS_2 powder, where apical and bridging sulfur species were prominent before and after HER, indicating more dynamic surface chemistry and possibly degradation under operating conditions (**Figure 4.10a,b**). Morphological analysis via SEM before and after HER shows no significant change in surface texture or catalyst degradation. EDX elemental mapping confirms the persistent and uniform distribution of Mo, S, and C, indicating no leaching or surface restructuring. Additionally, EDX quantitative data after HER verifies that the elemental composition remains consistent, further supporting the stability of the composite electrode (**Figure4.10d,e**). Given the vast reserves of hydrogen

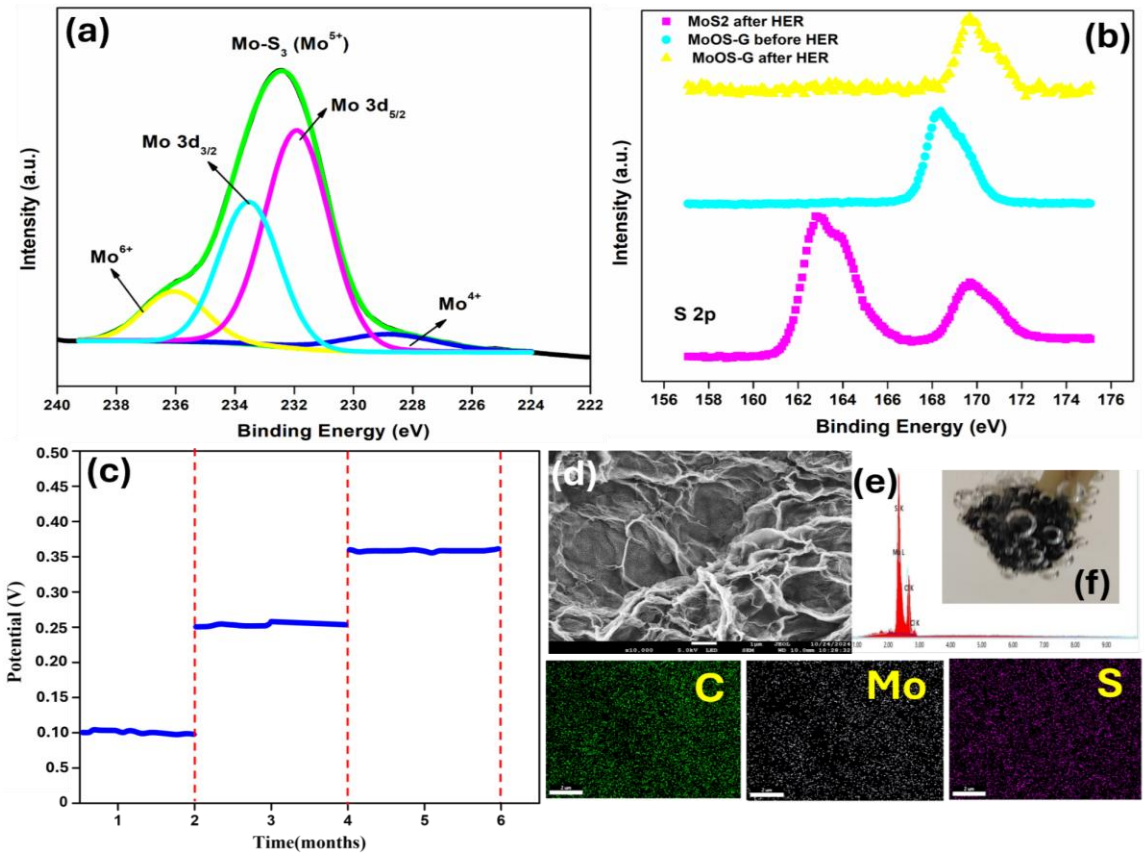

Figure 4.10 Post-HER characterization of the MoOS-G electrocatalyst in futile seawater and acidic media: (a-b) High-resolution XPS spectra of Mo 3d and S 2p regions (c) Chronopotentiometry curve showing stable and stepwise potential response at increasing current densities (10, 25, and 35 mA/cm^2) (d,e) SEM images and corresponding EDX elemental maps (f) HER evolution activity of the MoOS-G electrode post prolonged use.

sulfide-rich water in natural anaerobic environments like the Black Sea, developing electrocatalysts such as MoOS-G, capable of efficiently electrolyzing such sources is of great significance. Motivated by this, we evaluated the electrochemical stability and reproducibility of MoOS-G, during H_2S electrolysis via chronopotentiometry. The chronopotentiometry curve exhibits a stepwise increase in potential corresponding to incremental increases in current density (10 → 25 → 35 mA cm^{-2}), with stable plateaus at each level (**Figure 4.10c**). This behavior reflects not only the excellent durability of the catalyst but also its reliable and responsive electrochemical behavior, a hallmark of a robust

electrode under realistic operating conditions. Together, these multi-technique characterizations clearly demonstrate that MoOS-G retains its structural, chemical, and electrochemical integrity even after aggressive HER operation, making it a reliable and durable multifunctional electrocatalyst. The excellent gas evolution activity of the electrode remains intact with prolonged use and can be seen in **Figure 4.10f**.

4.5.5 Electrochemical ORR Studies in KOH media

Since MoS_2 has been widely explored as an ORR electrocatalyst for fuel cells [390], we tested the ORR activity of our most active electrode (MoOS-G) in H_2SO_4 and KOH media. The ORR performance of MoOS-G was first evaluated in an O_2-saturated 0.1 M KOH solution using the rotating disk electrode (RDE). **Figure 4.11a** shows the CV curves of MoOS-G for oxygen reduction reaction (ORR) in aerated and oxygen-saturated systems in the potential window from -0.2 V to +1.0 V vs RHE at the scan rate of 5 mV/s in 0.1 M KOH.CV data reveals a notable reduction peak at 0.81 V, suggesting MoOS-G has good electrocatalytic ORR activity. Further, to get more insight into the mechanism and calculating the e^- transfer number (n) of MoOS-G, ORR polarization curve was recorded in the potential range from -0.2 V to +1.0 V vs. RHE using rotating ring disk electrodes (RRDE) at 5 mV/s. The rotation speed of the electrode was limited from 200 to 2400 rpm. The resulting Koutecky–Levich (K-L) plot [391] (j^{-1} versus angular speed$^{-1/2}$) for different potentials (0.66, 0.68, 0.70, 0.72 V) was used to estimate the average number of electrons transferred per catalytic event. The transferred number of electrons during the ORR process were found to be 4 in the subjected potentials.

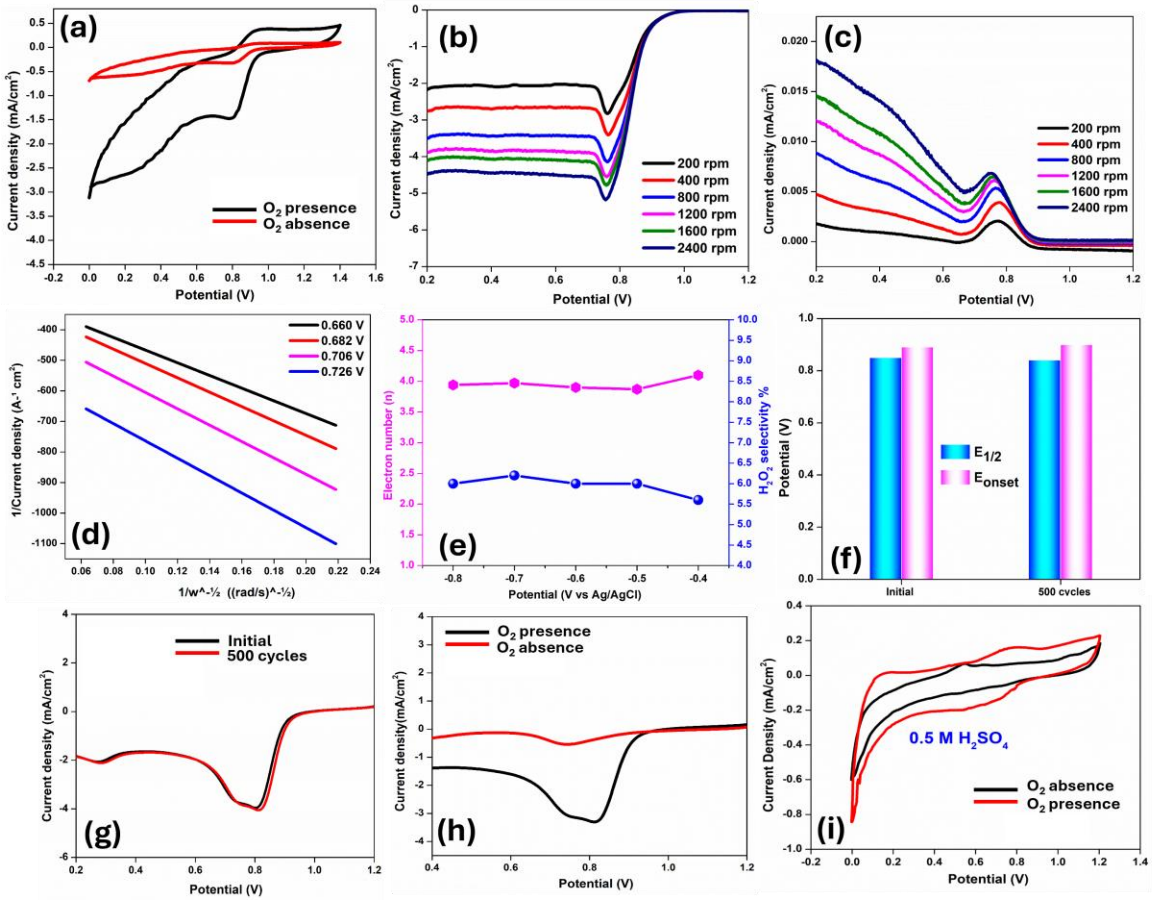

Figure 4.11 a) CV for ORR of MoOS-G recorded at scan rate 30 mV/s in aerated and O_2 saturated 0.1 M KOH (b, c) Disk and Ring current vs. disk potential for RRDE with ring polarized at 1.2 V vs. RHE in 0.1 M KOH (d) the resulting K-L plot (j^{-1} versus angular speed$^{-1/2}$) for different potentials (e) Electron transfer no and H_2O_2 Molar selectivity at different potentials (f) $E_{1/2}$ and E_{onset} at different time intervals (g) Stability data during ORR of MoOS-G (h) ORR activity of MoOS-G after a period of 6 months (i) ORR activity of MoOSe-G in H_2SO_4 media.

The below mentioned K-L equation (**equation 4.16 and 4.17**) has been used to calculate the number of electrons (n)

$$\frac{1}{j} = \frac{1}{j_L} + \frac{1}{j_K} = \frac{1}{B\omega^{0.5}} + \frac{1}{j_K} \qquad (4.16)$$

$$B = 0.62nFC_{O2}D_{O2}^{\frac{2}{3}}\nu^{-\frac{1}{6}} \qquad (4.17)$$

Where, j is the measured current density from the disk electrode of RRDE and ω is the electrode rotating rate or angular speed (rad s^{-1}). B is determined from the slope of the

Koutecky–Levich plot. J_L and J_K are the diffusion and kinetic-limiting current densities, n is the transferred electron number, F is the faraday constant (96485 C mol^{-1}), CO_2 is the concentration of oxygen in an oxygen-saturated solution (0.1 M KOH) (1.2 x 10^{-6} mol cm^{-3}), Do_2 is the diffusion coefficient of O_2 (1.9 x 10^{-5} cm^2 s^{-1}), and *v* is the kinetic viscosity (1.01 x 10^{-2} cm^2 s^{-1}) [235,392] .The constant 0.62 is used when the rotation speed is expressed in rad s^{-1}. The $4e^-$ pathway was also validated by spotting H_2O_2 with the help of the ring electrode of RRDE. **Figure 4.11b-c** shows the disk, and the ring current recorded in the RRDE experiment in 0.1 M KOH. For this evaluation, potential 1.2 V vs. RHE was applied to the Pt ring and the respective KL plots were plotted (**Figure 4.11d**) confirming the 4 e- pathway. Further , the H_2O_2 yield [393] was estimated and a yield <6% was calculated over the potential range of 0.8−0.2 V, suggesting negligible formation of H_2O_2 (**Figure 4.11e**).The LSV measurements confirmed that MoOS-G had an onset potential and half-wave potential ($E_{1/2}$) of 9.0 and 0.85 V, respectively, close to Pt/C (1.01 and 0.90 V) (**Figure 4.11f**), suggesting a good ORR performance. Also, the ORR curve after 500 CV cycles suggested negligible shifting in the half wave potentials of MoOG-S (**Figure 4.11g**). The electrode was frequently tested for a period of 6 months and each time it retained its ORR activity (**Figure 4.11h**), highlighting its stability as an effective ORR electrocatayst. Thus, together, all these results confirm the superior ORR kinetics of the MoOS-G surface predominately, via $4e^-$ pathway under the subjected electrolyte and potentials. From our previous observations, we can conclude that the reason behind the ORR activity of MoOS-G might be attributed to the edge sites of MoS_2 (S vacancies, Mo atoms), which are highly active for ORR. Since, RGO prevents the excessive stacking of MoS_2, exposing more edge sites, thereby improving its ORR catalytic activity. Besides the S vacancies in MoS_2 serve

as active centers, promoting the adsorption of oxygen intermediates (O_2, OOH^-, OH^-). The ORR activity of MoOS-G was nil in the 1 M H_2SO_4 media (**Figure 4.11h**).

4.6 Conclusion

Multifunctional electrocatalysts active for electrode reactions such as ORR, OER, and HER is vital for sustainable energy systems. We developed three-dimensional (3D), self-assembled, freestanding graphene-based composites named MoOS-G (sulfide), MoOSe-G (selenide), and MoO-G (oxide), as electrocatalysts operative in acidic (H_2SO_4), alkaline (KOH), and sulfide-rich (H_2S) media. Among them, MoOS-G demonstrated the highest electrocatalytic performance and long-term stability, achieving a current density of 25 mA cm^{-2} at 350 mV overpotential for HER/OER in acidic media. In alkaline conditions, MoOS-G remained structurally stable, though with moderate activity. Notably, in a Na_2S + NaCl electrolyte, MoOS-G enabled selective H_2S electrolysis at a low cell voltage of 0.8 V, achieving 35 mA cm^{-2}, vastly outperforming conventional water splitting (which required 1.9 V to reach 10 mA cm^{-2}). Concurrently, high-purity sulfur (~99%) was recovered at the counter electrode. Additionally, RRDE measurements confirmed a 4-electron ORR pathway with a high onset potential of 0.97 V in alkaline solution. These results establish MoOS-G as a robust, chloride-tolerant, and multifunctional electrocatalyst capable of driving diverse energy-relevant reactions, offering a promising platform for integrated and efficient energy conversion technologies.

Chapter 5: Development of Palladium decorated Nitrogen Doped Graphene For dual applications in energy conversion and electrochemical Sensing.

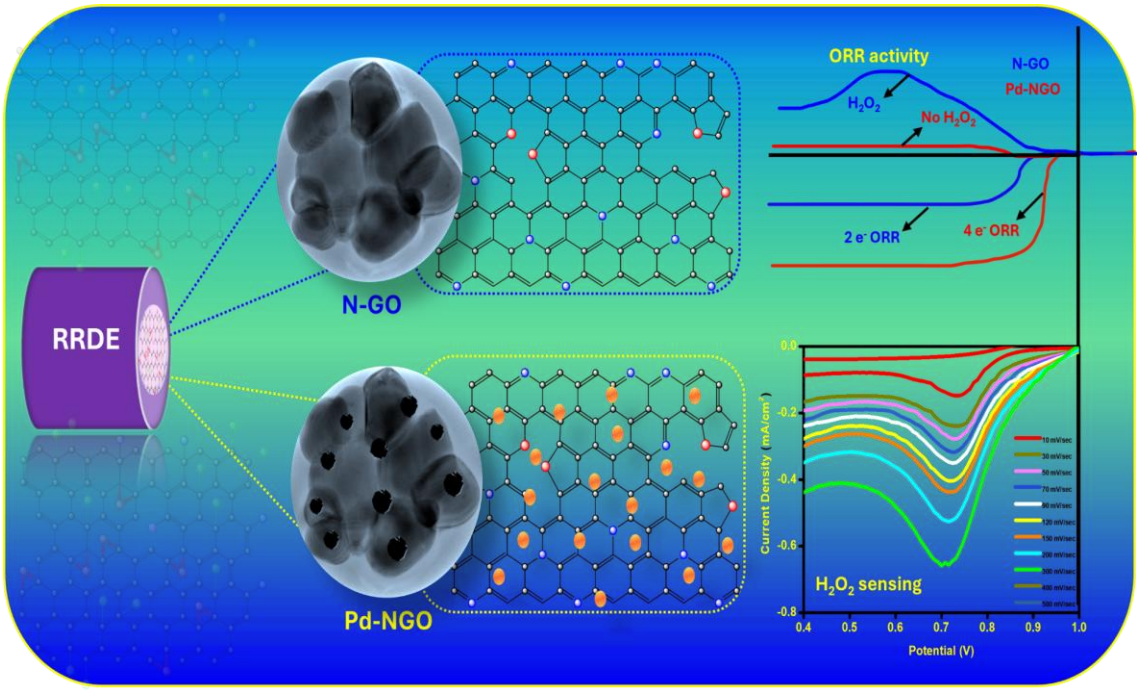

We developed Pd-NGO as an efficient ORR electrocatalyst with integrated sensing capabilities, which addresses both energy conversion and real-time monitoring in a single material platform. This dual-functionality enables next-generation smart electrochemical systems for wearable electronics, implantable biosensors, and autonomous energy-sensing device

(This work is published in ACS Applied Nano Materials, 2025, DOI:10.1021/acsanm.5c03065).

5.1 Abstract

This study presents a Pd-N-doped reduced graphene oxide (Pd-NGO) composite as a promising catalyst for the oxygen reduction reaction (ORR) and a platform for non-enzymatic H_2O_2 sensing. Pd-NGO was synthesized via a simple reduction method using $PdCl_2$ without capping agents or stabilizers. XPS confirmed the successful incorporation of Pd into N-doped graphene oxide (NGO), while TEM revealed Pd nanoparticles (3-8 nm) dispersed on the NGO sheets. The increase in Pd 3d binding energy and changes in Raman spectra indicated interactions between Pd and nitrogen dopants, particularly 2D embedded pyridinic nitrogens, which are enriched at graphene edges and act as robust anchoring points. This coordination upshifts the Pd d-band center by +0.27 eV, as supported by density functional theory (DFT) calculations, enhancing oxygen adsorption and favoring the 4-electron ORR pathway in alkaline media, significantly enhancing its catalytic performance compared to NGO, which favors the 2-electron pathway. In contrast, pyrrolic N plays a complementary role, stabilizing Pd dispersion, mitigating nanoparticle migration, and preserving long-term durability. The versatility of Pd-NGO was further demonstrated by fabricating a non-enzymatic screen-printed electrode (SPE) for H_2O_2 detection. The sensor exhibited a low detection limit (260 μM), high sensitivity (0.055 $\mu A \mu M^{-1} cm^{-2}$), and remarkable selectivity, repeatability, and stability. The combination of exceptional ORR activity, facile and scalable synthesis, and robust dual functionality positions Pd-NGO as a promising candidate for both sustainable energy conversion and practical electrochemical sensing applications.

5.2 Introduction

Graphene, a two-dimensional sheet of sp^2-hybridized carbon atoms, is widely recognized as the fundamental building block for various graphitic materials such as carbon nanotubes (CNTs), fullerenes, and graphite [394]. Due to its exceptional chemical, mechanical, and optical properties, graphene has garnered significant attention for applications in energy storage and conversion devices [395], as well as in sensors [396,397]. In recent years, heteroatom-doped graphene incorporating elements such as nitrogen (N), boron (B), sulfur

(S), and phosphorus (P) have emerged as a promising material for the oxygen reduction reaction (ORR) in alkaline media [395]. Literature reports indicate that substituting carbon atoms in the graphene lattice with heteroatoms like nitrogen or boron significantly enhances its electrochemical properties [398,399].Nitrogen doping is particularly favorable due to its atomic size compatibility with carbon, and its lone pair electrons introduce n-type semiconducting behavior, thereby improving the electrocatalytic performance of graphene [400,401]. Notably, N-doped graphene has demonstrated excellent ORR catalytic activity and stability, even surpassing platinum in alkaline conditions [395].To date, N-doped graphene has been synthesized using methods such as chemical vapor deposition (CVD) [401], arc-discharge of graphitic electrodes in pyridine vapor [9], thermal exfoliation of graphite oxide (GO) in ammonia [402], and nitrogen plasma treatment [403]. However, these methods often involve toxic precursors, high costs, and limited control over nitrogen content and bonding configurations, which critically influence catalytic performance. While high-quality graphene is typically synthesized via CVD [398], the development of cost-effective, scalable, and environmentally friendly methods for producing high-quality graphene remains a significant challenge. Several studies attribute the enhanced ORR activity of N-doped graphene to specific nitrogen functionalities, particularly pyridinic and graphitic nitrogen sites [404,405]. Therefore, the development of a facile and scalable method for synthesizing N-doped graphene with controlled size and nitrogen functionalities remains an area of active research.

Palladium (Pd) nanoparticles have garnered significant attention in the field of non-enzymatic sensors due to their exceptional electrical conductivity, chemical stability, high catalytic activity, and tunable particle size [406]. These properties make them ideal

candidates for applications such as oxygen reduction reactions. These Pd Catalysts with active sites that facilitate ORR can also promote redox reactions of H_2O_2 such as its oxidation or reduction because the potential window used to probe ORR often overlaps with the potential range where H_2O_2 undergoes redox reactions [395]. This overlap means that a material designed for ORR is already electrochemically optimized to detect or convert H_2O_2 which makes them promising candidate for electrochemical sensing applications. However, one of the challenges in utilizing Pd nanoparticles is their tendency to aggregate due to high surface energy, which results in a reduced catalytic performance. This aggregation limits their practical applications by decreasing the effective surface area and, consequently, the number of accessible active sites for catalysis. To overcome this issue and enhance Pd utilization, Pd nanoparticles are often dispersed onto support materials that not only prevent aggregation but also increase the number of active sites available for catalysis. Carbon-based nanostructures, such as graphene and carbon nanotubes, have been widely explored as support matrices [407-409]. These materials provide a stable platform for the uniform dispersion of metal nanoparticles, ensuring that Pd remains highly accessible while maintaining its catalytic activity. Several synthetic strategies have been developed to anchor Pd nanoparticles onto carbon materials. Often, these methods involve the use of surfactants, stabilizers, or ligands to control the size, shape, and dispersion of Pd nanoparticles. For instance, Shen et al. [407] employed bromide ions (Br^-) as a capping agent and polyvinylpyrrolidone (PVP) as a stabilizer to synthesize Pd nanocubes on nitrogen-doped graphene for the non-enzymatic detection of nitrite. Similarly, Wu et al. [408] utilized poly (diallyl dimethylammonium chloride) as a capping agent to facilitate the in-situ growth of Pd nanoparticles on graphene, creating a

composite material that demonstrated efficient electrocatalytic activity for triclosan detection. Zhang's group [409] and Wang's group [410] also used PVP as a stabilizer to synthesize bimetallic Pd-based carbon composites for electrochemical sensing applications, such as hydrazine, acetaminophen, and 4-aminophenol detection, with remarkable sensitivity and low detection limits. Despite the effectiveness of surfactants and stabilizers in controlling nanoparticle size and dispersion, these additives can also have a drawback. Their presence on the nanoparticle surfaces can block active sites, hindering the full catalytic potential of the metal particles. This blockage can reduce the overall catalytic efficiency, making it essential to explore alternative approaches that do not compromise the performance of the material. As a result, there is a growing demand for surfactant-free, simple synthesis strategies that can ensure the uniform dispersion of Pd nanoparticles while preserving their catalytic activity.

As mentioned above, N-doped graphene oxide (N-GO) has emerged as an ideal carbon-based support for coupling with metal nanoparticles. Nitrogen doping not only promotes the uniform growth of nanoparticles on the graphene surface without the need for external capping agents but also enhances the catalytic activity of the resulting composites by modulating the electronic structure and improving metal-support interactions. Previously, our group reported the synthesis of nitrogen-doped graphene oxide nanospheres (N-GONs) via a simple "bottom-up" approach using dibenzo-pyrrole as the fundamental structural unit [235]. In this method, nitration served as an intermediate step, followed by hydrothermal treatment of the nitro derivatives, which introduced oxygen-containing functionalities. This was confirmed through CHNS and XPS analysis, indicating approximately 14% nitrogen and 39% oxygen content. These N-doped carbon hollow

spheres are considered ideal scaffolds for the deposition of nanomaterials, owing to their high surface area and tunable chemical functionalities, which can significantly enhance catalytic activity.

To explore their high-end electrocatalytic potential, palladium (Pd) nanoparticles were deposited onto the N-GON surface using sodium borohydride ($NaBH_4$) as a reducing agent, forming a Pd-NGO hybrid electrocatalyst. A key advantage of such metal/NGO composites is the uniform dispersion of ultrasmall Pd nanoparticles with narrow size distribution on the carbon matrix, which maximizes the number of accessible active sites and thereby enhances catalytic performance. Transmission electron microscopy (TEM) analysis revealed that Pd nanoparticles with sizes ranging from 3-8 nm were well-dispersed on the surface of N-GO sheets, with minimal aggregation observed in the Pd-NGO composite. X-ray photoelectron spectroscopy (XPS) confirmed the successful integration of palladium into the graphitic matrix, with nitrogen present exclusively in p-type pyrrolic and pyridinic configurations. A noticeable increase in the Pd 3d binding energy was observed, which can be attributed to the stronger electron-withdrawing (acidic) nature of pyrrolic nitrogen compared to pyridinic nitrogen. Complementary Raman spectroscopy further supported these findings, indicating a progressively defective graphitic structure as a result of the increased incorporation of five-membered pyrrolic rings. Importantly, the Pd-NGO nanocomposites demonstrated significantly enhanced oxygen reduction reaction (ORR) activity in alkaline media exceeding that of both undoped NGO and commercial Pt/C significantly. Additionally, control experiments using Ru-NGO indicated negligible ORR activity contributions from the NGO support under the present experimental conditions. These results underscore the critical role of nitrogen dopant type in tuning catalytic

performance and highlight a simple, energy-efficient strategy for synthesizing high-performance ORR catalysts based on heteroatom-doped GO-supported metal nanoparticles. The resulting electrocatalyst was later developed into an efficient non-enzymatic sensor which exhibited remarkable electrocatalytic activity toward hydrogen peroxide (H_2O_2) reduction with a detection limit (LOD) of 260 μM with a decent sensitivity of 0.055 $\mu A \mu M^{-1} cm^{-2}$. In addition, the sensor also showed excellent selectivity, repeatability, and stability for detecting H_2O_2. Given that Pd is significantly less expensive than noble metals like platinum and exhibits superior electrocatalytic activity and stability compared to many 3d transition metals (such as Ni, Co, and Fe), incorporating Pd nanoparticles into a high surface area N-doped graphene oxide matrix offers a promising strategy for developing efficient cathode catalysts for the oxygen reduction reaction (ORR) in fuel cells.

5.3 Experimental Section

5.3.1 Materials

Graphene oxide (GO) [prepared in lab by modified Hummer's method], NGONs (prepared in lab) [17] , Palladium chloride ($PdCL_2$)[Sigma Aldrich], Ruthenium chloride ($RuCl_3$) [Sigma Aldrich], Sodium Borohydride (NaBH4) [SRL], Hydrochloric acid (HCl) [Finer] ,Sodium hydroxide pellets (NaOH) [EMPARTA], N-methyl pyrrolidone (NMP) [SRL], polyvinyl butyral (PVB) [Otto], Ethanol (C_2H_5OH) [Changshu Hong-sheng Fine Chemical Co. Ltd], Acetone (C_3H_6O) [s d fine-ChemLimited], Methanol (CH_3OH) [s d fine-Chem Limited], Hexane [Merck Life Science Pvt. Ltd.], Hydrogen peroxide (H_2O_2) [Molychem], monobasic Sodium dihydrogen phosphate (NaH_2PO_4) [SRL], dibasic Disodium hydrogen phosphate (Na_2HPO_4) [SRL],Hexachloroplatinic acid hexahydrate ($H_2PtCl_6 \cdot 6H_2O$) [SRL],

Screen printed Carbon electrodes [Zensor].Deionized water (DI water) was prepared by redistillation of the double distilled water in a glass distillation apparatus.

5.3.2 Material characterization of Pd-NGO catalysts

Functional group identification was done by Thermo Electron Scientific Instruments LLC, Nicolet iS20, Fourier Transform Infrared Spectrometer (FTIR) in the spectral range of 350 cm^{-1} to 11000 cm^{-1}. Raman spectra of the samples were recorded in a Jasco NRS-5500 Laser Confocal Raman Spectrophotometer equipped with 1200 grooves per mm gratings, and laser spot intensity 0.0001% of microscope with objective. An Empyrean Panalytical X-ray diffraction spectrophotometer and a Rigaku Smart Lab 9 kW Powder type (without χcradle) were used to find the crystallite size, d-spacing and crystal planes. The samples were excited with a 532 nm wavelength laser from an Ar^{+} laser with fluorescent correction. The XPS measurements were recorded in the Thermo Fisher Scientific K-Alpha X-ray Photoelectron Spectrometer, which was outfitted with Al-Kα X-ray (1486.6 eV) as a primary excitation and an auto-firing, 3 filament TSP software. The curve fitting of the high-resolution spectra was performed with combined Gaussian−Lorentzian functions. The Jeol, NEOARM/JEM-ARM200F, AMI 300, High Resolution Transmission Electron Microscope (HR-TEM) was used to determine the structural identity, particle size distribution, elemental composition. Furthermore, we performed a JEOL JSM-7900F Field Emission Scanning Electron Microscope (HR-FE-SEM) to determine surface morphology and elemental confirmation.

5.3.3 Electrochemical Measurements

5.3.3.1 For electrochemical ORR studies

The ORR performances were evaluated in a conventional three-electrode setup with Ag/AgCl as a reference electrode and Pt wire as a counter electrode. The reference electrode was saturated with 3 M KCL and well calibrated with standard ferri/ferro cyanide system. For comparison, all potential values were converted and plotted with respect to reversible hydrogen electrode (RHE). The cyclic voltammograms (CV) were recorded in Argon saturated 0.1 M KOH electrolyte with a sweep rate of 10 mV s^{-1}. The ORR polarization curves were recorded in O_2 saturated 0.1 M KOH with a sweep rate of 10 mV s^{-1} at a rotation rate of 1600 rpm. The stability tests were performed at room temperature in the potential window of 0 to 1.2 V vs. RHE by applying cyclic sweeps in O_2 saturated 0.1 M KOH at 1600 rpm with a scan rate of 0.1 V s^{-1} up to 500 cycles. The electrochemical characterizations were performed using μ-AUTOLAB type-III (Serial number: μ3AUT70731). The RRDE experiments were carried out using Multi Autolab M 204 from Metrohm Autolab (Serial number: MAC90581) with a motor controller and a RRDE rotator (RRDE80292) equipped with a Pt disk (A=0.196 cm^2) and a Pt ring electrode. For peroxide detection, a potential of 1.2 V vs. RHE was applied to the Pt ring. All the potentials in this study were adjusted to the reversible hydrogen electrode (RHE) reference scale using the equation mentioned below.

E (*vs.* RHE) = applied potential (*vs*. Ag/AgCl) + E^0 [Ag/AgCl (3M KCl)] + 0.059 V (pH).

Throughout the electrochemical studies, there was a constant oxygen gas flow over the solution, and the ambient temperature was 27±1 °C.

5.3.3.2 RRDE- Collection efficiency calculation

In a typical Rotating Ring Disc Electrode (RRDE) collection efficiency experiment, the complete product generated at the disk electrode will not reach the ring electrode. The percentage of material which is collected at the ring electrode is often called the "collection efficiency" of the RRDE. One may empirically measure the collection efficiency of a specific RRDE before using it for any quantitative work. This is normally carried out using a well-defined electrochemical system such as the ferricyanide- ferrocyanide redox couple. This system can be used to measure stable collection efficiency at rates between 400 and 2000 rpm. The reactions taking place at the disk and rings are respectively: (**eq 5.1-5.2**)

$$Disk: Fe(CN)_6^{3-} + e^- \rightarrow Fe(CN)_6^{4-} \quad (5.1)$$

$$Ring: Fe(CN)_6^{4-} \rightarrow Fe(CN)_6^{3-} + e^- \quad (5.2)$$

We used an equimolar mixture (5 mM) of potassium ferricyanide [$K_3Fe(CN)_6$]and potassium ferrocyanide [$K_4Fe(CN)_6$] in a supporting electrolyte (0.1 M KOH). We performed linear sweep voltammetry a 50-mV sec^{-1} by setting the potential of the disk to 0.1 V to reduce ferricyanide to ferrocyanide and at the ring to 1.5 V to oxidize ferrocyanide to ferricyanide, respectively to record the disk current (I_d) and ring current (I_r) simultaneously under steady-state rotation. The measurement lasted 60 s and the disk and ring currents (I_d and I_r) at the last 10 s were averaged. The measurement was repeated once with the disk disconnected. The ring current (I_{r0}) at the last 10 s was averaged. I_{r0} includes all the anodic currents that are not from $Fe(CN)_6^{4-}$ reduced on the disk. They may be related to the oxidation of water, free $Fe(CN)_6^{4-}$ or any impurities. The collection efficiency value is calculated by using the following equation (**eq 5.3**):

$$N = \frac{I_r - I_{ro}}{I_d} \quad (5.3)$$

The ring collection efficiency was calculated to be 20% (or expressed as 0.20), as measured using a $[Fe(CN)_6]^{3-/4-}$ redox couple.

5.3.3.3 For Electrochemical Sensing of H_2O_2

The cyclic voltammetry and amperometry studies were performed in an electrochemical cell with an NGO and Pd-NGO coated screen-printed carbon electrode as the working electrode in the potential range of 0 to +1.5 V. All the electrochemical measurements were carried out in 10 mL of phosphate buffer solution (0.1 M, pH = 7.4) after being purged through with pure nitrogen for 15 min before the experiments. NGO/SPE and Pd-NGO/SPE were scanned for 50 cycles of oxidation and reduction in absence of analytes before use for H_2O_2 detection. Each set of experiments for detection is repeated three times.

5.3.3.4 Spin-polarized Density Functional Theory (DFT)

All calculations were carried out using density functional theory (DFT) as implemented in the Vienna Ab initio Simulation Package (VASP). The projector augmented wave (PAW) method was used in combination with the Perdew-Burke-Ernzerhof (PBE) exchange-correlation functional within the generalized gradient approximation (GGA). To account for long-range van der Waals interactions critical for the accurate description of cluster-substrate interactions, Grimme's DFT-D3 dispersion correction was employed. The simulation model consisted of a Pd_6 cluster supported on a nitrogen-doped graphene sheet, where nitrogen was incorporated in both pyridinic and pyrrolic configurations to reflect experimentally relevant defect types. The graphene supercell was constructed with sufficient lateral dimensions to minimize periodic interactions between adjacent Pd_6 clusters, and a vacuum spacing of at least 15 Å was applied perpendicular to the sheet to eliminate image interactions. A 2×2×1 Monkhorst-Pack k-point mesh was used for Brillouin zone sampling. The kinetic energy cutoff for the plane-wave basis set was chosen based on the default PAW-PBE potentials, and electronic convergence was achieved with a threshold of 10^{-6} eV for the total energy. Atomic positions were relaxed until the residual Hellmann-Feynman forces on all atoms were below 0.01 eV/Å.The d-band centre for every

Pd atom is calculated using VASPkit. The N-Pd bond distances are found to be 2.0 Å in the optimized structure, and the average Pd-Pd bond distance varies from 2.47 to 2.63 Å To probe the electronic structure of individual Pd atoms, their d-band centers (d_c) are calculated using the equation $d_c = \frac{\int_{-\infty}^{E_F} E\,\rho(E)dE}{\int_{-\infty}^{E_F} \rho(E)dE}$ where E is the energy of occupied d states of Pd atoms and $\rho(E)$ is the partial density of states of respective Pd atoms in the small energy interval dE. The energy window of integration is [-21.50 to 0.00]. The calculated band centres of the Pd atoms presented in the article are referenced to the Fermi level, i.e., E_F = 0 eV.

5.4 Electrocatalyst Synthesis

5.4.1 Synthesis of N doped Graphene Oxide Nanospheres (N-GONs)

A one-pot hydrothermal approach was used to synthesize N-doped graphene oxide (N-GO) material [235]. The as-prepared nitro-substituted dibenzopyrrole (1 g) was dispersed in 200 mL of 0.2M NaOH solution and sonicated for half an hour to restrain the agglomeration of precursor molecules. The well-dispersed suspension was then transferred into a Teflon-lined autoclave (500 mL capacity). The hydrothermal reaction was carried out at 200 °C for 10 h. After cooling at room temperature, the obtained dark color suspension was filtered using a 0.45 μm nylon membrane filter to remove large size particles. The resultant suspension was further purified in a well-sterilized dialysis bag until neutral conditions were reached. After purification, N-doped graphene oxide nanospheres (270 mg) were obtained and found highly dispersible in water.

5.4.2 Anchoring of Pd nanoparticles (Pd NPs) to N-doped graphene (Pd-NGO)

To synthesize the Pd-NGO nanocomposite, 0.1 g of palladium (II) chloride ($PdCl_2$) was first dissolved in 0.1 mL of concentrated hydrochloric acid (HCl) to form a clear solution.

This solution was then added to a dispersion of 60 mg of nitrogen-doped graphene (NG) in 60 mL of deionized water. The resulting suspension was subjected to ultrasonic agitation for 15 minutes to ensure uniform dispersion of Pd ions on the NG sheets. Subsequently, 0.021 g of freshly prepared sodium borohydride ($NaBH_4$), a strong reducing agent, was added to the mixture under continuous stirring to facilitate the in-situ reduction of Pd^{2+} to metallic Pd^0. The reduction process was allowed to proceed under mild agitation, followed by an additional 15 minutes of ultrasonication to enhance the dispersion and prevent agglomeration of the Pd nanoparticles. After the reaction, the suspension was filtered and thoroughly washed several times with ethanol to remove unreacted species and any residual impurities. The obtained solid was then dried at 60 °C for 2 hours in an oven. The final product appeared as a fine black powder, indicating successful formation of the palladium-decorated nitrogen-doped graphene composite. The catalyst was designated as **Pd-NGO**.

The as-prepared Pd-NGO composite was subsequently subjected to detailed microstructural and surface characterizations, including transmission electron microscopy (TEM), X-ray photoelectron spectroscopy (XPS), and Raman spectroscopy, to evaluate the morphology, chemical composition, and structural features of the material.

5.4.3 Anchoring of Ru nanoparticles (Ru NPs) to N-doped graphene (Ru-NGO)

Control experiments were also carried out where a stoichiometric amount (0.15 g) of $RuCl_3$ was used instead of $PdCl_2$ while keeping other experimental conditions unchanged, resulting in the formation of ruthenium nanoparticles supported on NGO. The composite was denoted as **Ru-NGO**.

5.4.4 Preparation of Pd-NGO/GCE for electrochemical ORR activity

A glassy carbon electrode (GCE) was first polished to a mirror-like finish using 1.0 μm and 0.3 μm alumina slurries in sequence to ensure a smooth and clean surface. After polishing, the electrode was thoroughly cleaned by sonication in ethanol and DI water for five minutes each to remove any residual polishing agents or surface contaminants. Separately, 5 mg of the Pd-NGO catalyst powder was dispersed in a mixture of 100 μL N-methyl-2-pyrrolidone (NMP) and 10 μL of a 2.5% (w/v) polyvinyl butyral (PVB) solution. The resulting suspension was ultrasonicated for 30 minutes to ensure uniform dispersion of the catalyst particles and formation of a stable ink. Following dispersion, 5 μL of the prepared catalyst ink was carefully drop-cast onto the surface of the pre-polished GCE using a precision microliter syringe. The modified electrode was then dried in an oven at 80 °C to facilitate solvent evaporation and strong adhesion of the catalyst film to the electrode surface for use as a working electrode. In a similar manner, the RRDE electrode was thoroughly cleaned and subsequently coated with the prepared electrocatalyst ink for ORR measurements.

5.4.5 Preparation of bulk modified screen-printed carbon electrodes (SPE) for electrochemical sensing (Pd-NGO/SPE):

Prior to electrochemical measurements, all carbon-based screen-printed electrodes (SPEs) were pre-treated by immersion in isopropanol for 20 minutes to remove any organic residues originating from the printing inks. The SPEs contained integrated silver reference and carbon counter electrodes. To prepare the catalyst ink, 5 mg of the Pd-NGO nanocomposite was dispersed in a mixture of 100 μL N-methyl-2-pyrrolidone (NMP) and 10 μL of 2.5% (w/v) polyvinyl butyral (PVB) solution. The dispersion was then

ultrasonicated for 30 minutes to achieve a stable and homogeneous suspension. For electrode modification, 10 μL of the prepared catalyst ink was drop-cast onto the working area of the pre-treated SPE. The prepared **Pd-NGO/SPE** electrode was subsequently dried at 50 °C for 30 minutes to ensure complete solvent evaporation and strong adhesion of the catalyst film.

5.5 Results and Discussions

5.5.1 Microstructural characterization of Pd-NGO electrocatalyst

Nitrogen doped graphene oxide nanospheres had been successfully synthesized *via* bottom-up synthesis approach using a nitrogen rich dibenzopyrrole *via* alkaline hydrothermal reaction and has ~13.7% of nitrogen [235]. Then, the decoration of Pd NPs was carried out on NGO by a reduction technique [411]. Further insights into the elemental compositions and valence states of the nanocomposites were obtained from the high-resolution scans of the C 1s, N 1s, and Pd 3d electrons by XPS measurements, which are depicted in Figure. The XPS survey spectrum of Pd-NGO reveals the presence of C, N, O, and Pd signals in the sample (**Figure A31, Appendix information**), which is consistent with the element composition of Pd-NGO. The high-resolution spectrum of C1s can be deconvoluted into three single peaks and these peaks correspond to C-C or C=C (284.6 eV), C-N (285.3 eV), C=N (286.5 eV), originating from the NGO layer in the Pd-NGO **(Figure 5.1a)** [412]. The main peak at 284.6 eV is associated with the C=C, implying that most of the carbon atoms in the Pd-NGO are arranged in a conjugated honeycomb lattice. The peaks at 285.35 eV and 286.5 eV confirm the presence of C=N and C–N bonding environments, indicating that pyridinic or pyrrolic nitrogen atoms have been successfully incorporated into the carbon lattice. In the N 1s XPS spectrum of Pd–NGO (**Figure 5.1b),**

two major components are observed upon deconvolution. The peak at 398.2 eV is attributed to pyridinic nitrogen, while the peak at 399.5 eV is assigned to pyrrolic nitrogen [413]. It should be noted that no quaternary nitrogen was identified at 401.7 eV as observed in the precursor N doped system without Pd [235]. Since the original NGO contained a very low percentage of quaternary nitrogen, it is likely that Pd loading further reduced or altered these sites, decreasing their concentration below the XPS detection limit. Also, the use of $NaBH_4$, a strong reducing agent, may have reduced some or all of the quaternary nitrogen atoms, transforming into other nitrogen configurations or removing entirely. So, the exclusive formation of p-type pyridinic and pyrrolic nitrogen species within the graphitic scaffold of Pd-NGO is likely due to the preferential binding affinity of palladium toward these nitrogen functionalities. As illustrated in **Figure 5.1b**, the relative abundance of pyridinic nitrogen markedly decreases, while that of pyrrolic nitrogen increases significantly in the Pd-NGO sample compared to the NGO precursor, where both nitrogen types were present in nearly comparable proportions [235]. This shift was further confirmed by the overlay of deconvoluted high-resolution N 1s spectra for NGO and Pd-NGO [**Figure A33** of **Appendix Information**].Quantitative analysis revealed that Pd-NGO contained ~8.25% pyridinic N and ~91.75% pyrrolic N, with graphitic N being negligible or below the detection limit. Given that pyrrolic nitrogen is more electron-withdrawing (acidic) than pyridinic nitrogen, the enrichment of pyrrolic sites likely leads to a notable decrease in the electron density of Pd, due to strong electronic interactions between palladium and the dopant sites. This observation is further confirmed by the Pd 3d XPS spectrum in **Figure 5.1c**, where a positive shift in Metallic Pd(0) and oxidized

Pd(+2) 3d binding energy is evident compared with the standard Pd(0) and Pd (+2) 3d binding energies [414], reflecting electron depletion from the Pd centers.

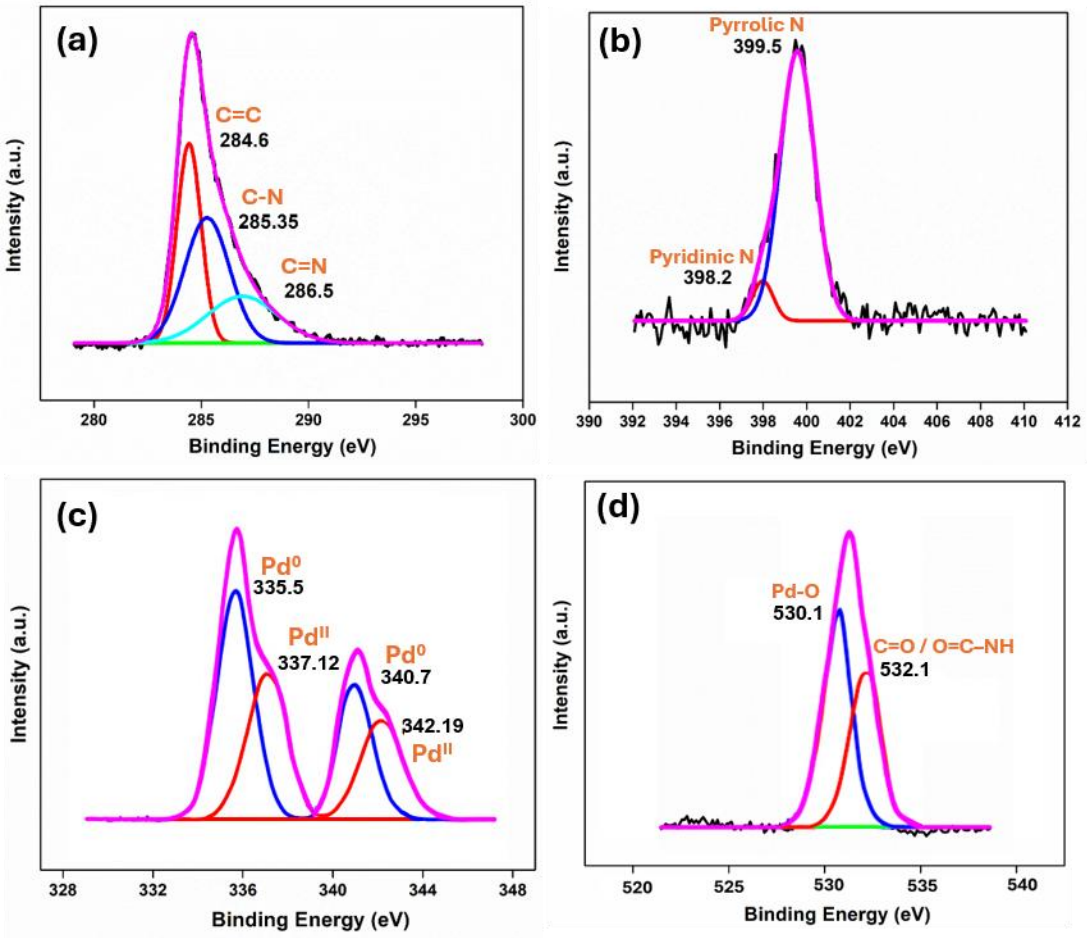

Figure 5.1 XPS analysis of Pd-NGO nanocomposite: (a) Deconvoluted C 1s spectrum showing various carbon bonding environments (b) N 1s spectrum indicating different nitrogen functionalities (c) Pd 3d spectrum illustrating the chemical state of palladium (d) O 1s spectrum representing oxygen-containing functional groups.

As shown in **Figure 5.1c**, the Pd 3d spectrum comprises two spin-orbit doublets, corresponding to metallic Pd (0) and oxidized Pd (II) states, indicating the co-existence of distinct electronic environments in the catalyst. The distinct peaks at 335.5 and 340.7 eV are assigned to Pd (0), and the weak peaks at 337.12 and 342.2 eV indicate the presence of

Pd (II) due to the partially oxidized Pd in the Pd-NGO. The O 1s XPS spectrum of a Pd-NGO Shows a peak around 530.1 eV which can be denoted to Metal-Oxygen (Pd-O) bonds arrising from Pd^{2+} species (e.g., PdO or Pd–OH) [415] (**Figure 5.1d).** The peak around 531.5–532 eV depicts Oxygen in C=O or O=C-NH Groups which might be because of the Carbonyl (C=O) groups on the GO or the possible amide or lactam-like environments due to pyrrolic nitrogen bonding [235]. Thus, XPS confirmed the incorporation of Pd nanoparticles onto the nitrogen doped 3D-Graphene matrix.

The High-resolution scanning electron microscopy (SEM) at different magnifications also were employed to investigate the morphology of the obtained Pd-NGO electrocatalyst. Typical sheet-like morphology of graphene sheets was visible as shown in **Figure A32a** of **Appendix information**. Due to the small size of Pd nanoparticles [spheres of diameter in the range 2-5 nm, as confirmed by TEM, discussed later in this section] anchored between the graphene layers, it is difficult to see the individual Pd nanoparticles via SEM imaging. However, the bigger N doped graphene nanospheres of nearly 50-60 nm size are visible with a sphere morphology (**Figure 5.2a; A32b** of **Appendix information**). TEM was used to examine the nanoparticles and interfaces in Pd-NGO with extremely high resolution. The TEM images of Pd-NGO clearly show NGO nanospheres acting as anchoring platforms for the Pd nanoparticles as lots of small Pd nanoparticles (particle sizes of 3–8 nm) have been uniformly dispersed on the NGO surface even without any additional protective reagent or surfactant in the system. These anchored Pd nanoparticles can effectively alleviate the aggregation of NGO sheets and provide more active sites, which might enhance the stability and catalytic property of the resulting Pd-NGO composite

(**Figure 5.2b;A32g, h** of **Appendix information**). To determine the elemental composition and spatial distribution of elements in Pd-NGO, EDX mapping was done.

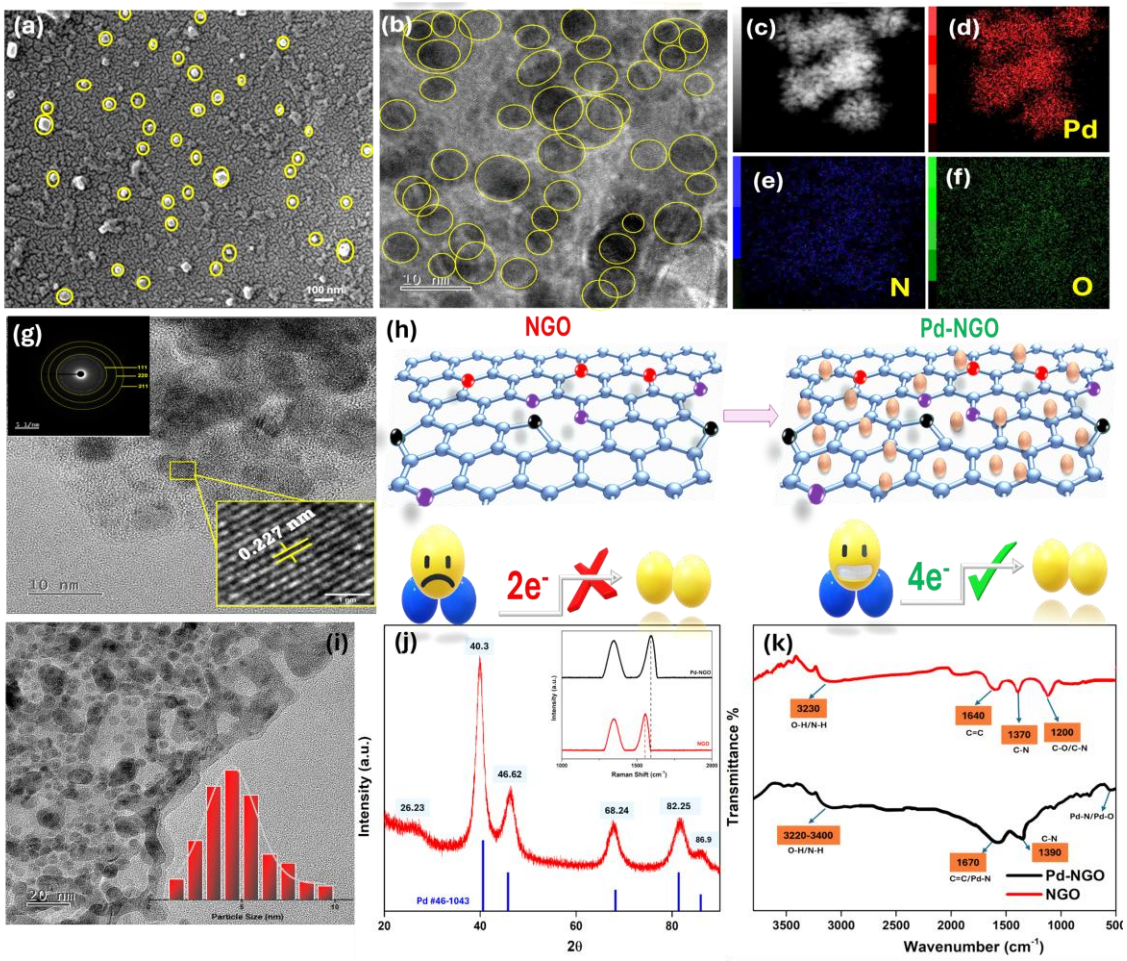

Figure 5.2 (a) SEM image of NGO (b) SEM image of Pd-NGO (c-f) EDX spectrum of Pd-NGO confirming elemental composition (g) TEM image of Pd-NGO with selected area electron diffraction (SAED) pattern and lattice fringe image shown in the inset (h) 2D surface representation of NGO and Pd-NGO (i) Particle size distribution of Pd-NGO nanoparticles (j) XRD pattern of Pd-NGO (k) FT-IR spectra of NGO and Pd-NGO composites, highlighting functional group differences.

The mapping images of NGO (**Figure A32c-f** of **Appendix information**) and Pd-NGO (**Figure 5.2c-f; A32i-l** of **Appendix information**) show the uniform distribution of the elements Pd, C, N and O over the Pd nanospheres. The lattice fringe spacing of Pd

nanoparticles was 0.224 nm (**Figure 5.2g**)**,** which corresponding to the (111) plane spacing of Pd [416]. The result shows that Pd nanoparticles grew along an extremely stable (111) direction on NGO. **Figure 5.2h** presents the 2D surface representation of NGO and Pd–NGO, as observed through SEM and TEM, providing a visual insight into their structural differences**.** Moreover, the particle size distribution of Pd nanoparticles for Pd-NGO confirmed that the average particle size of Pd nanoparticles was 4.86 nm (**Figure 5.2i)** (80 particles were considered for analysis). The results of particle size are basically consistent with those calculated by XRD (discussed later). **Figure 5.2j** shows the XRD patterns of the prepared Pd-NGO electrocatalysts. The four strong, sharp peaks at 40.38 , 46.62 , 68.24, 82.25 and 86.96 are indexed to the miller indices (111), (200), (220), (311), (222) respectively, for the face-centered-cubic (fcc) lattice crystal structure facets of the Pd (JCPDF#46-1043) [416].However, the prepared Pd-NGO exhibits obvious characteristic peaks at 2θ of 40.3, which may be due to the smaller grains. In addition, the average particle size of Pd could be calculated according to Scherrer formula and Pd (111) crystal plane [417]. The average particle sizes of Pd in Pd-NGO catalysts were calculated to be 3.9-4.6 nm, respectively which are well corelated with particle size obtained from TEM.

The formation of Pd-NGO nanocomposites was further confirmed by Raman spectroscopic measurements. The characteristic “D” and “G” bands are clearly seen in the Raman spectra of both NGO and Pd-NGO samples. The “D” band, also known as the disorder or defect band, is a representative of a mode from sp^3 -bonded carbon. The “G” band, on the other hand, is an outcome of the in-plane vibrational mode involving the sp^2 -hybridized carbon atoms that constitute the graphene network [418]. For instance, whereas the D band positions are very consistent among the NGO and Pd-NGO samples at 1360 cm^{-1}, the G

band positions are markedly different. Specifically, the G band energy increased in the order of NGO (1538 cm^{-1}) < Pd-NGO (1584 cm^{-1}), suggesting the shrinking C sp^2 domains of the resulting Pd-NGO (**inset of Figure 5.2j**). Consistent results were obtained in the comparison of the I_D/I_G ratio, which increased in the same order of NGO (0.7) < Pd-NGO (0.9) indicating an increasingly defective structure of the Pd-NGO. The increased I_D/I_G ratio for Pd-NGO is indicative of a more defective carbon lattice, which can arise from strong interactions between Pd nanoparticles and nitrogen dopants, particularly, pyridinic-N as well as pyrrolic-N which can locally distort the graphene lattice and disrupt the sp^2 domains.

The FT-IR spectra of Pd–NGO hybrids and pristine NGO samples are presented in **Figure 5.2k**. Both samples exhibit broad absorption bands in the range of 3000-3400 cm^{-1}, which are attributed to the stretching vibrations of adsorbed -OH or -NH groups, commonly associated with alcohols, phenols, or amine functionalities [419,420]. These groups are often residual from the synthesis process and contribute to the hydrophilicity of the material. Notably, in the Pd-NGO spectrum, new peaks emerge in the region of approximately 400-750 cm^{-1}. These are assigned to Pd-N and/or Pd-O vibrational modes [421,422], providing strong evidence of successful coordination between the palladium nanoparticles and the nitrogen and oxygen-containing functional sites of NGO. This coordination is crucial as it influences both the dispersion of Pd nanoparticles and the electronic interactions at the metal-support interface, which are key to the electrocatalytic performance. Additionally, the peak near 1640 cm^{-1} in NGO, typically associated with C=C stretching and/or C=O bending vibrations, becomes broader and slightly shifts to around 1670 cm^{-1} in the Pd-NGO hybrid [423]. This spectral change suggests overlapping

contributions from possible Pd-N interactions and conjugated C=C stretching, indicating that palladium incorporation alters the local electronic environment of the graphene framework. Further, the characteristic peaks for C-N and N-H stretching modes also display noticeable shifts in Pd-NGO compared to the pristine NGO sample. This confirms strong interactions between palladium and nitrogen-doped sites specifically pyrrolic and pyridinic nitrogen groups which are known to act as anchoring points for metal nanoparticles. A marked decrease in the intensity of the carbonyl (C=O) stretching peak is observed in the Pd-NGO spectrum. This reduction could be attributed to two factors: (i) the chemical reduction of GO during synthesis, which reduces oxygen-containing groups, and (ii) the possible coordination or binding of Pd to oxygen-containing functional groups, such as carbonyls or hydroxyls, on the NGO surface.

Together, these FT-IR observations confirm the successful functional integration of Pd nanoparticles with the NGO scaffold through both nitrogen and oxygen functionalities, supporting their structural and electronic synergy in electrocatalytic applications.

5.5.2 Electrochemical Activity of Pd−NGO Nanocomposites for Oxygen Reduction Reactions in Alkaline Media.

In alkaline media, the oxygen reduction reaction pathway can proceed by: (**eq 5.4 to 5.6**) [424]

(i) Efficient four-electron process where O_2 is completely reduced to OH^-

$$2H_2O + O_2 + 4e^- = 4OH^- \quad (5.4)$$

or

(ii) Two electron-mechanism where O_2 is reduced to peroxide intermediates:

$$H_2O + O_2 + 2e^- = 4HO_2^- + OH^- \quad (5.5)$$

$$2H_2O + HO_2^- + 2e^- = 3OH^- \quad (5.6)$$

The HO_2^- detected on the ring of the rotating-ring disc electrode (RRDE) can be used to calculate the peroxide intermediate yield, and the no. of electrons transferred (ne^-) too can be estimated for deducing the ORR mechanism according to the following **eq 5.7, 5.8** [425]

$$\% H_2O_2 = 200\, X \frac{\frac{I_R}{N}}{I_D + \frac{I_R}{N}} \quad (5.7)$$

$$n = 4\, X \frac{I_D}{I_D + I_R/N} \quad (5.8)$$

where I_R and I_D are the ring and disk current densities, respectively, and N is the ring collection efficiency. Accurate knowledge of **N** is essential for quantifying intermediate species such as H_2O_2 during ORR. To determine **N** for our setup, we employed a well-established redox couple, ferricyanide/ferrocyanide ($K_3Fe(CN)_6/K_4Fe(CN)_6$) in 0.1 M KOH (see 5.3.3.2 under Electrochemical measurement section for experimental details). The ORR experimental setup and evaluation scheme along with the CV and LSV curves obtained with the Fe^{+3}/Fe^{+4} systems for calculating N are presented in **Figure 5.3a-c**.The obtained N value was approximately 0.20, which was subsequently used for quantitative analysis in our ORR studies. The oxygen reduction reaction (ORR) activities of the N-doped graphene oxide (NGO) and palladium-decorated N-doped graphene oxide (Pd-NGO) systems were systematically evaluated in an O_2-saturated 0.1 M KOH electrolyte. The GCE exhibited minimal ORR activity with negligible current response difference between N_2 and O_2 saturation (**Figure 5.4a)**, whereas the introduction of nitrogen functionalities in NGO and further incorporation of Pd nanoparticles significantly

enhanced the electrocatalytic activity, evidenced by larger cathodic currents in O_2-saturated conditions.

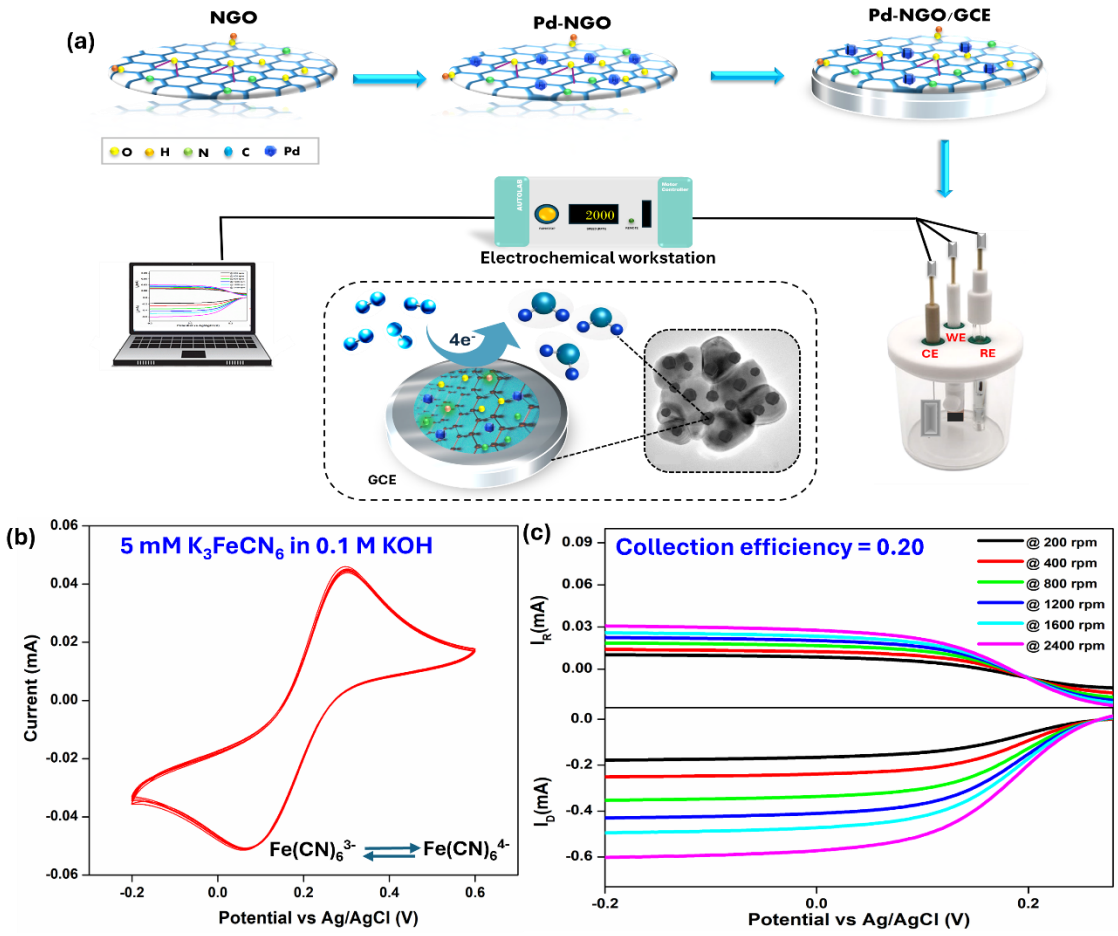

Figure5.3(a)Electrocatalyst modified electrode mediated reduction of oxygen (b) Cyclic voltammograms obtained for 5 mM of ferro/ferricyanide in the presence of a 0.1 M KOH supporting electrolyte using an unmodified GC electrode at 50 mV sec^{-1} (c) The corresponding ring and disk currents obtained from RRDE.

The RRDE voltammograms in **Figure 5.4d, e** depicts ring and disc current densities obtained using a RRDE at 1600 rpm and 5 mV s^{-1} for NGO and Pd-NGO in 0.1 M KOH saturated with O_2 at room temperature. It can be seen that for both Pd-NGO and NGO, nonzero current started to occur as the potential was swept negatively past +0.99 V, increased rapidly with electrode potentials, and reached a plateau at potentials more

negative than around +0.70 V, indicating marked electrocatalytic activity of the NGO and Pd-NGO nanocomposites toward oxygen reduction reaction with limiting current densities of 0.94 and 4.75 mA cm^{-2} for NGO and Pd-NGO respectively.

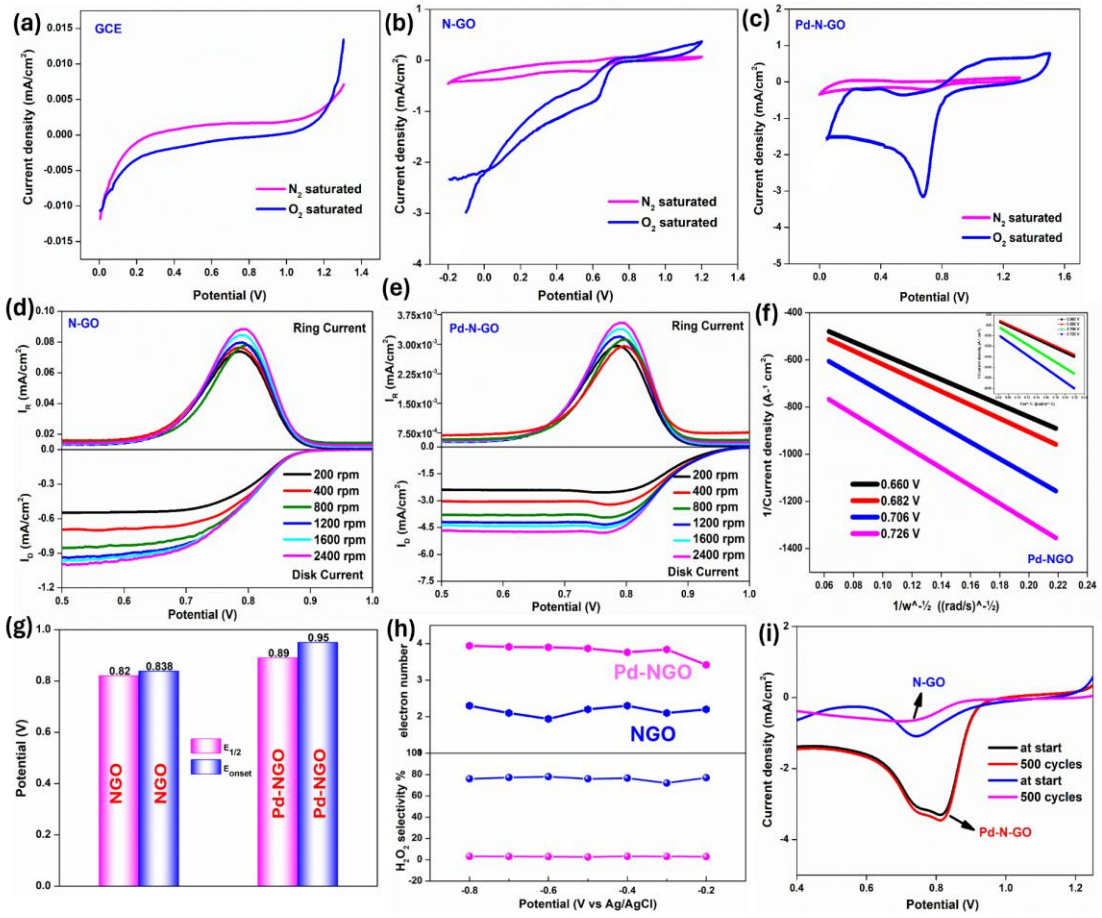

Figure 5.4 Cyclic voltammetry (CV) curves of (a) bare glassy carbon electrode (GCE) (b) NGO (c) Pd-NGO recorded at a scan rate of 30 mV/s under N_2 and O_2 saturated conditions(d) Rotating ring-disk electrode (RRDE) voltammograms of NGO and (e) Pd-NGO showing disk current (bottom) and ring current (top) at various rotation rates (200-2400 rpm); the ring electrode was held at 1.2 V vs. RHE (f) Corresponding Koutecky-Levich (K–L) plots (j^{-1} vs. $\omega^{-1/2}$) derived from RRDE measurements, comparing NGO(inset) and Pd-NGO (g) Comparison of onset potential (E_{onset}) and half-wave potential ($E_{1/2}$) for NGO and Pd-NGO, highlighting improved ORR kinetics for Pd-NGO (h) Calculated electron transfer number (n) and H_2O_2 molar selectivity (%) as a function of potential [Blue-NGO, pink -Pd-NGO](g) Durability test comparing initial and post-500-cycle CVs of NGO and Pd-NGO.

The absence of a ring current between 1.2 to 0.8 V vs RHE for the Pd-NGO indicates negligible production of peroxide intermediates whereas the increasing ring current between the said potential range for NGO indicates the significant generation of the intermediate H_2O_2 which confirms that for the NGO , the preferred pathway for oxygen reduction is via the reduction to H_2O_2 to H_2O whereas, for Pd-NGO , oxygen is directly reduced to water without any generation of H_2O_2 intermediate.

The overall number of the electron transferred (n) per O_2 molecule over the surface of NGO and Pd-NGO electrocatalyst was calculated using the Koutecky−Levich equation **(eq 5.9, 5.10)** given below, [235]

$$\frac{1}{j} = \frac{1}{j_{\mathrm{L}}} + \frac{1}{j_{\mathrm{K}}} = \frac{1}{B\omega^{0.5}} + \frac{1}{j_K} \tag{5.9}$$

$$B = 0.62nFC_{O2}D_{O2}^{\frac{2}{3}}\nu^{-\frac{1}{6}} \tag{5.10}$$

Where, j is the measured current density from the disk electrode of RRDE and ω is the electrode rotating rate or angular speed (rad s^{-1}). B is determined from the slope of the Koutecky–Levich plot. J_L and J_K are the diffusion and kinetic-limiting current densities, n is the transferred electron number, F is the faraday constant (96485 C mol^{-1}), CO_2 is the concentration of oxygen in an oxygen-saturated solution (0.1 M KOH) (12.6 x 10^{-6} mol cm^{-3}), Do_2 is the diffusion coefficient of O_2 (1.9 x 10^{-5} cm^2 s^{-1}), and v is the kinetic viscosity (1.01 x 10^{-2} cm^2 s^{-1}) [235] The constant 0.62 is used when the rotation speed is expressed in rad s^{-1}. The KL plot (j^{-1} versus angular $speed^{-1/2}$) for different potentials (0.66, 0.68, 0.70, and 0.72 V) and the average number of electrons transferred per catalytic event along with the % H_2O_2 yield was calculated as per **eq 5.7-5.10**. **Figure 5.4f** shows that the current densities of the synthesized Pd-NGO catalysts were linearly dependent on the rotation

speed. The KL plot for Pd-NGO exhibits excellent linear dependence indicating first-order ORR kinetics with respect to the concentration of dissolved O_2 in the electrolyte. While Pd-NGO nanocomposite mostly catalyzed the $4e^-$ reduction of O_2 in alkaline media, the no. of electrons transferred was estimated to be 2.2 respectively, for NGO. Further, the LSV measurements confirmed that Pd-NGO had an onset potential and half-wave potential ($E_{1/2}$) of 0.95 and 0.85 V, respectively, close to Pt/C (1.01 and 0.90 V) (**Figure 5.4g**)suggesting a good ORR performance compared to NGO. H_2O_2 yield based on the results obtained using the rotating ring disc electrode voltammograms along with the no. of electrons transferred in 0.7 to 0.1 V range has been combinedly plotted in Figure 4h and the % H_2O_2 yield was estimated and a yield <2% for Pd-NGO over the potential range of 0.8−0.2 V, suggesting negligible formation of H_2O_2. However, the H_2O_2 yield with the NGO electrocatalyst was significantly high (~80%). **Table 5.1** lists and compares the NGO and Pd-NGO's acquired ORR evaluation parameters.

For checking the stability of the Pd-NGO electrocatalyst, the ORR curve after 500 CV cycles were monitored which suggested negligible shifting in the half wave potentials of Pd-NGO compared to NGO which showed a significant shift accounting for the lesser stability of the later compared to the former (**Figure 5.4h**).

Table 5.1 The ORR evaluation parameters obtained with NGO and Pd-NGO

S.no	$E_{1/2}$	E_{onset}	No. of e^-	H_2O_2 yield %
N-GO	**0.82**	**0.838**	**2.2**	**79.2**
Pd-N-GO	**0.89**	**0.95**	**3.8**	**2**

The electrode was frequently tested for a period of 6 months and each time it retained its ORR activity, highlighting its stability as an effective ORR electrocatayst. Thus, together, all these results confirm the superior ORR kinetics of the Pd-NGO following conclusions can be made:

(i) NGO support materials only catalyzed the $2e^-$ electron reduction of oxygen to peroxide intermediates, and were mainly responsible for peroxide generation

(ii) Pd−NGO nanocomposites had enhanced electro kinetics and catalyzed the direct 4^-electron reduction reaction of O_2 to OH^- via the $4e^-$ mechanism

5.6 Plausible active sites in NGO and Pd-NGO for ORR

It is well reported that nitrogen-doped graphene derivatives exhibit high electrocatalytic activity toward ORR, which is largely attributed to carbons bonded to pyridinic or graphitic nitrogens [426]. In the present study, there is an abundance of pyrrolic nitrogen (N_{pyr}) over the pyridinic nitrogens (N_{pyd}) along with additional palladium nanoparticles in our Pd-NGO system. Since the nitrogen types present and the ORR activities of both the NGO and Pd-NGO system varies drastically, it is important to find out the active sites in both the systems. For finding out the responsible species (N_{pyr} or N_{pyd} or Pd) for the ORR activity in Pd-NGO, control experiments were conducted using Ru-NGO which were prepared under similar conditions to Pd-NGO. By using Ru instead of Pd, the control experiment keeps the morphology, synthesis method, and interaction with NGO consistent, changing only the metal identity. Since both Pd-NGO and Ru-NGO have the same nitrogen-doped graphene support, comparing their ORR activity allows you to determine whether metal identity (Pd vs. Ru) or N-doping is responsible for the enhanced performance. It can be seen that XPS measurements of Ru-NGO composites exhibited peaks centered at 398.5 eV

and 400.0 eV (higher intensity), indicating the formation of pyridinic and majorly pyrrolic nitrogen with insignificant signal from quaternary nitrogen centers (**Figure 5.5a**) similar to the case of Pd-NGO. In the TEM images shown in **Figure 5.5b-c**, similar morphological characteristics of the ruthenium nanoparticles to the Pd-NGO were found where Ru nanoparticle with a diameter of 3-6 nm in size (**upper left inset of Figure 5.5d**), and lattice fringes of 0.22 nm width in good agreement with the interplanar distance between Ru(100) crystalline planes [427] were found which were nearly equal to the fringe width seen in the TEM of Pd-NGO. Raman measurements (**Figure 5.5d**) showed the characteristic D and G bands, along with the I_D/I_G ratio, that were consistent with those of the Pd-NGO sample. As noted above, the defect ratio of Ru-NGO was nearly identical to that of Pd-NGO, which can be attributed to the increased abundance of pyrrolic nitrogen moieties in both systems. These five-membered pyrrolic rings induce greater geometric strain in the graphitic matrix compared to the six-membered pyridinic rings, thereby contributing to higher defect densities. The Ru-NGO system was tested for ORR activity in similar testing conditions of Pd-NGO, and it demonstrated a poor ORR activity which suggests that the NGO support (even with N-doping) contributes minimally to the overall catalytic activity in the Pd-NGO system. This implies that Pd nanoparticles are likely the primary active sites in Pd-NGO. The onset potential for Ru-NGO was approximately +0.72 V, which is about 230 mV more negative than that observed for any of the Pd-NGO composites (**Figure 5.5d**). The CV curve, shown in the lower right inset of **Figure 5.5d**, further highlights the poor ORR activity. Notably, Ru-NGO failed to reach a current plateau even at potentials more negative than +0.50 V, and the current density remained significantly lower. These observations suggest that, in this study, the ORR activity is primarily driven by the presence

of Pd in Pd-NGO, rather than the nitrogen dopants. However, the nitrogens do have a role towards making the Pd active for ORR, which has been proven by Density Functional Theory (DFT) results performed with a Pd_6 cluster supported on a nitrogen-doped graphene sheet (**Figure 5.5e**).Pd coordinated with pyridinic N (Pd-N@C_6) exhibits a higher d-band center (-2.56 eV) than Pd bound to pyrrolic N (Pd-N@C_5, -2.83 eV), and this upward shift of 0.27 eV arises from the stronger lone pair-Pd d-state interactions (**Figure 5.5f**). XPS confirms that the pronounced reduction in pyridinic-N content after Pd loading (**Figure A33** of **Appendix information**), results from the preferential coordination of Pd with these nitrogen sites. Pyridinic nitrogen, with its localized lone pair at graphene edges, serves as a strong ligand for Pd^{2+}/Pd, forming Pd-N bonds that alter the nitrogen's chemical environment, redistributes the electron density, and shifts the N 1s binding energy. When fixed peak positions are used during XPS deconvolution, such shifts can cause Pd-bound pyridinic species to be misassigned as metal-N, oxidized N, or broadened pyrrolic-like features, lowering the apparent pyridinic signal. This tuning of Pd's electronic structure promotes oxygen adsorption and the 4-electron ORR pathway in alkaline media. While the Pd atoms, which are not directly bonded to nitrogen, display even higher d-band centers (-2.48 to -1.08 eV) (Figure 5.5f), nitrogen doping remains essential for anchoring Pd_6 clusters. Experimental evidence shows that pristine graphene cannot effectively anchor Pd, resulting in nanoparticle aggregation or desorption, whereas nitrogen doping introduces localized electronic states and anchoring points. XPS further shows that pyrrolic-N content remains largely unchanged upon Pd loading, suggesting a less direct role in electronic modulation.

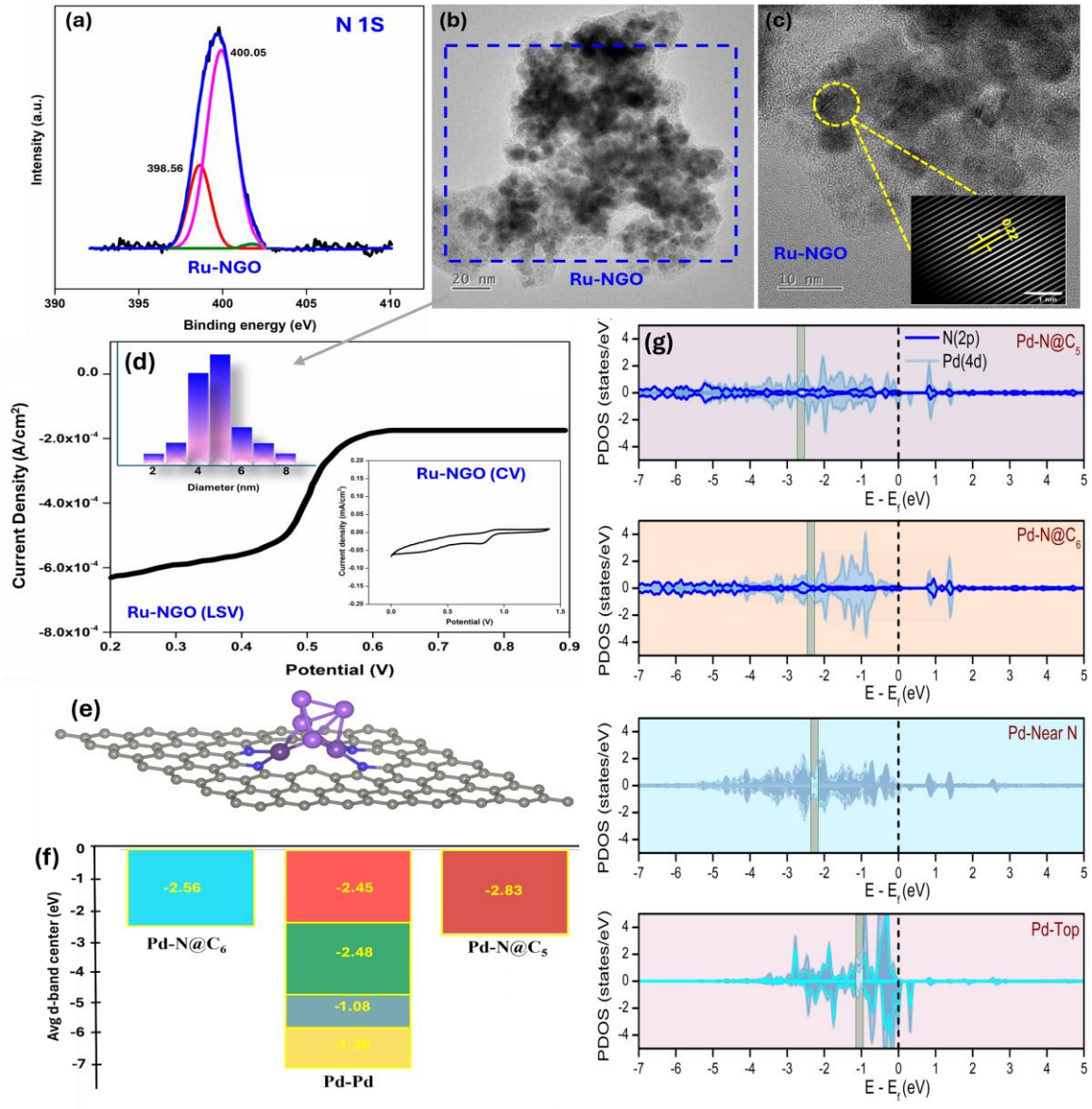

Figure 5.5(a) XPS spectra of N 1s of Ru-NGO, (b,c) Representative TEM images of Ru-NGO nanocomposites, (d) RDE voltammogram of Ru-NGO in in oxygen-saturated 0.1 M KOH at the electrode rotation rate of 1600 RPM.(Other experimental conditions are the same as those used with Pd-NGO) (e) Atomic structure of a Pd_6 cluster supported on N-doped graphene. Grey spheres represent graphene C atoms, violet spheres denote Pd atoms, dark violet highlights Pd bonded to pyridinic N sites, and light violet marks Pd near pyrrolic N sites (f) Average d band center (in eV) for Pd atoms in different coordination environments, with blue and red labels for Pd–N bonding (pyridinic and pyrrolic), and yellow for Pd-Pd bonding (g) Projected density of states (PDOS) for Pd(4d) and N(2p) orbitals in representative coordination cases. Green shaded regions indicate the d-band centers relative to the Fermi level (Ef = 0 eV).

However, its structural contributions are significant: defect generation, enhanced Pd dispersion, and possible stabilization of intermediates near Pd-pyridinic sites, which is supported by the Partial Density of States (PDOS) analysis (**Figure 5.5g**), which indicates that Pd-pyrrolic N exhibits stronger Pd-N orbital overlap and a deeper d-band center, moderating adsorption strength and balancing catalytic energetics. The prevalence of pyrrolic N likely stems from its lower formation energy in defective GO under synthesis conditions and its superior ability to immobilize Pd clusters, mitigating migration and Ostwald ripening. Overall, pyridinic N acts as the primary electronic activator for ORR, while pyrrolic N plays a complementary structural role, ensuring dispersion, stability, and durability, together achieving an optimal balance between high activity and long-term performance.

To identify the active sites in the NGO system, high-resolution and high-sensitivity XPS was employed to investigate the chemical composition changes before and after the ORR test.The changes in nitrogen contents before and after ORR test marks some important observations for the different pathways followed by NGO and Pd-NGO towards oxygen reduction reaction. The intensity of the pyrrolic nitrogen peak increased after ORR, while that of the pyridinic nitrogen decreased compared to its intensity before ORR. To understand this shift, the carbon and oxygen XPS spectra were examined. Both the O 1s and C 1s spectra showed an increase in -OH groups, a known intermediate in ORR (**Figure 5.6a, b**). Specifically, **Figure 5.6a** shows that the C(aliphatic)-OH/C-O-C peak at 532.0 eV (red) decreased, while the C(aromatic)-OH peak at 533.3 eV (blue) increased as ORR progressed [428,429], indicating a rise in -OH groups attached to aromatic carbon atoms. Likewise, the C 1s spectra (**Figure 5.6b**) displayed a substantial increase in the C-OH peak

at 285.4 eV after ORR. The inset of **Figure 5.6b** shows the initial C 1s spectrum of NGO before ORR, where the C-OH peak is much weaker. These findings suggest that changes in the nitrogen 1s spectrum (**Figure 5.6c**) are due to alterations in the chemical environment of nitrogen atoms during ORR, likely caused by the attachment of -OH groups to the carbon atoms bonded to nitrogen. It has been reported that the attachment of -OH to pyridinic nitrogen can shift its N 1s XPS binding energy from 398.8 eV to approximately 400.2 eV [430]. Similarly, when -OH groups bind to carbon atoms adjacent to pyridinic nitrogen in graphene, the binding energy is expected to shift upward, approaching the 399.8 eV region typically associated with pyrrolic nitrogen. Therefore, the observed decrease in the pyridinic peak intensity and the simultaneous increase in the pyrrolic-like peak after ORR may be attributed to this transformation where, pristine pyridinic nitrogen converts into a modified pyridinic nitrogen environment with adjacent -OH groups, as illustrated in **Figure 5.6c**. In other words, the apparent increase in the "pyrrolic" nitrogen signal after ORR in the XPS spectra is not due to an actual rise in pyrrolic nitrogen content, but rather to the formation of -OH functionalized pyridinic nitrogen, which exhibits a binding energy similar to that of pyrrolic nitrogen. This interpretation of the altered nitrogen environment is strongly supported by Fourier Transform Infrared Spectroscopy (FTIR) analysis of the NGO sample following the ORR reaction. In **Figure 5.6d**, the prominent -OH stretching peak at ~3440 cm^{-1} intensifies significantly in NGO after ORR, supporting the formation of -OH functionalized pyridinic nitrogen. This suggests that pyridinic N and its neighboring carbon atoms are key active sites in the ORR process [431,432]. Thus, NGO catalysis is driven by direct N-C active sites undergoing chemical transformation, whereas Pd-NGO activity arises from Pd-N coordination synergistically supported by a pyrrolic-N-rich

matrix. So, based on our experimental observations, the active sites responsible for ORR in both NGO and Pd-NGO electrocatalysts have been systematically identified.

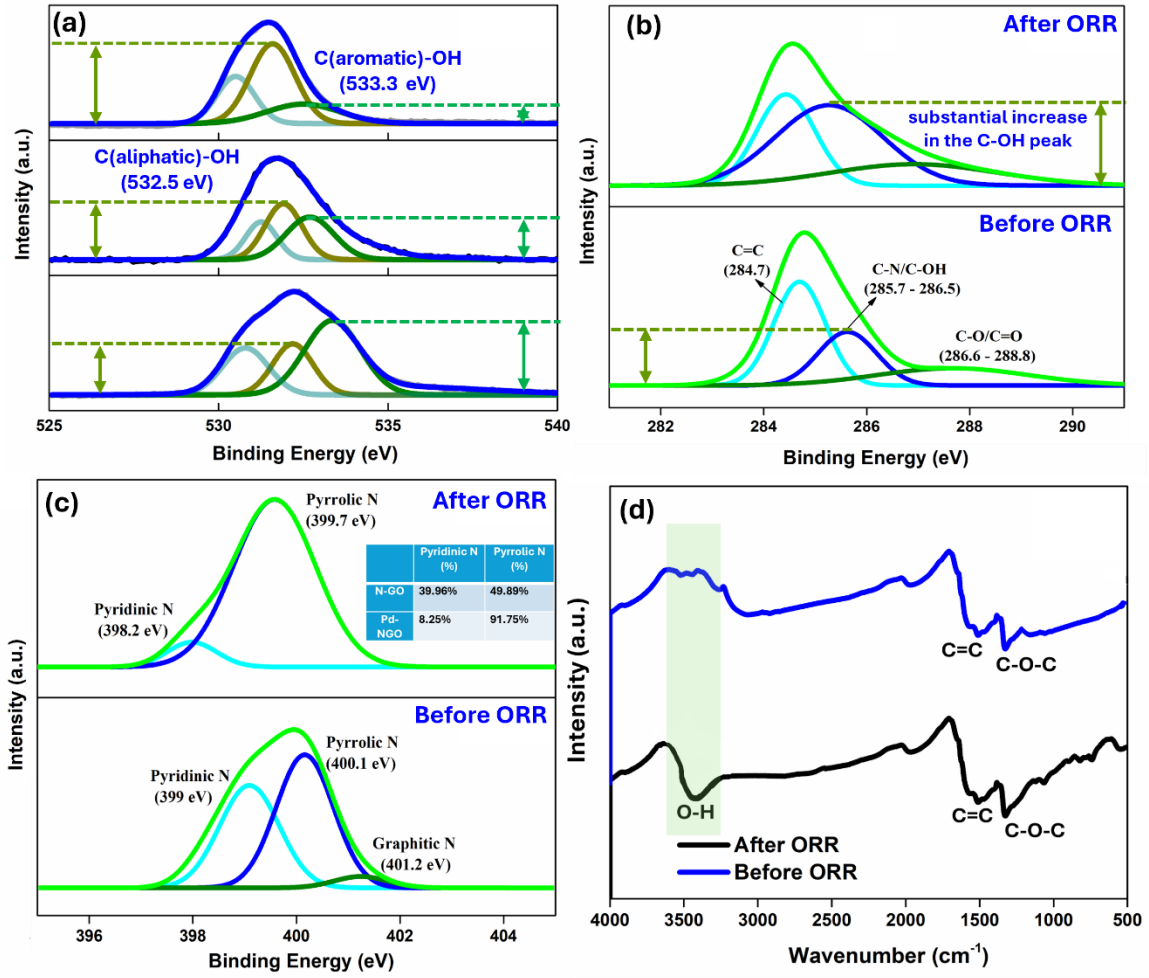

Figure 5.6 XPS analysis of NGO nanocomposite: Deconvoluted (a) O 1s spectrum monitored timely during ORR process (b) C 1s spectrum post ORR (c) N 1s spectrum post ORR (d) FTIR spectra of NGO before and post ORR activity.

5.7 Electrochemical Sensor development with Pd-NGO

Following the comprehensive evaluation of Pd-NGO as an electrocatalyst for the oxygen reduction reaction (ORR), its high activity, excellent stability, and efficient electron-transfer kinetics became evident. Given that hydrogen peroxide (H_2O_2) is often formed as an intermediate or product during ORR, and that ORR and H_2O_2 sensing share mechanistic

and electrochemical similarities, it is not surprising that materials active for ORR often exhibit strong electrocatalytic response toward H_2O_2 as well [433-435]. Among various analytes, H_2O_2 holds particular importance due to its widespread relevance in environmental monitoring, biological systems, and industrial processes [435]. By leveraging the intrinsic reactivity and robustness of Pd-NGO demonstrated in ORR, the same catalyst was explored for H_2O_2 detection, with expectations of achieving low detection limits, fast response times, and high selectivity. Rather than developing a separate sensing platform, extending Pd-NGO's application to electrochemical sensing offers a logical and resource-efficient strategy, showcasing the multifunctionality of the catalyst. This transition also broadens the scope of Pd-NGO, demonstrating its dual applicability in both energy conversion and analytical sensing, which is particularly valuable for real-world, multifunctional device applications. The fabrication of the Pd-NGO/SPE sensor has been shown in **Figure 5.7**.

The electrochemical behavior of Pd-NGO and NGO over SPE were studied using CV measurements in the presence of N_2 degassed 5 mL PBS (0.1 M, pH 7.4, without Cl^-) containing 5 mM H_2O_2 at a scan rate of 5 mV s^{-1}. In a reported study, the influence of electrolyte pH on the electrochemical detection of H_2O_2 has been systematically investigated in the range of pH 5.8 to 7.6 [436]. The researchers purposefully excluded lower pH values, anticipating that at higher proton concentrations, palladium might adsorb hydrogen onto its surface, potentially interfering with H_2O_2 detection. Their results demonstrated that the voltammetric response for H_2O_2 reduction at Pd-modified electrodes improved with increasing pH, reaching a maximum at pH 7.4. This finding guided our selection of optimal pH conditions for further electroanalytical experiments.

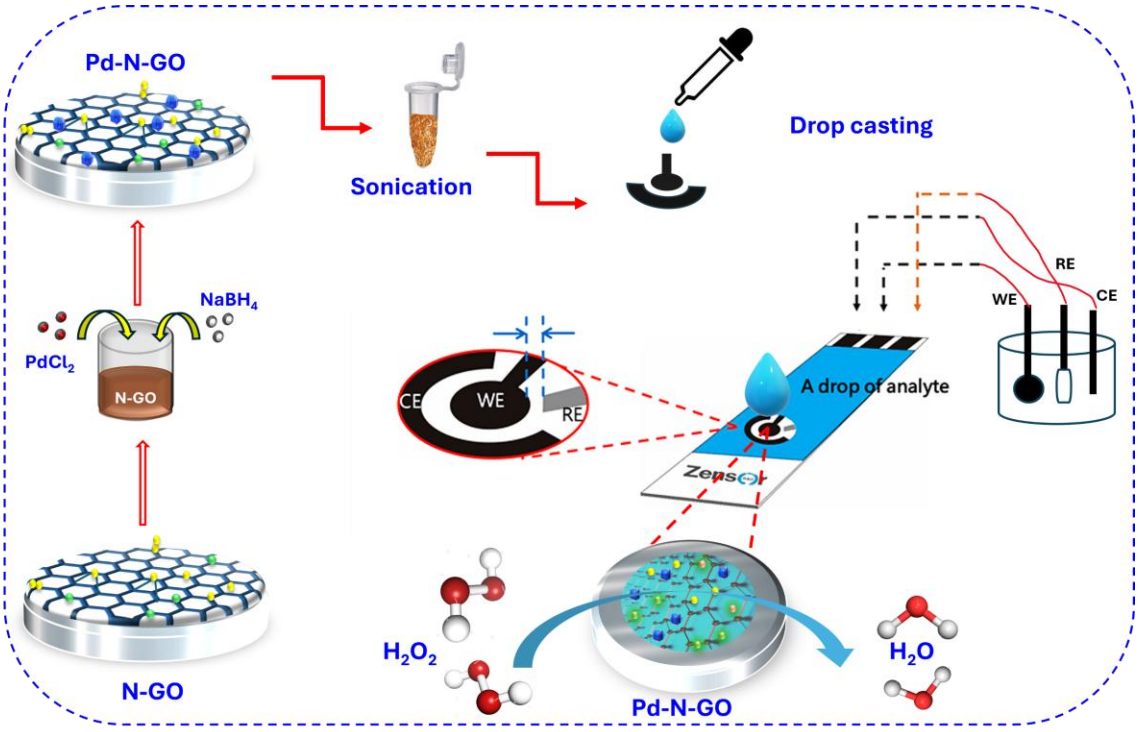

Figure 5.7 Fabrication process of Pd-NGO/SPCE sensor

As shown in **Figure A34 of Appendix information**, the NGO/SPE did not exhibit any response up to 5 mM concentration of H_2O_2. However, with Pd-NGO/SPE, a cathodic peak has been observed at +0.80 V due to a well-known characteristic electro reduction of H_2O_2 facilitated over the electrocatalyst surface [436]. So, the Pd-NGO electrode exhibits high electrocatalytic activity towards H_2O_2 reduction compared to NGO electrodes as a prominent reduction peak is visible around 0.8 V.

To get more insight into the proposed mechanism of hydrogen peroxide electro reduction, we have performed cyclic voltammetry of Pd-NGO/SPE in response of H_2O_2 (1 mM) with varying scan rate 5 - 500 mV s^{-1} is recorded in a N_2 purged PBS solution (0.1 M, pH = 7.4). As the scan rate increases, the reduction peak potential corresponding to electroreduction of H_2O_2 slightly shift to negative potential (**Figure 5.8a**). Increase in only the reduction

peak current (I_{pc}) on increasing the n implies the irreversible electro catalytic reduction of H_2O_2[179].

The Tafel slope (b) can be determined from the plot of cathodic peak potential (E_{pc}) versus log (scan rate, ν) using the following eq **5.11** [437,438]

$$E_{pc} = b\log(\nu)/2+\text{constant} \quad (5.11)$$

For an irreversible, diffusion-controlled electrochemical reduction process, the Tafel slope is related to the transfer coefficient (α) and the number of electrons involved in the rate-determining step (n_a) according to eq **5.12**

$$b = 2.303RT/(\alpha)n_aF \quad (5.12)$$

where *R* is the universal gas constant, *T* is the temperature (298 K), and *F* is the Faraday constant. In this study, for the cathodic electro-reduction of hydrogen peroxide (H_2O_2), the Tafel slope was obtained as 27 mV/decade (**Figure 5.8b**). Similar values of tafel slope have been recently reported in literature for H_2O_2 RR [439]. The corresponding plots of the cathodic peak currents against the square root of scan rate (**Figure 5.8c**) have shown linear relationships indicating to the predominant occurrence of diffusion controlled redox process [179].

The basic analytical parameters such as a limit of detection, sensitivity, response time and linear range response of Pd-NGO/SPE were evaluated using Cyclic voltammetry measurement (i–v) in 5 mL of 0.1 M PBS (pH 7.4), by successive additions of H_2O_2 with different concentrations (0.1 to 3 mM). As shown in **Figure 5.8d**, the reduction current increases with increasing H_2O_2 concentration.

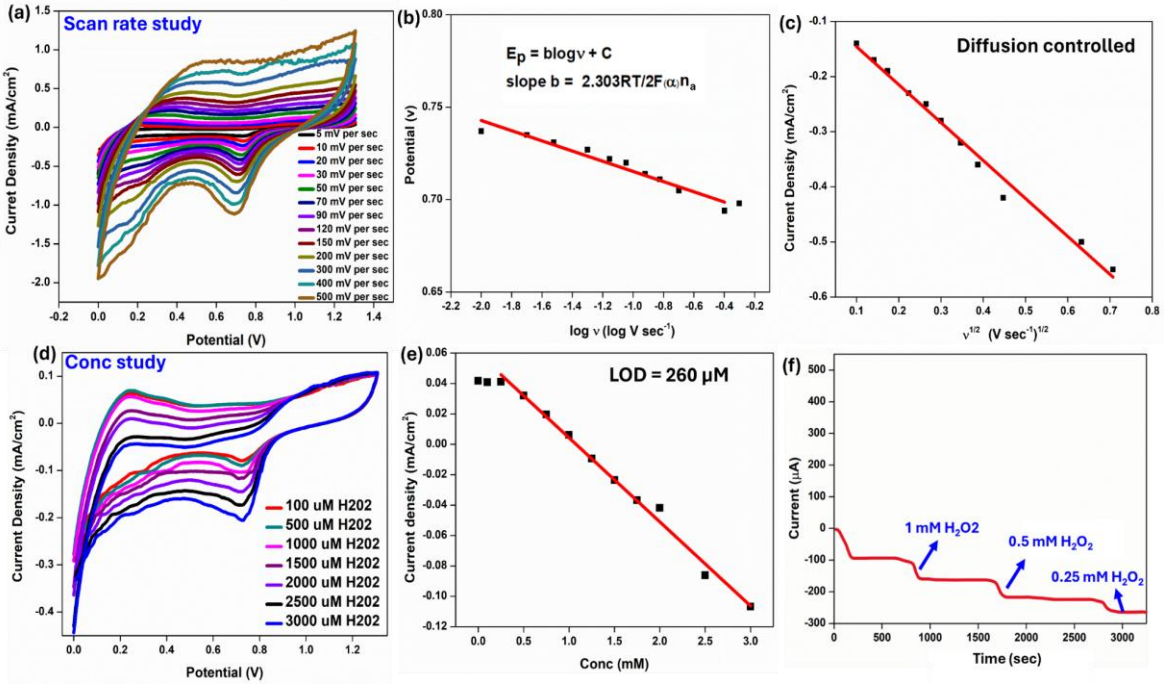

Figure 5.8 (a) Cyclic voltammograms of Pd-NGO/SPE recorded in a N_2 purged PBS solution (0.1 M, pH = 7.4) in response of H_2O_2 (1 mM) at varying scan rate (5-500 mV/s) and corresponding plots of (b) cathodic (E_{pc}) peak potentials against log of scan rate (log V/s) (c) cathodic (I_{pc}) peak currents against square root of scan rate (V/s)$^{1/2}$(d) Cyclic voltammograms of Pd-NGO/SPE in the presence of different concentration (0.1-3 mM) of H_2O_2 recorded in a N_2 purged PBS solution (0.1 M, pH= 7.4) at the scan rate of 0.03 V s^{-1} (e) Calibration curve obtained using CV voltammograms of Pd-NGO/SPE showing cathodic peak current change with respect to the concentration of H_2O_2 (f) Amperometric response of the Pd-NGO/SPE recorded in 100 mL of PBS, pH 7.4, with successive additions of H_2O_2 with varying concentration.

Figure 5.8e exhibits the calibration curve between H_2O_2 concentration and current response. It can be seen that there is a good linear relationship between the concentration of H_2O_2 and the current response in the wide range from 1 µM to 3000 µM. The equation of linear regression is:

$$I\ (Ma/cm^2) = -0.05531C\ (mM) + 0.05961\ (R^2 = 0.9996) \quad (5.14)$$

The calculated value of sensitivity was 0.055 µA µM^{-1} cm^{-2}. The LOD is estimated to be 260 µM based on the following eq 5.15

$$LOD = 3\ \sigma/S \quad (5.15)$$

where σ is the Standard deviation of the blank signal (e.g., from 3 runs of buffer with no analyte) and S represent the and slope of the calibration curve, respectively. The linear response range was 0-1.6 mM H_2O_2.

Furthermore, selectivity, reproducibility, and stability are also important analytical parameters to evaluate the electrochemical efficiency of the electrode. These analytical parameters measurements were carried out using the Amperometric method in the 5 mL of 0.1 M PBS solution (pH 7.0) at .826 V vs RHE. First, the selectivity of the fabricated Pd-N-GO/SPE sensor was investigated by comparison of its response towards addition of different concentrations i.e. 0.25 to 1 mM H_2O_2 at different intervals of time and each time the electrode showed an increase in current upon H_2O_2 addition (**Figure 5.8f**) highlighting its selectivity towards the H_2O_2 analyte. The jump in current was directly proportional to the quantity of H_2O_2 added. On further addition of 1 mM of some interfering substances such as Glucose (G), Uric acid (UA) and Citric acid (CA) which are preferably found with H_2O_2 in biological fluidic samples [50], as shown in **Figure 5.9a**, negligible Amperometric current response was obtained. However, an instant clear current response appeared upon addition of 1 mM and 3 mM of H_2O_2 to the above electrolyte. This good selectivity result of Pd-NGO electrode towards nonenzymatic H_2O_2 sensing is probably attributed to its unique structure merits and the catalytic activity of the incorporated Pd NPs. Furthermore, when the Pd-NGO-modified electrodes were stored at -4 °C and compared with freshly prepared Pd-NGO inks cast onto SPEs, both sensors maintained at least **98.9%** of their original current response toward 3 mM H_2O_2 after continuous measurements over a one-week period. This excellent retention of sensitivity, as illustrated in **Figure 5.9b**,

demonstrates the long-term stability and reproducibility of the Pd-NGO-modified electrode.

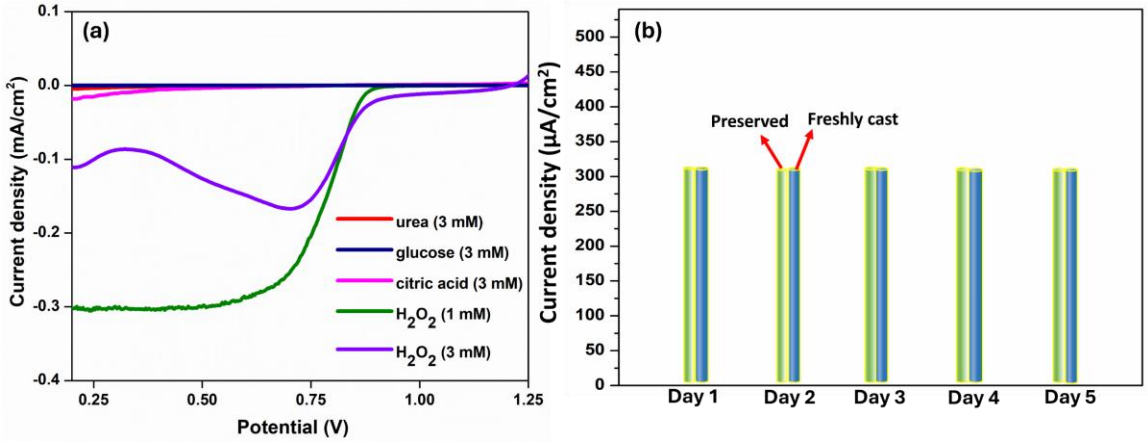

Figure 5.9(a) Amperometric response of the Pd-NGO/SPE in 100 mL of 0.1 M phosphate-buffered solution (PBS, pH 7.4) toward 1 mM H_2O_2, recorded before and after the successive addition of 1 mM of common interfering species such as glucose, uric acid derivative (UA), and citric acid (CA) (b) The long-term stability of the sensor tested for a week.

To assess the practical applicability and analytical performance of the Pd-NGO-based electrochemical sensor for hydrogen peroxide (H_2O_2) detection, a standard addition method was employed using standard samples. Electrochemical measurements were carried out using the Pd-N-GO/SPE as the working electrode. The experiments were conducted in nitrogen-purged phosphate-buffered saline (PBS, 0.1 M, pH 7.40) to eliminate dissolved oxygen interference, using a scan rate of 30 mV/s. Known concentrations of H_2O_2 [0.35, .5, 1, 1.5 mM H_2O_2] were spiked into the standard samples, and the resulting current responses were recorded. The recovery values were calculated by comparing the detected concentrations to the known added amounts. The sensor exhibited excellent recovery rates, typically ranging from [~99% to 104%], indicating high accuracy and minimal matrix interference.

Table 5.2 The recoveries of H_2O_2 determination in the standard samples (n = 3).

Sr. No	Known amount of H_2O_2 added (mM) (standard)	Estimated Amount of H_2O_2 in samples (mM)	Recovery (%)	RSD (%)
1	0.350	.349	99.70	0.527
2	.500	.520	104	1.10
3	1.00	1.04	104	0.55
4	1.50	1.49	99.7	1.42

These results confirm the reliability, reproducibility, and potential of the Pd-NGO/SPE sensor for accurate H_2O_2 determination in real or complex sample matrices. The above **Table 5.2** displays the recovery values at different H_2O_2 concentrations, suggesting that the fabricated Pd-NGO/SPE sensor demonstrates high accuracy and reliability for hydrogen peroxide determination in prepared samples. These results highlight the sensor's strong analytical performance, including excellent recovery, sensitivity, and selectivity, confirming its potential applicability for real-sample analysis and routine detection of H_2O_2 in environmental or biological matrices.

5.8 Conclusion

In this work, we successfully developed a palladium-incorporated nitrogen-doped reduced graphene oxide (Pd-NGO) nanocomposite as a cost-effective, multifunctional electrocatalyst for both the oxygen reduction reaction (ORR) and non-enzymatic hydrogen peroxide (H_2O_2) detection. The surfactant-free reduction of $PdCl_2$ yielded uniformly dispersed Pd nanoparticles (3-8 nm) anchored on the NGO matrix, eliminating the need for capping agents or complex synthesis steps. Control experiments with Ru-NGO confirmed that the superior ORR activity arises primarily from Pd active sites, while the NGO matrix alone contributes negligibly.Electrochemical studies demonstrated that Pd-NGO

predominantly follows a direct four-electron pathway for the reduction of O_2 to H_2O, outperforming the two-electron pathway typically associated with NGO. This enhanced activity correlates strongly with the electronic and structural effects of nitrogen doping. XPS and Raman analyses, supported by DFT and PDOS calculations, revealed that Pd coordinated with pyridinic nitrogen (Pd-N@C_6) exhibits a higher d-band center (-2.56 eV) compared to Pd bound to pyrrolic nitrogen (-2.83 eV), with a +0.27 eV upward shift attributed to strong lone-pair-Pd d-state interactions. This shift optimizes oxygen adsorption energies, facilitating ORR kinetics. Pyridinic nitrogen thus serves as the primary electronic activator, whereas pyrrolic nitrogen provides complementary structural stabilization by creating defects, enhancing Pd dispersion, and suppressing Ostwald ripening.Beyond energy conversion, Pd-NGO was integrated into a screen-printed carbon electrode (SPE) for H_2O_2 detection, exhibiting a low detection limit (260 μM), high sensitivity (0.055 $\mu A\ \mu M^{-1}cm^{-2}$), and excellent selectivity, repeatability, and stability. These results underscore the synergistic interplay between Pd and nitrogen dopants in tuning electronic structure, improving catalytic efficiency, and ensuring long-term durability. The combination of outstanding ORR activity, robust sensing performance, facile synthesis, and scalability makes Pd-NGO a promising candidate for next-generation fuel cells, electrochemical sensors, and other sustainable energy and environmental monitoring technologies.

Chapter 6: Summary and Future Scope

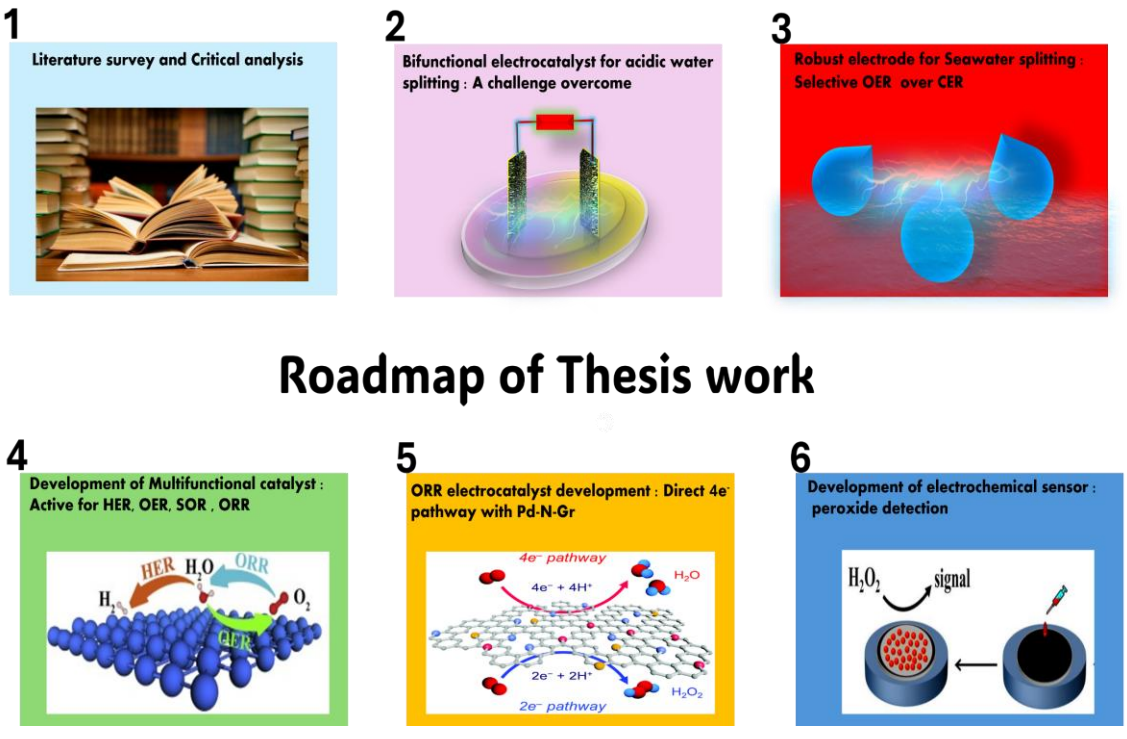

"From Pages to Potentials: Our Journey in Crafting Next-Gen Electrocatalysts and Smart Sensors"

The research work in this thesis is dedicated to the synthesis of sustainable electrocatalysts and the fabrication of stable electrodes for various electrochemical reactions such as HER, OER, SOR which are prime reactions in electrochemical conversion processes such as water/seawater and hydrogen-sulfide electrolysis along with other important reactions such as ORR, H_2O_2 RR typically catalyzed in fuel cells and metal-air batteries.

In the first chapter, we give a brief introduction of Transition metal compounds (TMCs) and TMCs-graphene derived electrocatalysts. An overview of the fundamental principles related to different electrochemical reactions as well as the parameters used to assess the

performance of electrocatalysts have been discussed. Finally, the most recent developments in the development of transition metals-graphene compounds for various electrochemical applications have been summarized.

In our second chapter, we reported a free-standing 3D Graphene-Tungsten oxide based self-assembled bifunctional electrode (SA-GWO) for acidic water splitting [136]. The morphological switching of SA-GWO at different polarization potentials in acidic media indicated the phase transitions inside WO_3. We experimentally demonstrated that the conversion of SAGWO into tungsten bronze during cathodic polarization results in nanotunnels like nano structural patterns that facilitate the hydrogen evolution reaction. The in-depth mechanistic studies behind switching phenomena are yet to be unraveled, for which we have been carrying out DFT studies, which can give a clear idea about the route followed by tungsten bronze during cathodic HER activity. While freshwater electrolysis is effective, it places additional stress on already limited freshwater resources, especially in regions facing water scarcity. Seawater electrolysis, on the other hand, offers a more sustainable alternative. So, we worked upon developing an effective and robust seawater electrocatalyst in our next chapter and developed GNiMoOS electrocatalyst system which is a double-layer anode that is composed of a molybdenum sulfide electrocatalyst layer that is uniformly deposited over a Sulfonated Graphene-Ni foam electrode using a straightforward one-step hydrothermal method. The in situ-generated polyatomic sulfate ions imbibed over the graphene sheets having repellant properties towards chlorine along with contribution from GO towards conserving the mechanical integrity during OER, were responsible for activity, durability, and superior corrosion resistance of the seawater-splitting anode. The successful in-situ functionalization of sulphonic moieties onto the

graphene oxide skeleton and the development of MoS_2 flower-like nanostructures was well confirmed by XPS, RAMAN, SEM, TEM, and IR techniques. The density of states (DOS) and DFT calculations clearly validated the preference of sulphonic moieties towards OH^- and repellence towards Cl^- ions validating the role of sulfonated graphene towards imparting stability and OER selectivity to the GNiMoOS system duringanodic overpotentials. Outstanding and stable OER and HER activity in harsh sea has been observed at a very low overpotential of 180 and 165 mV, respectively, to reach current densities of 100 mA cm^{-2} at 27ºC.

Among the two electrodes that we prepared so far, the SA-GWO catalyst demonstrated excellent stability and catalytic performance under acidic conditions. However, it exhibited significant instability in alkaline media, limiting its versatility. Conversely, the GNiMoOS electrocatalyst, synthesized using Ni foam as a structural precursor, showed exceptional activity and long-term stability in both alkaline and seawater environments. Nonetheless, its performance deteriorated under acidic conditions, primarily due to the corrosion and degradation of the Ni foam in low pH environments. These contrasting behaviours highlighted a critical limitation: the lack of a single electrocatalyst capable of maintaining stability and functionality across a broad pH range. This challenge underscored the need to develop a robust, pH-universal electrocatalyst that can efficiently catalyze reactions in acidic, neutral, and alkaline media, thereby enabling its application in diverse electrochemical systems. This offers several key benefits such as reducing the need for multiple specialized catalysts, lowering material and development costs and such catalyst can be used in various electrochemical systems, including different types of electrolyzers (acidic/alkaline/neutral), fuel cells, and wastewater treatment setups. So, in our third

chapter, we have presented another 3D self-assembled free-standing Graphene-Transition metal sulfides electrode (MoOS-G) which is capable of direct electrolysis of hydrogen sulfide at relatively half the energy in comparison to the splitting requisite for H_2O in salt rich-Na_2S media (futile seawater). Besides being an effective H_2S splitting electrocatalysts, it acts as a bifunctional electrocatalyst for water splitting in acidic media (1 M H_2SO_4). This catalyst can be termed as a multifunctional electrocatalyst as it also catalyzes ORR reaction via a 4-electron pathway in alkaline KOH media. A theoretical DFT study has been separately planned in future to explain the selective catalytic behavior of MoOS-G electrode in different electrolyte medias with associated mechanisms to decode the factors responsible for the peculiar multifunctional behaviour. While HER and OER are crucial for water splitting and green hydrogen production, ORR is equally important for the utilization of hydrogen in proton exchange membrane fuel cells (PEMFCs). Platinum is the most effective ORR catalyst; it is expensive and scarce. Pd is less expensive and more abundant than Pt, offering a more economical option for fuel cells and metal-air batteries. On its integration with nitrogen doped Graphene, the anchoring of Pd nanoparticles onto the graphene surface is improved, preventing agglomeration and leaching during operation, hence providing higher durability and long-term stability. Keeping all this in mind, we synthesized palladium incorporated nitrogen doped graphene oxide nanospheres (Pd-N-GO) for the application of ORR and H_2O_2RR in our fourth chapter. SEM, TEM, IR, XRD, RAMAN and XPS confirm the successful incorporation of palladium into the base architecture of graphene nanospheres. The electrochemical reduction of oxygen on Pd-N-GO catalyst in alkaline solutions, along with its detailed mechanism, has been investigated using the RRDE method. The RRDE results indicated that Pd-N-GO catalyzes a 4-electron

reduction of oxygen whereas the bare N-GONs reduces oxygen *via* a two-electron pathway in alkaline medium. This was correlated strongly with the electronic and structural effects of nitrogen doping, supported by DFT and PDOS calculations. Furthermore, a screen-printed electrochemical sensor (Pd-N-GO/SPCE) was fabricated via the drop-casting of Pd-N-GO over SPCE for the sensitive electrochemical detection of H_2O_2 *via* H_2O_2 RR, it exhibited an excellent detection limit (LOD) of 260 μM with a decent sensitivity of 0.055 $\mu A \mu M^{-1} cm^{-2}$. In addition, Pd-N-GO/SPE also showed excellent selectivity, repeatability, and stability for detecting H_2O_2.

In summary, the development of graphene-transition metal-based electrocatalysts offers a dynamic and high-impact research area with the potential to revolutionize how we produce and store clean energy, manage industrial waste, and transition toward a more sustainable and equitable energy future. The integration of TMC compounds with graphene has led to significant improvements in electrocatalytic activity and stability of individual material via a synergistic effect. Nevertheless, those breakthroughs still stay at the stage of experimental synthesis and lack of in-depth understanding of fundamental principles of the active site on the catalyst surface and catalytic reaction mechanisms, which seriously limits the development of efficient catalysts. DFT methods have become similarly ubiquitous in electrocatalysis research over the last few years, with many research groups integrating DFT with experimental efforts to advance both fundamental understanding and practical design.

Our future research in this domain is expected to focus on:

a) The rational design of advanced material architectures such as single-atom catalysts (SACs), dual- or multi-metallic systems, 2D heterostructures, and porous

or hierarchical structures, which can enhance catalytic activity, selectivity, and stability under real-world conditions.

b) These developments will be increasingly supported by theoretical modeling using Density Functional Theory (DFT), providing atomic-level insights into reaction mechanisms, active site identification, and activity descriptors. Moreover, the integration of machine learning (ML) and data-driven approaches with experimental and theoretical studies is set to accelerate catalyst discovery and optimization by enabling high-throughput screening of material libraries.

c) The use of in situ and operando characterization techniques (e.g., X-ray absorption spectroscopy, Raman, FTIR, electrochemical impedance) for understanding catalyst behavior under working conditions and guiding material optimization.

d) Finally, the ultimate objective of research on TMC-based electrocatalyst systems is to implement them in a real-world condition to accomplish commercial scale hydrogen production. So, as research advances toward practical implementation, we have planned to work toward addressing key challenges such as large-scale material production, long-term stability, and seamless integration into functional devices.

e) Interdisciplinary collaboration, particularly with experts in materials science, chemical engineering, AI, and environmental science, to develop integrated systems that meet real-world demands.

Appendix Information

Chapter 2

Table A1. WO_3-based electrocatalyst for electrocatalytic water splitting or electro catalytic HER and OER evolution.

Catalyst	Substrate used for deposition	Electrolyte	η HER @ 10 mA/cm^2	Tafel HER mvdec^{-1}	η OER @ 10 mA/cm^2	Tafel OER mv dec^{-1}
$WO_3.H_2O$	GCE	0.5 M H_2SO4	147	43.9	---	----
WO_{3-x}/CF	Pt/C-GCE	0.5 M H_2SO4	185	89	---	----
WO_3@NPrGO	GCE	0.5 M H_2SO4	660	87	---	----
Pt/WO_3	CFC	0.5 M H_2SO4	42	61	---	----
Pt/WO_3	GCE	0.5 M H_2SO4	39	32.3	---	----
WO_3 nps	Chitosan	1 M H_2SO4	620	---		
IrW-WO_3 nanosheet arrays	Carbon paper	0.5 M H_2SO4	49	36	229	88
POM-derived Ir/WO_x/rGO	graphene	1 M KOH	53	43	265	62
Biomass activated carbon decorated WO_3	stainless steel plate	1 M KOH	360	14	328	48
Sm doped WO_3	GCE	0.5M H_2SO4	123	54	245	82
Ir-doped WO_3	CARBON FIBRE PAPER	0.5M H_2SO4	36	72	258	48
SA-GWO (This work)	Not required	1 M H_2SO_4 at 50 ºC	352	117	311	659

* GCE is glassy carbon electrode.

Figure A1. Fabrication procedure of self assembled SA-GWO electrodes.

Table A2. hkl planes identified for SA-GWO self-assembled architecture.

2 theta values	d spacing (Å)	h	k	l
23.0993	3.8505	**0**	**0**	**2**
23.5755	3.77379	**0**	**2**	**0**
24.3168	3.6604	**2**	**0**	**0**
26.5582	3.35635	**1**	**2**	**0**
28.8958	3.08992	**1**	**1**	**2**
33.2404	2.69533	**0**	**2**	**2**
33.5371	2.67216	**2**	**0**	**-2**
34.1094	2.62862	**2**	**0**	**2**
41.8752	2.15736	**2**	**2**	**2**
47.2412	1.92408	**0**	**0**	**4**
48.2697	1.88546	**0**	**4**	**0**
49.8817	1.82824	**2**	**3**	**-2**
55.9001	1.64483	**1**	**4**	**2**
61.9501	1.49794	**3**	**0**	**4**
76.6916	1.24263	**5**	**3**	**1**

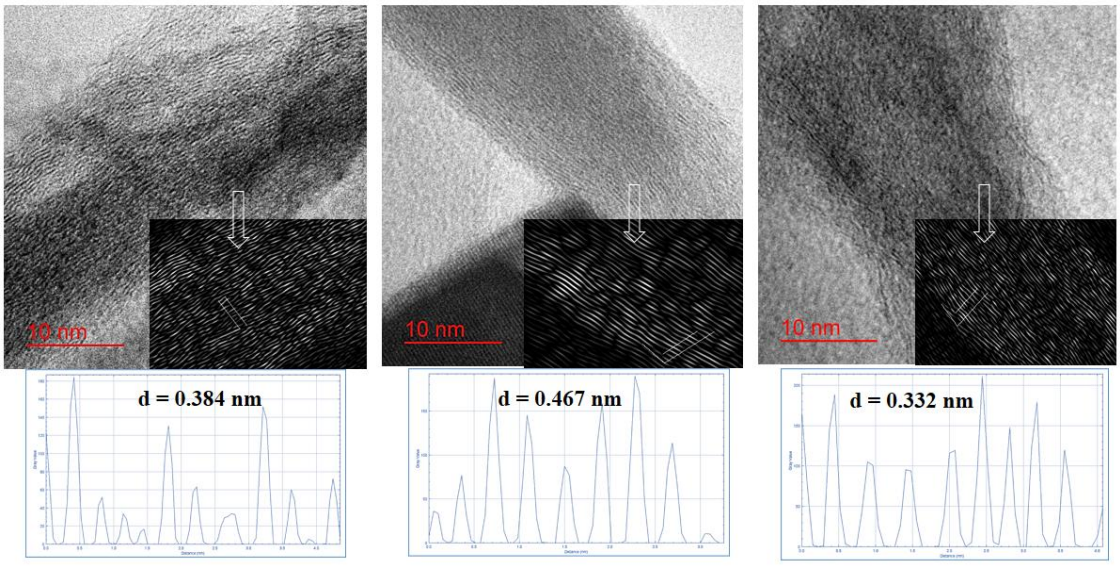

Figure A2. Plot profile of RGO at different spots.

Table A3. d-spacing of respective RGO and WO3 component revealed *via* SAED diffraction study.

Sr. No	Material	d-spacing Values (nm)	Miller Indices (hkl)	References
1.	WO_3	0.383	0 0 2	JCPDS data file 01-072-1465
		0.378	0 2 0	
		0.214	0 4 0	
		0.125	5 3 0	
2.	RGO	0.331	0 0 2	Energy & Environmental Materials 2021, 4, 681-686.
		0.208	1 0 0	
		0.122	1 1 0	

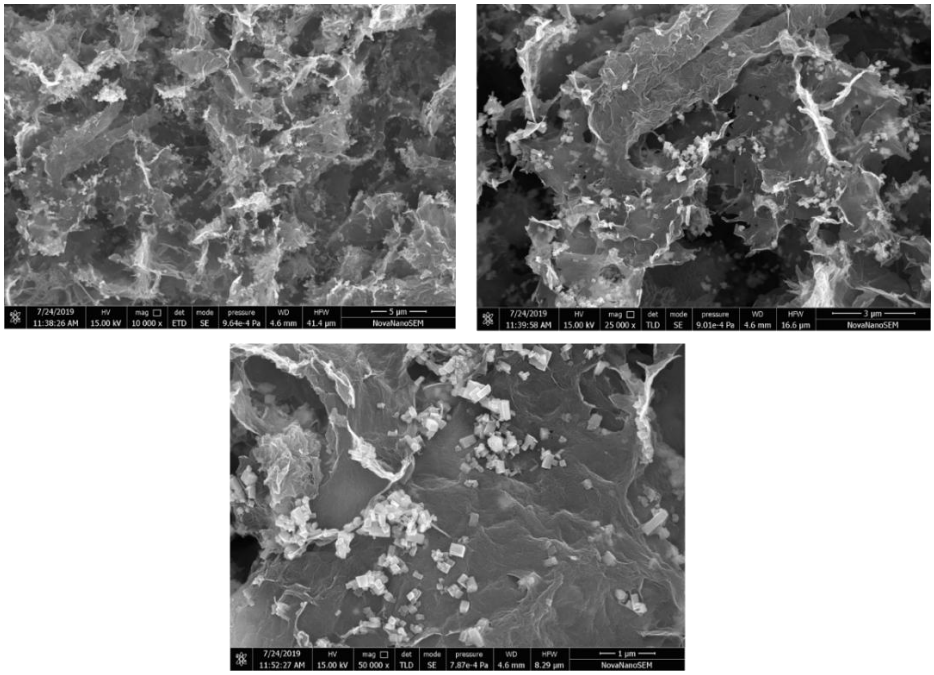

Figure A3. SEM images at low resolution (5, 3 and 1 µm), the electrode extracted from 3D SA-GWO was used directly for SEM surface characterization.

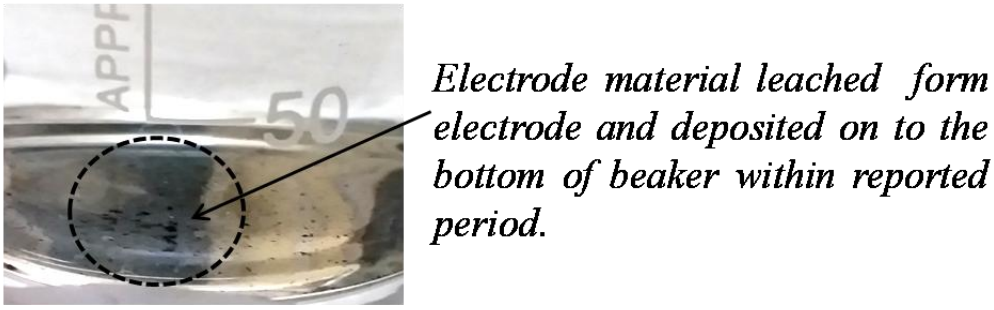

Figure A4. Image displays the leaching of material from the electrode surface SA-GWO particularly in KOH medium.

Table A4. Stability of SA-GWO in 1 M H_2SO_4 @ different temperature: Measuring OCV potential of SA-GWO in H_2SO_4 (1 M) @ different temperature vs. Time.

Electrolyte H_2SO_4 (1 M)	Temp (°C)		Time (min)				
			0	5	15	30	60
	13	OCP (V)	0.45	0.45	0.47	0.47	0.47
	36		0.47	0.47	0.47	0.47	0.47
	60		0.47	0.47	0.47	0.47	0.47

Table A5. Solution resistance (Rs) and Charge transfer resistance (Rct) value of SA-GWO obtained by fitting of EIS data uses ZSimpWin 3.1 data analysis software.

Sr. No	Concentration H_2SO_4	R1 (Solution Resistance)	R2 (Charge Transfer Resistance)
1	@ 0.5 M	**18.70**	**33.20**
2	@ 1 M	**5.31**	**22.78**

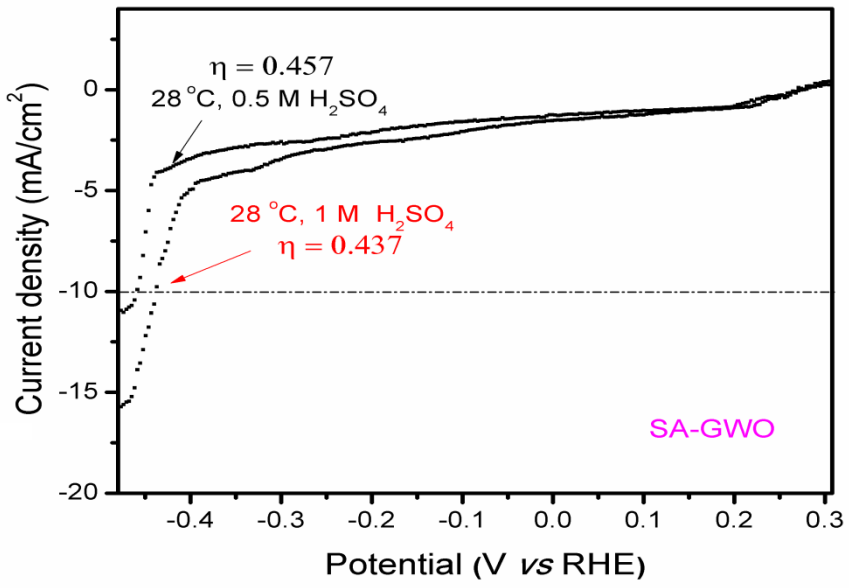

Figure A5. LSV responses of the SA-GWO in acidic medium (0.5 and 1.0 M H_2SO_4) at scan rate 5 mV/s.

Table A6. Overpotential, Tafel slope and exchange current density of SA-GWO measured at different temperature in 1M H_2SO_4.

Sr. No	Temperature (°C)	η[mV]@ 10 mA cm^{-2}	Tafel Slope (mV/dec)	Exchange current density (mA/cm^{-2})
1	@28	0.44	117	1.73×10^{-3}
2	@50	0.35	117	5.42×10^{-3}
3	@70	0.25	241	4.89×10^{-1}

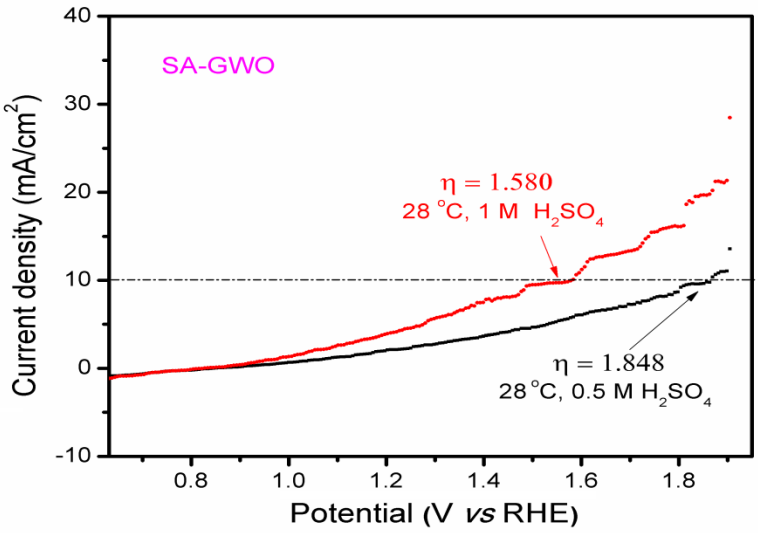

Figure A6. LSV responses of the SA-GWO in acidic medium (0.5 and 1.0 M H_2SO_4) at scan rate 5 mV/s.

E1. Electrochemical optimization of WO_3 as electrocatalyst.

Bare WO_3 was synthesized *via* the same procedure as standardized for the SA-GWO electrode. The basic difference in the synthesis procedure is that the reaction was carried out in the absence of graphene oxide and the resultant product obtained was purely WO3 and it's in powder form.

Further, The FTO surface was cleaned with alumina slurry (0.05 mm) for 2-4 minutes, then washed with distilled water, then transferred into 2% phosphoric acid for 1 hour, washed again with excess distilled water, then with acetone, and finally dried. Thereafter, WO_3 (1.0 mg) dispersed via ultra-sonication in deionized water (1 mL) containing 1.00% nafion was dropped (200 µL) over the clean surface of FTO. Finally, these modified electrodes (WO_3 deposited on FTO plate) were dried at room temperature and used as working electrodes.

The electrolytic performance of WO3 (powdered form) was tested using a three-electrode system that included WO3 deposited on FTO plate as the working electrode, Ag/AgCl as the reference electrode, and Pt as the counter electrode. The performance was evaluated in the potential range of -0.70 to -1.7 V vs RHE.

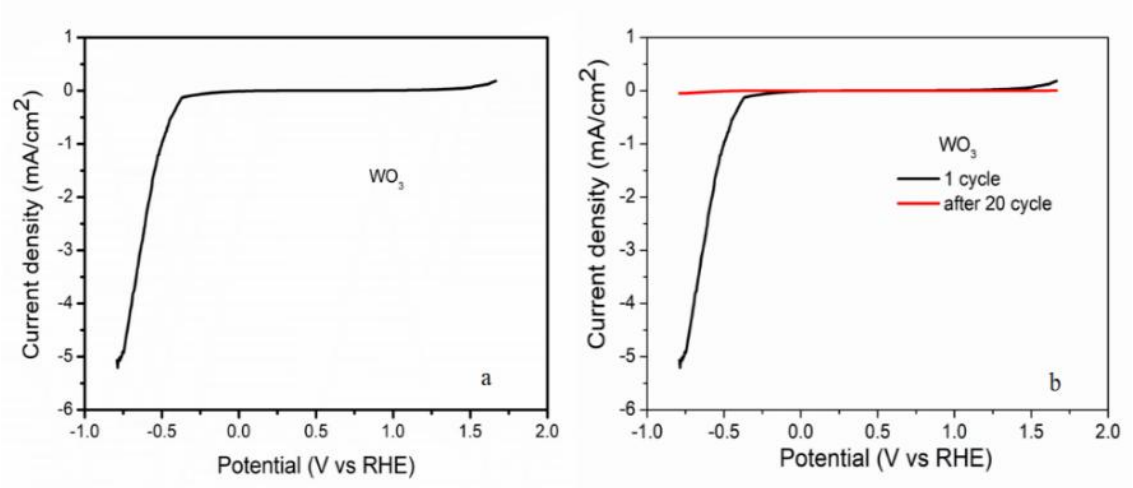

Figure A7. (a) LSV responses of the WO_3 catalyst deposited on FTO plate at scan rate 5 mV/s (1.0 M H_2SO_4) (b) the same recorded after 20 cycles of performance.

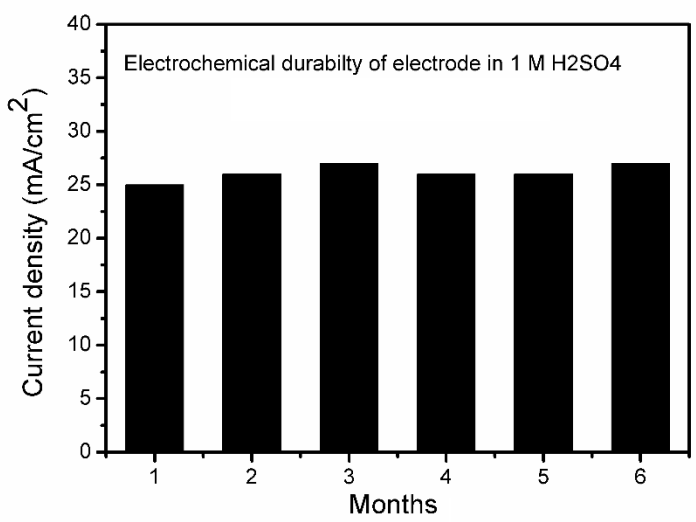

Figure A8. Electrochemical durability of SA-GWO in 1 M H_2SO_4 evaluated periodically.

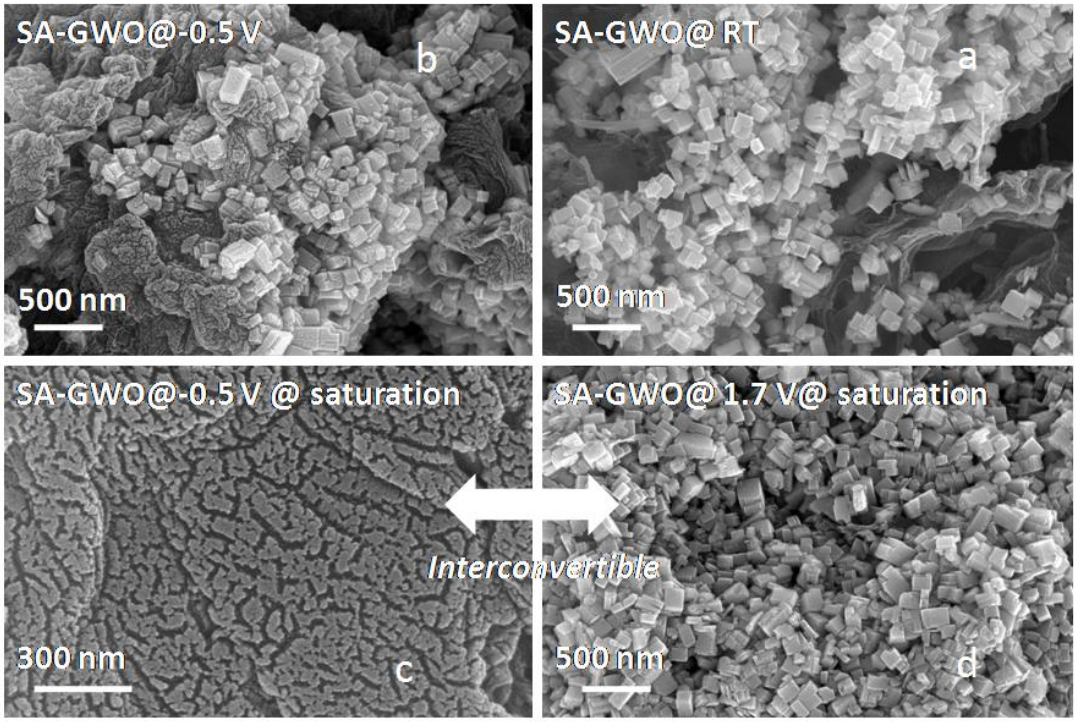

Figure A9. SEM images of SA-GWO electrode at the potential of (a) 0 V (fresh, untreated) (b) fixed -@0.5 V for 15 min (c) fixed at -0.5 V for 2 h (saturation) and (d) the same fixed at 1.7 V for 2 h.

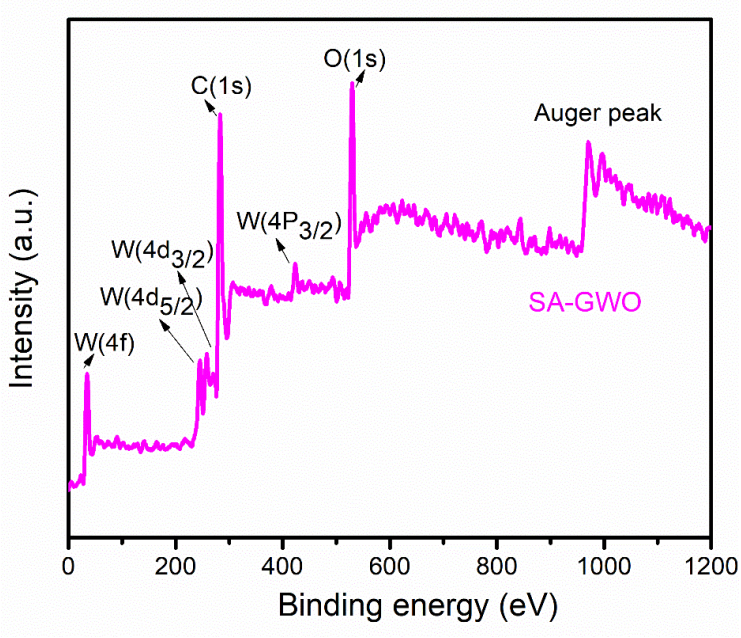

Figure A10. XPS spectrum of SA-GWO.

Chapter 3

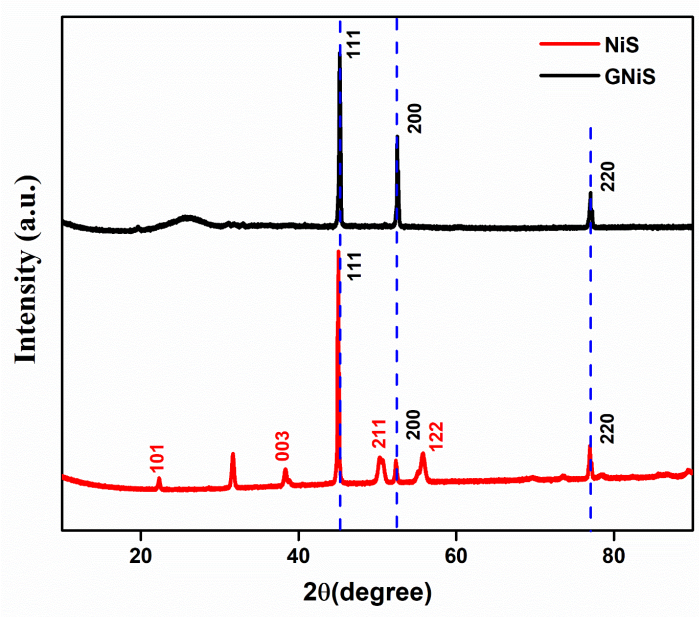

Figure A11. XRD Profile of the samples NiS powder and GNiS electrode.

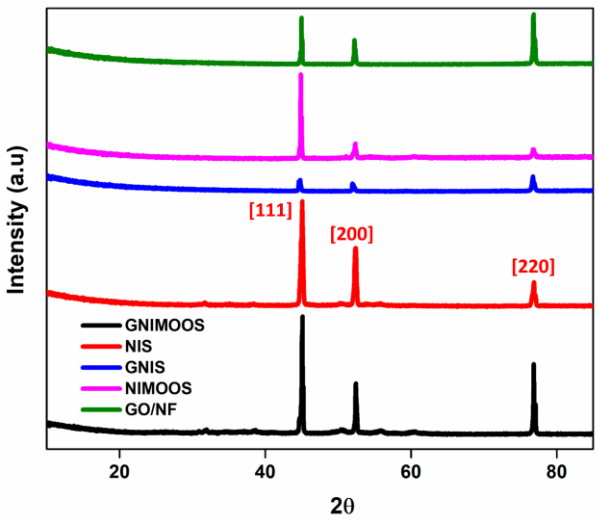

Figure A12. Combined XRD Profile of the NiS and GNiS, NiMoOS, RGO/NF and GNiMoOS electrodes.

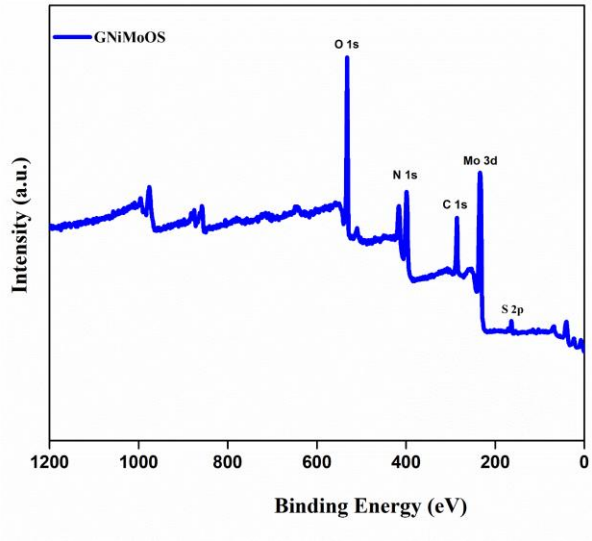

Figure A13. The full survey XPS spectrum of GNiMoOS.

Table A7. The percentage area of peak A (162-164 eV) and B (168.8 eV) corresponding to different sulfur species in MoS_2, NiMoOS and GNiMoOS**.**

S.no	% area peak A (Apical S^{2-} and Bridging S_2^{2-} species of MoS2)	% area peak B (SO_4^{2-}, SO_3H-Graphene)
MoOS	**72**	**28**
Ni-MoOS	**81**	**19**
G-Ni-MoOS	**7.12**	**92.872**

E2. iR Correction Procedure

In this work , the experimental data points are manually corrected with a predetermined resistance which is obtained by fitting the high-frequency region of the electrochemical impedance spectroscopy (EIS) data with an equivalent circuit (often the Randles circuit).This resistance is then multiplied by the cell current (IR) and then substracted from the actual potential values (V_{actual} -IR).This value is then plotted with respect to the current values .

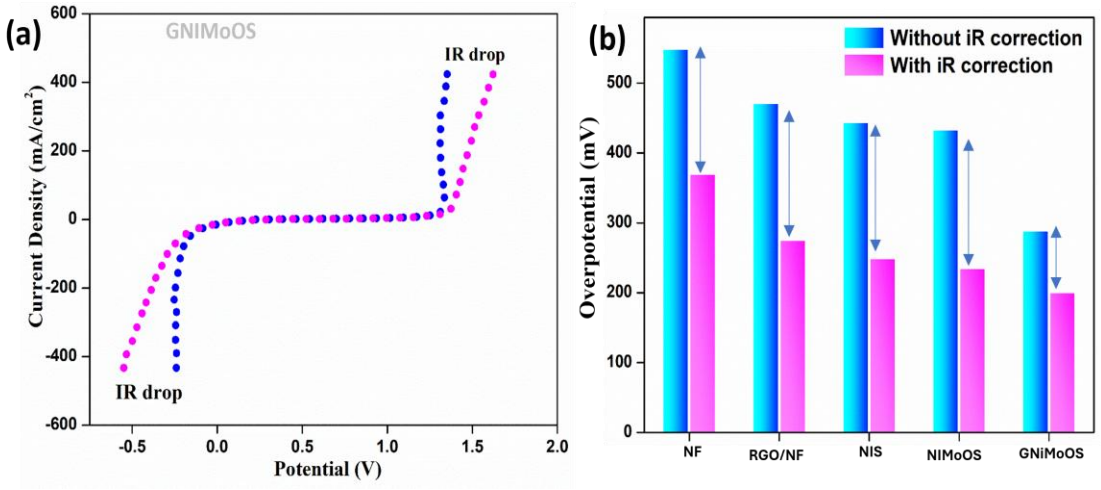

Figure A14. (a) iR drop corrected data of GNiMoOS (b)Overpotential values of the electrodes for HER before and after iR correction for 100 mA cm^{-2} current density.

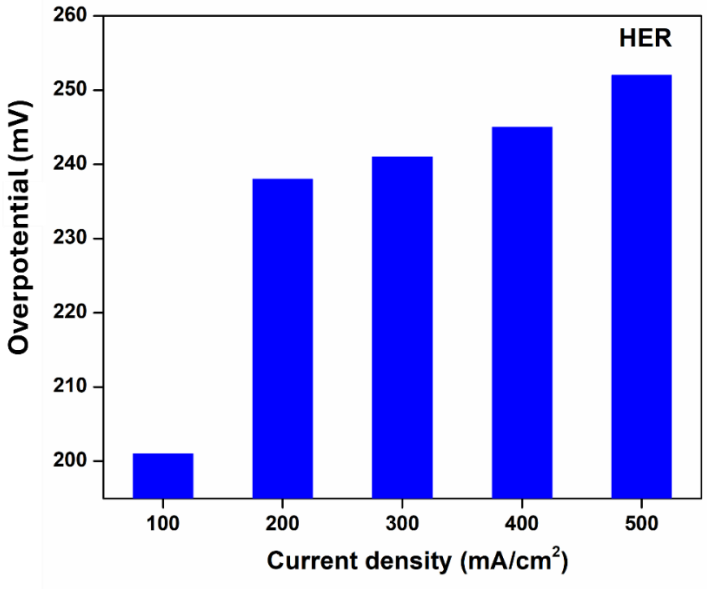

Figure A15. iR corrected potentials of GNiMoOS for 100 -500 mA cm^{-2} current density in simulated seawater media.

E3. Determining of Electrochemical active surface area (ECSA)

Electrochemical capacitance measurements were used to determine the active surface area of catalyst. To measure the electrochemical capacitance, CV curves with various scan rates (20 mV sec^{-1} to 100 mV sec^{-1}) were measured in non-Faradic potential window (0.5 to 0.7 V vs RHE). By plotting the capacitive currents (ΔJ=Janodic -Jcathodic) against the scanning rate at the central voltage and following with a linear fit, the double layer capacitance (C_{dl}) can be estimated as half of the slope. From the double layer capacitance (Cdl) and capacitance of an atomically smooth planar surface (C_s), the ECSA was calculated using the following equation:

$ECSA = C_{dl} / C_s$

Where Cs is the specific capacitance for a flat surface, which was generally found to be in the range of 20-60 $\mu F \cdot cm^{-2}$.

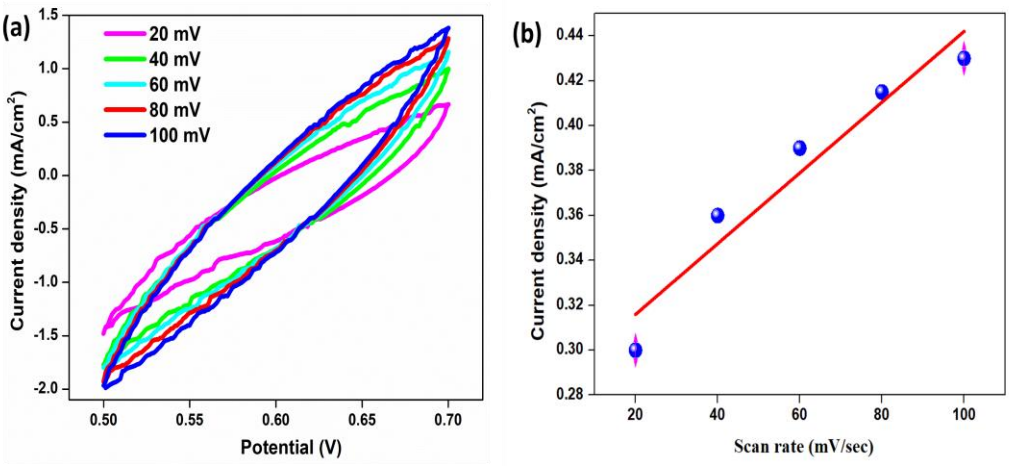

Figure A16. (a) CV curves of GNiMoOS at different scan rates from 20 to 100 mV s^{-1} at the potential window of 0.5 to 0.7 V vs RHE (b) ECSA linear plot of GNiMoOS.

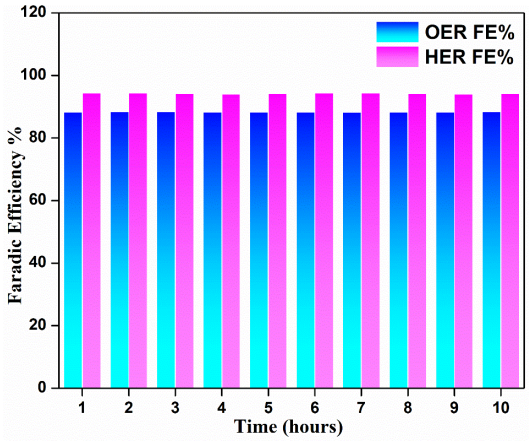

Figure A17. Faradic efficiency % of GNiMoOS for HER and OER with time in simulated seawater.

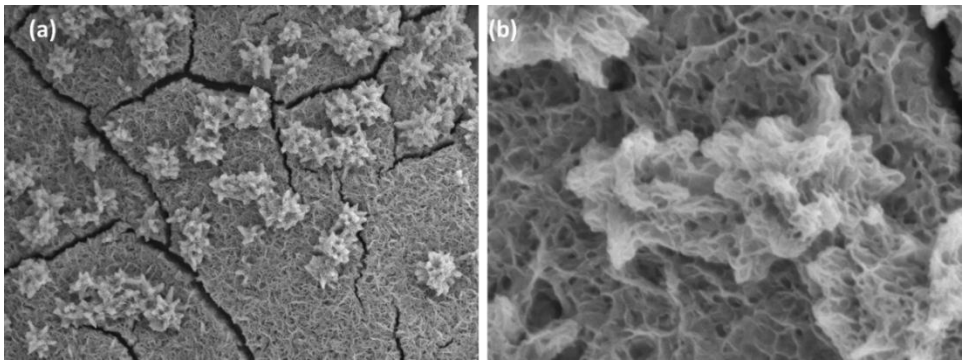

Figure A18. SEM images of GNiMoOS at 1 µm (a) and 100 nm (b) after 400-h durability test.

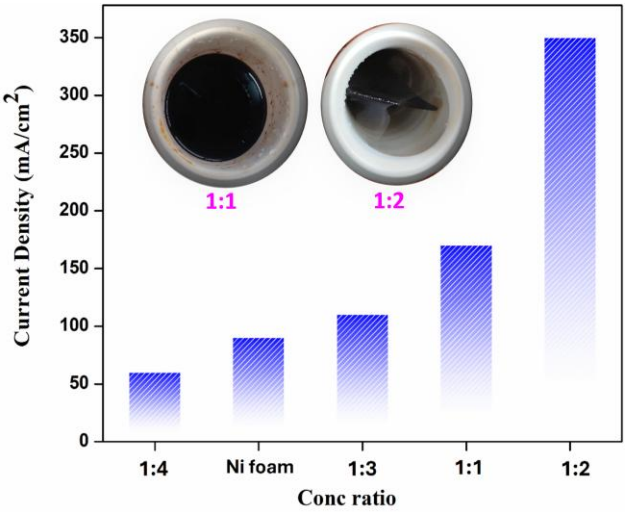

Figure A19. HER activity of GNiMoOS with varying Molar ratios of Mo:S.

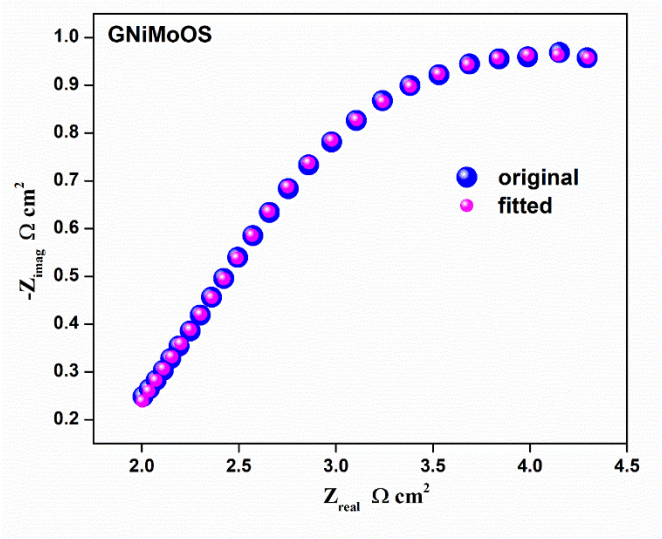

Figure A20. Fitted EIS spectra of GNiMoOS.

Chapter 4

E4. Synthesis of graphene oxide-GO

GO was synthesized by modified Hummer's method. Typically, 3 grams of natural graphite flakes were added into 9:1 mixture of concentrated H_2SO_4: H_3PO_4 (360:40 mL). After that, 18 g of KMnO4 was added very slowly about 1 hour. Then, the reaction was heated to 55 °C and stirred for 12 h. The resultant solution mixture was poured to ice cooled water contained 3 mL 10% H_2O_2. Thereafter, the resultant product was repeatedly washed with excess of DI water by centrifugation at 10000 rpm for 30 minutes, process repeated until pH of solution reaches to 7. Finally, it was washed with absolute ethanol to dissolve organic debris, if any! Then the same was collected and stored at room temperature for use.

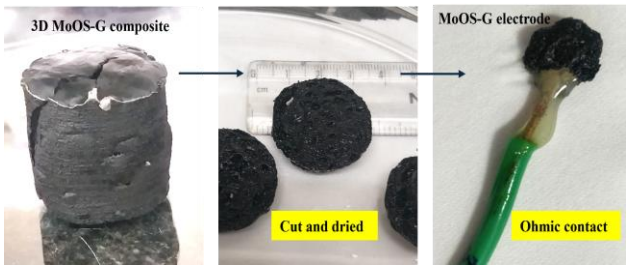

Figure A21. MoOS-G electrode fabrication.

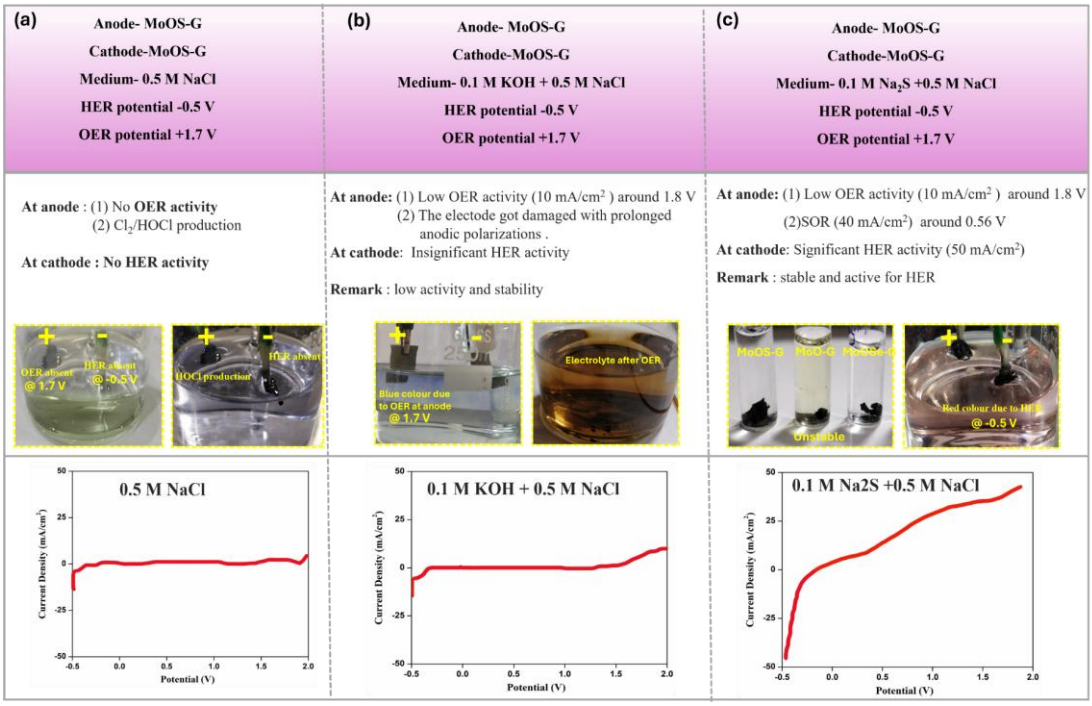

Figure A22. pre-optimizations of the prepared electrodes in neutral and alkaline media with universal indicator.

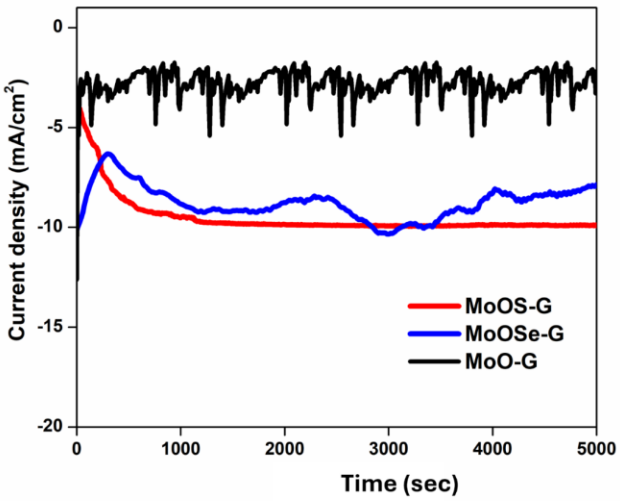

Figure A23. Stability of MoOS-G, MoOSe-G and Graphite rod in 0.1M Na2S+0.5 M salt at 1.7 V.

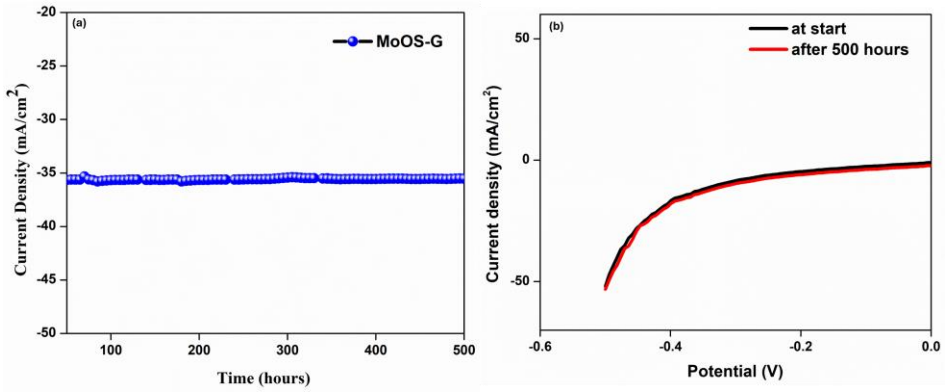

Figure A24. (a) Durability data during HER activity with MoOS-G for 500 hours (b)LSV data before and after 500 hours [Cathode-MoOS-G, Anode –Pt, electrolyte - 0.1 M Na_2S + 0.5 M salt, temperature 25^{o}C].

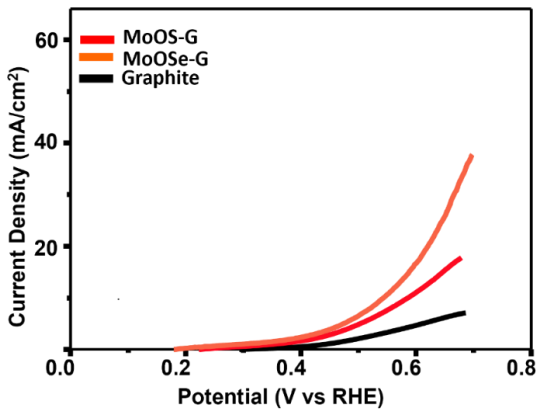

Figure A25. SOR activity with MoOS-G, MoOSe-G and Graphite rod in 0.1 M Na_2S + 0.5 M salt.

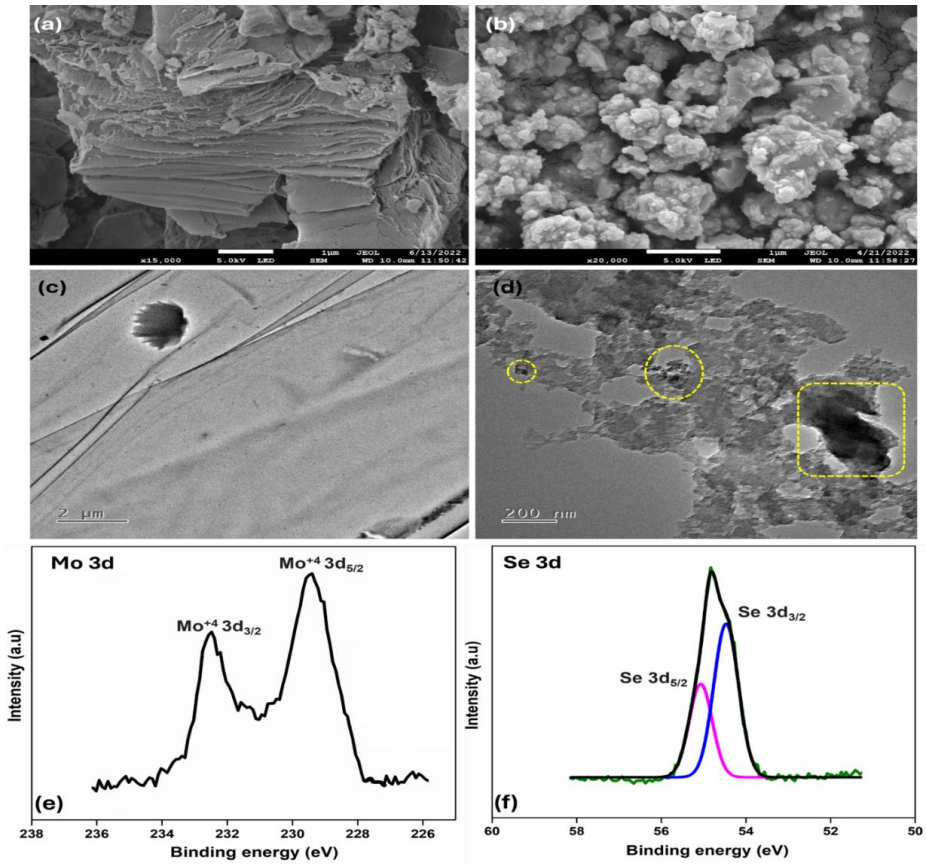

Figure A26. SEM (a, b) and TEM (c, d) images of MoOSe-G (e) XPS Mo 3d spectra of MoOSe-G (f) Se 3d deconvoluted spectra of MoOSe-G.

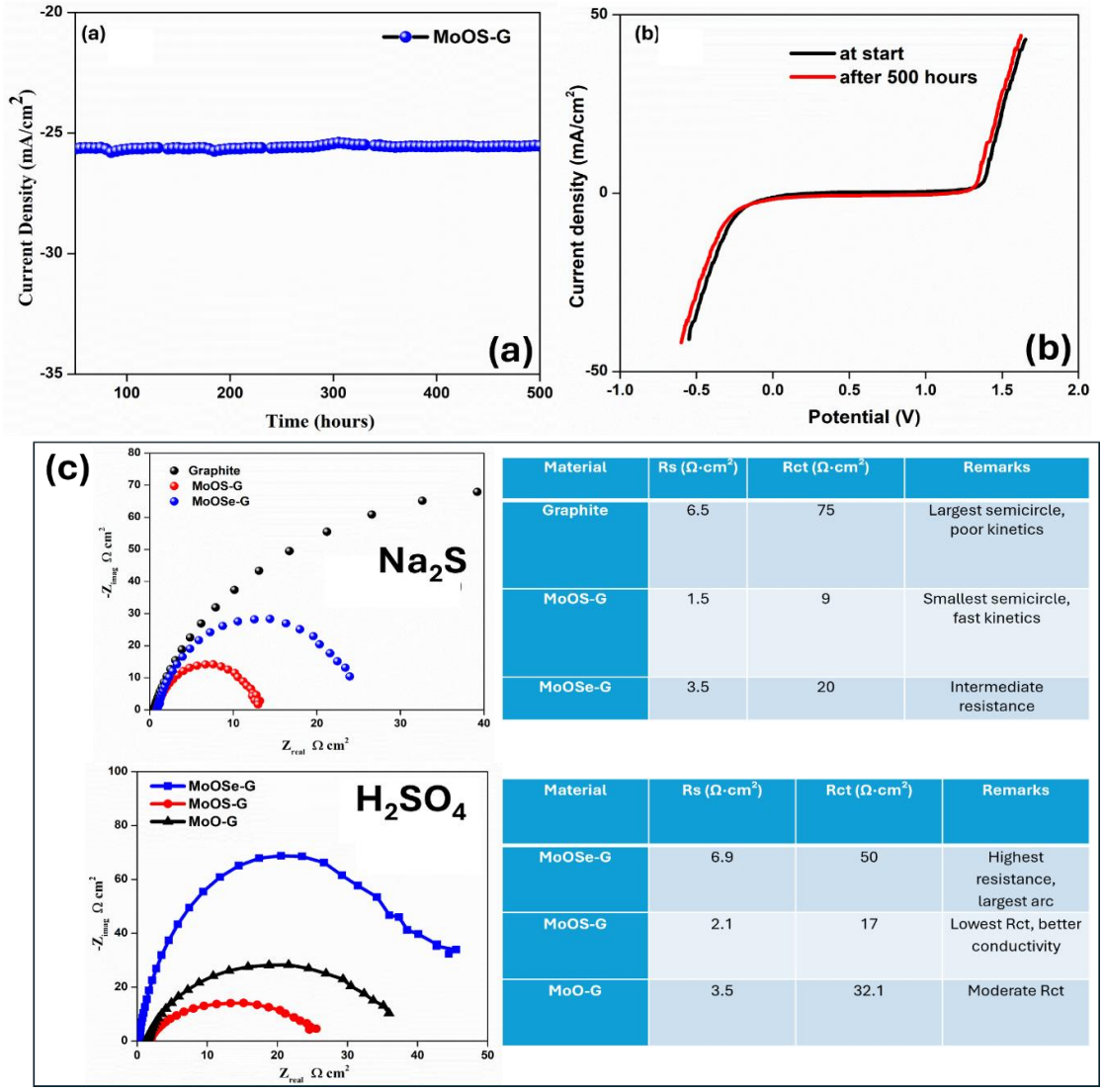

Material	Rs (Ω·cm^2)	Rct (Ω·cm^2)	Remarks
Graphite	6.5	75	Largest semicircle, poor kinetics
MoOS-G	1.5	9	Smallest semicircle, fast kinetics
MoOSe-G	3.5	20	Intermediate resistance

Material	Rs (Ω·cm^2)	Rct (Ω·cm^2)	Remarks
MoOSe-G	6.9	50	Highest resistance, largest arc
MoOS-G	2.1	17	Lowest Rct, better conductivity
MoO-G	3.5	32.1	Moderate Rct

Figure A27. (a). Durability data during HER activity with MoOS-G for 500 hours (b) LSV data before and after 500 hours [Cathode-MoOS-G, Anode –Pt, electrolyte - 1 M H_2SO_4, temperature 25ºC]. (c) The measured solution resistance (R_S) and charge transfer resistance (R_{CT}) of the respective electrodes in Na_2S media(above) and H_2SO_4 media (below).

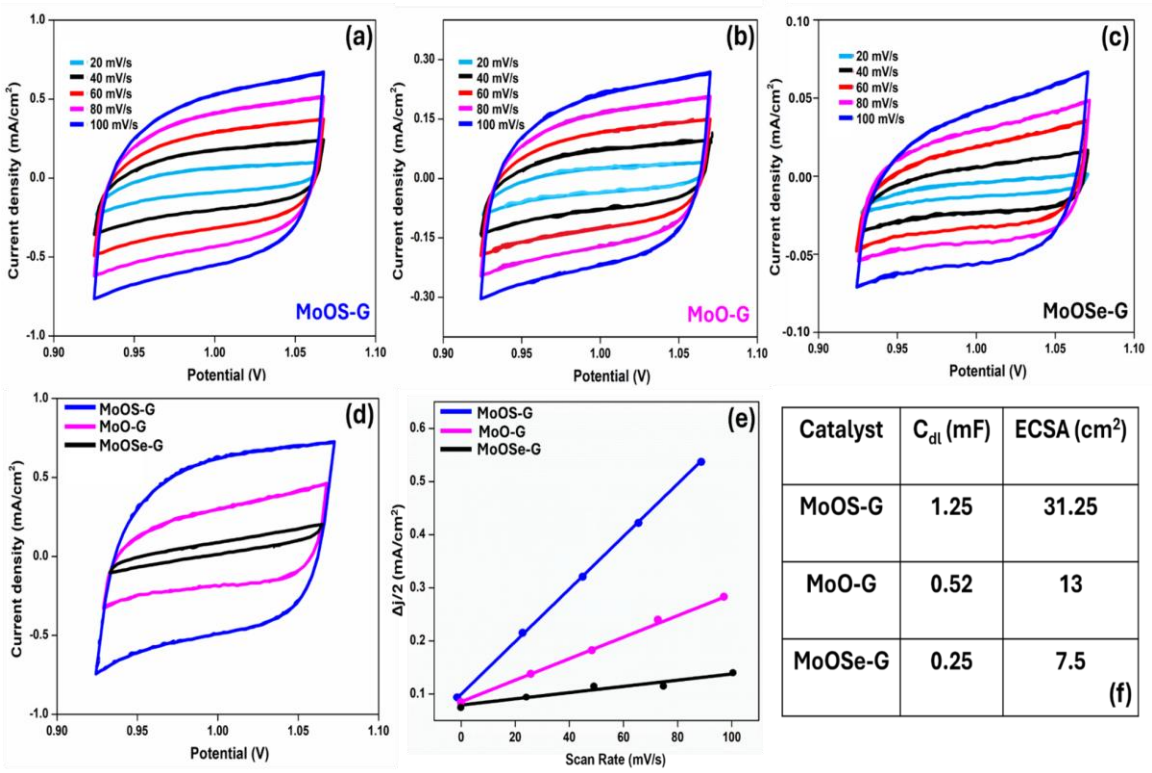

Catalyst	C_{dl} (mF)	ECSA (cm^2)
MoOS-G	1.25	31.25
MoO-G	0.52	13
MoOSe-G	0.25	7.5

(f)

Figure A28. (a-c) CV of (a) MoOS-G, (b) MoO-G, and (c) MoOSe-G recorded at various scan rates (20-100 mV/s) in a non-faradaic potential window (d) Comparative CV curves at 100 mV/s (e) Corresponding linear fits of ΔJ/2 (anodic–cathodic current) vs. scan rate for all three samples (f) ECSA values of the respective electrodes.

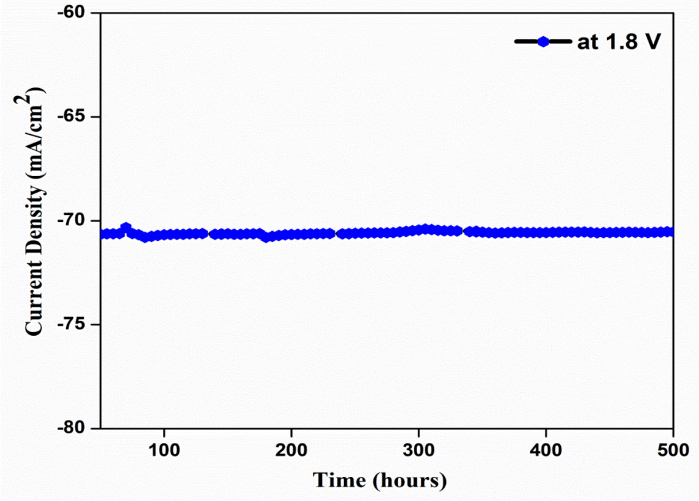

Figure A29. Bifunctional activity with MoOS-G at 1.8 V with DC source in 1 M H_2SO_4.

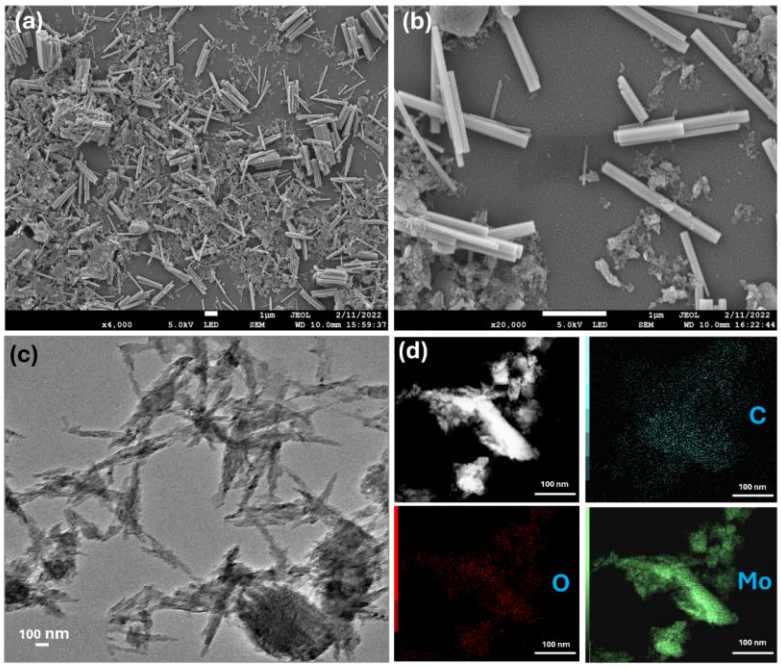

Figure A30. SEM (a, b) and TEM(c)images of MoO-G SEM (d) EDAX data of MoO-G.

Chapter 5

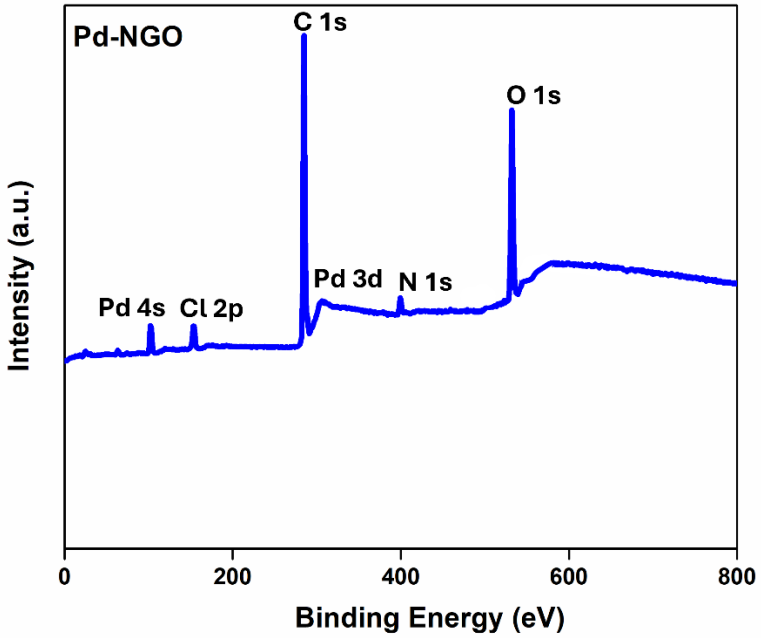

Figure A31. XPS Full survey spectrum of Pd-NGO nanocomposite, confirming the of presence of all key elements Pd, C, N, and O in the composite.

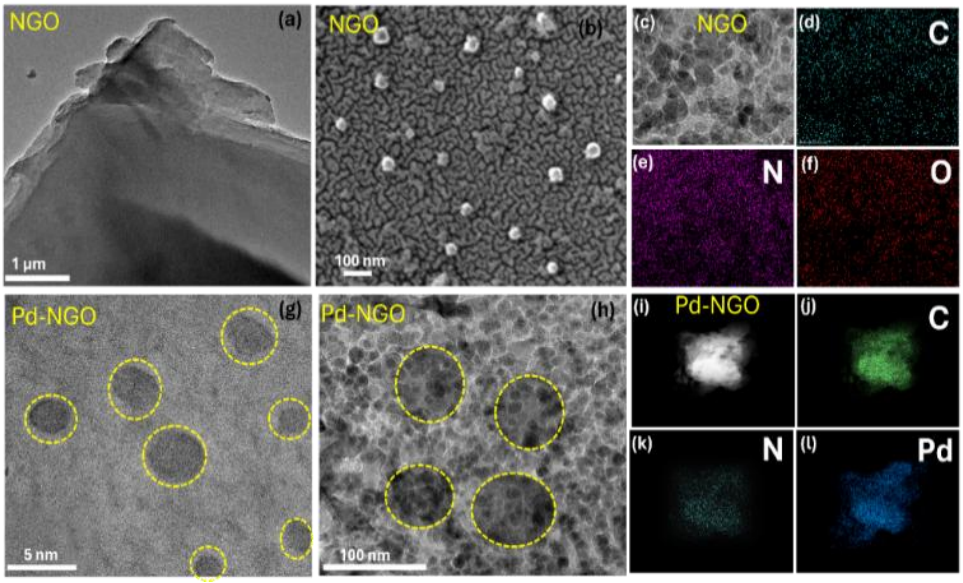

Figure A32. (a) TEM image of NGO sheets b) SEM image of NGO surface (c–f) TEM image and corresponding EDX elemental mapping of NGO (g, h) High-resolution TEM images of Pd-NGO (highlighted with yellow dashed circles) into the NGO matrix (i-l) TEM image and corresponding EDX elemental mapping of Pd-NGO.

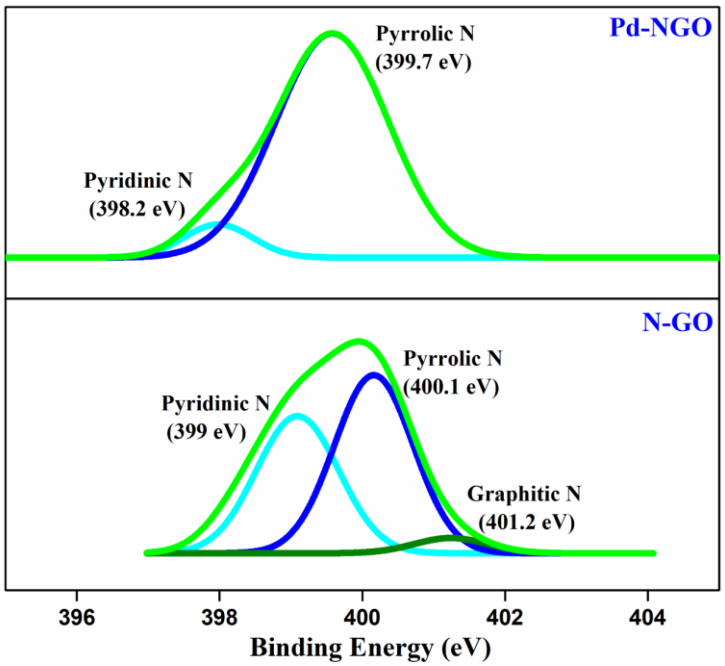

Figure A33. Deconvoluted high-resolution N 1s XPS spectra of N-GO and Pd-NGO.

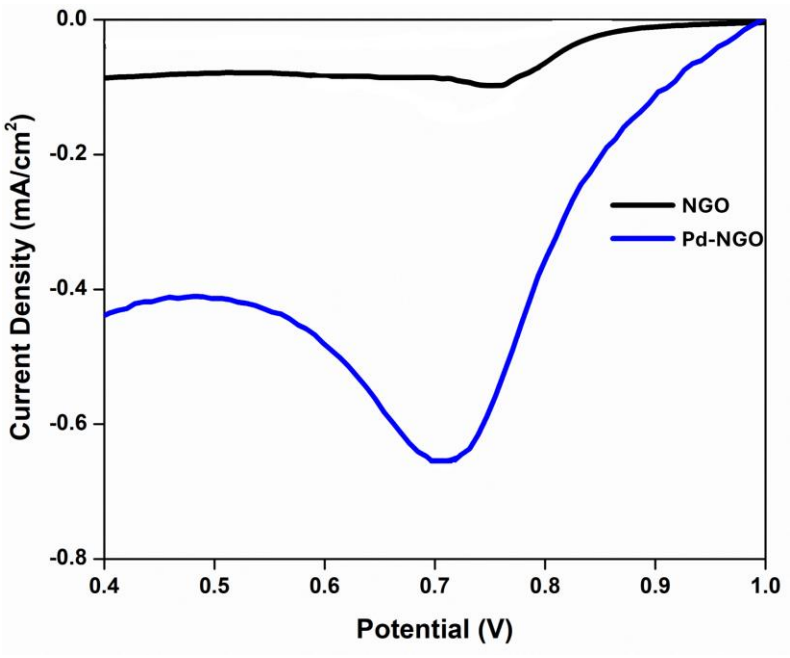

Figure A34. The current response of NGO/SPCE and Pd-NGO/SPCE up to 5 mM H_2O_2 addition highlighting Pd-NGO as an effective electrochemical sensor towards H_2O_2 detection.

References

[1] UCS, Benefits of renewable energy use, https://www.ucsusa.org/resources/benefits-renewable-energy-use

[2] Chen, H.; Cong, T. N.; Yang, W.; Tan, C.; Li, Y.; Ding, Y. Progress in electrical energy storage system: A critical review. *Progress in Natural Science* **2009**, *19* (3), 291-312.

[3] Al-Badi, A.; and AlMubarak, I. Growing energy demand in the GCC countries. *Arab Journal of Basic and Applied Sciences* **2019**, *26* (1), 488-496.

[4] Al Shaqsi, A. Z.; Sopian, K.; Al-Hinai, A. Review of energy storage services, applications, limitations, and benefits. *Energy Reports* **2020**, *6*, 288-306.

[5] Bodha, K. D.; Kumar, Y. V.; and Mukherjee, V. A novel quantum inspired hybrid metaheuristic for dispatch of power system including solar photovoltaic generation. *Energy Sources, Part B: Economics, Planning, and Policy* **2021**, *16* (6), 558-583.

[6] Enerdata,Global energy consumption 2020 [Online]. Available:https://yearbook.enerdata.net/total-energy/world-consumption-statistics.html

[7] Statistical review of world energy,Energy consumers[Online]Available: https://www.bp.com/en/global/corporate/energy-economics/statistical-review-of-world-energy.html (2021)

[8] Amir, M.; Deshmukh, R. G.; Khalid, H. M.; Said, Z.; Raza, A.; Muyeen, S. M.; Nizami, A.-S.; Elavarasan, R. M.; Saidur, R.; Sopian, K., Energy storage technologies: An integrated survey of developments, global economical/environmental effects, optimal scheduling model, and sustainable adaption policies. *Journal of Energy Storage* **2023,** *72*, 108694.

[9] Serat, Z., Optimizing renewable energy systems for 100 % clean energy target: A comparative study of solar, hydro, pumped hydro, and battery storage technologies. *Journal of Energy Storage* **2024,** *104*, 114441.

[10] Höök, M.; Tang, X. Depletion of fossil fuels and anthropogenic climate change— A review. *Energy Policy* **2013**, *52*, 797-809.

[11] Liang, Y.; Li, Y.; Wang, H.; Dai, H. Strongly Coupled Inorganic/Nanocarbon Hybrid Materials for Advanced Electrocatalysis. *Journal of the American Chemical Society* **2013**, *135* (6), 2013-2036.

[12] Ribeiro, A. E. D.; Arouca, M. C.; Coelho, D. M. Electric energy generation from small-scale solar and wind power in Brazil: The influence of location, area and shape. *Renewable Energy* **2016**, *85*, 554-563.

[13] Shao, Y.; Cheng, Y.; Duan, W.; Wang, W.; Lin, Y.; Wang, Y.; Liu, J. Nanostructured Electrocatalysts for PEM Fuel Cells and Redox Flow Batteries: A Selected Review. *ACS Catalysis* **2015**, *5* (12), 7288-7298.

[14] Zhao, Y.; Yang, N.; Yu, R.; Zhang, Y.; Zhang, J.; Li, Y.; Wang, D. Unique structural advances of graphdiyne for energy applications. *EnergyChem* **2020**, *2* (5), 100041.

[15] Escobar-Yonoff, R.; Maestre-Cambronel, D.; Charry, S.; Rincón-Montenegro, A.; Portnoy, I. Performance assessment and economic perspectives of integrated PEM fuel cell and PEM electrolyzer for electric power generation. *Heliyon* **2021**, *7* (3).

[16] Li, J. Oxygen Evolution Reaction in Energy Conversion and Storage: Design Strategies Under and Beyond the Energy Scaling Relationship. *Nano-Micro Letters* **2022**, *14* (1), 112.

[17] Liu, X.; Yuan, Y.; Liu, J.; Liu, B.; Chen, X.; Ding, J.; Han, X.; Deng, Y.; Zhong, C.; Hu, W. Utilizing solar energy to improve the oxygen evolution reaction kinetics in zinc–air battery. *Nature Communications* **2019**, *10* (1), 4767.

[18] Haichao, L.; Li, H.; Bubakir, M.; Yang, W.; Barhoum, A. Engineering Nanofibers as Electrode and Membrane Materials for Batteries, Supercapacitors, and Fuel Cells. 2019; pp 1105-1130.

[19] An, L.; Zhao, T. S.; Zhou, X. L.; Yan, X. H.; Jung, C. Y. A low-cost, high-performance zinc–hydrogen peroxide fuel cell. *Journal of Power Sources* **2015**, *275*, 831-834.

[20] Tran, D. T.; Tran, P. K. L.; Malhotra, D.; Nguyen, T. H.; Nguyen, T. T. A.; Duong, N. T. A.; Kim, N. H.; Lee, J. H. Current status of developed electrocatalysts for water splitting technologies: from experimental to industrial perspective. *Nano Convergence* **2025**, *12* (1), 9.

[21] Li, W.; Wang, C.; Lu, X. Integrated transition metal and compounds with carbon nanomaterials for electrochemical water splitting. *Journal of Materials Chemistry A* **2021**, *9* (7), 3786-3827.

[22] Wang, J.; Yue, X.; Yang, Y.; Sirisomboonchai, S.; Wang, P.; Ma, X.; Abudula, A.; Guan, G. Earth-abundant transition-metal-based bifunctional catalysts for overall electrochemical water splitting: A review. *Journal of Alloys and Compounds* **2020**, *819*, 153346.

[23] Suen, N.-T.; Hung, S.-F.; Quan, Q.; Zhang, N.; Xu, Y.-J.; Chen, H. M. Electrocatalysis for the oxygen evolution reaction: recent development and future perspectives. *Chemical Society Reviews* **2017**, *46* (2), 337-365.

[24] Rossmeisl, J.; Qu, Z. W.; Zhu, H.; Kroes, G. J.; Nørskov, J. K. Electrolysis of water on oxide surfaces. *Journal of Electroanalytical Chemistry* **2007**, *607* (1), 83-89.

[25] Bockris, J. O. M. Kinetics of Activation Controlled Consecutive Electrochemical Reactions: Anodic Evolution of Oxygen. *The Journal of Chemical Physics* **1956**, *24* (4), 817-827.

[26] Wang, S.; Lu, A.; Zhong, C.-J., Hydrogen production from water electrolysis: role of catalysts. *Nano Convergence* **2021,** *8* (1), 4.

[27] Xie, X.; Du, L.; Yan, L.; Park, S.; Qiu, Y.; Sokolowski, J.; Wang, W.; Shao, Y., Oxygen Evolution Reaction in Alkaline Environment: Material Challenges and Solutions. *Advanced Functional Materials* **2022**, *32* (21), 2110036.

[28] Montoya, J. H.; Seitz, L. C.; Chakthranont, P.; Vojvodic, A.; Jaramillo, T. F.; Nørskov, J. K., Materials for solar fuels and chemicals. *Nature Materials* **2017,** *16* (1), 70-81.

[29] Huang, Z.-F.; Song, J.; Du, Y.; Xi, S.; Dou, S.; Nsanzimana, J. M. V.; Wang, C.; Xu, Z. J.; Wang, X., Chemical and structural origin of lattice oxygen oxidation in Co–Zn oxyhydroxide oxygen evolution electrocatalysts. *Nature Energy* **2019,** *4* (4), 329-338.

[30] Zhang, N.; Chai, Y., Lattice oxygen redox chemistry in solid-state electrocatalysts for water oxidation. *Energy & Environmental Science* **2021,** *14* (9), 4647-4671.

[31] Ke, S.-C.; Chen, R.; Chen, G.-H.; Ma, X.-L. Mini Review onElectrocatalyst Design for Seawater Splitting: Recent Progress and Perspectives. *Energy Fuels* **2021**, *35* (16), 12948−12956.

[32] Ayyub, M. M.; Chhetri, M.; Gupta, U.; Roy, A.; Rao, C. N. R., Photochemical and Photoelectrochemical Hydrogen Generation by Splitting Seawater. *Chemistry – A European Journal* **2018,** *24* (69), 18455-18462.

[33] Luo, W.; Yang, Z.; Li, Z.; Zhang, J.; Liu, J.; Zhao, Z.; Wang, Z.; Yan, S.; Yu, T.; Zou, Z., Solar hydrogen generation from seawater with a modified BiVO4 photoanode. *Energy & Environmental Science* **2011,** *4* (10), 4046-4051.

[34] Jiang, S.; Suo, H.; Zhang, T.; Liao, C.; Wang, Y.; Zhao, Q.; Lai,W. Recent Advances in Seawater Electrolysis. *Catalysts* **2022**, *12*,123−147

[35] Venkatkarthick, R.; Elamathi, S.; Sangeetha, D.; Balaji, R.; Suresh Kannan, B.; Vasudevan, S.; Jonas Davidson, D.; Sozhan, G.; Ravichandran, S., Studies on polymer modified metal oxide anode for oxygen evolution reaction in saline water. *Journal of Electroanalytical Chemistry* **2013,** *697*, 1-4.

[36] Zhao, L.; Li, X.; Yu, J.; Zhou, W. Design Strategy of Corrosion-Resistant Electrodes for Seawater Electrolysis *Materials* [Online], 2023.

[37] Tong, W.; Forster, M.; Dionigi, F.; Dresp, S.; Sadeghi Erami, R.; Strasser, P.; Cowan, A.; Farràs, P., Electrolysis of low-grade and saline surface water. *Nature Energy* **2020,** *5*, 367–377.

[38] Shen, X.; Zhang, X.; Li, G.; Lie, T. T.; Hong, L., Experimental study on the external electrical thermal and dynamic power characteristics of alkaline water electrolyzer. *International Journal of Energy Research* **2018,** *42* (10), 3244-3257.

[39] Shiva Kumar, S.; Himabindu, V., Hydrogen production by PEM water electrolysis – A review. *Materials Science for Energy Technologies* **2019,** *2* (3), 442-454.

[40] Marinkas, A.; Struźyńska-Piron, I.; Lee, Y.; Lim, A.; Park, H. S.; Jang, J. H.; Kim, H.-J.; Kim, J.; Maljusch, A.; Conradi, O.; Henkensmeier, D., Anion-conductive membranes based on 2-mesityl-benzimidazolium functionalised poly(2,6-dimethyl-1,4-phenylene oxide) and their use in alkaline water electrolysis. *Polymer* **2018,** *145*, 242-251.

[41] David, M.; Ocampo-Martínez, C.; Sánchez-Peña, R., Advances in alkaline water electrolyzers: A review. *Journal of Energy Storage* **2019,** *23*, 392-403.

[42] Reier, T.; Nong, H. N.; Teschner, D.; Schlögl, R.; Strasser, P., Electrocatalytic Oxygen Evolution Reaction in Acidic Environments – Reaction Mechanisms and Catalysts. *Advanced Energy Materials* **2017,** *7* (1), 1601275.

[43] Hermans, Y.; Murcia-López, S.; Klein, A.; Jaegermann, W. BiVO4 Surface Reduction upon Water Exposure. *ACS Energy Letters* **2019**, *4* (10), 2522-2528.

[44] Kim, K.; Lee, C. Recent progress in electrochemical hydrogen sulfide splitting: Strategies for enabling Sulfur-tolerant anodic reactions. *Chemical Engineering Journal* **2023**, *469*, 143861.

[45] Zhang, L.; Wang, Z.; Qiu, J. Energy-Saving Hydrogen Production by Seawater Electrolysis Coupling Sulfion Degradation. *Advanced Materials* **2022**, *34* (16), 2109321.

[46] McHugh, P. J.; Stergiou, A. D.; Symes, M. D. Decoupled Electrochemical Water Splitting: From Fundamentals to Applications. *Advanced Energy Materials* **2020**, *10* (44), 2002453.

[47] De Crisci, A. G.; Moniri, A.; Xu, Y. Hydrogen from hydrogen sulfide: towards a more sustainable hydrogen economy. *International Journal of Hydrogen Energy* **2019**, *44* (3), 1299-1327.

[48] Kumar, M.; Nagaiah, T. C. Pure hydrogen and sulfur production from H2S by an electrochemical approach using a NiCu–MoS2 catalyst. *Journal of Materials Chemistry A* **2022**, *10* (24), 13031-13041, 10.1039/D2TA02751H.

[49] Mao, Z.; Anani, A.; White, R. E.; Srinivasan, S.; Appleby, A. J. A Modified Electrochemical Process for the Decomposition of Hydrogen Sulfide in an Aqueous Alkaline Solution. *Journal of The Electrochemical Society* **1991**, *138* (5), 1299.

[50] Ateya, B. G.; AlKharafi, F. M.; Al-Azab, A. S. Electrodeposition of Sulfur from Sulfide Contaminated Brines. *Electrochemical and Solid-State Letters* **2003**, *6* (9), C137.

[51] Zhang, M.; Guan, J.; Tu, Y.; Chen, S.; Wang, Y.; Wang, S.; Yu, L.; Ma, C.; Deng, D.; Bao, X. Highly Efficient H2 Production from H2S via a Robust Graphene Encapsulating Metal Catalyst. *Energy & Environmental Science* **2019**, *13*.

[52] Aykut, Y.; Bayrakçeken Yurtcan, A. Nanostructured electrocatalysts for low-temperature water splitting: A review. *Electrochimica Acta* **2023**, *471*, 143335.

[53] Shi, Y.; Zhang, B. Recent advances in transition metal phosphide nanomaterials: synthesis and applications in hydrogen evolution reaction. *Chemical Society Reviews* **2016**, *45* (6), 1529-1541, 10.1039/C5CS00434A.

[54] Stuve, E. M. Overpotentials in Electrochemical Cells. In *Encyclopedia of Applied Electrochemistry*, Kreysa, G., Ota, K.-i., Savinell, R. F. Eds.; Springer New York, 2014; pp 1445-1453.

[55] Ge, Z.; Fu, B.; Zhao, J.; Li, X.; Ma, B.; Chen, Y. A review of the electrocatalysts on hydrogen evolution reaction with an emphasis on Fe, Co and Ni-based phosphides. *Journal of Materials Science* **2020**, *55* (29), 14081-14104.

[56] VAnantharaj, S.; Kundu, S.; Noda, S. Progress in nickel chalcogenide electrocatalyzed hydrogen evolution reaction. *Journal of Materials Chemistry A* **2020**, *8* (8), 4174-4192, 10.1039/C9TA14037A.

[57] Li, T.; Hu, T.; Dai, L.; Li, C. M. Metal-free photo- and electro-catalysts for hydrogen evolution reaction. *Journal of Materials Chemistry A* **2020**, *8* (45), 23674-23698, 10.1039/D0TA08704A.

[58] Fletcher, S. Tafel slopes from first principles. *Journal of Solid State Electrochemistry* **2009**, *13* (4), 537-549.

[59] Anantharaj, S.; Noda, S.; Driess, M.; Menezes, P. W. The Pitfalls of Using Potentiodynamic Polarization Curves for Tafel Analysis in Electrocatalytic Water Splitting. *ACS Energy Letters* **2021**, *6* (4), 1607-1611.

[60] Guo, Y.; Park, T.; Yi, J. W.; Henzie, J.; Kim, J.; Wang, Z.; Jiang, B.; Bando, Y.; Sugahara, Y.; Tang, J.; et al. Nanoarchitectonics for Transition-Metal-Sulfide-Based Electrocatalysts for Water Splitting. *Advanced Materials* **2019**, *31* (17), 1807134.

[61] Kempler, P. A.; Nielander, A. C. Reliable reporting of Faradaic efficiencies for electrocatalysis research. *Nature Communications* **2023**, *14* (1), 1158.

[62] Chen, J.; Cheng, H.; Ding, L.-X.; Wang, H. Competing hydrogen evolution reaction: a challenge in electrocatalytic nitrogen fixation. *Materials Chemistry Frontiers* **2021**, *5* (16), 5954-5969, 10.1039/D1QM00546D.

[63] Anantharaj, S.; Ede, S. R.; Sakthikumar, K.; Karthick, K.; Mishra, S.; Kundu, S. Recent Trends and Perspectives in Electrochemical Water Splitting with an Emphasis on Sulfide, Selenide, and Phosphide Catalysts of Fe, Co, and Ni: A Review. *ACS Catalysis* **2016**, *6* (12), 8069-8097.

[64] Martínez-Hincapié, R.; Wegner, J.; Anwar, M. U.; Raza-Khan, A.; Franzka, S.; Kleszczynski, S.; Čolić, V., The determination of the electrochemically active surface area and its effects on the electrocatalytic properties of structured nickel electrodes produced by additive manufacturing. *Electrochimica Acta* **2024,** *476*, 143663.

[65] Jiao, Y.; Zheng, Y.; Jaroniec, M.; Qiao, S. Z. Design of electrocatalysts for oxygen- and hydrogen-involving energy conversion reactions. *Chemical Society Reviews* **2015**, *44* (8), 2060-2086, 10.1039/C4CS00470A.

[66] Kazemi, A.; Manteghi, F.; Tehrani, Z. Metal Electrocatalysts for Hydrogen Production in Water Splitting. *ACS Omega* **2024**, *9* (7), 7310-7335.

[67] Zhu, J.; Hu, L.; Zhao, P.; Lee, L. Y. S.; Wong, K.-Y. Recent Advances in Electrocatalytic Hydrogen Evolution Using Nanoparticles. *Chemical Reviews* **2020**, *120* (2), 851-918.

[68] Wang, J.; Xu, F.; Jin, H.; Chen, Y.; Wang, Y. Non-Noble Metal-based Carbon Composites in Hydrogen Evolution Reaction: Fundamentals to Applications. *Advanced Materials* **2017**, *29* (14), 1605838.

[69] Xu, H. G.; Zhang, X. Y.; Ding, Y.; Fu, H. Q.; Wang, R.; Mao, F.; Liu, P. F.; Yang, H. G., Rational Design of Hydrogen Evolution Reaction Electrocatalysts for Commercial Alkaline Water Electrolysis. *Small Structures* **2023,** *4* (8), 2200404.

[70] Raveendran, A.; Chandran, M.; Dhanusuraman, R., A comprehensive review on the electrochemical parameters and recent material development of electrochemical water splitting electrocatalysts. *RSC Advances* **2023,** *13* (6), 3843-3876.

[71] Song, C.; Zhang, J. Electrocatalytic Oxygen Reduction Reaction. In *PEM Fuel Cell Electrocatalysts and Catalyst Layers: Fundamentals and Applications*, Zhang, J. Ed.; Springer London, 2008; pp 89-134.

[72] Meng, H.; Zeng, D.; Xie, F. Recent Development of Pd-Based Electrocatalysts for Proton Exchange Membrane Fuel Cells. In *Catalysts*, 2015; Vol. 5, pp 1221-1274.

[73] Nørskov, J. K.; Rossmeisl, J.; Logadottir, A.; Lindqvist, L.; Kitchin, J. R.; Bligaard, T.; Jónsson, H. Origin of the Overpotential for Oxygen Reduction at a Fuel-Cell Cathode. *The Journal of Physical Chemistry B* **2004**, *108* (46), 17886-17892.

[74] Worku, A. K.; Ayele, D. W.; Habtu, N. G. Recent advances and future perspectives in engineering of bifunctional electrocatalysts for rechargeable zinc–air batteries. *Materials Today Advances* **2021**, *9*, 100116.

[75] Das, S.; Ghosh, S.; Kuila, T.; Murmu, N. C.; Kundu, A. Biomass-Derived Advanced Carbon-Based Electrocatalysts for Oxygen Reduction Reaction. In *Biomass*, 2022; Vol. 2, pp 155-177.

[76] Kundu, A.; Samanta, A.; Raj, C. R. Hierarchical Hollow MOF-Derived Bamboo-like N-doped Carbon Nanotube-Encapsulated Co0.25Ni0.75 Alloy: An Efficient Bifunctional Oxygen Electrocatalyst for Zinc–Air Battery. *ACS Applied Materials & Interfaces* **2021**, *13* (26), 30486-30496.

[77] Xia, Y.-F.; Guo, P.; Li, J.-Z.; Zhao, L.; Sui, X.-L.; Wang, Y.; Wang, Z.-B. How to appropriately assess the oxygen reduction reaction activity of platinum group metal catalysts with rotating disk electrode. *iScience* **2021**, *24* (9).

[78] Phadikar, U.; Panda, B.; Das, S.; Dhak, D.; Kundu, A.; Murmu, N. C.; Kuila, T., Tailoring the numerous intimate sites between the interfaces of CoCu-LDH@FeNi2S4–FeNiS2@CoNi2S4/NF heterogeneous electrode: Monitoring the synergistic interplay and connecting the dots for alkaline water electrolysis. *International Journal of Hydrogen Energy* **2025,** *129*, 75-90.

[79] Gebreslase, G. A.; Martínez-Huerta, M. V.; Lázaro, M. J. Recent progress on bimetallic NiCo and CoFe based electrocatalysts for alkaline oxygen evolution reaction: A review. *Journal of Energy Chemistry* **2022**, *67*, 101-137.

[80] Yu, X. Y.; Yu, L.; Lou, X. W., Metal sulfide hollow nanostructures for electrochemical energy storage. *Advanced Energy Materials* **2016,** *6* (3), 1501333.

[81] Li, H.; Su, Y.; Sun, W.; Wang, Y., Carbon Nanotubes Rooted in Porous Ternary Metal Sulfide@ N/S-Doped Carbon Dodecahedron: Bimetal-Organic-Frameworks Derivation and Electrochemical Application for High-Capacity and Long-Life Lithium-Ion Batteries. *Advanced Functional Materials* **2016,** *26* (45), 8345-8353.

[82] Ganesan, P.; Prabu, M.; Sanetuntikul, J.; Shanmugam, S., Cobalt sulfide nanoparticles grown on nitrogen and sulfur codoped graphene oxide: an efficient electrocatalyst for oxygen reduction and evolution reactions. *ACS catalysis* **2015,** *5* (6), 3625-3637.

[83] Al-Naggar, A. H.; Shinde, N. M.; Kim, J.-S.; Mane, R. S., Water splitting performance of metal and non-metal-doped transition metal oxide electrocatalysts. *Coordination Chemistry Reviews* **2023,** *474*, 214864.

[84] Zeng, J.; Liu, Y.; Huang, Z.; Qiao, H.; Qi, X., Transition Metal Dichalcogenides in electrocatalytic water splitting. *Catalysts* **2024,** *14* (10), 689.

[85] Yu, Z.; Deng, Z.; Li, Y.; Wang, X., Advances in Electrocatalyst Design and Mechanism for Sulfide Oxidation Reaction in Hydrogen Sulfide Splitting. *Advanced Functional Materials* **2024,** *34* (39), 2403435.

[86] Tripathi, P.; Verma, A. K.; Sinha, A. S. K.; Singh, S., Graphene-Transition Metal Electrocatalysts for Sustainable Water Electrolysis. *ChemistrySelect* **2024,** *9* (40), e202403155.

[87] Mo, R.; Lei, Z.; Sun, K.; Rooney, D., Facile synthesis of anatase TiO2 quantum-dot/graphene-nanosheet composites with enhanced electrochemical performance for lithium-ion batteries. *Advanced materials* **2014,** *26* (13), 2084-2088.

[88] Dave, K.; Gomes, V. G., Carbon quantum dot-based composites for energy storage and electrocatalysis: Mechanism, applications and future prospects. *Nano Energy* **2019,** *66*, 104093.

[89] Yang, X.; Cai, C.; Zou, Y.; Xiang, C.; Chu, H.; Yan, E.; Qiu, S.; Sun, L.; Xu, F.; Hu, X., Co3O4-doped two-dimensional carbon nanosheet as an electrode material for high-performance asymmetric supercapacitors. *Electrochimica Acta* **2020,** *335*, 135611.

[90] HAN, X.-M.; WU, Y.-B.; ZHAO, H.-Y.; BI, J.; WEI, B.-B., Preparation and supercapacitor properties of carbon-coated SnO2 hollow fibers. *Acta Physico-Chimica Sinica* **2015,** *31* (11), 2220-2228.

[91] Wang, Y.; Zhang, L.; Hou, H.; Xu, W.; Duan, G.; He, S.; Liu, K.; Jiang, S., Recent progress in carbon-based materials for supercapacitor electrodes: a review. *Journal of Materials Science* **2021,** *56*, 173-200.

[92] Zheng, L.; Song, J.; Ye, X.; Wang, Y.; Shi, X.; Zheng, H., Construction of self-supported hierarchical NiCo-S nanosheet arrays for supercapacitors with ultrahigh specific capacitance. *Nanoscale* **2020,** *12* (25), 13811-13821.

[93] Wang, T.; Chen, H. C.; Yu, F.; Zhao, X.; Wang, H., Boosting the cycling stability of transition metal compounds-based supercapacitors. *Energy Storage Materials* **2019,** *16*, 545-573.

[94] Ren, K.; Liu, Z.; Wei, T.; Fan, Z., Recent developments of transition metal compounds-carbon hybrid electrodes for high energy/power supercapacitors. *Nano-Micro Letters* **2021,** *13* (1), 129.

[95] Burkholder, M. B.; Rahman, F. B. A.; Chandler Jr, E. H.; Regalbuto, J.; Gupton, B.; Tengco, J. M. M., Metal supported graphene catalysis: A review on the benefits of nanoparticular supported specialty sp2 carbon catalysts on enhancing the activities of multiple chemical transformations. *Carbon Trends* **2022,** *9*, 100196.

[96] Luo, M.; Yang, Y.; Sun, Y.; Qin, Y.; Li, C.; Li, Y.; Li, M.; Zhang, S.; Su, D.; Guo, S., Ultrathin two-dimensional metallic nanocrystals for renewable energy electrocatalysis. *Materials Today* **2019,** *23*, 45-56.

[97] Allen, M. J.; Tung, V. C.; Kaner, R. B., Honeycomb carbon: a review of graphene. *Chemical reviews* **2010,** *110* (1), 132-145.

[98] Lee, G.-D.; Wang, C.; Yoon, E.; Hwang, N.-M.; Kim, D.-Y.; Ho, K., Diffusion, coalescence, and reconstruction of vacancy defects in graphene layers. *Physical review letters* **2005,** *95* (20), 205501.

[99] Qin, X.; Ola, O.; Zhao, J.; Yang, Z.; Tiwari, S. K.; Wang, N.; Zhu, Y., Recent progress in graphene-based electrocatalysts for hydrogen evolution reaction. *Nanomaterials* **2022,** *12* (11), 1806.

[100] Zhang, H.; Lv, R., Defect engineering of two-dimensional materials for efficient electrocatalysis. *Journal of Materiomics* **2018,** *4* (2), 95-107.

[101] Tang, T.; Wang, Z.; Guan, J., A review of defect engineering in two-dimensional materials for electrocatalytic hydrogen evolution reaction. *Chinese Journal of Catalysis* **2022,** *43* (3), 636-678.

[102] Bei, H. P.; Yang, Y.; Zhang, Q.; Tian, Y.; Luo, X.; Yang, M.; Zhao, X., Graphene-based nanocomposites for neural tissue engineering. *Molecules* **2019,** *24* (4), 658.

[103] Huang, Z.; Liao, Z.; Yang, W.; Zhou, H.; Fu, C.; Gong, Y.; Chen, L.; Kuang, Y., Different types of nitrogen species in nitrogen-doped carbon material: The formation mechanism and catalytic role on oxygen reduction reaction. *Electrochimica Acta* **2017,** *245*, 957-966.

[104] Yan, Y.; Miao, J.; Yang, Z.; Xiao, F.-X.; Yang, H. B.; Liu, B.; Yang, Y., Carbon nanotube catalysts: recent advances in synthesis, characterization and applications. *Chemical Society Reviews* **2015,** *44* (10), 3295-3346.

[105] Zhang, L. H.; Shi, Y.; Wang, Y.; Shiju, N. R., Nanocarbon catalysts: recent understanding regarding the active sites. *Advanced Science* **2020,** *7* (5), 1902126.

[106] Wu, Y.; Yang, Y.; Zhao, X.; Tan, Y.; Liu, Y.; Wang, Z.; Ran, F., A novel hierarchical porous 3D structured vanadium nitride/carbon membranes for high-performance supercapacitor negative electrodes. *Nano-Micro Letters* **2018,** *10*, 1-11.

[107] Liu, Y.; Xin, N.; Yang, Q.; Shi, W., 3D CNTs/graphene network conductive substrate supported MOFs-derived CoZnNiS nanosheet arrays for ultra-high volumetric/gravimetric energy density hybrid supercapacitor. *Journal of Colloid and Interface Science* **2021,** *583*, 288-298.

[108] Shen, T.; Yang, L.; Pam, M. E.; Shi, Y.; Yang, H. Y., Quantum dot-carbonaceous nanohybrid composites: preparation and application in electrochemical energy storage. *Journal of Materials Chemistry A* **2020,** *8* (43), 22488-22506.

[109] Hu, Q.; Liu, X.; Zhu, B.; Fan, L.; Chai, X.; Zhang, Q.; Liu, J.; He, C.; Lin, Z., Crafting MoC2-doped bimetallic alloy nanoparticles encapsulated within N-doped graphene as roust bifunctional electrocatalysts for overall water splitting. *Nano energy* **2018,** *50*, 212-219.

[110] Pu, Z.; Amiinu, I. S.; Zhang, C.; Wang, M.; Kou, Z.; Mu, S., Phytic acid-derivative transition metal phosphides encapsulated in N, P-codoped carbon: an efficient and durable hydrogen evolution electrocatalyst in a wide pH range. *Nanoscale* **2017,** *9* (10), 3555-3560.

[111] Meng, Y.; Huang, X.; Lin, H.; Zhang, P.; Gao, Q.; Li, W., Carbon-Based Nanomaterials as Sustainable Noble-Metal-Free Electrocatalysts. *Frontiers in Chemistry* **2019,** *Volume 7 - 2019*.

[112] Xiong, P.; Tan, J.; Lee, H.; Ha, N.; Lee, S. J.; Yang, W.; Park, H. S., Two-dimensional carbon-based heterostructures as bifunctional electrocatalysts for water splitting and metal–air batteries. *Nano Materials Science* **2022**..

[113] Hu, Q.; Liu, X.; Tang, C.; Fan, L.; Chai, X.; Zhang, Q.; Liu, J.; He, C., Facile fabrication of a 3D network composed of N-doped carbon-coated core–shell metal oxides/phosphides for highly efficient water splitting. *Sustainable Energy & Fuels* **2018,** *2* (5), 1085-1092.

[114] Li, G.; Sun, Y.; Rao, J.; Wu, J.; Kumar, A.; Xu, Q. N.; Fu, C.; Liu, E.; Blake, G. R.; Werner, P., Carbon-tailored semimetal MoP as an efficient hydrogen evolution electrocatalyst in both alkaline and acid media. *Advanced Energy Materials* **2018,** *8* (24), 1801258.

[115] Higgins, D.; Zamani, P.; Yu, A.; Chen, Z., The application of graphene and its composites in oxygen reduction electrocatalysis: a perspective and review of recent progress. *Energy & Environmental Science* **2016,** *9* (2), 357-390.

[116] Kim, K.; Lee, C., Recent progress in electrochemical hydrogen sulfide splitting: Strategies for enabling Sulfur-tolerant anodic reactions. *Chemical Engineering Journal* **2023,** *469*, 143861.

[117] Wang, H., Hydrogen production from a chemical cycle of H2S splitting. *International Journal of Hydrogen Energy* **2007,** *32* (16), 3907-3914.

[118] Zhang, L.; Wang, Z.; Qiu, J., Energy-saving hydrogen production by seawater electrolysis coupling sulfion degradation. *Advanced Materials* **2022,** *34* (16), 2109321.

[119] Lakhan, M. N.; Hanan, A.; Hussain, A.; Ali Soomro, I.; Wang, Y.; Ahmed, M.; Aftab, U.; Sun, H.; Arandiyan, H., Transition metal-based electrocatalysts for alkaline overall water splitting: advancements, challenges, and perspectives. *Chemical Communications* **2024,** *60* (39), 5104-5135.

[120] Dinh, K. N.; Liang, Q.; Du, C.-F.; Zhao, J.; Tok, A. I. Y.; Mao, H.; Yan, Q., Nanostructured metallic transition metal carbides, nitrides, phosphides, and borides for energy storage and conversion. *Nano Today* **2019,** *25*, 99-121.

[121] Liu, Z.; Li, N.; Zhao, H.; Du, Y., Colloidally synthesized MoSe 2/graphene hybrid nanostructures as efficient electrocatalysts for hydrogen evolution. *Journal of Materials Chemistry A* **2015,** *3* (39), 19706-19710.

[122] Zhang, Z.; Lu, B.; Hao, J.; Yang, W.; Tang, J., FeP nanoparticles grown on graphene sheets as highly active non-precious-metal electrocatalysts for hydrogen evolution reaction. *Chemical communications* **2014,** *50* (78), 11554-11557.

[123] Tang, Y. J.; Gao, M. R.; Liu, C. H.; Li, S. L.; Jiang, H. L.; Lan, Y. Q.; Han, M.; Yu, S. H., Porous molybdenum-based hybrid catalysts for highly efficient hydrogen evolution. *Angewandte Chemie* **2015,** *127* (44), 13120-13124.

[124] Tang, C.; Zhong, L.; Zhang, B.; Wang, H. F.; Zhang, Q., 3D mesoporous van der Waals heterostructures for trifunctional energy electrocatalysis. *Advanced materials* **2018,** *30* (5), 1705110.

[125] Xu, Y.; Tu, W.; Zhang, B.; Yin, S.; Huang, Y.; Kraft, M.; Xu, R., Nickel nanoparticles encapsulated in few-layer nitrogen-doped graphene derived from metal–organic frameworks as efficient bifunctional electrocatalysts for overall water splitting. *Advanced Materials* **2017,** *29* (11), 1605957.

[126] Yan, L.; Xu, Y.; Chen, P.; Zhang, S.; Jiang, H.; Yang, L.; Wang, Y.; Zhang, L.; Shen, J.; Zhao, X., A freestanding 3D heterostructure film stitched by MOF-derived carbon nanotube microsphere superstructure and reduced graphene oxide sheets: a superior multifunctional electrode for overall water splitting and Zn–air batteries. *Advanced Materials* **2020,** *32* (48), 2003313.

[127] Tripathi, P.; Verma, A. K.; Sinha, A. S. K.; Singh, S., Cutting-Edge OER Electrocatalysts for Sustainable Seawater Electrolysis: Progress, Obstacles, and Future Prospects. *Energy & Fuels* **2025,** *39* (5), 2348-2380.

[128] Gao, M.-R.; Liang, J.-X.; Zheng, Y.-R.; Xu, Y.-F.; Jiang, J.; Gao, Q.; Li, J.; Yu, S.-H., An efficient molybdenum disulfide/cobalt diselenide hybrid catalyst for electrochemical hydrogen generation. *Nature communications* **2015,** *6* (1), 5982.

[129] Wang, J.; Cui, W.; Liu, Q.; Xing, Z.; Asiri, A. M.; Sun, X., Recent progress in cobalt-based heterogeneous catalysts for electrochemical water splitting. *Advanced materials* **2016,** *28* (2), 215-230.

[130] Yan, H.; Xie, Y.; Jiao, Y.; Wu, A.; Tian, C.; Zhang, X.; Wang, L.; Fu, H., Holey reduced graphene oxide coupled with an Mo2N–Mo2C heterojunction for efficient hydrogen evolution. *Advanced Materials* **2018,** *30* (2), 1704156.

[131] Jin, H.; Liu, X.; Chen, S.; Vasileff, A.; Li, L.; Jiao, Y.; Song, L.; Zheng, Y.; Qiao, S.-Z., Heteroatom-doped transition metal electrocatalysts for hydrogen evolution reaction. *ACS Energy Letters* **2019,** *4* (4), 805-810.

[132] Thirumal, V.; Yuvakkumar, R.; Kumar, P. S.; Ravi, G.; Shobana, M.; Saravanakumar, B.; Velauthapillai, D., Nitrogen and nitrogen-sulfur doped graphene nanosheets for efficient hydrogen productions for HER studies. *International Journal of Hydrogen Energy* **2022,** *47* (98), 41461-41467.

[133] Lai, C.; Gong, M.; Zhou, Y.; Fang, J.; Huang, L.; Deng, Z.; Liu, X.; Zhao, T.; Lin, R.; Wang, K., Sulphur modulated Ni3FeN supported on N/S co-doped graphene boosts rechargeable/flexible Zn-air battery performance. *Applied Catalysis B: Environmental* **2020,** *274*, 119086.

[134] Omeiza, L. A.; Abdalla, A. M.; Wei, B.; Dhanasekaran, A.; Subramanian, Y.; Afroze, S.; Reza, M. S.; Bakar, S. A.; Azad, A. K., Nanostructured electrocatalysts for advanced applications in fuel cells. *Energies* **2023,** *16* (4), 1876.

[135] Liu, Y.; Duan, W.; Pei, H.; Sun, P.; Sun, Y.; Zhuang, Y.; Li, Z., Multi-level Porous Fe, Co, N, S Co-doped Three-Dimensional Graphene-like Catalyst as the Excellent Trifunctional Electrocatalyst for Liquid and Flexible All-Solid-State Zinc–Air Batteries. *ACS Applied Energy Materials* **2023,** *6* (13), 7194-7204.

[136] Tripathi, P.; Verma, A. K.; Vishwakarma, A.; Mitra, K.; Ray, B.; Sinha, A.; Singh, S., Fabrication and evaluation of a self-standing reduced graphene-tungsten oxides hybrid electrode for acidic water splitting. *International Journal of Hydrogen Energy* **2022,** *47* (86), 36381-36396.

[137] Qi, L.; Li, A.; Wang, M.; Zhang, Y.; Zhang, K.; Li, X., Stable and efficient oxygen evolution from seawater enabled by graphene-supported sub-nanometer arrays of transition metal phosphides. *Advanced Materials Interfaces* **2022,** *9* (2), 2101720.

[138] Jadhav, A. R.; Kumar, A.; Lee, J.; Yang, T.; Na, S.; Lee, J.; Luo, Y.; Liu, X.; Hwang, Y.; Liu, Y., Stable complete seawater electrolysis by using interfacial chloride ion blocking layer on catalyst surface. *Journal of Materials Chemistry A* **2020,** *8* (46), 24501-24514.

[139] Jia, S.; Gao, Y.; Ma, X.; Cao, Y.; Huang, Q.; Zhang, Q.; Wang, Z.; Wang, Y.; Li, Y.; Li, D., V-doped Co2P Anchored on the N–P-Doped Three-Dimensional Covalently Cross-Linked Graphene As a Hydrogen Evolution Reaction Catalyst for Alkaline Water/Seawater Splitting. *Inorganic Chemistry* **2025**.

[140] Duan, J.; Zheng, Y.; Chen, S.; Tang, Y.; Jaroniec, M.; Qiao, S., Mesoporous hybrid material composed of Mn 3 O 4 nanoparticles on nitrogen-doped graphene for highly efficient oxygen reduction reaction. *Chemical Communications* **2013,** *49* (70), 7705-7707.

[141] Wang, H.; Liang, Y.; Li, Y.; Dai, H., Co1− xS–graphene hybrid: a high-performance metal chalcogenide electrocatalyst for oxygen reduction. *Angewandte Chemie International Edition* **2011,** *50* (46), 10969-10972.

[142] Liu, Q.; Jin, J.; Zhang, J., NiCo2S4@ graphene as a bifunctional electrocatalyst for oxygen reduction and evolution reactions. *ACS applied materials & interfaces* **2013,** *5* (11), 5002-5008.

[143] Moghaddam, M. S.; Bahari, A.; Litkohi, H. R., Using the synergistic effects of MoS2/rGO and bimetallic hybrids as a high-performance nanoelectrocatalyst for oxygen reduction reaction. *International Journal of Hydrogen Energy* **2023,** *48* (85), 33139-33154.

[144] Z.W. Seh, J. Kibsgaard, C.F. Dickens, I. Chorkendorff, J.K. Nørskov, T.F. Jaramillo, Combining theory and experiment in electrocatalysis: Insights into materials design, **2017**, 355, eaad4998.

[145] X. Li, X. Hao, A. Abudula, G. Guan, Nanostructured catalysts for electrochemical water splitting: current state and prospects, Journal of Materials Chemistry A **2016**, 4, 11973-12000.

[146] Yin, H.; Zhao, S.; Zhao, K.; Muqsit, A.; Tang, H.; Chang, L.; Zhao, H.; Gao, Y.; Tang , Z., Ultrathin platinum nanowires grown on singlelayered nickel hydroxide with h igh hydrogen evolution activity. Nat. Commun. **2015**, 6, 6430.

[147] Subbaraman., R.; Markovic., N. M., Enhancing Hydrogen Evolution Activity in Wate r Splitting by Tailoring Li+-Ni(OH)2-Pt Interfaces. Science **2011**, 334, 1256-1260.

[148] Lei, Z.; Wang, T.; Zhao, B.; Cai, W.; Liu, Y.; Jiao, S.; Li, Q.; Cao, R.; Liu, M., Recent Progress in Electrocatalysts for Acidic Water Oxidation. *Advanced Energy Materials* **2020,** *10* (23), 2000478.

[149] Peng, X.; Yan, Y.; Xiong, S.; Miao, Y.; Wen, J.; Liu, Z.; Gao, B.; Hu, L.; Chu, P. K., Se-NiSe2 hybrid nanosheet arrays with self-regulated elemental Se for efficient alkaline water splitting. *Journal of Materials Science & Technology* **2022,** *118*, 136-143.

[150] Wang, M.; Zhang, L.; He, Y.; Zhu, H., Recent advances in transition-metal-sulfide-based bifunctional electrocatalysts for overall water splitting. *Journal of Materials Chemistry A* **2021,** *9* (9), 5320-5363.

[151] Yao, M.; Hu, H.; Sun, B.; Wang, N.; Hu, W.; Komarneni, S., Self-Supportive Mesoporous Ni/Co/Fe Phosphosulfide Nanorods Derived from Novel Hydrothermal Electrodeposition as a Highly Efficient Electrocatalyst for Overall Water Splitting. *Small* **2019,** *15* (50), 1905201.

[152] Wei, Z.-X.; Zhu, Y.-T.; Liu, J.-Y.; Zhang, Z.-C.; Hu, W.-P.; Xu, H.; Feng, Y.-Z.; Ma, J.-M., Recent advance in single-atom catalysis. *Rare Metals* **2021,** *40* (4), 767-789. – single atom catalysis.

[153] J. Chen, H. Yang, X. Sang, Z. Su, D. Li, Q. Wang, Oxygen vacancy rich tungsten oxide with nitrogen doped mesoporous carbon as matrix for overall water splitting and 4-nitrophenol reductive removal, Solid State Sciences **2018**, 83, 23-30.

[154] Wang, J. Tang, X. Zhang, L. Qian, H. Yang, WO3 nanoflakes decorated with CuO clusters for enhanced photoelectrochemical water splitting, Progress in Natural Science: Materials International **2018**, 28, 200-204.

[155] J. Kulesza P J, Faulkner L. R. J. Electrocatalytic properties of Bifunctional Pt/W (VI,V) oxide microstructures electrodeposited on carbon substrate. Electroanal. Chem. **1989**, **259,** 81.

[156] X. Shang, Y. Rao, S.-S. Lu, B. Dong, L.-M. Zhang, X.-H. Liu, X. Li, Y.-R. Liu, Y.-M. Chai, C.- G. Liu, Novel WS2/WO3 heterostructured nanosheets as efficient electrocatalyst for hydrogen evolution reaction, Materials Chemistry and Physics **2017**, 197, 123-128.

[157] Y. Lv, Y. Liu, C. Chen, T. Wang, M. Zhang, Octopus tentacles-like WO3/C@CoO as high property and long life-time electrocatalyst for hydrogen evolution reaction, Electrochimica Acta **2018**, 281,1- 8

[158] T.H. Wondimu, G.-C. Chen, D.M. Kabtamu, H.-Y. Chen, A.W. Bayeh, H.-C. Huang, C.H. Wang, Highly efficient and durable phosphine reduced iron-doped tungsten oxide/reduced graphene oxide nanocomposites for the hydrogen evolution reaction, International Journal of Hydrogen Energy **2018**, 43, 6481-6490.

[159] Chekin, F.; Bagheri, S.; Abd Hamid, S. B., Synthesis of Tungsten Oxide Nanorods by the Controlling Precipitation Reaction: Application for Hydrogen Evolution Reaction on a WO3 Nanorods/Carbon Nanotubes Composite Film Modified Electrode. Journal of the Chinese Chemical Society **2013**, 60, 447-451.

[160] W. Kong, X. Zhang, S. Liu, Y. Zhou, B. Chang, S. Zhang, H. Fan, B. Yang, N Doped Carbon Dot Modified WO3 Nanoflakes for Efficient Photoelectrochemical Water Oxidation, **2019**, 6, 1801653.

[161] Zhang, L.; Jia, Y.; Gao, G.; Yan, X.; Chen, N.; Chen, J.; Soo, M. T.; Wood, B.; Yang, D.; Du, A., Graphene Defects Trap Atomic Ni Species for Hydrogen and Oxygen Evolution Reactions. Chem, **2018**, 4 (2), 285-297.

[162] Nayak, A. K.; Verma, M.; Sohn, Y.; Deshpande, P. A.; Pradhan, D., Highly Active Tungsten Oxide Nanoplate Electrocatalysts for the Hydrogen Evolution Reaction in Acidic and Near Neutral Electrolytes. *ACS Omega* **2017,** *2* (10), 7039-7047.

[163] Chen, J.; Yu, D.; Liao, W.; Zheng, M.; Xiao, L.; Zhu, H.; Zhang, M.; Du, M.; Yao, J., WO3–x Nanoplates Grown on Carbon Nanofibers for an Efficient Electrocatalytic Hydrogen Evolution Reaction. *ACS Applied Materials & Interfaces* **2016,** *8* (28), 18132-18139.

[164] Hu, G.; Li, J.; Liu, P.; Zhu, X.; Li, X.; Ali, R. N.; Xiang, B., Enhanced electrocatalytic activity of WO3@NPRGO composite in a hydrogen evolution reaction. *Applied Surface Science* **2019,** *463*, 275-282.

[165] Tian, H.; Cui, X.; Zeng, L.; Su, L.; Song, Y.; Shi, J., Oxygen vacancy-assisted hydrogen evolution reaction of the Pt/WO3 electrocatalyst. *Journal of Materials Chemistry A* **2019,** *7* (11), 6285-6293

[166] Xie, C.; Chen, W.; Du, S.; Yan, D.; Zhang, Y.; Chen, J.; Liu, B.; Wang, S., In-situ phase transition of WO3 boosting electron and hydrogen transfer for enhancing hydrogen evolution on Pt. *Nano Energy* **2020,** *71*, 104653

[167] Ganesan, R.; Gedanken, A., Synthesis of WO₃nanoparticles using a biopolymer as a template for electrocatalytic hydrogen evolution. *Nanotechnology* **2007,** *19* (2), 025702.

[168] Zhou, D.; He, M.; Ding, Y.; Yu, J.; Fan, K.; Sun, L., WO3 Nanosheet-Supported IrW Alloy for High-Performance Acidic Overall Water Splitting with Low Ir Loading. *ACS Applied Energy Materials* **2022,** *5* (1), 970-980.

[169] Huang, B.; Ma, Y.; Xiong, Z.; Xiao, Z.; Wu, P.; Jiang, P.; Liang, M., Polyoxometalate-Derived Ir/WOx/rGO Nanocomposites for Enhanced Electrocatalytic Water Splitting. *Energy & Environmental Materials* **2021,** *4* (4), 681-686.

[170] Sekar, S.; Aqueel Ahmed, A. T.; Pawar, S. M.; Lee, Y.; Im, H.; Kim, D. Y.; Lee, S., Enhanced water splitting performance of biomass activated carbon-anchored WO3 nanoflakes. *Applied Surface Science* **2020,** *508*, 145127.

[171] Rajalakshmi, R.; Viswanathan, C.; Ponpandian, N., Sm3+ rare-earth doping in non-noble metal oxide –WO3 grown on carbon cloth fibre as a bifunctional electrocatalyst for high-performance water electrolysis. *Sustainable Energy & Fuels* **2021,** *5* (22), 5851-5865.

[172] Li, P.; Duan, X.; Kuang, Y.; Sun, X., Iridium in Tungsten Trioxide Matrix as an Efficient Bi-Functional Electrocatalyst for Overall Water Splitting in Acidic Media. *Small* **2021,** *17* (45), 2102078.

[173] Cheng, S.; Liu, H.; Logan, B. E. Power Densities using Different Cathode Catalysts (Pt and CoTMPP) and Polymer Binders (Nafion and PTFE) in Single Chamber Microbial Fuel Cells. Environ. Sci. Technol. **2006**, 40, 364−369

[174] Shahrokhian, S.; Naderi, L.; Mohammadi, R., High-Performance Fiber-Shaped Flexible Asymmetric Microsupercapacitor Based on Ni(OH)2 Nanoparticles-Decorated Porous Dendritic Ni–Cu Film/Cu Wire and Reduced Graphene Oxide/Carbon Fiber Electrodes. *ACS Sustainable Chemistry & Engineering* **2018,** *6* (11), 14574-14588.

[175] Singh, S.; Mitra, K.; Shukla, A.; Singh, R.; Gundampati, R. K.; Misra, N.; Maiti, P.; Ray, B., Brominated Graphene as Mimetic Peroxidase for Sulfide Ion Recognition. *Analytical Chemistry* **2017,** *89* (1), 783-791.

[176] Kim, J.; Jeon, J.-H.; Kim, H.-J.; Lim, H.; Oh, I.-K., Durable and Water-Floatable Ionic Polymer Actuator with Hydrophobic and Asymmetrically Laser-Scribed Reduced Graphene Oxide Paper Electrodes. *ACS Nano* **2014,** *8* (3), 2986-2997.

[177] Loh, K. P.; Tong, S. W.; Wu, J., Graphene and Graphene-like Molecules: Prospects in Solar Cells. *Journal of the American Chemical Society* **2016,** *138* (4), 1095-1102.

[178] Singh, S.; Mitra, K.; Senapati, S.; Singh, R.; Biswas, Y.; Sen Gupta, S. K.; Misra, N.; Mandal, T. K.; Maiti, P.; Ray, B., Water Soluble Fluorescent Graphene Nanodots. *ChemNanoMat* **2018,** *4* (11), 1177-1188.

[179] Singh, S.; Singh, M.; Mitra, K.; Singh, R.; Sen Gupta, S. K.; Tiwari, I.; Ray, B., Electrochemical sensing of hydrogen peroxide using brominated graphene as mimetic catalase. *Electrochimica Acta* **2017,** *258*, 1435-1444

[180] Ercolani, G., Assessment of Cooperativity in Self-Assembly. *Journal of the American Chemical Society* **2003,** *125* (51), 16097-16103.

[181] Ganesan, M.; Juvekar, V. A., Reduction Self-Assembly of Three-Dimensional Graphene Hydrogels: Implication as Adsorbents. *ACS Applied Nano Materials* **2020,** *3* (11), 10823-10834.

[182] You, H.; Wu, D.; Chen, Z.-n.; Sun, F.; Zhang, H.; Chen, Z.; Cao, M.; Zhuang, W.; Cao, R., Highly Active and Stable Water Splitting in Acidic Media Using a Bifunctional Iridium/Cucurbit[6]uril Catalyst. ACS Energy Letters **2019;** 4 (6): 1301-1307.

[183] Singh, S.; Gundampati, R. K.; Mitra, K.; Ramesh, K.; Jagannadham, M. V.; Misra, N.; Ray, B., Enhanced catalytic and antibacterial activities of silver nanoparticles immobilized on poly(N-vinyl pyrrolidone)-grafted graphene oxide. RSC Advances **2015;** 5 (100): 81994-82004.

[184] Fu, L.; Xia, T.; Zheng, Y.; Yang, J.; Wang, A.; Wang, Z., Preparation of WO3–reduced graphene oxide nanocomposites With Enhanced Photocatalytic Property. Ceramics International **2015;** 41: 5903-5908.

[185] Yu, W.; Shen, Z.; Peng, F.; Lu, Y.; Ge, M.; Fu, X.; Sun, Y.; Chen, X.; Dai, N., Improving gas sensing performance by oxygen vacancies in sub-stoichiometric WO3−x. RSC Advances **2019;** 9 (14): 7723-7728.

[186] Baek, Y.; Yong, K., Controlled Growth and Characterization of Tungsten Oxide Nanowires Using Thermal Evaporation of WO3 Powder. The Journal of Physical Chemistry C **2007;** 111 (3): 1213-1218.

[187] Jayatissa, A. H.; Cheng, S.-T.; Gupta, T., Annealing effect on the formation of nanocrystals in thermally evaporated tungsten oxide thin films. Materials Science and Engineering: B **2004;** 109 (1): 269-275.

[188] Qian, J.; Zhao, Z.; Shen, Z.; Zhang, G.; Peng, Z.; Fu, X., Oxide vacancies enhanced visible active photocatalytic W19O55 NMRs via strong adsorption. RSC Advances **2016;** 6 (10): 8061-8069.

[189] Ahmed, B.; Ojha, A. K.; Singh, A.; Hirsch, F.; Fischer, I.; Patrice, D.; Materny, A., Well-controlled in-situ growth of 2D WO3 rectangular sheets on reduced graphene oxide with strong photocatalytic and antibacterial properties. J Hazard Mater **2018;** 347: 266-278.

[190] Chandra, V.; Park, J.; Chun, Y.; Lee, J. W.; Hwang, I.-C.; Kim, K. S., Water-Dispersible Magnetite-Reduced Graphene Oxide Composites for Arsenic Removal. ACS Nano **2010;** 4 (7): 3979-3986.

[191] Wei, L.; Mao, Y., Enhanced hydrogen storage performance of reduced graphene oxide hybrids with nickel or its metallic mixtures based on spillover mechanism. International Journal of Hydrogen Energy **2016;** 41 (27): 11692-11699.

[192] Jänes, A.; Thomberg, T.; Tonurist, K.; Kurig, H.; Laheäär, A.; Lust, E., Micro- and Mesoporous Carbide-Derived Carbon Materials and Polymer Membranes for Supercapacitors. ECS Transactions **2008;** 16: 57.

[193] Cao, J.; Luo, B.; Lin, H.; Xu, B.; Chen, S., Thermodecomposition synthesis of WO3/H2WO4 heterostructures with enhanced visible light photocatalytic properties. Applied Catalysis B: Environmental **2012;** 111-112: 288-296.

[194] Ramar, V.; Balasubramanian, K., Charge transfer induced tunable bandgap and enhanced saturable absorption behavior in rGO/WO3 composites. Applied Physics A **2018;** 124 (11): 779.

[195] Dayal, J.; Anand, K.; Anand, K., WO3 nanolamellae/reduced graphene oxide nanocomposites for highly sensitive and selective acetone sensing. *Journal of Materials Science* **2018,** *53*

[196] Jose, P.; Kala, M.; Joseph, A.; Kalarikkal, N.; Thomas, S., Reduced graphene oxide/silver nanohybrid as a multifunctional material for antibacterial, anticancer, and SERS applications. *Applied Physics A* **2019,** *126*.

[197] Harnchana, V.; Chaiyachad, S.; Pimanpang, S.; Saiyasombat, C.; Srepusharawoot, P.; Amornkitbamrung, V., Hierarchical Fe3O4-reduced graphene oxide nanocomposite grown on NaCl crystals for triiodide reduction in dye-sensitized solar cells. *Scientific Reports* **2019,** *9* (1), 1494

[198] Nagarajan, S.; G, K.; K Jose, J.; Barshilia, H., Sprayable reduced graphene oxide based high-temperature solar absorber coatings for concentrated solar power applications. *International Journal of Energy Research* **2021,** *45*.

[199] Manceriu, L.; Carcel, R. A., Prediction of TiO 2 and WO 3 nanopowders surface charge by the evaluation of point of zero charge (PZC). Environmental engineering and management journal **2011;** 10: 1021-1026.

[200] Saji, V. S.; Lee, C.-W., Molybdenum, Molybdenum Oxides, and their Electrochemistry. ChemSusChem **2012;** 5 (7): 1146-1161.

[201] Martin, M. H.; Lasia, A., Influence of experimental factors on the constant phase element behavior of Pt electrodes. Electrochimica Acta **2011;** 56 (23): 8058-8068.

[202] Abdelghani-Idrissi, S.; Dubouis, N.; Grimaud, A.; Stevens, P.; Toussaint, G.; Colin, A., Effect of electrolyte flow on a gas evolution electrode. *Scientific Reports* **2021,** *11* (1), 4677.

[203] Yuvaraj, A. L.; Daniel, S., A Systematic Study on Electrolytic Production of Hydrogen Gas by Using Graphite as Electrode. *Materials Research* **2014,** *17*, 83-87.

[204] Chanda, D.; Hnát, J.; Dobrota, A. S.; Pašti, I. A.; Paidar, M.; Bouzek, K., The effect of surface modification by reduced graphene oxide on the electrocatalytic activity of nickel towards the hydrogen evolution reaction. Physical Chemistry Chemical Physics **2015;** 17 (40): 26864-26874.

[205] Gnanasekar, P.; Periyanagounder, D.; Kulandaivel, J., Vertically aligned MoS2 nanosheets on graphene for highly stable electrocatalytic hydrogen evolution reactions. Nanoscale **2019;** 11 (5): 2439-2446.

[206] Besnardiere, J.; Ma, B.; Torres-Pardo, A.; Wallez, G.; Kabbour, H.; González-Calbet, J. M.; Von Bardeleben, H. J.; Fleury, B.; Buissette, V.; Sanchez, C.; Le Mercier, T.; Cassaignon, S.; Portehault, D., Structure and electrochromism of two-dimensional octahedral molecular sieve h'-WO3. Nature Communications **2019;** 10 (1): 327.

[207] Cong, S.; Yuan, Y.; Chen, Z.; Hou, J.; Yang, M.; Su, Y.; Zhang, Y.; Li, L.; Li, Q.; Geng, F.; Zhao, Z., Noble metal-comparable SERS enhancement from semiconducting metal oxides by making oxygen vacancies. Nature Communications **2015;** 6 (1): 7800.

[208] Gerand, B.; Nowogrocki, G.; Guenot, J.; Figlarz, M., Structural study of a new hexagonal form of tungsten trioxide. Journal of Solid State Chemistry **1979;** 29 (3): 429-434.

[209] Chen, W. P.; He, K. F.; Wang, Y.; Chan, H. L. W.; Yan, Z., Highly mobile and reactive state of hydrogen in metal oxide semiconductors at room temperature. *Scientific Reports* **2013,** *3* (1), 3149.

[210] Dickens, P. G.; Crouch-Baker, S.; Weller, M. T., Hydrogen insertion in oxides. *Solid State Ionics* **1986,** *18-19*, 89-97.

[211] Huynh, M.; Bediako, D. K.; Nocera, D. G., A Functionally Stable Manganese Oxide Oxygen Evolution Catalyst in Acid. Journal of the American Chemical Society **2014;** 136 (16): 6002-6010.

[212] Suen, N.-T.; Hung, S.-F.; Quan, Q.; Zhang, N.; Xu, Y.-J.; Chen, H. M., Electrocatalysis for the oxygen evolution reaction: recent development and future perspectives. Chemical Society Reviews **2017;** 46 (2): 337-365.

[213] Wang, H.; Chen, Z.-n.; Wu, D.; Cao, M.; Sun, F.; Zhang, H.; You, H.; Zhuang, W.; Cao, R., Significantly Enhanced Overall Water Splitting Performance by Partial Oxidation of Ir through Au Modification in Core–Shell Alloy Structure. Journal of the American Chemical Society **2021;** 143 (12): 4639-4645.

[214] Zhu, J.; Chen, Z.; Xie, M.; Lyu, Z.; Chi, M.; Mavrikakis, M.; Jin, W.; Xia, Y., Iridium-Based Cubic Nanocages with 1.1-nm-Thick Walls: A Highly Efficient and Durable Electrocatalyst for Water Oxidation in an Acidic Medium. Angewandte Chemie International Edition **2019;** 58 (22): 7244-7248.

[215] Kamal, H.; Akl, A. A.; Abdel-Hady, K.; Influence of proton insertion on the conductivity, structural and optical properties of amorphous and crystalline electrochromic WO3 films. Phys. B **2004**; 349: 192–205.

[216] Zhang, X.; Hao, W.; Tsang, C.-S.; Liu, M.; Hwang, G. S.; Lee, L. Y. S., Psesudocubic Phase Tungsten Oxide as a Photocatalyst for Hydrogen Evolution Reaction. ACS Applied Energy Materials **2019;** 2 (12): 8792-8800.

[217] Li, Y.; Tang, Z.; Zhang, J.; Zhang, Z., Defect Engineering of Air-Treated WO3 and Its Enhanced Visible-Light-Driven Photocatalytic and Electrochemical Performance. The Journal of Physical Chemistry C **2016;** 120 (18): 9750-9763.

[218] Liu, F.; Chen, X.; Xia, Q.; Tian, L.; Chen, X., Ultrathin tungsten oxide nanowires: oleylamine assisted nonhydrolytic growth, oxygen vacancies and good photocatalytic properties. RSC Advances **2015;** 5 (94): 77423-77428.

[219] Boruah, P. J.; Khanikar, R. R.; Bailung, H., Synthesis and Characterization of Oxygen Vacancy Induced Narrow Bandgap Tungsten Oxide (WO3−x) Nanoparticles by Plasma Discharge in Liquid and Its Photocatalytic Activity. Plasma Chemistry and Plasma Processing **2020;** 40 (4): 1019-1036.

[220] Lee, Y.; Lee, T.; Jang, W.; Soon, A., Unraveling the Intercalation Chemistry of Hexagonal Tungsten Bronze and Its Optical Responses. Chemistry of Materials **2016;** 28 (13): 4528-4535.

[221] Long, X.; Li, J.; Xiao, S.; Yan, K.; Wang, Z.; Chen, H.; Yang, S., A Strongly Coupled Graphene and FeNi Double Hydroxide Hybrid as an Excellent Electrocatalyst for the Oxygen Evolution Reaction. Angewandte Chemie International Edition **2014;** 53 (29): 7584-7588.

[222] Tang, C.; Wang, H.-S.; Wang, H.-F.; Zhang, Q.; Tian, G.-L.; Nie, J.-Q.; Wei, F., Spatially Confined Hybridization of Nanometer-Sized NiFe Hydroxides into Nitrogen-Doped Graphene Frameworks Leading to Superior Oxygen Evolution Reactivity. Advanced Materials **2015;** 27 (30): 4516-4522.

[223] Chen, S.; Duan, J.; Jaroniec, M.; Qiao, S. Z., Three-Dimensional N-Doped Graphene Hydrogel/NiCo Double Hydroxide Electrocatalysts for Highly Efficient Oxygen Evolution. Angewandte Chemie International Edition **2013;** 52 (51): 13567-13570.

[224] Tang, C.; Wang, H.-F.; Zhu, X.-L.; Li, B.-Q.; Zhang, Q., Advances in Hybrid Electrocatalysts for Oxygen Evolution Reactions: Rational Integration of NiFe Layered Double Hydroxides and Nanocarbon. Particle & Particle Systems Characterization **2016;** 33 (8): 473-486.

[225] Giddaerappa; Naseem, K.; Deshpande, U.; Sannegowda, L. K., Cobalt Phthalocyanine Based Metal–Organic Framework as an Efficient Bifunctional Electrocatalyst for Water Electrolysis. *Energy & Fuels* **2024,** *38* (9), 8249-8261.

[226] Khatun, S.; Hirani, H.; Roy, P., Seawater electrocatalysis: activity and selectivity. *Journal of Materials Chemistry A* **2021,** *9* (1), 74-86.

[227] Are Metal Chalcogenides, Nitrides, and Phosphides Oxygen Evolution Catalysts or Bifunctional Catalysts? *ACS Energy Letters* **2017,** *2* (8), 1937-1938.

[228] Aralekallu, S.; Sannegowda Lokesh, K.; Singh, V., Advanced bifunctional catalysts for energy production by electrolysis of earth-abundant water. *Fuel* **2024,** *357*, 129753.

[229] Vos, J. G.; Wezendonk, T. A.; Jeremiasse, A. W.; Koper, M. T. M., MnOx/IrOx as Selective Oxygen Evolution Electrocatalyst in Acidic Chloride Solution. *Journal of the American Chemical Society* **2018,** *140* (32), 10270-10281.

[230] Kuang, Y.; Kenney, M. J.; Meng, Y.; Hung, W.-H.; Liu, Y.; Huang, J. E.; Prasanna, R.; Li, P.; Li, Y.; Wang, L.; Lin, M.-C.; McGehee, M. D.; Sun, X.; Dai, H., Solar-driven, highly sustained splitting of seawater into hydrogen and oxygen fuels. *Proceedings of the National Academy of Sciences* **2019,** *116* (14), 6624-6629.

[231] Yu, L.; Wu, L.; McElhenny, B.; Song, S.; Luo, D.; Zhang, F.; Yu, Y.; Chen, S.; Ren, Z., Ultrafast room-temperature synthesis of porous S-doped Ni/Fe (oxy)hydroxide electrodes for oxygen evolution catalysis in seawater splitting. *Energy & Environmental Science* **2020,** *13* (10), 3439-3446.

[232] Feng, K.; Zhang, D.; Liu, F.; Li, H.; Xu, J.; Xia, Y.; Li, Y.; Lin, H.; Wang, S.; Shao, M.; Kang, Z.; Zhong, J., Highly Efficient Oxygen Evolution by a Thermocatalytic Process Cascaded Electrocatalysis Over Sulfur-Treated Fe-Based Metal–Organic-Frameworks. *Advanced Energy Materials* **2020,** *10* (16), 2000184.

[233] Zhu, W.; Chen, S.; Liao, F.; Zhao, X.; Shi, H.; Shi, Y.; Xu, L.; Shao, Q.; Kang, Z.; Shao, M., Electric field polarized sulfonated carbon dots/NiFe layerd double hydroxide as highly efficient electrocatalyst for oxygen evolution reaction. *Chemical Engineering Journal* **2021,** *420*, 129690.

[234] Lee, C.; Wei, X.; Kysar, J. W.; Hone, J., Measurement of the Elastic Properties and Intrinsic Strength of Monolayer Graphene. *Science* **2008,** *321* (5887), 385-388.

[235] Verma, A. K.; Tripathi, P.; Alam, Z.; Mishra, S. K.; Ray, B.; Sinha, A. S. K.; Singh, S., Photocatalytic Production of Oxygen by Nitrogen Doped Graphene Oxide Nanospheres: Synthesized via Bottom-Up Approach Using Dibenzopyrrole. *ChemistrySelect* **2022,** *7* (42), e202202813.

[236] Begum, H.; Ahmed, M. S.; Jeon, S., δ-MnO2 nanoflowers on sulfonated graphene sheets for stable oxygen reduction and hydrogen evolution reaction. *Electrochimica Acta* **2019,** *296*, 235-242.

[237] Saada, H.; Fabre, B.; Loget, G.; Benoit, G., Is Direct Seawater Splitting Realistic with Conventional Electrolyzer Technologies? *ACS Energy Letters* **2024,** *9* (7), 3351-3368.

[238] Zhang, Y.; Zhang, Y.; Li, Z.; Yu, E.; Ye, H.; Li, Z.; Guo, X.; Zhou, D.; Wang, C.; Sha, Q.; Kuang, Y. A Review of Hydrogen Production via Seawater Electrolysis: Current Status and Challenges *Catalysts* [Online], 2024.

[239] Hausmann, J. N.; Schlögl, R.; Menezes, P. W.; Driess, M., Is direct seawater splitting economically meaningful? *Energy & Environmental Science* **2021,** *14* (7), 3679-3685.

[240] Liu, G.; Xu, Y.; Yang, T.; Jiang, L., Recent advances in electrocatalysts for seawater splitting. *Nano Materials Science* **2023,** *5* (1), 101-116.

[241] Yang, Y.; Zhang, K.; Lin, H.; Li, X.; Chan, H. C.; Yang, L.; Gao, Q., MoS2–Ni3S2 Heteronanorods as Efficient and Stable Bifunctional Electrocatalysts for Overall Water Splitting. *ACS Catalysis* **2017,** *7* (4), 2357-2366.

[242] Rabi, O.; Pervaiz, E.; Ali, M.; Zahra, R., Bifunctional molybdenum carbide-based hybrids for electrocatalytic water splitting. *Ceramics International* **2021,** *47* (17), 24949-24958.

[243] Gao, Y.; Wang, Q.; He, T.; Zhang, J.-Y.; Sun, H.; Zhao, B.; Xia, B. Y.; Yan, Y.; Chen, Y., Defective crystalline molybdenum phosphides as bifunctional catalysts for hydrogen evolution and hydrazine oxidation reactions during water splitting. *Inorganic Chemistry Frontiers* **2019,** *6* (10), 2686-2695.

[244] Jiang, Y.; Lu, Y., Designing transition-metal-boride-based electrocatalysts for applications in electrochemical water splitting. *Nanoscale* **2020,** *12* (17), 9327-9351.

[245] Guo, H.; Wu, A.; Xie, Y.; Yan, H.; Wang, D.; Wang, L.; Tian, C., 2D porous molybdenum nitride/cobalt nitride heterojunction nanosheets with interfacial electron redistribution for effective electrocatalytic overall water splitting. *Journal of Materials Chemistry A* **2021,** *9* (13), 8620-8629.

[246] Salarizadeh, P.; Askari, M. B.; Di Bartolomeo, A., MoS2/Ni3S2/Reduced Graphene Oxide Nanostructure as an Electrocatalyst for Alcohol Fuel Cells. *ACS Applied Nano Materials* **2022,** *5* (3), 3361-3373.

[247] Saha, D.; Bhardwaj, A.; Wang, J.; Pande, V.; Hengstebeck, R.; Bai, P.; Watkins, J. J., Probing Electrocatalytic Synergy in Graphene/MoS2/Nickel Networks for Water Splitting through a Combined Experimental and Theoretical Lens. *ACS Applied Materials & Interfaces* **2024,** *16* (32), 42254-42269.

[248] Lonkar, S. P.; Pillai, V. V.; Alhassan, S. M., Scalable solid-state synthesis of MoS2–NiS2/graphene nanohybrids as bifunctional electrocatalysts for enhanced overall water splitting. *Materials Advances* **2020,** *1* (4), 794-803.

[249] Khan, M. S.; Noor, T.; Pervaiz, E.; Iqbal, N.; Zaman, N., Fabrication of MoS2/rGO hybrids as electrocatalyst for water splitting applications††Electronic supplementary information (ESI) available. See DOI: https://doi.org/10.1039/d4ra00697f. *RSC Advances* **2024,** *14* (18), 12742-12753.

[250] Afreen, U.; Singh, N. K., Exploring layered nanocomposite of MoS2 and rGO as a highly efficient supercapattery and OER electrocatalyst. *Journal of Materials Chemistry A* **2025,** *13* (15), 10945-10966.

[251] Wang, D.; Xu, Y.; Guo, X.; Fu, Z.; Yang, Z.; Sun, W., Nickel foam as conductive substrate enhanced low-crystallinity two-dimensional iron hydrogen phosphate for oxygen evolution reaction. *Journal of Alloys and Compounds* **2021,** *870*, 159472.

[252] Chaudhari, N. K.; Jin, H.; Kim, B.; Lee, K., Nanostructured materials on 3D nickel foam as electrocatalysts for water splitting. *Nanoscale* **2017,** *9* (34), 12231-12247.

[253] Kresse, G.; Joubert, D., From ultrasoft pseudopotentials to the projector augmented-wave method. *Physical Review B* **1999,** *59* (3), 1758-1775.

[254] Blöchl, P. E., Projector augmented-wave method. *Physical Review B* **1994,** *50* (24), 17953-17979.

[255] Jian, J.; Kang, H.; Yu, D.; Qiao, X.; Liu, Y.; Li, Y.; Qin, W.; Wu, X., Bi-Functional Co/Al Modified 1T-MoS2/rGO Catalyst for Enhanced Uranium Extraction and Hydrogen Evolution Reaction in Seawater. *Small* **2023,** *19* (21), 2207378.

[256] Denisdon, S.; Senthil Kumar, P.; Boobalan, C.; Rangasamy, G., Hydrothermally Synthesized rGO/MnO2/MoS2 Nanohybrids as Superior Bifunctional Electrocatalysts for Oxygen and Hydrogen Evolution Reactions. *Langmuir* **2024,** *40* (33), 17753-17766.

[257] Khan, M. S.; Noor, T.; Pervaiz, E.; Iqbal, N.; Zaman, N., Fabrication of MoS2/rGO hybrids as electrocatalyst for water splitting applications. *RSC Advances* **2024,** *14* (18), 12742-12753.

[258] Bai, X.; Cao, T.; Xia, T.; Wu, C.; Feng, M.; Li, X.; Mei, Z.; Gao, H.; Huo, D.; Ren, X.; Li, S.; Guo, H.; Wang, R. MoS2/NiSe2/rGO Multiple-Interfaced Sandwich-like Nanostructures as Efficient Electrocatalysts for Overall Water Splitting *Nanomaterials* [Online], 2023.

[259] Vikraman, D.; Hussain, S.; Ali, M.; Karuppasamy, K.; Santhoshkumar, P.; Hwang, J.-H.; Jung, J.; Kim, H.-S., Theoretical evaluation and experimental investigation of layered 2H/1T-phase MoS2 and its reduced graphene-oxide hybrids for hydrogen evolution reactions. *Journal of Alloys and Compounds* **2021,** *868*, 159272.

[260] Zhang, X.; Hua, S.; Lai, L.; Wang, Z.; Liao, T.; He, L.; Tang, H.; Wan, X., Strategies to improve electrocatalytic performance of MoS2-based catalysts for hydrogen evolution reactions. *RSC Advances* **2022,** *12* (28), 17959-17983.

[261] Cao, Y., Roadmap and Direction toward High-Performance MoS2 Hydrogen Evolution Catalysts. *ACS Nano* **2021,** *15* (7), 11014-11039.

[262] Xu, L.; Song, Z.; Chen, H.; Li, Y.; Li, J.; Li, R., Recent progress of MoS2 for photocatalytic and electrocatalytic hydrogen generation—A review. *Clean Energy Science and Technology* **2024,** *2*, 157.

[263] Hidayah, N. M. S.; Liu, W.-W.; Lai, C.-W.; Noriman, N. Z.; Khe, C.-S.; Hashim, U.; Lee, H. C., Comparison on graphite, graphene oxide and reduced graphene oxide: Synthesis and characterization. *AIP Conference Proceedings* **2017,** *1892* (1), 150002.

[264] Guo, Y.; Ma, Q.; Cao, F.; Zhao, Q.; Ji, X., Colorimetric detection of hypochlorite in tap water based on the oxidation of 3,3′,5,5′-tetramethyl benzidine. *Analytical Methods* **2015,** *7* (10), 4055-4058.

[265] Mi, L.; Wei, W.; Huang, S.; Cui, S.; Zhang, W.; Hou, H.; Chen, W., A nest-like Ni@Ni1.4Co1.6S2 electrode for flexible high-performance rolling supercapacitor device design. *Journal of Materials Chemistry A* **2015,** *3* (42), 20973-20982.

[266] Chen, M.; Kitiphatpiboon, N.; Feng, C.; Abudula, A.; Ma, Y.; Guan, G., Recent progress in transition-metal-oxide-based electrocatalysts for the oxygen evolution reaction in natural seawater splitting: A critical review. *eScience* **2023,** *3* (2), 100111.

[267] Zeng, L.; Liu, Y.; Liu, C., Facile Synthesis of Fe-Doped Ni3S2 Nanoparticles Supported on Ni Foam as Highly Active Electrocatalyst for Water Splitting. *IOP Conference Series: Earth and Environmental Science* **2018,** *186* (2), 012002.

[268] Yan, J.; Huang, Y.; Zhang, L.; Zhou, M.; Yang, P.; Chen, W.; Deng, X.; Yang, H., Preparation of MoS2-Graphene-NiO@Ni foam composite by sol coating for

(photo)electrocatalytic hydrogen evolution reaction. *Journal of Sol-Gel Science and Technology* **2020,** *93* (2), 462-470.

[269] Senthilkumar, R.; Ramakrishnan, S.; Balu, M.; Ramamurthy, P. C.; Kumaresan, D.; Kothurkar, N. K., One-step hydrothermal synthesis of marigold flower-like nanostructured MoS2 as a counter electrode for dye-sensitized solar cells. *Journal of Solid State Electrochemistry* **2018,** *22* (11), 3331-3341.

[270] Sharma, C. H.; Surendran, A. P.; Varghese, A.; Thalakulam, M., Stable and scalable 1T MoS2 with low temperature-coefficient of resistance. *Scientific Reports* **2018,** *8* (1), 12463.

[271] Lalithambika, K. C.; Shanmugapriya, K.; Sriram, S., Photocatalytic activity of MoS2 nanoparticles: an experimental and DFT analysis. *Applied Physics A* **2019,** *125* (12), 817.

[272] Li, B.; Jiang, L.; Li, X.; Ran, P.; Zuo, P.; Wang, A.; Qu, L.; Zhao, Y.; Cheng, Z.; Lu, Y., Preparation of Monolayer MoS2 Quantum Dots using Temporally Shaped Femtosecond Laser Ablation of Bulk MoS2 Targets in Water. *Scientific Reports* **2017,** *7* (1), 11182.

[273] Abinaya, M.; Saravanakumar, K.; Jeyabharathi, E.; Muthuraj, V., Synthesis and Characterization of 1D-MoO3 Nanorods Using Abutilon indicum Extract for the Photoreduction of Hexavalent Chromium. *Journal of Inorganic and Organometallic Polymers and Materials* **2019,** *29* (1), 101-110.

[274] Zhang, L.; He, X.; Zhou, Q.; Hu, X., Fabrication of 1T-MoS2 nanosheets and the high-efficiency removal of toxic metals in aquatic systems: Performance and mechanisms. *Chemical Engineering Journal* **2020,** *386*, 123996.

[275] Cui, P.; Lee, J.; Hwang, E.; Lee, H., One-pot reduction of graphene oxide at subzero temperatures. *Chemical Communications* **2011,** *47* (45), 12370-12372.

[276] Chang, K.; Chen, W., l-Cysteine-Assisted Synthesis of Layered MoS2/Graphene Composites with Excellent Electrochemical Performances for Lithium-Ion Batteries. *ACS Nano* **2011,** *5* (6), 4720-4728.

[277] Benck, J. D.; Chen, Z.; Kuritzky, L. Y.; Forman, A. J.; Jaramillo, T. F., Amorphous Molybdenum Sulfide Catalysts for Electrochemical Hydrogen Production: Insights into the Origin of their Catalytic Activity. *ACS Catalysis* **2012,** *2* (9), 1916-1923.

[278] Bahuguna, A.; Kumar, S.; Sharma, V.; Reddy, K. L.; Bhattacharyya, K.; Ravikumar, P. C.; Krishnan, V., Nanocomposite of MoS2-RGO as Facile, Heterogeneous, Recyclable, and Highly Efficient Green Catalyst for One-Pot Synthesis of Indole Alkaloids. *ACS Sustainable Chemistry & Engineering* **2017,** *5* (10), 8551-8567

[279] Li, H.; Zhang, Q.; Yap, C. C. R.; Tay, B. K.; Edwin, T. H. T.; Olivier, A.; Baillargeat, D., From Bulk to Monolayer MoS2: Evolution of Raman Scattering. *Advanced Functional Materials* **2012,** *22* (7), 1385-1390.

[280] Valmalette, J.-C.; Tan, Z.; Abe, H.; Ohara, S., Raman scattering of linear chains of strongly coupled Ag nanoparticles on SWCNTs. *Scientific Reports* **2014,** *4* (1), 5238.

[281] Yan-Min, Z., Study on Naphthalene Sulfonic Acid Formaldehyde Condensate by Ultraviolet Absorption Spectrum. *Journal of Physics: Conference Series* **2019,** *1237* (2), 022107.

[282] McDonnell, S.; Azcatl, A.; Addou, R.; Gong, C.; Battaglia, C.; Chuang, S.; Cho, K.; Javey, A.; Wallace, R. M., Hole Contacts on Transition Metal Dichalcogenides: Interface Chemistry and Band Alignments. *ACS Nano* **2014,** *8* (6), 6265-6272.

[283] Huang, Q.; Hu, S.; Zhuang, J.; Wang, X., MoO3–-Based Hybrids with Tunable Localized Surface Plasmon Resonances: Chemical Oxidation Driving Transformation from Ultrathin Nanosheets to Nanotubes. *Chemistry – A European Journal* **2012,** *18* (48), 15283-15287.

[284] Xu, Y.-Z.; Yuan, C.-Z.; Chen, X.-P., One-pot synthesis nickel sulfide/amorphous molybdenum sulfide nanosheets array on nickel foam as a robust oxygen evolution reaction electrocatalyst. *Journal of Solid State Chemistry* **2017,** *256*, 124-129.

[285] Zou, L.; Qu, R.; Gao, H.; Guan, X.; Qi, X.; Liu, C.; Zhang, Z.; Lei, X., MoS2/RGO hybrids prepared by a hydrothermal route as a highly efficient catalytic for sonocatalytic degradation of methylene blue. *Results in Physics* **2019,** *14*, 102458.

[286] Yin, Z.; Zhao, J.; Wang, B.; Xu, Y.; Li, Z.; Ma, X., Insight for the effect of bridging S22- in molybdenum sulfide catalysts toward sulfur-resistant methanation. *Applied Surface Science* **2019,** *471*, 670-677.

[287] Baik, S.; Zhang, H.; Kim, Y. K.; Harbottle, D.; Lee, J. W., Enhanced adsorption capacity and selectivity towards strontium ions in aqueous systems by sulfonation of CO2 derived porous carbon. *RSC Advances* **2017,** *7* (86), 54546-54553.

[288] Du, F.-P.; Cao, N.-N.; Zhang, Y.-F.; Fu, P.; Wu, Y.-G.; Lin, Z.-D.; Shi, R.; Amini, A.; Cheng, C., PEDOT:PSS/graphene quantum dots films with enhanced thermoelectric properties via strong interfacial interaction and phase separation. *Scientific Reports* **2018,** *8* (1), 6441.

[289] Abdolmaleki, A.; Mallakpour, S.; Mahmoudian, M., Preparation and Evaluation of Edge Selective Sulfonated Graphene by Chlorosulfuric Acid as an Active Metal- Free Electrocatalyst for Oxygen Reduction Reaction in Alkaline Media. *ChemistrySelect* **2017,** *2* (34), 11211-11217.

[290] Wan, C.; Ling, Y.; Wang, S.; Pu, H.; Huang, Y.; Duan, X., Unraveling and Resolving the Inconsistencies in Tafel Analysis for Hydrogen Evolution Reactions. *ACS Central Science* **2024,** *10* (3), 658-665.

[291] Wagner, H., Influence of temperature on electrical conductivity of diluted aqueous solutions. **2012,** *92*, 82-89.

[292] Yuvaraj, A. L.; Daniel, S., A Systematic Study on Electrolytic Production of Hydrogen Gas by Using Graphite as Electrode. *Materials Research* **2014,** *17*, 83-87.

[293] Zhao, L.; Li, X.; Yu, J.; Zhou, W. Design Strategy of Corrosion-Resistant Electrodes for Seawater Electrolysis *Materials* [Online], 2023.

[294] Sudheer; Quraishi, M. A., Electrochemical and theoretical investigation of triazole derivatives on corrosion inhibition behavior of copper in hydrochloric acid medium. *Corrosion Science* **2013,** *70*, 161-169.

[295] Zhang, Y.-C.; Han, C.; Gao, J.; Pan, L.; Wu, J.; Zhu, X.-D.; Zou, J.-J., NiCo-Based Electrocatalysts for the Alkaline Oxygen Evolution Reaction: A Review. *ACS Catalysis* **2021,** *11* (20), 12485-12509.

[296] Jian, J.; Kang, H.; Yu, D.; Qiao, X.; Liu, Y.; Li, Y.; Qin, W.; Wu, X., Bi-Functional Co/Al Modified 1T-MoS2/rGO Catalyst for Enhanced Uranium Extraction and Hydrogen Evolution Reaction in Seawater. *Small* **2023,** *19* (21), 2207378.

[297] Phan, L. P.; Tran, T. T. N.; Truong, T.-K.; Yu, J.; Nguyen, H.-V. T.; Phan, T. B.; Thi Tran, N. H.; Tran, N. Q., Highly Efficient and Stable Hydrogen Evolution from Natural Seawater by Boron-Doped Three-Dimensional Ni2P–MoO2 Heterostructure Microrod Arrays. *The Journal of Physical Chemistry Letters* **2023,** *14* (32), 7264-7273.

[298] Zhang, H.; Wang, Y.; Zhang, B.; Zhang, S.; Ma, Y.; Wu, Z.; Zhu, Y.; Liu, F.; Xiao, Z.; Wang, L., Interwoven N-doped carbon nanotubes with capped Ni-doped FeP as double-functional electrocatalysts for overall seawater electrolysis. *Science China Materials* **2023,** *66* (12), 4630-4638.

[299] Lu, X.; Pan, J.; Lovell, E.; Tan, T. H.; Ng, Y. H.; Amal, R., A sea-change: manganese doped nickel/nickel oxide electrocatalysts for hydrogen generation from seawater. *Energy & Environmental Science* **2018,** *11* (7), 1898-1910.

[300] Yu, L.; Wu, L.; Song, S.; McElhenny, B.; Zhang, F.; Chen, S.; Ren, Z., Hydrogen Generation from Seawater Electrolysis over a Sandwich-like NiCoN|NixP|NiCoN Microsheet Array Catalyst. *ACS Energy Letters* **2020,** *5* (8), 2681-2689.

[301] Wu, W.; Zhang, X.; Xiao, Y.; Cheng, Z.; Yang, T.; Lv, J.; Yuan, M.; Liu, J.; Zhao, Y., Highly Salt-tolerant hydrogen evolution reaction based on dendritic urchin-like MoC/MoS2 heterojunction in seawater. *Chemical Engineering Journal* **2024,** *480*, 148085.

[302] Zhao, Y.; Tang, Q.; He, B.; Yang, P., Carbide decorated carbon nanotube electrocatalyst for high-efficiency hydrogen evolution from seawater. *RSC Advances* **2016,** *6* (96), 93267-93274.

[303] Zhang, H.-M.; Li, J.; Gao, Y.; Sun, J.; Geng, S.; Meng, Y., High-valence Mo, Mn co-doped amorphous bimetallic sulfide for efficient overall alkaline water/seawater electrolysis. *Fuel* **2024,** *371*, 132111.

[304] Wu, L.; Yu, L.; Zhang, F.; McElhenny, B.; Luo, D.; Karim, A.; Chen, S.; Ren, Z., Heterogeneous Bimetallic Phosphide Ni2P-Fe2P as an Efficient Bifunctional Catalyst for Water/Seawater Splitting. *Advanced Functional Materials* **2021,** *31* (1), 2006484.

[305] Wang, S.; Yang, P.; Sun, X.; Xing, H.; Hu, J.; Chen, P.; Cui, Z.; Zhu, W.; Ma, Z., Synthesis of 3D heterostructure Co-doped Fe2P electrocatalyst for overall seawater electrolysis. *Applied Catalysis B: Environmental* **2021,** *297*, 120386.

[306] Wu, L.; Yu, L.; McElhenny, B.; Xing, X.; Luo, D.; Zhang, F.; Bao, J.; Chen, S.; Ren, Z., Rational design of core-shell-structured CoPx@FeOOH for efficient seawater electrolysis. *Applied Catalysis B: Environmental* **2021,** *294*, 120256.

[307] Chen, Z.; Li, Q.; Xiang, H.; Wang, Y.; Yang, P.; Dai, C.; Zhang, H.; Xiao, W.; Wu, Z.; Wang, L., Hierarchical porous NiFe-P@NC as an efficient electrocatalyst for alkaline hydrogen production and seawater electrolysis at high current density. *Inorganic Chemistry Frontiers* **2023,** *10* (5), 1493-1500.

[308] Song, M.; Yang, X.; Ma, J.; Deng, X.; Gao, H., Tailored nanocomposite FeNiB/MnO2/rGO@NF electrocatalyst for highly efficient and stable oxygen evolution reaction in freshwater and seawater environments. *Materials Today Chemistry* **2024,** *36*, 101957.

[309] Tu, Q.; Liu, W.; Jiang, M.; Wang, W.; Kang, Q.; Wang, P.; Zhou, W.; Zhou, F., Preferential Adsorption of Hydroxide Ions onto Partially Crystalline NiFe-Layered Double Hydroxides Leads to Efficient and Selective OER in Alkaline Seawater. *ACS Applied Energy Materials* **2021,** *4* (5), 4630-4637.

[310] Zhang, J.; Lv, B.; Qiao, Z.; Ji, D.; Yuan, D.; Li, Z.; Wu, H., Electronic structure engineering of CNTs@NiFe-LDH composite via heteroatom doping for efficient seawater electrolysis. *International Journal of Hydrogen Energy* **2024,** *83*, 803-810.

[311] Aghamohammadi, P.; Hüner, B.; Altıncı, O. C.; Akgul, E. T.; Teymur, B.; Simsek, U. B.; Demir, M. Recent advances in the electrocatalytic applications (HER, OER, ORR, water splitting) of transition metal borides (MBenes) materials. *International Journal of Hydrogen Energy* **2024**, *87*, 179-198.

[312] Yan, W.; Wu, W.; Wang, K.; Tang, Z.; Chen, S. Oxygen reduction reaction and hydrogen evolution reaction catalyzed by carbon-supported molybdenum-coated palladium nanotubes. *International Journal of Hydrogen Energy* **2018**, *43* (36), 17132-17141.

[313] Hüner, B.; Kıstı, M.; Özdoğan, E.; Demir, N.; Kaya, M. F. Pt Thin Film-Coated 3D-Printed Polymer Anode Gas Diffusion Electrodes for PEM Water Electrolyzers. *Energy & Fuels* **2024**, *38* (14), 13228-13244.

[314] Jahan, M.; Liu, Z.; Loh, K. A Graphene Oxide and Copper-Centered Metal Organic Framework Composite as a Tri-Functional Catalyst for HER, OER, and ORR. *Advanced Functional Materials* **2013**, *23*.

[315] Yang, F.; Zhu, X.; Jia, B.; Hao, J.; Ma, Y.; Lu, P.; Li, D. Trifunctional electrocatalysts of single transition metal atom doped g-C4N3 with high performance for OER, ORR and HER. *International Journal of Hydrogen Energy* **2024**, *51*, 195-206.

[316] Liang, H.; Li, J.; Zhang, J.; Peng, W.; Li, J.; Liu, J. Tri-functional Fe-based electrocatalyst with sturdy three-dimensional frame construction for the ORR, OER and HER. *Journal of Materials Chemistry A* **2024**, *12* (30), 19344-19351,

[317] Zhang, Y.; Luo, M.; Yang, Y.; Li, Y.; Guo, S. Advanced Multifunctional Electrocatalysts for Energy Conversion. *ACS Energy Letters* **2019**, *4* (7), 1672-1680.

[318] Xu, C.; Yang, X.; Hu, C.; Su, C.; Zhang, J.; Yang, L.; Yin, S. Self-assemble strategy to fabricate multifunctional electrocatalyst for efficient and energy-saving water splitting. *International Journal of Hydrogen Energy* **2024**, *55*, 645-653

[319] Ingsel, T.; Gupta, R. K. 5 - Transition metal chalcogenides-based electrocatalysts for ORR, OER, and HER. In *Nanomaterials for Electrocatalysis*, Maiyalagan, T., Khandelwal, M., Kumar, A., Nguyen, T. A., Yasin, G. Eds.; Elsevier, 2022; pp 83-111.

[320] Majhi, K. C.; Yadav, M. Transition Metal-Based Chalcogenides as Electrocatalysts for Overall Water Splitting. *ACS Engineering Au* **2023**, *3* (5), 278-284.

[321] Shahzad, U.; Saeed, M.; Marwani, H. M.; Al-Humaidi, J. Y.; Rehman, S. u.; Althomali, R. H.; Rahman, M. M. Transition metal-based chalcogenides as electrocatalysts for overall water splitting in hydrogen energy production. *International Journal of Hydrogen Energy* **2024**, *65*, 215-224.

[322] Al-Naggar, A. H.; Shinde, N. M.; Kim, J.-S.; Mane, R. S. Water splitting performance of metal and non-metal-doped transition metal oxide electrocatalysts. *Coordination Chemistry Reviews* **2023**, *474*, 214864.

[323] Wang, M.; Zhang, L.; He, Y.; Zhu, H. Recent advances in transition-metal-sulfide-based bifunctional electrocatalysts for overall water splitting. *Journal of Materials Chemistry A* **2021**, *9* (9), 5320-5363, 10.1039/D0TA12152E.

[324] Chandrasekaran, S.; Yao, L.; Deng, L.; Bowen, C.; Zhang, Y.; Chen, S.; Lin, Z.; Peng, F.; Zhang, P. Recent advances in metal sulfides: from controlled fabrication to electrocatalytic, photocatalytic and photoelectrochemical water splitting and beyond. *Chemical Society Reviews* **2019**, *48* (15), 4178-4280, 10.1039/C8CS00664D.

[325] Kong, D.; Wang, H.; Cha, J. J.; Pasta, M.; Koski, K. J.; Yao, J.; Cui, Y. Synthesis of MoS2 and MoSe2 Films with Vertically Aligned Layers. *Nano Letters* **2013**, *13* (3), 1341-1347.

[326] Petrov, K.; Baykara, S. Z.; Ebrasu, D.; Gulin, M.; Veziroglu, A. An assessment of electrolytic hydrogen production from H2S in Black Sea waters. *International Journal of Hydrogen Energy* **2011**, *36* (15), 8936-8942.

[327] Kılkış, B.; Taseli, B. Two-step onboard hydrogen generation from Black Sea H 2 S reserves. *International Journal of Energy Research* **2021**, *45*. DOI: 10.1002/er.6304.

[328] Wang, Z.; Wang, Q.-N.; Ma, W.; Liu, T.; Zhang, W.; Zhou, P.; Li, M.; Liu, X.; Chang, Q.; Zheng, H.; et al. Hydrogen Sulfide Splitting into Hydrogen and Sulfur through Off-Field Electrocatalysis. *Environmental Science & Technology* **2024**, *58* (24), 10515-10523.

[329] Kim, K.; Lee, C. Recent progress in electrochemical hydrogen sulfide splitting: Strategies for enabling Sulfur-tolerant anodic reactions. *Chemical Engineering Journal* **2023**, *469*, 143861.

[330] Yu, Z.; Deng, Z.; Li, Y.; Wang, X. Advances in Electrocatalyst Design and Mechanism for Sulfide Oxidation Reaction in Hydrogen Sulfide Splitting. *Advanced Functional Materials* **2024**, *34* (39), 2403435.

[331] Zhang, M.; Guan, J.; Tu, Y.; Chen, S.; Wang, Y.; Wang, S.; Yu, L.; Ma, C.; Deng, D.; Bao, X. Highly Efficient H2 Production from H2S via a Robust Graphene Encapsulating Metal Catalyst. *Energy & Environmental Science* **2019**, *13*.

[332] Zhang, L.; Wang, Z.; Qiu, J. Energy-Saving Hydrogen Production by Seawater Electrolysis Coupling Sulfion Degradation. *Advanced Materials* **2022**, *34* (16), 2109321.

[333] Shen, W.; Zhu, J.; Hu, Y.; Yin, J.; Zheng, Y.; Xi, P. Applications of Rare Earth Promoted Transition Metal Sulfides in Electrocatalysis. *Chinese Journal of Chemistry* **2023**, *41* (14), 1740-1752.

[334] Marimuthu, S.; Kannan, P.; Maduraiveeran, G. Transition metal sulfide nanostructures: synthesis and application in metal-air batteries. *Nano Express* **2024**, *5* (2), 022005.

[335] Feng, G.; Wei, A.; Zhao, Y.; Liu, J. Synthesis of flower-like MoS2 nanosheets microspheres by hydrothermal method. *Journal of Materials Science: Materials in Electronics* **2015**, *26* (10), 8160-8166.

[336] Fareza, A. R.; Nugroho, F. A. A.; Fauzia, V. Facile Synthesis of 1T-MoS2 Nanoflowers Using Hydrothermal Method. *Materials Science Forum* **2021**, *1028*, 173-178. DOI: 10.4028/www.scientific.net/MSF.1028.173.

[337] Rmuš Mravik, J.; Milanović, I.; Milošević Govedarović, S.; Mraković, A.; Korneeva, E.; Stojković Simatović, I.; Kurko, S. Improvement of MoS2 electrocatalytic activity for hydrogen evolution reaction by ion irradiation. *International Journal of Hydrogen Energy* **2023**, *48* (98), 38676-38685.

[338] Feng, Y.-Y.; Deng, G.; Wang, X.-Y.; Zhu, M.; Bian, Q.-N.; Guo, B.-S. MoS2/NiFeS2 heterostructure as a highly efficient electrocatalyst for overall water splitting at high current densities. *International Journal of Hydrogen Energy* **2023**, *48* (33), 12354-12363.

[339] Yao, H.-R.; Yin, Y.-X.; Guo, Y.-G. Size effects in lithium ion batteries*. *Chinese Physics B* **2016**, *25* (1), 018203.

[340] Li, W.; Wang, C.; Lu, X. Integrated transition metal and compounds with carbon nanomaterials for electrochemical water splitting. *Journal of Materials Chemistry A* **2021**, *9* (7), 3786-3827, 10.1039/D0TA09495A.

[341] Kamaruzaman, N. A.; Khairul, W. M.; Md Saleh, N.; Yusoff, F. Advancements in carbon-based transition metal compounds for enhanced hydrogen production via electrochemical water splitting. *International Journal of Electrochemical Science* **2024**, *19* (9), 100740.

[342] Rasouli, Z.; Abdollahi, H.; Maeder, M. Generalized indicator-based determination of solution pH. *Analytica Chimica Acta* **2020**, *1109*, 90-97.

[343] Aracena, A.; Sanino, A.; Jerez, O. Dissolution kinetics of molybdite in KOH media at different temperatures. *Transactions of Nonferrous Metals Society of China* **2018**, *28* (1), 177-185.

[344] Wang, Z.; von dem Bussche, A.; Qiu, Y.; Valentin, T. M.; Gion, K.; Kane, A. B.; Hurt, R. H. Chemical Dissolution Pathways of MoS2 Nanosheets in Biological and Environmental Media. *Environmental Science & Technology* **2016**, *50* (13), 7208-7217.

[345] Zhang, H. P.; Lin, H. F.; Zheng, Y.; Hu, Y. F.; MacLennan, A. The catalytic activity and chemical structure of nano MoS2 synthesized in a controlled environment. *Reaction Chemistry & Engineering* **2016**, *1* (2), 165-175.

[346] He, S.; Wu, M.; Li, S.; Jiang, Z.; Hong, H.; Cloutier, S. G.; Yang, H.; Omanovic, S.; Sun, S.; Zhang, G. Research Progress on Graphite-Derived Materials for Electrocatalysis in Energy Conversion and Storage. In *Molecules*, 2022; Vol. 27.

[347] Mahmoudabadi, Z. S.; Rashidi, A.; Tavasoli, A. Synthesis of MoS2 quantum dots as a nanocatalyst for hydrodesulfurization of Naphtha: Experimental and DFT study. *Journal of Environmental Chemical Engineering* **2020**, *8* (3), 103736.

[348] Pimerzin, A.; Savinov, A.; Vutolkina, A.; Makova, A.; Glotov, A.; Vinokurov, V.; Pimerzin, A. Transition Metal Sulfides- and Noble Metal-Based Catalysts for N-Hexadecane Hydroisomerization: A Study of Poisons Tolerance. In *Catalysts*, 2020; Vol. 10.

[349] Ding, X.; Duan, J.; Jia, M.; Fan, H.; Lyu, Y.; Fu, J.; Liu, X. Advanced Zeolite-Based Catalysts for CO2 Hydrogenation to Targeted High-Value Chemicals and Fuels. *Chemistry – An Asian Journal* **2025**, *20* (8), e202401703.

[350] van Veen, J. A. R.; Colijn, H. A.; Hendriks, P. A. J. M.; van Welsenes, A. J. On the formation of type I and type II NiMoS phases in NiMo/Al2O3 hydrotreating catalysts and its catalytic implications. *Fuel Processing Technology* **1993**, *35* (1), 137-157.

[351] Kim, K.; Lee, C. Recent progress in electrochemical hydrogen sulfide splitting: Strategies for enabling Sulfur-tolerant anodic reactions. *Chemical Engineering Journal* **2023**, *469*, 143861.

[352] Mao, Z.; Anani, A.; White, R. E.; Srinivasan, S.; Appleby, A. J. A Modified Electrochemical Process for the Decomposition of Hydrogen Sulfide in an Aqueous Alkaline Solution. *Journal of The Electrochemical Society* **1991**, *138* (5), 1299.

[353] Lawrence, N. S.; Deo, R. P.; Wang, J., Electrochemical determination of hydrogen sulfide at carbon nanotube modified electrodes. *Analytica Chimica Acta* **2004,** *517* (1), 131-137.

[354] Yang, J.; Smulders, V.; Smits, J. J. T.; Mei, B. T.; Mul, G. Electrochemical oxidation of H2S on polycrystalline Ni electrodes. *Journal of Applied Electrochemistry* **2019**, *49* (9), 929-936.

[355] Anani, A. A.; Mao, Z.; White, R. E.; Srinivasan, S.; Appleby, A. J. Electrochemical Production of Hydrogen and Sulfur by Low-Temperature Decomposition of Hydrogen Sulfide in an Aqueous Alkaline Solution. *Journal of The Electrochemical Society* **1990**, *137* (9), 2703.

[356] Pan, C.; Lv, F.; Kégl, T.; Horváth, A. K.; Gao, Q., Kinetics and Mechanism of the Concurrent Reactions of Hexathionate with S(IV) and Thiosulfate in a Slightly Acidic Medium. *The Journal of Physical Chemistry A* **2019,** *123* (26), 5418-5427.

[357] Steudel, R., Mechanism for the Formation of Elemental Sulfur from Aqueous Sulfide in Chemical and Microbiological Desulfurization Processes. *Industrial & Engineering Chemistry Research* **1996,** *35* (4), 1417-1423.

[358] Li, P.; Deng, J.; Li, J.; Zeng, M.; Wang, L.; Guo, J., Multifunctional hollow spheres as sulfur hosts for high-performance Li–S batteries. *Journal of Materials Science* **2020,** *55* (9), 3964-3973.

[359] Chen, Z.; Hao, X.; Wen, Q.; Jia, Y.; Samak, N. A.; Yang, M.; Xing, J., Alleviating the thiols-induced inhibition of bio-sulfur particles and bio-oxidation in the biological desulfurization process under haloalkaline conditions. *Chemical Engineering Journal* **2024,** *496*, 153683.

[360] Lee, J.; Choi, W., Surface Modification of Sulfur Cathodes with PEDOT:PSS Conducting Polymer in Lithium-Sulfur Batteries. *Journal of The Electrochemical Society* **2015,** *162*, A935-A939.

[361] Wang, M.; Peng, Z.; Qian, J.; Li, H.; Zhao, Z.; Fu, X., Highly efficient solar-driven photocatalytic degradation on environmental pollutants over a novel C fibers@MoSe2 nanoplates core-shell composite. *Journal of Hazardous Materials* **2018,** *347*, 403-411.

[362] Huang, Y.; Cui, F.; Zhao, Y.; Lian, J.; Bao, J.; Liu, T.; Li, H., 3D hierarchical CMF/MoSe2 composite foam as highly efficient electrocatalyst for hydrogen evolution. *Electrochimica Acta* **2018,** *263*, 94-101.

[363] Viprya, P.; Kumar, D.; Kowshik, S. Study of Different Properties of Graphene Oxide (GO) and Reduced Graphene Oxide (rGO) *Engineering Proceedings* [Online], 2023.

[364] Mao, S.; Wen, Z.; Ci, S.; Guo, X.; Ostrikov, K.; Chen, J., Perpendicularly Oriented MoSe2/Graphene Nanosheets as Advanced Electrocatalysts for Hydrogen Evolution. *Small* **2015,** *11* (4), 414-419.

[365] Li, Y.; Wang, H.; Xie, L.; Liang, Y.; Hong, G.; Dai, H., MoS2 Nanoparticles Grown on Graphene: An Advanced Catalyst for the Hydrogen Evolution Reaction. *Journal of the American Chemical Society* **2011,** *133* (19), 7296-7299.

[366] Muthukumar, K.; Leban, L.; Sekar, A.; Elangovan, A.; Sarkar, N.; Li, J., Tuning the defects in MoS2/reduced graphene oxide 2D hybrid materials for optimizing battery performance. *Sustainable Energy & Fuels* **2021,** *5* (16), 4002-4014.

[367] Stankovich, S.; Dikin, D. A.; Piner, R. D.; Kohlhaas, K. A.; Kleinhammes, A.; Jia, Y.; Wu, Y.; Nguyen, S. T.; Ruoff, R. S., Synthesis of graphene-based nanosheets via chemical reduction of exfoliated graphite oxide. *Carbon* **2007,** *45* (7), 1558-1565.

[368] Barvat, A.; Prakash, N.; Singh, D. K.; Dogra, A.; Khanna, S. P.; Singh, S.; Pal, P., Mixed Phase Compositions of MoS2 Ultra Thin Film Grown by Pulsed Laser Deposition. *Materials Today: Proceedings* **2018,** *5* (1, Part 2), 2241-2245.

[369] Yu, C.; Cao, Z.; Chen, S.; Wang, S.; Zhong, H., Promoting the hydrogen evolution performance of 1T-MoSe2-Se: Optimizing the two-dimensional structure of MoSe2 by layered double hydroxide limited growth. *Applied Surface Science* **2020,** *509*, 145364.

[370] Hong, Z.; Hong, W.; Wang, B.; Cai, Q.; He, X.; Liu, W., Stable 1T –2H MoS2 heterostructures for efficient electrocatalytic hydrogen evolution. *Chemical Engineering Journal* **2023,** *460*, 141858.

[371] Silveira, J. V.; Batista, J. A.; Saraiva, G. D.; Mendes Filho, J.; Souza Filho, A. G.; Hu, S.; Wang, X., Temperature dependent behavior of single walled MoO3 nanotubes: A Raman spectroscopy study. *Vibrational Spectroscopy* **2010,** *54* (2), 179-183.

[372] Zhou, L.; Xia, T.; Cao, T.; Wang, L.; Chen, Y.; Li, S.; Wang, R.; Guo, H., Morphology/phase-dependent MoS2 nanostructures for high-efficiency electrochemical activity. *Journal of Alloys and Compounds* **2020,** *818*, 152909.

[373] Cai, R.; Qin, H.; Yu, X.; Yan, F.; Wang, X.; Zhao, Y.; Wang, B.; Zhang, X., Kirkendall effect-assisted synthesis of hollow MoS2 nanospheres with interlayer expansion for improved magnesium diffusion kinetics and durability. *Journal of Materials Chemistry A* **2025,** *13* (4), 2574-2582.

[374] Mouloua, D.; Vicart, T.; Rajput, N. S.; Asbani, B.; El Marssi, M.; El Khakani, M. A.; Jouiad, M., Core/shell 1T/2H-MoS2 nanoparticle induced synergistic effects for enhanced hydrogen evolution reaction. *Journal of Colloid and Interface Science* **2025,** *687*, 851-859.

[375] Lassalle-Kaiser, B.; Merki, D.; Vrubel, H.; Gul, S.; Yachandra, V. K.; Hu, X.; Yano, J., Evidence from in Situ X-ray Absorption Spectroscopy for the Involvement of Terminal Disulfide in the Reduction of Protons by an Amorphous Molybdenum Sulfide Electrocatalyst. *Journal of the American Chemical Society* **2015,** *137* (1), 314-321.

[376] Shukla, A.; Bhat, S. D.; Pillai, V. K., Simultaneous unzipping and sulfonation of multi-walled carbon nanotubes to sulfonated graphene nanoribbons for nanocomposite membranes in polymer electrolyte fuel cells. *Journal of Membrane Science* **2016,** *520*, 657-670.

[377] Yin, Z.; Zhao, J.; Wang, B.; Xu, Y.; Li, Z.; Ma, X., Insight for the effect of bridging S22- in molybdenum sulfide catalysts toward sulfur-resistant methanation. *Applied Surface Science* **2019,** *471*, 670-677.

[378] Zou, L.; Qu, R.; Gao, H.; Guan, X.; Qi, X.; Liu, C.; Zhang, Z.; Lei, X., degradation of methylene blue. *Results in Physics* **2019,** *14*, 102458.MoS2/RGO hybrids prepared by a hydrothermal route as a highly efficient catalytic for sonocatalytic

[379] Zhang, Y.; Wang, L.; Chen, Q.; Cao, J.; Zhang, C., Recent progress of electrochemical hydrogen evolution over 1T-MoS2 catalysts. *Frontiers in Chemistry* **2022,** *Volume 10 - 2022*.

[380] Duraisamy, S.; Ganguly, A.; Sharma, P. K.; Benson, J.; Davis, J.; Papakonstantinou, P., One-Step Hydrothermal Synthesis of Phase-Engineered MoS2/MoO3

Electrocatalysts for Hydrogen Evolution Reaction. *ACS Applied Nano Materials* **2021,** *4* (3), 2642-2656.

[381] Guo, J.; Shi, Y.; Bai, X.; Wang, X.; Ma, T., Atomically thin MoSe2/graphene and WSe2/graphene nanosheets for the highly efficient oxygen reduction reaction. *Journal of Materials Chemistry A* **2015,** *3* (48), 24397-24404.

[382] Pham Thi Thuy, P.; Duy, N. P. H.; Tai, V.; Huan, N.; Phuc, N. H. H.; Loc, L., Facile synthesis of a green metastable MoO3 for the selective oxidation of methanol to formaldehyde. *Reaction Kinetics, Mechanisms and Catalysis* **2015,** *117*.

[383] Diaz-Droguett, D. E.; El Far, R.; Fuenzalida, V. M.; Cabrera, A. L., In situ-Raman studies on thermally induced structural changes of porous MoO3 prepared in vapor phase under He and H2. *Materials Chemistry and Physics* **2012,** *134* (2), 631-638.

[384] Mizushima, T.; Moriya, Y.; Phuc, N. H. H.; Ohkita, H.; Kakuta, N., Soft chemical transformation of α-MoO3 to β-MoO3 as a catalyst for vapor-phase oxidation of methanol. *Catalysis Communications* **2011,** *13* (1), 10-13.

[385] Muthamizh, S.; Sengottaiyan, C.; Jayavel, R.; Narayanan, V., Facile Synthesis of Phase Tunable MoO_3 Nanostructures and Their Electrochemical Sensing Properties. (1533-4899 (Electronic)).

[386] Li, L.; Ruan, M.; Tian, D.; Zhang, X.; Hou, X.; Zhong, K.; Cheng, F.; Tong, Y.; Fang, Z., Dual regulation mechanism of MoS2/MoO3 heterostructure for polysulfide and volume effect enables stable and durable lithium storage. *Applied Surface Science* **2024,** *646*, 158949.

[387] Nagyné-Kovács, T.; Studnicka, L.; Lukács, I. E.; László, K.; Pasierb, P.; Szilágyi, I. M.; Pokol, G. Hydrothermal Synthesis and Gas Sensing of Monoclinic MoO3 Nanosheets *Nanomaterials* [Online], 2020.

[388] Desai, N.; Mali, S., Chemically Grown MoO3 Nanorods for Antibacterial Activity Study. *Journal of Nanomedicine & Nanotechnology* **2015,** *06*.

[389] Lian, Z.; Mao, X.; Song, Y.; Yao, K.; Zhang, R.; Yan, X.; Li, M. The Preparation of High-Performance MoO3 Nanorods for 2.1 V Aqueous Asymmetric Supercapacitor *Nanomaterials* [Online], 2024.

[390] Mao, J.; Liu, P.; Du, C.; Liang, D.; Yan, J.; Song, W., Tailoring 2D MoS2 heterointerfaces for promising oxygen reduction reaction electrocatalysis. *Journal of Materials Chemistry A* **2019,** *7* (15), 8785-8789.

[391] Guo, S.; Yuan, P.; Zhang, J.; Jin, P.; Sun, H.; Lei, K.; Pang, X.; Xu, Q.; Cheng, F., Atomic-scaled cobalt encapsulated in P,N-doped carbon sheaths over carbon nanotubes for enhanced oxygen reduction electrocatalysis under acidic and alkaline media. *Chemical Communications* **2017,** *53* (71), 9862-9865.

[392] Lee, C.; Ozden, S.; Tewari, C. S.; Park, O.-K.; Vajtai, R.; Chatterjee, K.; Ajayan, P. M., MoS2–Carbon Nanotube Porous 3 D Network for Enhanced Oxygen Reduction Reaction. *ChemSusChem* **2018,** *11* (17), 2960-2966.

[393] Xia, Y.; Zhao, X.; Xia, C.; Wu, Z.-Y.; Zhu, P.; Kim, J. Y.; Bai, X.; Gao, G.; Hu, Y.; Zhong, J.; Liu, Y.; Wang, H., Highly active and selective oxygen reduction to H2O2 on boron-doped carbon for high production rates. *Nature Communications* **2021,** *12* (1), 4225.

[394] Zhang, M.; Guan, J.; Tu, Y.; Chen, S.; Wang, Y.; Wang, S.; Yu, L.; Ma, C.; Deng, D.; Bao, X., Highly efficient H2 production from H2S via a robust graphene-encapsulated metal catalyst. *Energy & Environmental Science* **2020,** *13* (1), 119-126.

[395] Novoselov, K. S.; Geim, A. K.; Morozov, S. V.; Jiang, D.; Katsnelson, M. I.; Grigorieva, I. V.; Dubonos, S. V.; Firsov, A. A., Two-dimensional gas of massless Dirac fermions in graphene. *nature* **2005,** *438* (7065), 197-200.

[396] Kumar, M. P.; Raju, M. M.; Arunchander, A.; Selvaraj, S.; Kalita, G.; Narayanan, T. N.; Sahu, A.; Pattanayak, D. K., Nitrogen doped graphene as metal free electrocatalyst for efficient oxygen reduction reaction in alkaline media and its application in anion exchange membrane fuel cells. *Journal of The Electrochemical Society* **2016,** *163* (8), F848.

[397] Robinson, J. T.; Perkins, F. K.; Snow, E. S.; Wei, Z.; Sheehan, P. E., Reduced graphene oxide molecular sensors. *Nano letters* **2008,** *8* (10), 3137-3140.

[398] Lu, C.-H.; Zhu, C.-L.; Li, J.; Liu, J.-J.; Chen, X.; Yang, H.-H., Using graphene to protect DNA from cleavage during cellular delivery. *Chemical Communications* **2010,** *46* (18), 3116-3118.

[399] Wei, D.; Liu, Y.; Wang, Y.; Zhang, H.; Huang, L.; Yu, G., Synthesis of N-doped graphene by chemical vapor deposition and its electrical properties. *Nano letters* **2009,** *9* (5), 1752-1758.

[400] Wang, X.; Li, X.; Zhang, L.; Yoon, Y.; Weber, P. K.; Wang, H.; Guo, J.; Dai, H., N-doping of graphene through electrothermal reactions with ammonia. *science* **2009,** *324* (5928), 768-771.

[401] Qu, L.; Liu, Y.; Baek, J.-B.; Dai, L., Nitrogen-doped graphene as efficient metal-free electrocatalyst for oxygen reduction in fuel cells. *ACS nano* **2010,** *4* (3), 1321-1326.

[402] Sheng, Z.-H.; Shao, L.; Chen, J.-J.; Bao, W.-J.; Wang, F.-B.; Xia, X.-H., Catalyst-free synthesis of nitrogen-doped graphene via thermal annealing graphite oxide with melamine and its excellent electrocatalysis. *ACS nano* **2011,** *5* (6), 4350-4358.

[403] Panchakarla, L.; Subrahmanyam, K.; Saha, S.; Govindaraj, A.; Krishnamurthy, H.; Waghmare, U.; Rao, C., Synthesis, structure, and properties of boron-and nitrogen-doped graphene. *Advanced Materials* **2009,** *21* (46), 4726-4730.

[404] Lin, Z.; Waller, G.; Liu, Y.; Liu, M.; Wong, C. P., Facile synthesis of nitrogen-doped graphene via pyrolysis of graphene oxide and urea, and its electrocatalytic activity toward the oxygen-reduction reaction. *Advanced Energy Materials* **2012,** *2* (7), 884-888.

[405] Liu, R.; Wu, D.; Feng, X.; Müllen, K., Bottom-up fabrication of photoluminescent graphene quantum dots with uniform morphology. *Journal of the American Chemical Society* **2011,** *133* (39), 15221-15223.

[406] Yang, S.; Zhi, L.; Tang, K.; Feng, X.; Maier, J.; Müllen, K., Efficient synthesis of heteroatom (N or S)-doped graphene based on ultrathin graphene oxide-porous silica sheets for oxygen reduction reactions. *Advanced Functional Materials* **2012,** *22* (17), 3634-3640.

[407] Shen, Y.; Rao, D.; Bai, W.; Sheng, Q.; Zheng, J., Preparation of high-quality palladium nanocubes heavily deposited on nitrogen-doped graphene nanocomposites and their application for enhanced electrochemical sensing. *Talanta* **2017,** *165*, 304-312.

[408] Wu, T.; Li, T.; Liu, Z.; Guo, Y.; Dong, C., Electrochemical sensor for sensitive detection of triclosan based on graphene/palladium nanoparticles hybrids. *Talanta* **2017,** *164*, 556-562.

[409] Zhang, Y.; Huang, B.; Ye, J.; Ye, J., A sensitive and selective amperometric hydrazine sensor based on palladium nanoparticles loaded on cobalt-wrapped nitrogen-doped carbon nanotubes. *Journal of Electroanalytical Chemistry* **2017,** *801*, 215-223.

[410] Wang, H.; Zhang, S.; Li, S.; Qu, J., Electrochemical sensor based on palladium-reduced graphene oxide modified with gold nanoparticles for simultaneous determination of acetaminophen and 4-aminophenol. *Talanta* **2018,** *178*, 188-194.

[411] Jukk, K.; Kongi, N.; Matisen, L.; Kallio, T.; Kontturi, K.; Tammeveski, K., Electroreduction of oxygen on palladium nanoparticles supported on nitrogen-doped graphene nanosheets. *Electrochimica Acta* **2014,** *137*, 206-212.

[412] Xi, J.; Xie, C.; Zhang, Y.; Wang, L.; Xiao, J.; Duan, X.; Ren, J.; Xiao, F.; Wang, S., Pd nanoparticles decorated N-doped graphene quantum dots@ N-doped carbon hollow nanospheres with high electrochemical sensing performance in cancer detection. *ACS applied materials & interfaces* **2016,** *8* (34), 22563-22573.

[413] Zhang, S.; Deng, X.; Chen, A.; Zhou, H.; Xie, Z.; Liang, Y.; Zeng, F., Facile synthesis of Pd supported on Shewanella as an efficient catalyst for oxygen reduction reaction. *international journal of hydrogen energy* **2019,** *44* (39), 21759-21768.

[414] Yang, Z.-Z.; Liu, L.; Wang, A.-J.; Yuan, J.; Feng, J.-J.; Xu, Q.-Q., Simple wet-chemical strategy for large-scaled synthesis of snowflake-like PdAu alloy nanostructures as effective electrocatalysts of ethanol and ethylene glycol oxidation. *International Journal of Hydrogen Energy* **2017,** *42* (4), 2034-2044.

[415] Kuniyil, M.; Kumar, J. S.; Adil, S. F.; Shaik, M. R.; Khan, M.; Assal, M. E.; Siddiqui, M. R. H.; Al-Warthan, A., One-pot synthesized Pd@ N-doped graphene: An efficient catalyst for Suzuki–Miyaura couplings. *Catalysts* **2019,** *9* (5), 469.

[416] Xie, S.; Deng, L.; Huang, H.; Yuan, J.; Xu, J.; Yue, R., One-pot synthesis of porous Pd-polypyrrole/nitrogen-doped graphene nanocomposite as highly efficient catalyst for

electrooxidation of alcohols. *Journal of colloid and interface science* **2022,** *608*, 3130-3140.

[417] Labulo, A. H.; Omondi, B.; Nyamori, V. O., Suzuki–Miyaura reaction and solventfree oxidation of benzyl alcohol by Pd/nitrogen-doped CNTs catalyst. *Journal of Materials Science* **2018,** *53* (23), 15817-15836.

[418] Wani, A. A.; Bhat, A. Y.; Ingole, P. P.; Bhat, M. A., Shape-Directed Growth of Palladium Nanocubes over Nitrogen-Doped Reduced Graphene Oxide: A Simple Approach for the Fabrication of an Efficient and Durable Electrocatalyst for Formic Acid and Methanol Oxidation Reactions. *Energy & Fuels* **2025,** *39* (1), 739-749.

[419] Gunes, B. A.; Kirlangic, O. F.; Kilic, M.; Sunguroglu, A.; Ozgurtas, T.; Sezginer, E. K.; Boyacioglu, B.; Unver, H.; Yildiz, M., Palladium metal nanocomposites based on PEI-functionalized nitrogen-doped graphene quantum dots: synthesis, characterization, density functional theory modeling, and cell cycle arrest effects on human ovarian cancer cells. *Acs Omega* **2024,** *9* (11), 13342-13358.

[420] Oh, Y.-J.; Cho, S. M.; Chung, C.-H., An in situ ATR-FTIR study on palladium displacement reaction on hydrogen-terminated silicon surface. *Journal of The Electrochemical Society* **2005,** *152* (6), C348.

[421] Sarmah, M.; Neog, A. B.; Boruah, P. K.; Das, M. R.; Bharali, P.; Bora, U., Effect of substrates on catalytic activity of biogenic palladium nanoparticles in C–C cross-coupling reactions. *ACS omega* **2019,** *4* (2), 3329-3340.

[422] Mohammed, L. S.; Hamza, I. S.; AL-Deen, F. R. M.; Muhyedeen, B. R., DFT and MP2 Study of Pd (II) and Ni (II) PhCN, DMSO and Dithiooxamide Complexes—Part II: Theoretical. *Journal of Applicable Chemistry* **2014,** *3* (5), 2102-2122.

[423] Bang, G. S.; Shim, G. W.; Shin, G. H.; Jung, D. Y.; Park, H.; Hong, W. G.; Choi, J.; Lee, J.; Choi, S.-Y., Pyridinic-N-doped graphene paper from perforated graphene oxide for efficient oxygen reduction. *ACS omega* **2018,** *3* (5), 5522-5530.

[424] Li, Y.; Li, Q.; Wang, H.; Zhang, L.; Wilkinson, D. P.; Zhang, J., Recent Progresses in Oxygen Reduction Reaction Electrocatalysts for Electrochemical Energy Applications. *Electrochemical Energy Reviews* **2019,** *2* (4), 518-538.

[425] Das, S.; Ghosh, S.; Kuila, T.; Murmu, N. C.; Kundu, A., Biomass-derived advanced carbon-based electrocatalysts for oxygen reduction reaction. *Biomass* **2022,** *2* (3), 155-177.

[426] Miao, H.; Li, S.; Wang, Z.; Sun, S.; Kuang, M.; Liu, Z.; Yuan, J., Enhancing the pyridinic N content of Nitrogen-doped graphene and improving its catalytic activity for oxygen reduction reaction. *International Journal of Hydrogen Energy* **2017,** *42* (47), 28298-28308.

[427] Ghosh, D.; Chen, S., Solid-state electronic conductivity of ruthenium nanoparticles passivated by metal–carbon covalent bonds. *Chemical Physics Letters* **2008,** *465* (1-3), 115-119.

[428] Ganguly, A.; Sharma, S.; Papakonstantinou, P.; Hamilton, J., Probing the thermal deoxygenation of graphene oxide using high-resolution in situ X-ray-based spectroscopies. *The Journal of Physical Chemistry C* **2011,** *115* (34), 17009-17019.

[429] Yang, D.; Velamakanni, A.; Bozoklu, G.; Park, S.; Stoller, M.; Piner, R. D.; Stankovich, S.; Jung, I.; Field, D. A.; Ventrice Jr, C. A., Chemical analysis of graphene oxide films after heat and chemical treatments by X-ray photoelectron and Micro-Raman spectroscopy. *Carbon* **2009,** *47* (1), 145-152.

[430] Xing, T.; Zheng, Y.; Li, L. H.; Cowie, B. C.; Gunzelmann, D.; Qiao, S. Z.; Huang, S.; Chen, Y., Observation of active sites for oxygen reduction reaction on nitrogen-doped multilayer graphene. *ACS nano* **2014,** *8* (7), 6856-6862.

[431] Zhang, L.; Xia, Z., Mechanisms of oxygen reduction reaction on nitrogen-doped graphene for fuel cells. *The Journal of Physical Chemistry C* **2011,** *115* (22), 11170-11176.

[432] Boukhvalov, D. W.; Son, Y.-W., Oxygen reduction reactions on pure and nitrogen-doped graphene: a first-principles modeling. *Nanoscale* **2012,** *4* (2), 417-420.

[433] Li, Y.; Zhou, W.; Wang, H.; Xie, L.; Liang, Y.; Wei, F.; Idrobo, J.-C.; Pennycook, S. J.; Dai, H., An oxygen reduction electrocatalyst based on carbon nanotube–graphene complexes. *Nature nanotechnology* **2012,** *7* (6), 394-400.

[434] Liu, Y.; Zhang, J.; Lu, X.; Zhang, G.-R.; Qi, K.; Bai, Y.; Qi, W., Highly efficient electroreduction of oxygen to hydrogen peroxide on carbon catalyst via electrode-electrolyte interface engineering. *Chemical Engineering Journal* **2022,** *444*, 136665.

[435] Li, L.; Lyu, X.; Liang, S.; Liu, Z., Efficient detection of hydrogen peroxide based on hollow SiO2 photonic crystals and Rhodamine 6G. *Microchemical Journal* **2023,** *193*, 109189.

[436] Kitte, A. S.; Assresahegn, D. B.; Soreta, R. T., Electrochemical determination of hydrogen peroxide at glassy carbon electrode modified with palladium nanoparticles. *Journal of the Serbian Chemical Society* **2013,** *78* (5), 701-711.

[437] Benvidi, A.; Nafar, M. T.; Jahanbani, S.; Tezerjani, M. D.; Rezaeinasab, M.; Dalirnasab, S., Developing an electrochemical sensor based on a carbon paste electrode modified with nano-composite of reduced graphene oxide and CuFe2O4 nanoparticles for determination of hydrogen peroxide. *Materials Science and Engineering: C* **2017,** *75*, 1435-1447.

[438] Rastogi, P. K.; Ganesan, V.; Krishnamoorthi, S., A promising electrochemical sensing platform based on a silver nanoparticles decorated copolymer for sensitive nitrite determination. *Journal of Materials Chemistry A* **2014,** *2* (4), 933-943.

[439] Cai, X.; Tanner, E. E.; Lin, C.; Ngamchuea, K.; Foord, J. S.; Compton, R. G., The mechanism of electrochemical reduction of hydrogen peroxide on silver nanoparticles. *Physical Chemistry Chemical Physics* **2018,** *20* (3), 1608-1614.

Publications

1. **P. Tripathi**, A. K. Verma, A. Vishwakarma, K. Mitra, B. Ray, A. S. K. Sinha, S. Singh, "Fabrication and Evaluation of a Self-standing Reduced Graphene-tungsten Oxides Hybrid Electrode for Acidic Water Splitting", **International Journal of Hydrogen Energy**, 2022, 47, 86, 36381-36396.
2. **P. Tripathi**, A. K. Verma, A. S. K. Sinha, S. Singh, "Graphene-Transition Metal Electrocatalysts for Sustainable Water Electrolysis", **Wiley ChemistrySelect**, 2024, 9, e202403155.
3. **P. Tripathi**, A. K. Verma, A. S. K. Sinha, S. Singh, "Cutting -Edge OER Electrocatalysts for Sustainable Seawater Electrolysis", **ACS Energy & Fuels**, 2025, 39, 5, 2348-2380. (Featured on Front Cover Page)
4. **P. Tripathi**, R. Shakir, A. K. Verma, J. Karthikeyan A. S. K. Sinha, S. Singh, "Enhanced Activity and Chlorine Protection in Prolonged Seawater Electrolysis using MoS_2/Sulfonated Reduced Graphene Oxide", **RSC Sustainable Energy Fuels**, 2025, 9, 4300-4319.
5. **P. Tripathi**, A. K. Verma, A. S. K. Sinha, S. Singh, "A trifunctional 3-D Self Assembled Graphene-Molybdenum Sulfide defensible electrode for green electrode reactions", **RSC New Journal of Chemistry**, 2025, (https://doi.org/10.1039/D5NJ02817E).
6. **P. Tripathi**, A. K. Verma, A. S. K. Sinha, S. Singh. "Palladium incorporated Nitrogen doped graphene as Bifunctional Electrocatalyst for Energy conversion and Sensing Applications", **ACS Applied Nano Materials**, 2025, (https://doi.org/10.1021/acsanm.5c03065).
7. **P. Tripathi**, A. K. Verma, A. S. K. Sinha, S. Singh. "Engineering MoS_2-Based Electrocatalysts for Water Splitting: A Comprehensive Review of Doping, Heterostructures, and Support Integration Strategies", **RSC Journal of Material Chemistry A**, 2025, (https://doi.org/10.1039/D5TA05734E).
8. A. K. Verma, **P. Tripathi**, A. Dubey, N. K. Vishwakarma, A. S. K. Sinha, S. Singh, "Visible Light-Promoted Enhanced Photocatalytic Hydrogen Generation by the CeF_3: Ho^{3+} Incorporated TiO_2 Nanosystem", **ACS Applied Energy Materials**, 2023, 6, 5739-5752. (Featured on Front Cover Page)
9. A. K. Verma, **P. Tripathi**, Z. Alam, S. K. Mishra, B. Ray, A. S. K. Sinha, S. Singh, "Photocatalytic Production of Oxygen by Nitrogen Doped Graphene Oxide Nanospheres: Synthesized via Bottom-Up Approach Using Dibenzopyrrole", **Wiley ChemistrySelect,** 2022, 7, e202202813.

10. A. K. Verma, **P. Tripathi**, A. S. K. Sinha, S. Singh, "Transforming β-SiC for Solar Hydrogen Evolution: Synergizing $YAlO_3:Ho^{3+}/Er^{3+}$ Upconversion, Conductive Polydopamine, and a Thermoelectric Device", 2025, (Manuscript under revision in **ChemSusChem**; Manuscript ID csc.202501580)

11. A. K. Verma, **P. Tripathi**, A. S. K. Sinha, S. Singh, "Engineering Upconversion Semiconductor Nanostructures: Unravelling the Morphology-Performance Relationship for Photocatalytic Hydrogen Generation". **ACS Applied. Energy Materials,** 2025, 8, 16, 11977–11987.

Book chapters:

1. A. K. Verma, **P. Tripathi**, A. S. K. Sinha, S. Singh, "Advanced Materials in Energy Conversion Devices": Fuel Cells and Biofuel Cells, Scrivener Publishing, Wiley (ISBN: 9781394185818), 2023, 273 – 284.

2. A. K. Verma, **P. Tripathi,** A. S. K. Sinha, S. Singh, "Sustaining Sub-bandgap Photons via Upconversion for Solar Splitting Cells", Intechopen Publishing, (ISBN: 978-0-85466-880-9), 2024, 227 – 246.

Patents:

1. Patent: "Layered electrode for seawater electrolysis" (Indian Patent Application No. 202211011767). NTPC-NETRA 2022.

2. Patent: "Molybdic transformation to efficient catalyst systems for sea water electro splitting and generation of hydrogen and oxygen"
(Indian Patent Application No. 202311053855). NTPC- NETRA 2023.

Conferences

1. "International Conference on Recent trends in Energy Science and Engineering" **ICRTESE-2021** (Virtual mode), October 26th -28th 2021, Rajiv Gandhi Institute of Petroleum Technology.
(**Oral presentation-** Development of Durable and Efficient Electrode for Sea Water Splitting Application).
Awarded with Best Oral Presentation.

2. "Chemical Engineering Congress" **CHEMCON-2022**, December 27th to 30th 2022, HBTU Kanpur.
(**Oral Presentation-** Stepping Towards a Successful Acidic Electrolyzer World with the Development of a Free-Standing, Three-Dimensional (3D) Reduced Graphene-Non-Noble Tungsten Oxide Electrode).

3. "International conference on Nano Materials for Sustainable Applications" **NANO-SA-2023,** Jan. 10th and 11th 2023, ICT Mumbai. (Participation).

4. "2nd International Conference on Energy Materials and Devices" **ICEMD-2024**, March 19th to 21st 2024, BHU Varanasi.
(**Poster Presentation-**Fabrication of Nitrogen-Doped Graphene Oxide Nanosphere with Palladium Embedded for Multipurpose Application).

5. "20th Annual session of Student's Chemical Engineers Congress" **IIChE-SCHEMCON 2024, September 20th-21st 2024**, Rajiv Gandhi Institute of Petroleum Technology
(**Oral Presentation-**Performance statistics of graphene -transition metal-based compounds in global scenario of water splitting).
Awarded with the Best Oral Presentation; paper recommended for "IIChE-SCHEMCON-2024 Best Paper Award"

6. "13th International Symposium on Electrochemical Science and Technology" **iSAEST-13**, January 8th to 10th, 2025, Thiruvananthapuram, Kerala.
(**Poster Presentation -**Functionalized Graphene Oxide as Chlorine Repellant for Seawater Electrolysis**).**

7. Royal Society of Chemistry's 2025 **#RSCPoster Conference** (virtual mode) **(Poster Presentation-**Sustainable Seawater Electrolysis using Functionalized Graphene sheets having barrier properties towards Chloride ion**).**

8. "1st International Conference on Materials for Next-Generation Technologies 2025" **ICMNT-2025** (Virtual mode), July 10th-11th 2025, Chandigarh University, Mohali.
(**Oral Presentation-**Sulfonated Graphene/MoS_2 as a durability booster for seawater electrolysis).

Workshop:

9. Basic Training Program in Nano Science and Technology (Online) by INUP Centre for Nano Science and Engineering (CeNSE), Indian Institute of Science (IISc), Bangalore-560012, India